FEDERAL UNIVERSITY OF TECHNOLOGY – PARANA

POST-GRADUATION PROGRAM IN CIVIL ENGINEERING

KIRILL ALEKSEEV

HAZARDOUS BAUXITE RESIDUE, BLAST FURNACE SLAG, AND FOUNDRY SAND APPLICATION AS THE MAIN COMPONENTS FOR ENVIRONMENTALLY FRIENDLY RED CERAMICS PRODUCTION

DOCTORAL THESIS

CURITIBA

2017

KIRILL ALEKSEEV

HAZARDOUS BAUXITE RESIDUE, BLAST FURNACE SLAG, AND FOUNDRY SAND APPLICATION AS THE MAIN COMPONENTS FOR ENVIRONMENTALLY FRIENDLY RED CERAMICS PRODUCTION

This thesis is presented in the Post-graduation Program in Civil Engineering, of the Federal University of Technology – Parana, in order to obtain doctoral degree in Civil Engineering, Concentration Area of Civil Construction, Research Line of Construction Materials and Components.
Advisor: Prof. Dr. Vsevolod Mymrin

CURITIBA

2017

ABSTRACT

ALEKSEEV, Kirill. **Hazardous bauxite residue, blast furnace slag, and foundry sand application as the main components for environmentally friendly red ceramics production**. 2017. 188 p. Thesis (PhD. in Civil Engineering) – Post-graduation Program in Civil Engineering, Federal University Of Technology - Parana. Curitiba, 2017.

In the presented research were used residues of aluminum and iron production. Bauxite residue, which is also called bauxite tailings or red mud, and blast furnace slag are the key wastes of metallurgical industry. There was also used foundry sand, which is a residue of casting process. These three components were used together to develop ceramic construction material. The main idea was to use industrial wastes only, no traditional natural materials. The waste glass and wood ash were added to the compositions in order to decrease melting point of the samples. In the research 24 compositions were sintered at 800-1225°C and their properties were studied. Their mechanical characteristics were analyzed using flexural strength test, measuring water absorption, density, and linear shrinkage. Physicochemical properties were studied by XRF, XRD, AAS, SEM, EDS, LAMMA, mapping, DTA, and TGA. The main reason for high results of flexural strength (19.78 MPa) of the samples was identified as a development of new amorphous formations. As a result of research, some compositions were suggested for specific construction materials production. Compositions containing red mud (40-100%), blast furnace slag (0-50%), foundry sand (0-50%), waste glass (0-20%), and wood ash (0-20%), according to Brazilian Norms and regulations for construction materials, may substitute traditional ceramic materials, which involve enormous exploration of natural resources.

Keywords: Bauxite residue; Red mud; Ceramic construction materials; Industrial waste application; Environmentally friendly ceramics production.

RESUMO

ALEKSEEV, Kirill. **Utilização da lama vermelha, da escória siderúrgica e da areia de fundição para a produção de materiais cerâmicos ambientalmente amigáveis**. 2017. 188 f. Tese (Doutorado em Engenharia Civil) – Programa de Pós-Graduação em Engenharia Civil - PPGEC, Universidade Tecnológica Federal do Paraná. Curitiba, 2017.

Nesta pesquisa foram utilizados resíduos da produção de alumínio e ferro. Resíduo de bauxita, que também é chamado de rejeitos de bauxita ou lama vermelha, e escória siderúrgica são os principais resíduos da indústria metalúrgica. Também foi utilizada areia de fundição, que é um resíduo do processo de fundição. Estes três componentes foram utilizados em conjunto para desenvolver material cerâmico de construção. A idéia principal era usar apenas resíduos industriais, sem materiais naturais tradicionais. Os residuos de vidro e as cinzas de madeira foram adicionados às composições para deminuir o ponto de fusão das amostras. Na pesquisa, 24 composições foram queimadas a 800-1225°C e suas propriedades foram estudadas. As características mecânicas das amostras foram analisadas através do teste de resistência à flexão, medindo-se a absorção de água, densidade e retração linear. As propriedades físico-quimicas foram estudadas por XRF, XRD, AAS, SEM, EDS, LAMMA, mapeamento, DTA e TGA. O principal motivo para os resultados elevados de resistência à flexão (19,78 MPa) das amostras foi identificado como o desenvolvimento de novas formações amorfas. Como resultado da pesquisa, algumas composições foram sugeridas para a produção específica de materiais de construção. Composições contendo lama vermelha (40-100%), escória siderúrgica (0-50%), areia de fundição (0-50%), resíduo de vidro (0-20%) e cinzas de madeira (0-20%), atenderam normas e regulamentos brasileiros para materiais de construção, podem substituir materiais cerâmicos tradicionais, que envolvem a enorme exploração de recursos naturais.

Palavras-chave: Resíduo de bauxita; Lama vermelha; Materiais cerâmicos de construção; Aplicação de resíduos industriais; Produção de cerâmica ecológica.

LIST OF FIGURES

LIST OF TABLES

LIST OF ABBREVIATIONS AND ACRONYMS

BFS – blast furnace slag
CPS – counts per second (XRD intensity)
DTA – differential thermal analysis
EDS – energy-dispersive X-ray spectroscopy
FS – foundry sand
NC – natural clay
RM – red mud
SEM – scanning electron microscope
TGA – thermogravimetric analysis
WA – wood ash
WG – waste glass
XRD – X-ray diffraction
XRF – X-ray fluorescence

TABLE OF CONTENTS

1 INTRODUCTION

Civil construction is one of the most important sectors in modern economy. It involves participation of many stakeholders, which leads to creation of working places. Data on the construction companies is usually used by economists to determine the country's economy condition. For example, employment rate and investment climate have straight correlation with civil construction sector. The development of this sector is a common way to boost country's economy. At the same time, it is important to mention that today civil construction is one of the main resource consumers. A major part of these resources is non-renewable, which also leads to negative impact on environment. That is why it is crucial to find alternative materials as society is going to run out of traditional materials very soon.

Mining industry is one of the major producers of by-products or industrial wastes. Every year billions of tons of tailings and wastes are being stocked in the dams. This attracts attention of many researchers, who treat this material as a potentially useful for consuming sector of civil construction. In this research five industrial wastes were used to create alternative construction material, which would solve various problems at the same time.

The main component is bauxite residue, which is also called bauxite tailings or red mud. It is a material that is produced when the Bayer process is applied to bauxite ore in order to obtain aluminium oxide. According to the World Aluminium database, only in April 2016 9.2 million tons of alumina were produced[1], which means that approximately 15 to 20 million tons of bauxite tailings were added to storage ponds around the world. Such large scale production puts great pressure on the storage infrastructure of alumina refineries, which has caused some of the notorious catastrophes around the world. For example, in October 2010 the corner of a red mud storage dam in western Hungary collapsed and a wave of red mud flooded the streets of a neighbouring city causing the deaths of nine people[2]. From an environmental point of view it is important to mention that the spill poured into the Danube and polluted 40 km^2 of land, contaminating the soil in the region. The two main reasons for treating this accident as an environmental disaster are: the high pH of red mud (13), due to the sodium oxide content; and a seven times higher content of heavy metals than in normal soil. In reality the problem is not the red mud itself, but in the approach to residue storage. There have been a variety of similar accidents involving different types of tailings and mine waste. The most recent incident in November 2015 was a spill of iron ore tailings in Mariana, Brazil,

---

[1] http://www.world-aluminium.org/statistics/alumina-production/#linegraph

[2] http://index.hu/belfold/2010/10/04/iszapomles_veszprem_megyeben/

which killed 12 people[3]. Described as the worst environmental disaster in the country's history, the flood contaminated a large stretch of the Doce River and eventually reached the Atlantic Ocean. It means that, even if advanced techniques are applied and storage is properly controlled, there is still a high risk of accidents. The only way to prevent such catastrophes is to stop storing tailings and to start recycling them.

Another component is blast furnace slag. Despite the fact that industrial scale of steel production was reached at the same time as an industrial scale of aluminum production in the middle of XIX century, the use of it’s byproduct, blast furnace slag, is much widely spread around the world. The main consumer of the slag is cement production industry. Due to the high content of CaO, blast furnace slag has positive impact on bending properties of the mortar. Unfortunately, there are still many deposits in which the slag stored without any use. According to Reuter et al. (2004) the amount of blast furnace slag production depends highly on the ore and other materials used during smelting. It is varied between 200 and 600 kg for production of one ton of iron. World steel association[4] presented data, that in 2015 66 countries, which produce 99% of world steel, have produced 1.6 billion ton of steel. It means that there are large amounts of blast furnace slag being accumulated as not all the types of blast furnace slag might be used by cement production industry.

Foundry sand is not a mining waste, but it is involved into the next stage of metal treatment – casting and molding. The forms, which are used to pour into a liquid metal, are made of sand with low content of binding material. As a result, the sand, which has a direct contact with liquid metal, receives a thermal shock, which leads to changes in properties of the sand. Normally, the same mold is used only once, but not everywhere. For this reason, the volumes of the foundry sand production are significant. The main problem about recycling of this sand is that because of the thermal shock it’s properties differ from the properties of the original sand, which may lead to some unpredictable problems. Because of that, this material is dumped without any use.

All these materials look promising in terms of construction material production. The attempt was made to substitute the traditional natural materials with presented byproducts and wastes.

---

[3] https://www.theguardian.com/sustainable-business/2015/nov/25/brazils-mining-tragedy-dam-preventable-disaster-samarco-vale-bhp-billiton

[4] https://www.worldsteel.org/statistics/crude-steel-production0.html

1.1 THE CONTEXT

The presented work is a practical research. It has gone through the experimental and analytical stages. The analysis of the data was quantitative and qualitative and relies on hypothetico-deductive method.

1.2 HYPOTHESIS AND QUESTIONS

The main hypothesis is based on the question if it is possible to receive ceramic material, which will attend the norms and regulations for such products, using only industrial wastes, without any addition of natural traditional materials.

There was also a group of questions, which appeared during the experiment and provoked further development of the whole concept. If the red mud used as a main component, which another component would increase the flexural strength and improve other properties: blast furnace slag or foundry sand? What is the impact of high and lower content of these components on mechanical properties of the final sample? If the high strength obtained at the high temperatures, what should be added to low the melting point of the samples: wood ash or waste glass? Is it possible to produce ceramics, which would have high strength at the low firing temperature? How the developed materials should be applied? What are the exact products that could be made of these materials?

1.3 OBJECTIVE

1.3.1 The main objective

The main objective of the research was to develop ceramic construction material, which would not contain any natural material and at the same time would fit into the norms and demands for traditional ceramic products for civil construction.

When different compositions were developed, according with their properties, were suggested the most efficient ways of application.

1.3.2 The specific objectives

The specific objectives are the following:

- To characterize the materials used in this research;
- To develop compositions, which attend Brazilian norms for construction materials;

- To study physicochemical processes in the samples during firing process;
- To determine the influence and the role of each component of the mixtures;
- Explain the origin of new formations and what do they mean.

1.4 METHODOLOGY

In order to achieve the before mentioned objectives, all the raw materials and prepared ceramics were analyzed by various complementary methods: XRF, using a Philips/Panalytical, model PW 2400 to conduct chemical analysis; XRD with a Philips, model PW 1830 to identify the mineralogical composition; SEM, using a Jeol JSM-6360 LV to determine the morphological structure of the particles; EDS with a Jeol JSM-5410 LV to identify the specific chemical composition of single particles of material; and LAMMA, using a LAMMA-1000, model X-ACT to determine the isotopic composition of samples; solubility and lixiviation of metals from liquid acid extracts - by AAS on a Perkin Elmer 4100 spectrometer; three points of flexural strength, using an EMIC DL-10; water absorption, density and linear shrinkage were also studied.

1.5 THE SHAPE OF THE DISSERTATION

The dissertation has been divided in chapters in the following way:

1. Introduction – contains the description of the chosen topic, the problem that could be solved by using presented in the research approach, the hypothesis of the research, objectives and methodology of the research and the structure of the dissertation.
2. Literature review – contains the description of what already has been done in the world in terms of the presented research’s objectives, briefly presented achievements of other researches, who have worked with the same materials.
3. Methodology – presents the detailed description of how the research has been carried out and which equipment has been used to identify characteristics of both raw materials and already prepared samples.
4. Raw materials characterization – gives characterization of materials that are being used in the research.
5. Characterization of the developed ceramics – analysis of the ceramic material properties.

6. Physicochemical processes of ceramics structure formation – explanation of what stood behind the mechanical properties of the samples.
7. Environmental characteristics of the developed ceramics – presentation of the information about environmental aspects of the developed method.
8. Conclusion – presents answers to the questions listed in the objectives and gives detailed conclusion on every stage of the research.
9. Reference list – lists the researches that were mentioned in this paper and gives links to norms and rules, which were used as a reference.

2 LITERATURE REVIEW

In this literature review have been presented brief summaries on achievements of researchers all around the world, who used the same materials or suggested similar approaches to their treatment as those used in the presented research.

2.1 RED MUD

According to Schwarz et al. (2012) there are more than 1500 patents related to red mud that were registered in patent database. Samal et al. (2013) and Liu (2009) gave explanation that one of the problems of red mud recycling is that costumer does not want to use the products made of waste material, especially hazardous waste material. Another obstacle for all these patents implementation is the large quantity of bauxite residues production. The limited consumption and markets for products made of red mud should be considered seriously. Some researches such as Liu et al. (2014) suggested classify red mud as a general industrial waste instead of hazardous waste in order to stimulate recycling.

There were many reviews made on red mud as material in general and main characteristics have been described: behavior of red mud, which is likely as clay soil with considerably high strength compared to conventional clay soil (SUSHIL et al. 2008); variety of chemical composition (DEELWAL et al. 2014); possible ways of utilization (SILVA FILHO et al. 2007); physical properties during firing process (WU et al. 2012); presence of hazardous elements such as As, Pb, Cr and Hg (GONDA1-ZSOMBOR et al. 2014); complex composition and small grain size (LIU 2009); the use of red mud as a building material and filler material is the most effective way to reduce the stockpiling (LIU et al. 2012); humidity content between 40% and 50% (YALCIN et al. 2001); surface chemistry characteristics (HIND et al. 1999). Still there are many things to discover about red mud. For example, Snars et al. (2009) compared eleven different samples of red mud, which were taken in Australia and overseas with pH values ranging from 8.4 to 12.6. The highest alkalinity had red mud from Spain and the lowest had Australian red mud, which was leached with dilute acid.

Besides chemical composition there are many other physical properties of red mud that already have been analyzed. For example, Hai et al. (2014) analyzed red mud from Vietnam and resumed that it does not contain artificial radioactive isotopes such as 137Cs, 7Be. Concentration of uranium and thorium is less than average concentration values of uranium (2ppm) and thorium (12ppm) in the earth’s crust.

Power et al. (2011), Grafe et al. (2011) and Klauber et al. (2011) have published research in four parts on red mud. Review on history of red mud production, ways of utilization, chemical properties of material and obstacles for bioremediation had been presented. The focus of research was on impact of red mud storage to the nature, especially on soil and plants. Courtney (2012) analyzed red mud from Ireland, where gypsum is applied as an amendment to reduce pH and sodicity. The author recommends that excessive Al uptake in restores residue can be avoided by adding adequate calcium and other nutrients, so nutrient recycling is encouraged as part of the grassland restoration programme.

After Ajka alumina plant accident in 2010 problem of red mud storage attracted attention of public. It became clear that it is not only inefficient to store red mud, but also dangerous. Milacic et al. (2012) compared red mud of Ajka's deposit in Hungary, which caused catastrophe, and red mud from deposit in Kidricevo, Slovenia. He concluded that Slovenian red mud had lower pH, approximately 9 and lower Al solubility, which is environmentally safer and carries a smaller risk of ecological accidents. But still Slovenian red mud is not neutral and in case of the same catastrophe it will spoil rivers and soils.

Some researchers suggested ways of filtration of red mud before storage, so in case of accident it would not be so harmful for the environment. For example, Borges et al. (2011) described technique of red mud filtration for reduction of caustic content. The study had practical part at alumina refinery in Para, Brazil. Four filters were applied and in the first filter soda concentration ranged from 4.5 to 8.5 grams per liter, while in the fourth filter the range was between 8.5 and 11.0 grammas per liter, which means that the goal of the study has been achieved.

Looking for alternative methods to utilize red mud some researchers suggested to use red mud as a tool instead of using it as an object. Zhang et al. (2014) presented method of treating sewage sludge conditioning with red mud combined with Fenton's reagent. Sludge dewatering performance was effectively improved and economic assessment has been presented. It seems useful in terms of global pollution. Same approach, but for another material was suggested by Browner (1995), who presented red mud as a suitable pH modifier for the gold industry.

Considering all information presented in international publications and patents, it is important to choose main fields and areas, where red mud could be treated reaching maximum efficiency. It could be divided in a following way: ceramics production using red mud as a raw material; leaching of different elements (rare earth elements, iron, titanium etc.) from red mud; blocks production without firing or sintering using red mud; application of red mud in cement and concrete production.

2.1.1 Leaching of materials from red mud

To begin with, it is important to mention main patents in the field of leaching iron, rare earth materials and other elements from red mud. The first one is a patent of Zimmer et al. who in 1978 presented “Reclamation treatment of red mud”, a technique of heating red mud with addition of concentrated sulfuric acid. When heated between 250°C and 350°C with sulfuric acid, major elements mostly are presented as sulfates. After that solid sulfates heated to the range of 900°C to 1000°C in order to decompose the sulfates of aluminum and iron, which later are separated by Bayer process.

Another registered patent is Fulford et al. (1991), which is focused on rare earth elements and called “Recovery of rare earth elements from Bayer process red mud”. The main three steps are: digesting red mud containing rare earth elements with dilute acid solution, separating the solution obtained from the solid residue and recovering the rare earth elements from the solution.

Taking into account some attempts to recover not only iron and rare earth materials, but other elements, important to mention Barnett et al. (2001), who registered a patent on a method for processing red mud to recover iron oxide, alumina, silica and titania values. The method is based on separation of salts with water treatment and further separation of metals. Completely opposite way of treating red mud suggested Boudreault et al. (2015) in the patent “Process for treating red mud”, which aimed to extract all valuable materials out of red mud using HCl. There are no examples of implementation of this technique, but theoretical part looks like a complex approach to red mud’s problem solution.

Articles on this topic are close in ideas to patents, which already have been registered. They can be divided in groups. First group is about leaching of iron from red mud. Liu et al. (2014) presented an overview of the current techniques employed for iron recovery from red mud and introduced several new techniques. The overview summarized that there are two basic methods to recover metals: pyrometallurgy and hydrometallurgy. The majority of researchers, who have worked on this topic, are from China, which is very rich in bauxite. Liu et al. (2009) proposed method of direct reduction roasting-magnetic separation process of iron form red mud and further use of its residue as a raw material for building materials. As regards iron leaching, the following conditions were suggested: roasting temperature of 1300°C, roasting time of 110 min, the carbon to red mud mass ratio of 18:100, the additives

($CaCO_3$ and $MgCO_3$) to red mass ratio of 6:100. As a result recovery rate reached 81.40%. After that brick made of residue has been prepared. The compressive strength reached 24.10 MPa at the content of hydrated lime of 13%.

There are some other methods, which do not have complete cycle of materials use. Li et al. (2009) described recovery of alumina and ferric oxide by reduction sintering. The conclusion is that alumina recovery can reach 89.71% and iron recovery can reach 60.67% with the grade of magnetite concentrate 61.78% under optimized conditions. Extraction of both aluminium and iron was also presented by Zhu et al. (2012) who added sodium carbonate. The result showed that the final product, assaying iron of 90.87% and aluminium oxide of 0.95% and metallization degree of 94.28% was obtained at an overall recovery of 95.76% under condition of adding 8% sodium carbonate and reduction roasting at 1050°C.

Basically, the majority of methods is about magnetic separation of iron. Liu et al. (2014) used pyrite (FeS_2) to transform iron oxide (Fe_2O_3) to magnetite (Fe_3O_4) in order to apply magnetic separation after co-roasting for iron leaching from red mud. The main concern of researches was the release of SO_2 during roasting, which was collected in water and then sulfuric acid could be produced. Another way is presented by Li et al. (2011), who applied high gradient superconducting magnetic separation system to separate red mud into high iron content part, containing 65% of iron oxide, and low iron content part, containing 45% of iron oxide. After eight separation stages 94.8-95.3% of iron has been recovered, depending on quality of red mud that had been used. In terms of magnetic separation Samouhos et al. (2013), also described research, focused on development of an alternative microwave reductive roasting process of red mud using lignite, followed by wet magnetic separation. Final product supposed to be suitable for sponge or cast iron production. The dielectric constants were determined at 2.45 GHz, in temperature range of 25-1100°C. As a result a magnetic concentrate with 35.1% total iron concentration and 69.3% metallization degree was obtained.

There were also researches with main focus not on iron. Liu et al. (2012) obtained 75.7% of Al and 80.7% of Na through sod-lime roasting followed by leaching of the roasted material. Also 51.2% of Fe was recovered with magnetic separation method. Borra et al. (2015) using HCl received the following results: dissolution of iron approximately 60%, extraction of rare earth elements around 80%, aluminium, silicon and titanium were between 30% and 50%, and sodium and calcium were completely dissolved. Another expensive metal to extract is titanium and Agatzini-Leonardou et al. (2008) described method of titanium leaching from red mud by diluted sulfuric acid as atmospheric pressure. As a result, the titanium recovery efficiency on the basis of red mud weight reached 64.5%.

There were also some papers focused on rare earth materials, not that many as on iron leaching, but still there are some. Li et al. (2013) discovered high concentration of rare earth materials in Wulong-Nanchuan bauxite deposit in China. The sum of all rare earth elements varied widely from 17 to 3610 ppm. Qu et al. (2013) described biological leaching of rare earth elements and radioactive elements from red mud. An acid-producing fungi named RM-10, Penicillium tricolor has been used. The highest extraction yields are achieved under two-step bioleaching process at 10% pulp density. The main lixiviants were oxalic and citric acids. Since bioleaching has been mentioned, important to introduce paper of Liu et al. (2015), who outlined another method of treating red mud – biometallurgy. Author comes to conclusion that nearly all the researches have used inorganic acids as leachant to extract valuable elements, especially for rare earth elements. Furthermore, it is stated that it is not profitable to recover valuable metals from red mud solely or one by one. The resulting residues after metal recovery can be used as a raw material for the preparation of building decorations, catalytic supporting materials, adsorbents, etc.

To finish this specific area important to mention completely different scientific achievements, which still are in the same field of research. Li et al. (2006) made research on using red mud and fly ash for removal of phosphate from wastewater. As a result, almost 99% phosphate was removed using red mud stirred with 0.25 M HCl. The amount of phosphate removal increased with the solute concentration.

And there are some methods which are not that complete, but still have an aim and means to achieve it. Vaclavikova et al. (2005) and Ju et al. (2012) both used red mud as a sorbent for the removal of toxic bivalent cations from aqueous solutions. Ju mixed red mud with cement in order to remove cadmium. Vaclavikova provided data that red mud can adsorb considerable amount of cadmium and zinc from near-neutral aqueous solutions. Smiciklas et al. (2013) used red mud for nickel removal from aqueous solutions. Collins et al. (2014) presented research on manganese, chromium, cobalt, nickel, copper and zinc removal using red mud.

2.1.2 Blocks production from red mud without firing

There are two patents being registered on the subject of blocks production using red mud without sintering. The first one made by Jaquays (2003) and called “Building and other materials containing treated bauxite tailings and process for making same”. Another one is

Skoda's et al. (2013) patent "Stabilized red mud and methods of making the same". Both patents do not have clear explanation of method or technique.

Jamaican researches have not just developed samples in the laboratory, but also made some successful attempts of implementation. Gordon et al. (1996) used Jamaican red mud for production of new construction materials, which had compressive strength in the range 15-18 MPa at 28 days and 18-22 MPa at 122 days. The author used different proportions of red mud, hydrated lime, condensed silica fume and limestone. It is stated that such a resistance is satisfactory taking into account the fact that there is no cement in composition.

Different way of paving block preparation without addition of cement was described by Kumar et al. (2013), who presented compositions containing only red mud and fly ash. Considering results of the paper, mixtures of 20% red mud and 80% of fly ash and 10% red mud and 90% of fly ash were the best. Water absorption was 6-7%, flexural strength 3.2-4.5 MPa. But long term durability tests are still needed. Familiar research has been made by Bhaskar et al. (2014), who investigated the way red mud reacts with fly ash and came with a decision that the best proportion is 50% of red mud and 50% of fly ash. Brick had 5.5 MPa compressive strength and 10% water absorption. At the same time, Zhang et al. (2014) presented geopolymer made of red mud and fly ash, which strength increased continuously with curing for up to 180 days.

Another approach, which is based on small addition of cement was suggested by Yang et al. (2008) and summed up the following composition of brick: 25-40% red mud, 18-28% fly ash, 30-35% sand, 8-10% lime, 1-3% gypsum and about 1% Portland cement. The properties of developed bricks are: compressive strength 19.43 MPa, flexural strength 5.05 MPa, water absorption 22.39%, compressive strength after 15 cycles of freezing-thawing from -20°C to 20°C 12.93 MPa.

2.1.3 Applications of red mud for cement and cementitious material production

The main problem of red mud addition in cementitious material production is that binding properties of red mud are not that visible and clear. The only patent which fits this topic is "Use of cement kiln dust and red mud to produce hydraulic cement" which was registered by Hassa Kunbargi in 1986. Author used red mud as an aggregate.

No positive influence of red mud on cement properties has been found in research of Tsakiridis et al. (2004), who studied red mud addition in the raw meal for the production of Portland cement clinker. The result of the physic-mechanical tests showed that the addition of red mud did not negatively affect the quality of produced cement. At the same time, Govindarajan et al. (2012) presented results showing that red mud calcined at 600°C is a good pozzolanic material. The compressive strength of cement containing 20% red mud was higher than that of ordinary Portland cement at all hydration periods.

Valuable properties of red mud were also described in paper of Nithya et al. (2016), who analyzed concrete in which red mud was used for replacement of cement with hydrated lime. It is stated that red mud can be effectively used as a replacement material for cement. It improved the cement quality, reduced the setting time and improved compressive strength. Replacement of 20% ordinary Portland cement by calcined red mud is thus possible. The result of pozzolanic activity by chemical and physical methods was very satisfactory and indicated the feasibility of red mud use as a pozzolan, in addition to Portland cement.

Zhang et al. (2009) presented mixture of red mud and coal gangue at 3:2 ratio with addition of blast furnace slag, clinker and gypsum. As a result, red mud and coal gangue can replace up to 50% of the raw materials to produce cementitious material. Two years later Zhang et al. (2011) developed cementitious material containing 30% of the bauxite-calcination-method red mud possessed compressive strength properties as a level similar to normal Portland cement, in the range of 45.3-49.5 MPa. Best compressive strength values were demonstrated by the specimen containing 30% bauxite-calcination-method red mud, 21% blast furnace slag, 10% fly ash, 30% clinker, 8% gypsum and 1% compound agent (Na_2SO_4:NaCl as 7:3 ratio).

Another idea was presented by Pontikes et al. (2013), who suggested use of red mud as a pozzolanic material for ordinary Portland cement production. It can take place in amounts close to 5% or most likely 3% depending on composition of red mud, in the raw meal. A dewatering step is needed and levels of Na, Ti and Cr are of interest and along with the Fe/Al ratio can determine maximum addition levels. Addition of red mud is preferably after calcinations. Considering calcination process, Liu et al. (2011) explained that red mud calcined at 600°C has good cementitious activity due to the formation of poorly-crystallized Ca_2SiO_4.

Senff et al. (2011) analyzed effect of red mud addition on the rheological behavior and on hardened state characteristics of cement mortars. Red mud showed small capacity to fix calcium ions that are presented in the aqueous solution, suggesting low pozzolanic activity. Bauxite residue increased the values of torque, especially on mixtures prepared with lower water levels. Red mud did not significantly delay the hydration process. Some real figures were presented in report of Yao et al. (2013). The author presented cementitious material that was mainly composed of red mud, coal refuse and coal fly ash. The designed material had higher strength in the middle to late curing age (180 and 360 days) than the ordinary Portland cement.

2.1.4 Ceramics production using red mud

To begin with, in 1975 Gerhard Bayer registered a patent called “Method for producing bricks from red mud”. The method is about firing mixture of up to 92% of red mud with clay at a temperature between 900°C and 1100°C. This patent is a fundamental for all researches which scientists do even nowadays, 40 years later. Gerhard Bayer is one of the founders of this method and approach to red mud recycling for fired bricks production in general.

Another researcher is Gregory Onyemauwa Iwu, who in 1976 created United States patent on “Method of treating bauxite waste red mud with acid and making construction bricks from the treated material”. In order to dissolve sodium content, red mud should be treated with hydrochloric acid. After that, the material should be mixed with kaolinitic clay and can be formed into construction bricks. Comparing with Gerhard Bayer’s patent the main difference of this method is an attempt to neutralize alkalinity of red mud before using it as a raw material.

In 1977 in Germany appeared the patent of Rudolf Riedel, who presented it with the following title “Ceramic products made from red mud and domestic refuse by baking without using primary energy source”. Composition of mixture is what makes it special. Domestic refuse can be fresh, dried, compost or the residue from a refuse incinerator. In this case final composition of mixture can vary a lot and it is difficult to control it when applied on industrial scale.

The last but not the least is Ferenc Puskas, who in 1983 registered a patent “Process for the utilization in the ceramics industry of red mud from alumina plants”. The idea was to mix 51-90% of red mud with 10-49% silicate containing material, to shape the mixture and fire at a temperature 950°-1250°C. The technological part of industrial production process helps this patent to stand out. Range of compositions and temperatures is wide and it seems like the author covered majority of brick production ways with his patent.

There is a big amount of papers, which described red mud and clay mixtures. One of the main papers is an article in two parts published by Sglavo et al. (2000) describing addition of red mud to clay for ceramics production. The conclusion that he made is simple – red mud can be added to clay for ceramics production. The weak point of this research is that Sglavo added only from 5% to 20% of red mud to clay, so the idea of recycling cannot be resolved in such a way, red mud should be used as a main raw material and not additional. He et al. (2012) presented the ideal proportion of clay to red mud as 80% to 20%, which is very alike to Sglavo's results. The fact that optimal temperature of 1050°C was chosen, means that temperatures above 1000°C should be taken into further consideration. The author concludes that content of more than 40% of red mud leads to formation of glass.

Dodoo-Arhin et al. (2013) and Perez-Villarejo et al. (2012) both have mixed red mud with clay, which has already been done by other researchers, but both of them came to solution that 50% of clay and 50% of red mud is the best proportion for bricks production, while other authors suggested adding less than 50% of red mud to clay. Perez-Villarejo showed results of uniaxial compression 52 MPa, 21% water absorption, linear shrinkage 0.46% and weight loss after sintering 12.6%. The same mixture of 50% red mud and 50% of clay at the same firing temperature of 950°C of Dodoo-Arhin showed flexural strength of 16.6 MPa. Instead of using traditional clay, Kavas (2006) used mixtures of 85% of red mud and 15% of fine and clay waste with addition of boron for better fusion. As a result, compressive strength is 453 kg/cm^2 at 900°C. This mixture showed also better than others results at lower temperatures 700°C and 800°C.

Besides studying compositions it is also important to analyze behavior of red mud while firing. For example, Pontikes et al. (2007) cited Prasad and Sharma (1986), who summarized their results in the article as following: minimum sintering temperature should be 1050°C and maximum is 1120°C, above 1120°C brick becomes dark and heavy. Pontikes et al. (2007) analyzed thermal behavior of red mud and came with result that firing above 950°C starts the second shrinkage zone. He also concluded that for better quality of red mud brick, it could be sintered in atmosphere with high content of N_2. On the other hand, it is composition of red mud which has the most influence on firing process, that is why Yang et al. (2008) presented thermal analysis and concluded that optimum nucleation temperature is about 697°C. He described red mud as a CaO-rich material, which can be used for glass-ceramics production. In his research red mud with high content of CaO and Al_2O_3 was combined with fly ash, which had high content of SiO_2. This combination resulted in glass-ceramics.

There were also some attempts to mix red mud with other wastes and observe the way they would react. Chen et al. (2013) made research on red mud and fly ash mixtures, but in this case sodium silicate has been used as a foaming agent. Firing temperature reached 900°C. Bulk density was 0.51-0.64 g/cm^3, compressive strength was between 4.04 and 10.63 MPa. Different results could be explained with different compositions that were prepared. These results were obtained by 40-50% of red mud, 26.25-40% fly ash, 15-20%

sodium borate and 5% sodium silicate. At the same time, Badanoiu et al. (2015) synthesized red mud and another waste – cullet soda-glass at 600-800°C in order to receive foamed geopolymer. The compressive strength was in the range of 2.1-8.6 MPa. SEM analysis showed that after sintering all components of mixture have fused, which gave good results on strength.

Yalcin et al. (2000) suggested different percentage of red mud content for different types of ceramic products. For porcelain glazes – 23%, vitreous glazes – 24%, tile glazes – 30% and electro-porcelain glazes – 37%. He also analyzed influence on color of the ceramics and came with conclusion to use red mud as a pigment material. It seems like this is the most complex approach to red mud treating in terms of ceramics production with variety of products that could be produced from waste. At the same time, Guo et al. (2014) had different approach to ceramics preparation. The aim was to make porous material, that is why foaming agent has been used. Mixture of fly ash and red mud was prepared in 40 to 60 ratio and $CaCO_3$ was added. As a result, low density 0.33-0.41 g/cm^3, low sintering temperature 760-840°C and compressive strength 0.33-2.74 MPa.

There are some types of red mud that have high radioactivity level. In general, radioactivity of red mud reported to be normal, but in Western Australia red mud showed high level of radioactivity. Qin et al. (2011) analyzed especially this physical property of red mud and stated that level of radioactivity has declined after red mud sintering from 6360 Bq to 4540 Bq.

Talking about different characteristics of red mud that depend on location of mine, it is important to mention that Liao et al. (2015) discovered compositional difference of red mud in terms of TiO_2 and quartz, which makes red mud from Chinese refinery Pingguo different in comparison with red mud from other regions of China. It means that bauxite residue differs depending on the place and exact refinery. That is why it is difficult to find common process of red mud recycling for the whole world.

2.2 BLAST FURNACE SLAG

In general, there are different types of slag. The main difference is the way the slag was produced. There are many factors that influence the production process: type of the furnace, materials used in process, chemical composition of the ore, and method of slag discharge after separation of the iron. For this reason, chemical composition of the blast furnace slag may differ significantly. Another problem is that sometimes researchers receive the material from the industry for experiments without information about what process exactly stood behind this material, which causes some errors when, for example, they call their material granulated slag instead of air-cooled slag. In terms of research it might be not a big deal as the main characteristic of the material is chemical composition. But when it comes to comparison of the results in attempt to explain the behavior of the material this uncertainty might lead to misunderstanding.

As it was mentioned before, the chemical composition of blast furnace slag may be absolutely different when two samples of slag are compared. Due to this fact, researchers use blast furnace slag for different purposes. The aim of the research might be achieved using properties of exact type of slag.

2.2.1 Applications for binder materials production

Some researchers presented idea of blast furnace slag use as a binder material. Kumar et al. (2008) presented Portland slag cement, which was prepared using mechanically activated clinker and slag. It was found that up to 85% replacement of clinker by slag is possible without impairing strength.

Blast furnace slag was also treated as a material, which can potentially replace cement. For that reason, Kim et al. (2013) presented study comparing CaO with $Ca(OH)_2$ as potential activators for non-cement binder production. As a result, the use of CaO provides a higher mechanical strength than $Ca(OH)_2$.

Strength is not the only characteristic to refer, when construction materials are produced. One of the crucial points is durability of material. Lukowski et al. (2015) investigated durability of mortars containing ground granulated blast furnace slag in acid and sulphate environment and concluded that strength development of the composites with slag is slower.

As it was mentioned before, some of the authors suggest different ways of use of the same developed material. The paper of Jamshidi et al. (2015) had focus on cement pastes, in which he described that blast furnace slag in cement pastes proportionally reduced the compressive strength after 7 days, which lead to 40 MPa for cement pastes containing 50-70% blast furnace slag. At the same time the compressive strength at 28 days increased.

2.2.2 Application for concrete production

Concrete is literally a fundamental material in the world of construction and this is the reason for researchers to keep on looking for better and cheaper ways of concrete production. Due to the fact that it is difficult to calculate economic output, scientists put stress on mechanical properties of concrete, which was produced using blast furnace slag. Etxeberria et al. (2010) concluded that concretes that were produced with electric arc furnace slag and blast furnace slag as replacement for raw coarse aggregates obtain higher compressive strength than the conventional concrete. At the same time, Lubeck et al. (2012) presented mixtures in which 50% and 70% white Portland cement was replaced with blast furnace slag, concluding that there was minimal difference between those and one which was composed of 100% white Portland cement. This indicates the feasibility of partially substituting white Portland cement for slag. Considering long-term behavior of material Ozbay et al. (2016) mentioned that one of advantages of ground granulated blast furnace slag use is enhancement of the long term compressive strength, especially after 40 days of curing.

Some of the scientist used blast furnace slag not as an active component, but as an aggregate. For example, Sumayya et al. (2016) concluded that black and dense electric arc furnace slag, when being cooled under natural conditions, shows better physical properties that natural aggregates.

There were also attempts to replace natural aggregates partially. Monosi et al. (2016) noticed while partial replacement of natural aggregates that electric arc furnace slag determines a significant increase in the compressive strength of concrete while it does not seem to affect the bending strength and drying shrinkage of cement mixtures. Another comparison of slag with natural materials was made by Yeih et al. (2015), who indicated that concrete made with air-cooling electric arc furnace slag had better mechanical strength than another one made with natural river gravels.

A bit different way of analysis was made by Sekar et al. (2016), who presented new approach to concrete preparing mixtures of ground granulated blast furnace slag, coconut shell and manufactured sand. It was stated that for 50% replacement of cement by slag compressive strength was reduced by 26%, 24% and 22% respectively for water cured, steam cured and conceal cured.

2.2.3 Blast furnace slag use in road construction

Road construction is one of the most material consuming spheres of construction in general. Many researches were made in this field, to replace traditional and natural materials with cheaper residues. For example, Mymrin et al. (2003) developed material, which can be used for production of different products: levee cores, dumps, tiles and bricks, roads basis. The idea is to activate binding properties of blast furnace slag and make CaO work. Strengthening process could be accelerated by addition of 2% Portland cement. The uniaxial strength of samples after one year of curing reached 47.6 MPa. In another paper, Mymrin et al. (2005) has discovered that mixture of soil and blast furnace slag gains resistance during hydration process. The main reason for that is high content of CaO in blast furnace slag, which makes it suitable for road base construction.

Pasetto et al. (2010) used electric arc furnace steel slag containing almost 30% CaO, he resumed that slag has shown physical-mechanical characteristics substantially equivalent to those of natural stone aggregates.

Mahieux et al. (2009) suggested a way of activation of ground granulated blast furnace slag with basic oxygen furnace slag to produce a hydraulic road binder. Composition of 52.5% ground granulated slag and 42.5% basic oxygen slag with 5% catalyst resulted in compressive strength higher than 10 MPa at 28 days.

Important research to show environmental impact of such a technique was made by Chaurand et al. (2007), who presented results of tests showing leaching values, which resulted in low chromium release and significant release of vanadium.

2.2.4 Application for ceramics production

There are researches being presented, in which blast furnace slag was added in compositions and then fired at high temperatures. Ozturk et al. (2015) added up to 33% blast furnace slag into raw mixture for wall tile production and received about 25% increase in strength. Four main mixtures were prepared containing clay, sand, limestone, kaolin and slag. Author sums up that blast furnace slag can be used to produce anorthite based quality tiling.

Similar conditions of research were presented by Ozdemir et al. (2007), who investigated mixtures of clay and blast furnace slag sintering at 1150°C, 1175°C and 1200°C for 1 hour. It was noticed that water absorption and apparent porosity values increased with the rise of blast furnace slag addition, but values of firing shrinkage decreased.

As it can be assumed, that blast furnace slag was used at high temperatures and played vital role in pores closing process. For achievement of this aim glass can be also added. For example, Ding et al. (2015) presented glass-ceramic foams, which were produced using blast furnace slag and waste glass. As a result, samples had low bulk density 0.79 g/cm^3, low water absorption 2.71% and high bending strength 14.34 MPa.

In contrast with high temperatures technique, there are some researches aiming to receive material with high porosity at the low temperatures. Francis et al. (2013) used glass cullet and blast furnace slag for porous glass-ceramics composites production.

To end up the list, absolutely different way of preparing compositions was presented by Wei et al. (2014) in which electric arc furnace slag and Taichung harbor sediment were used at ratios of 10/100-50/100 with firing temperature at 950-1050°C and 1100°C.

2.3 FOUNDRY SAND

Foundry sand, which is also called molding sand, is a residue of metal casting process, in which it is used to prepare shape. Basically, after being used it has same characteristics as normal sand, but sometimes it gets contaminated by liquid metal, with which it was in contact.

2.3.1 Foundry sand in concrete production

There were attempts to use foundry sand as an aggregate material in concrete production. Guney et al. (2010) replaced natural fine sand with waste foundry sand reaching up to 15% replacement. As a result, it was concluded that concrete with 10% waste foundry sand shows almost similar results to the traditional one. Singh et al. (2012) also made comparison of natural sand and waste foundry sand. He stated that replacement of sand with waste foundry sand enhanced the 28 days compressive strength by 8.3-17%, splitting tensile strength by 3.6-10.4% and showed continuous improvement in mechanical properties up to the ages of 365 days. Siddique et al. (2008) made conclusion that foundry sand could be conveniently used in making good quality concrete and construction materials. Strength of concrete mixtures increase with the increase of foundry sand content and also with the age. Later Siddique et al. (2015) has published research with comparison of natural sand and foundry sand in context of it’s influence on concrete. Test results indicate a marginal increase in strength and durability properties of plain concrete by inclusion of foundry sand as a partial replacement of fine aggregate. Prabhu et al. (2014) prepared different mixtures using foundry sand as a fine aggregate. The test results revealed that the strength properties of the concrete mixtures containing up to 20% foundry sand were relatively close to the strength value of the control mixture, which had no foundry sand. Basar et al. (2012) also received results which show that concrete containing 20% waste foundry sand exhibited almost similar results with the control mixture of concrete.

Different types of mixtures were analyzed by Pathak et al. (2012), who used also fly ash, which could be the main reason for such results, and concluded that while in self-compacting-concrete production spent foundry sand and fly ash reduce the strength of concrete, it is still possible to produce it with compressive strength ranging from 19.75 to 30.69 MPa at 28 days, 29.12 to 39.56 MPa at 91 days and 31.95 to 42.35 MPa at 365 days at elevated temperatures.

2.3.2 Foundry sand in cement blocks production

Production of cement blocks is similar to concrete production, which is the reason to test foundry sand in terms of blocks production. Mastella et al. (2014) presented idea that waste foundry sand can be used in masonry blocks and paver production, considering mechanical properties and data on leaching test. Mixtures which had 22% cement showed 35 MPa compressive strength in 28 days, while mixtures with 17% cement reached the same level only in 56 days.

2.3.3 Foundry sand in ceramics production

In the process of ceramics production, clay is the main component, and sand takes second place. That is why some researches have been made developing an idea of substitution of traditional sand with foundry sand. For example, Mymrin et al. (2014) suggested foundry sand along with other industrial wastes addition for ceramics production. As a result, after firing at 950-1050°C flexural strength of samples reached 14 MPa. The most important thing is that final product was completely environmentally friendly. Another research is made by Pytel (2014), who concluded that waste foundry sand after crushing and process of metal separation can become a component of ceramic bodies for manufacturing of construction materials. Pytel as Mymrin also received results on heavy metals leaching tests that allow using foundry sand for production of clean materials.

Similar tests were made by Furlani et al. (2012) and Alonso-Santurde et al. (2011). Furlani et al. (2012) added 10%, 20% and 40% foundry sand to red and yellow clay and sintered for 1 hour in range from 900°C to 1040°C, conforming the fact that foundry sand could have another function in shape of ceramic body. Alonso-Santurde et al. (2011) introduced into bricks up to 30% foundry sand and concluded that most of hazardous elements from the spent foundry sand are inertized during firing resulting in negligible environmental risk during brick's use.

2.4 WASTE GLASS

Attitude to waste glass treatment and reuse could be divided in two main groups: application for ceramics production, which includes firing, and application for mortar or cement blocks production without firing.

First of all, papers on implementation of waste glass for ceramics production should be presented. In general, main objective of glass addition to ceramics composition is to decrease firing temperature. For example, Phonphuak et al. (2016) added 10% waste glass to clay brick and received decrease in firing temperature almost for 100°C. It is stated that brick with glass fired at 900°C had similar properties to one without glass fired at 1000°C. Similar results were received by Wei et al. (2016), who prepared lightweight aggregates from waste glass and coal fly ash. Waste glass powder reduced sintering temperature leading to a method based on 10 minutes sintering process. Schwarz-Tatarin et al. (2010) described mineralogy of ceramics fired with waste glass, shrinkage, water absorption and strength was also measured to identify what makes them different.

Some researchers were using different types of glass. For example, Kim et al. (2015) tried to substitute feldspar by liquid crystal display waste glass in porcelain sanitary ware production. Even in cases of complete substitution good results were obtained, depending on sintering temperature. One year later Kim et al. (2016) used liquid crystal display waste glass as a flux material to substitute feldspar in ceramic tiles production. Results that were received showed advantage of glass over feldspar. It is mentioned that unfortunately this is not the best way to recycle liquid crystal display glass as after 2010 there is high content of toxic elements in it.

Mainly, it is not the glass that is the origin of toxic components, but other materials, which need glass addition to be neutralized by it. Ye et al. (2015) presented method of gold and cooper tailings treatment by sintering glass-ceramics. Good properties of samples were obtained even when 77.6% of tailings were added to mixture and only 22.4% of glass. Maximum bending strength reached up to 209.6 MPa. Mymrin et al. (2015) presented mixture of paper production sludge and scrap glass for preparation of glassy structure samples, which have low sintering temperatures and absolutely environmentally friendly characteristics.

There is also another approach being presented in international literature, main objective of which is foam ceramics production. Bai et al. (2014) presented preparation of foams from waste glass and fly ash. As a result, foam glass had bulk density of 0.267 g/cm^3, compressive strength of 0.98 MPa and porosity of 81.55%. Different components were used by Zhu et al. (2016), who prepared glass ceramic foams with the best proportion of coal fly ash, waste glass, borax and calcium carbonate, which showed low bulk density and low thermal conductivity. Gong et al. (2016) states that waste amber glass is primarily disposed into landfills, and only small amounts of it is reused. For that reason glass foams were presented as a possible way of waste glass utilization. The thing that makes this research special is addition of pork bones to mixtures for samples preparation.

Another group of researchers used waste glass as a valuable component in production of binding materials. Ling et al. (2013) expressed the idea that glass could be successfully used in different concrete products, such as concrete blocks, self-compacting concrete and architectural mortar. To almost the same conclusion came Jani et al. (2014) highlighting that waste glass can be used in cement and concrete, but the particle size of the waste glass plays a vital role in the alkali-silica reaction and have destructive impact on concrete. Bignozzi et al. (2015) analyzed effect of glass chemical composition on cementing materials by adding 25% of different types of recycled glass to mortar. As a result, the author concluded that pozzolanic and alkali-silica reactions are strictly related to the glass chemical composition. Avila-Lopez et al. (2015) made research on binders, which contained waste glass and limestone. The best way of activation was described.

Torres-Carrasco et al. (2015) used waste glass as an alkali activator for polymers on the basis of fly ash. As a result, the author states that waste glass can substitute commercial sodium silicate hydrate. Torres-Carrasco et al. (2015) presented another study in which alternative to Portland cement alkali-activated materials were analyzed. Idea of using waste glass was described.

Not only binders were studied, but also possibility of polymers production. For example, Bobirica et al. (2015) presented inorganic polymers, which contain spent fluorescent lamps glass, fly ash and blast furnace slag. The author outlines importance of SiO_2/Al_2O_3 ratio, explaining negative impact of glass and positive impact of slag.

Even possibility of using waste glass as an inert material was studied. Rashad (2014) made an overview on waste glass use as a fine aggregate in cementitious materials and concluded that in majority of papers presented data is confirming that drying shrinkage decreased with increase of glass sand content. At the same time, some studies reported on positive and some on negative influence of glass sand on abrasion resistance.

2.5 WOOD ASH

In presented study the wood ash had low content of SiO_2 (1.8%) and also low content of Al_2O_3 (1.5%), which means that it would not be useful in terms of pozzolanic activation. In the presented research the main focus was made on CaO (28.2%) and K_2O (22.8%) as flux materials, which would cause melting at lower temperatures.

The vast majority of researches on wood ash had special focus on an activation of pozzolanic activity of this material. For example, Ramos et al. (2013) presented mortar composition with wood waste ash. The author concluded that wood waste ash seems to be promising to be used as pozzolanic partial replacement material for cement, with no strength loss and leading to enhanced durability and thus contributing to sustainable construction. It is important to highlight that the chemical composition of the wood ash used by the author is mainly presented by SiO_2 (73.01%) and Al_2O_3 (11.93%), which is the main reason for pozzolanic activity.

Siddique (2012) noticed that strength properties of concrete mixtures decrease marginally with increase in wood ash content, but increase with age due to pozzolanic activity. When pozzolanic activity is out of main focus, it comes to substitution of cement. The author used different types of wood ash, which had high content of SiO_2 (8.1 – 50.7%) and Al_2O_3 (7.5 – 17.1%).

Ban et al. (2011) summarized that incorporation of wood ash as a partial cement replacement material in the formulation of concrete mix reduces mechanical strength of concrete, however, there were promising observations that inclusion of wood ash at low levels of cement replacement, such as 10%, contributed towards the enhancement of compressive strength in concrete mixtures. Four years later Ban et al. (2015) concluded that hybridization of high calcium wood ash and pulverized fuel ash can be suitably implemented for the fabrication of mortar block with adequate strength properties. Similar research was made by Chowdhury et al. (2015), who investigated addition of wood ash to concrete and showed following result: strength properties of concrete mixture decreased marginally with increase in wood ash content, but strength increased with later age. In another article Chowdhury et al.

(2015) made an overview stating that cement production is energy consuming process and there is an option for cement substitution by wood ash.

Because of low bulk density of wood ash there are some papers presenting idea of lightweight blocks production. Torkaman et al. (2014) presented experimental study, in which wood fiber waste, rice husk ash and limestone powder waste were used for preparation of lightweight concrete blocks. It was concluded that optimal percentage for replacement of traditional materials with residues, which provided good mechanical and physical properties of blocks is 25%. In addition to this research, Yliniemi et al. (2016) made research proving that it is possible to increase the utilization of ash and produce valuable products by simultaneous granulation and alkali activation for lightweight aggregates production.

Different type of application was chosen by Oburger et al. (2016), who presented field study on wood ash utilization in forest road construction. It was concluded that if quality of ash is appropriate and soil buffer capacity is sufficient wood ash application in forest road construction is generally acceptable.

Due to the fact, that wood ash is a valuable material there are some researches, which completely out of the field of construction materials production. For example, Rey-Salgueiro et al. (2016) used wood ash for soil characteristics improvement. At the same time, Uprety et al. (2016) presented idea of using wood ash as an alternative to prevailing chemical based heterogeneous catalysts for biodiesel production.

3 METHODOLOGY

The full study of the raw materials was carried out using the following analysis:

- XRF to analyze chemical composition,
- XRD to describe mineralogical composition,
- SEM to characterize the particles’ size and shape using high magnification,
- EDS to identify the quality of heterogeneity of the elements,
- Mapping the chemical states of an element inside a sample to identify density of elements in different points,
- LAMMA to determine isotopic composition of the samples,
- DTA to determine the behavior of the samples during firing process, studying endothermic and exothermic processes,
- TGA to identify weight loss or weight gain of the samples, due to loss on ignition or oxidation,
- Leaching and solubility tests of heavy metals from raw materials,
- Particle size distribution test,
- Tapped density test.

The red mud is the industrial waste of Bayer process. Bayer process is a method of bauxite ore treating with heat and chemical solutions to extract aluminium oxide. It involves crushing and milling, pressure application, heating and addition of NaOH. During this process the grains of bauxite ore are supposed to be distracted to the very small size for easier separation of the elements. For this reason it was important to determine whether red mud is a nanomaterial or not.

To confirm the real presence of the nanoparticles in red mud the method of transmission electron microscopy was additionally used. The sample preparation included the following steps: 5 grams of red mud was put into 2 liter of bidistilled water and was shaken for 3 minutes. 24 hours later, from the surface of the mixture 10 ml were pipeted and mixed with 50 ml of bidistilled water. After that, one drop, which was obtained from the surface of the mixture, was put on a cooper grid of sample holder, which was covered with graphene, and was drying for 24 hours in a vacuum camera. After this preparation process the samples of the red mud were studied by the method of transmission electron microscopy.

All the raw materials were subjected to X-ray fluorescence test, which performed in the following way:

- The material should be milled for 30 seconds,
- To 7 grams of the material 1.4 gram of the organic wax should be added and mixed very well,
- The mixture is pressed at the pressing machine in the shape of disk,
- The disk is installed in the Philips/Panalytical model 2400.

For X-ray diffraction analysis, SEM, EDS and mapping of the principal chemical elements no special preparation of the material was used except milling.

The leaching tests were made in accordance with NBR 10005/87.

The DTA and TGA test were carried out with increase of the temperature 10°C per minute up to 1226°C. The nitrogen was circulating in the equipment during the test and it was 100 ml of gas per minute of the analysis.

Particle size distribution test was made using sieves, and the red mud, which has fine particles, was also subjected to sedimentation test (NBR 7181).

Tapped density is the density of the milled sample when it is put into the determined volume and compacted with vibration only, without any extra effort.

The compositions were prepared on the basis of each material’s properties. For example, red mud was used as a binding material and it was difficult to use less than 50% of it in compositions. The only composition, which contains 40% of red mud, was very fragile after compaction and before firing. Due to this fact, content of blast furnace slag and foundry sand varied between 0 and 50%. Both materials do not tend to absorb water and become flexible, and for this reason it was irrational to use more than 50% of these materials. Wood ash and waste glass were used as additives. They did not have main role in the composition. As the objective was to complement already developed mixtures with flux materials the content of 20% was chosen as the optimal. In this case the role of the material is easy to notice and at the same time there is not too much material being used so that it becomes one of the main components.

Then the samples (60x20x10mm size) were prepared. Each sample was made of 20 grams of already humid mixture. That is why the thickness of the sample varied from 7 to 10 mm. For each temperature and composition were made 10 samples. This amount according to standard deviation was convenient. The samples were compacted at pressure of 4 MPa. The humidity of the crude composition for compacting varied between 10 and 17%. The optimal humidity was reached, when after compacting there was a little of water escaping from the body of the sample. This was the sign that there was enough water in the mixture for optimal compacting and excessive water escaped. When there was no water escaping after compacting it meant that the mixture is too dry. When there was too much water to escape from the body of the sample, so that the mixture turned into the humid mass that leaks out through the crevasse of the mold, it was the sign of excessive humidity.

All the samples were fired in the same conditions: there were no additional walls inside the furnace, which could prevent the direct influence of heat from metal-filament and improve distribution of the heat among the samples; all the samples were placed in the center of the furnace. For further researches it would be better to use the walls inside the furnace, as it helps to avoid problems of heat distribution during firing.

The firing temperatures were the following: 800°C, 900°C, 1000°C, 1050°C, 1100°C, 1150°C, 1200°C, 1225°C. The furnace had the following settings: the increase of the temperature was 5°C per minute up to the final firing temperature, than the temperature was maintained for 3 hours to let the heat enter the samples and not fire only their surface, and then the furnace turns off and it normally took about 12 hours for it to lose the heat.

After firing the samples the following tests and measurements were carried out to determine characteristics of the samples:

- Flexural strength (three point flexural test),
- Water absorption,
- Linear shrinkage,
- Density,
- XRD to determine formation of new crystalline structures,
- MEV to determine the influence of temperature increase on the particles inside the samples,
- EDS to identify chemical compositions of the exact points in the samples,
- Leaching and solubility tests to understand whether the samples are safe to use or not.

The flexural strength of the samples was calculated with the formula:

$$\sigma = \frac{3FL}{2bd^2}$$

Where:

σ is the flexural strength (MPa),

F is the load (force) at the fracture point (N), L is the distance between two pins,

b is the width of the sample,

d is the thickness of the sample.

The equipment was programmed to continue test until the full loss of resistance, so the test was only stopped when the sample was broken in two separated pieces. The speed of the loading pin was 0.5 mm per minute.

Water absorption of the samples was calculated using the following formula:

$$Water\ absorption = \frac{M_{moist} - M_{dry}}{M_{dry}}$$

Where:

M_{moist} is the weight of the sample after 24 hours in the water,

M_{dry} is the weight of the sample before water immersion,

The linear shrinkage of the samples was measured in the following way:

$$Linear\ shrinkage = \frac{L_{a.f.}}{L_{b.f.}} \times 100\%$$

Where:

$L_{a.f.}$ is the length of the sample after firing process,

$L_{b.f.}$ is the length of the sample before firing process.

The density of the samples was measured in the following way:

$$Density = \frac{M_{dry}}{a \times b \times c}$$

Where:

M_{dry} is the weight of the dry sample after firing,

a is the length of the sample,

b is the width of the sample,

c is the thickness of the sample.

The following equipment was used to receive the results of the test:

- For XRF was used Philips/Panalytical, model PW 2400,
- For XRD was used Philips, model PW 1830,
- SEM and EDS tests were made with Jeol JSM-6360 LV,
- LAMMA was determined using a LAMMA-1000, model X-ACT,
- Solubility and lixiviation of metals from liquid acid extracts was identified by AAS on a Perkin Elmer 4100 spectrometer,

- Three points flexural strength was determined using an EMIC DL-10.

4 RAW MATERIALS CHARACTERIZATION

All raw materials under study were obtained from industrial companies of Brazil. Red mud was obtained from one of Brazilian refineries, waste glass was received from automobile glass polishing plant, blast furnace slag was obtained from metallurgical plant, foundry sand was provided by casting company, and wood ash was obtained from the brick production factory. Natural clay is a common traditional material for local bricks and blocks factories and the one that is used in this study as a reference was obtained from a local brick factory.

4.1 PARTICLES SIZE DISTRIBUTION OF THE RAW MATERIALS

The grain size distribution of all raw materials has been determined (Table 4.1) using the sieves. Comparison of the results of these analyzes shows that the most uniform component is foundry sand. 85.17% of it is particles, which size is between 0.59 and 0.30 mm. The vast majority (66.39%) of blast furnace slag's particles is between 0.29 and 0.15 mm. The biggest part (39.38%) of waste glass's particles had size between 0.149 and 0.075 mm. It is important to notice that 18.78% of particles is less than 0.074 mm in diameter, which is due to polishing process of the glass. Wood ash has 51.47% of the particles, which size is between 0.59 and 0.30 mm.

Table 4.1 - Particles size distribution (wt. %), tapped density (g/cm^3) and humidity of raw materials (%)

	Size (mm)	Red mud	Blast furnace slag	Foundry sand	Glass waste	Wood ash
Grain size distribution	More than 1.2	0.00	0.00	0.00	0.00	0.00
	1.19 - 0.60	0.00	0.00	0.26	0.00	0.00
	0.59 - 0.30	11.78	14.63	85.17	23.29	51.47
	0.29 - 0.15	18.82	66.39	13.86	18.55	42.83
	0.149 - 0.075	26.73	17.63	0.62	39.38	3.75
	0.074 – 0.0	32.67	1.35	0.08	18.78	1.95
Tapped density (g/cm^3)		1.26	2.75	1.59	0.99	0.56
Humidity (%)		32.2	1.1	1.3	1.4	4.7

The red mud is the finest material of all being used in presented research. 32.67% of particles have diameter less than 0.074 mm, which was also mentioned in the research or Sushil et al. (2008) and Liu (2009). The reason for it to be so fine is the stages of Bayer technology. Bayer process supposed to separate particles of aluminium oxide (alumina) from the ore by chemical and thermal reactions. First of all, the bauxite ore is subjected to milling and crushing. The second stage is chemical decomposition of the particles using NaOH solution, which has pH equal to 13.5, pressure, and temperature of 150-200°C. The red mud, which was used by Snars et al. (2009) in Australia presented pH from 8.4 to 12.6. After this stage the red mud is separated from $Na[Al(OH)_4]$. The technology is based on deep separation. That is why the residue consists of such a small particles.

When red mud is dried and then milled, it tends to form agglomerates. These globs do not have any strength, but because of them the sieves test method does not describes the real situation. In order to obtain more exact data on red mud's grain size, the sedimentation method has been applied. In terms of the sedimentation test, the red mud does not tend to form globs as it is saluted in the water. Another benefit of the test is that it is very precise and allows determining the content of particles, which have size of 0.0014 mm (Table 4.2). The experiment was carried out according to Brazilian norm NBR 7181 (1984).

Table 4.2 - Red mud particles size distribution (%) by the method of sedimentation.

Time (min)	Specific gravity	Temperature °C	Size (mm)	% of the material
0.5	1.0420	21.9	0.0580 – 0.0413	1.25
1	1.0415	21.9	0.0413 – 0.0295	2.54
2	1.0405	21.8	0.0295 – 0.0189	3.71
5	1.0390	21.9	0.0189 – 0.0136	3.75
10	1.0375	21.9	0.0136 – 0.0080	5.16
30	1.0355	21.5	0.0080 – 0.0058	6.41
60	1.0330	21.1	0.0058 – 0.0043	7.62
120	1.0300	20.8	0.0043 – 0.0031	8.86
240	1.0265	20.5	0.0031 – 0.0023	8.90
480	1.0230	20.1	0.0023 – 0.0014	14.13
1440	1.0175	19.0	0.0014 - 0	37.68

According to the results of the Table 4.2, 37.68% of red mud is particles, which have size smaller than 0.0014 mm in diameter, which means less than 1400 nm. It is determined, that to classify a material as a material with nanoparticles, particles should be between 1 and 100 nanometers in size.

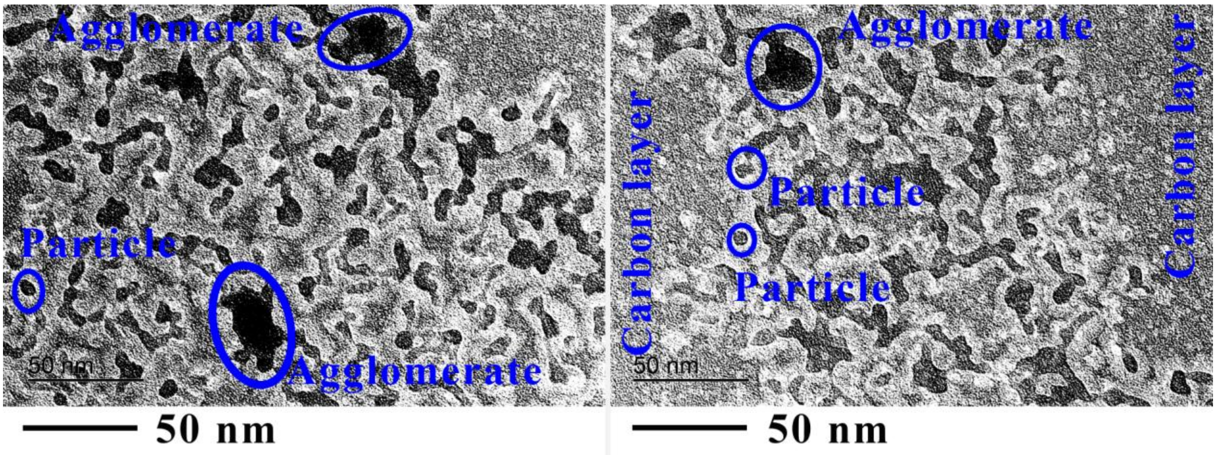

Figure 4.1 - Particles and agglomerates micro images of red mud by the method of transmission electron microscopy

When sedimentation test has been done, there is still uncertainty about the real size of the particles. It is important to determine the size of the particles, which are smaller than 1400 nm. Transmission electron microscopy presented valuable images of the red mud's particles. In the image Figure 4.1 agglomerates of the particles, separated particles and carbon layer are marked. It has been found that red mud particles tend to coalesce in water and form agglomerates of different sizes and shapes. The vast majority of the particles are so fine that it becomes completely or almost transparent to the electron flux. Therefore, the color on the particles on the photographs fuses with background, created by the supporting layer of carbon. Large units of agglomerated particles are easier to identify as they have contrast black color in the images.

Separated particles, which did not agglomerate with other particles, have size between 2 and 7 nm. Even particles, which have brighter color and might be agglomerates of several particles, do not exceed the size of 14 x 50 nm. In this case, the particles are still smaller than 100 nm in size and they can be classified as nanoparticles, meaning that red mud is nanomaterial.

4.2 TAPPED DENSITY AND HUMIDITY OF THE RAW MATERIALS

Tapped densities of the raw materials (Table 4.1) also differ from each other. The highest value (2.75 g/cm^3) has blast furnace slag due to very high content of iron. The next is foundry sand (1.59 g/cm^3) because of mainly siliceous composition. The red mud presented the lowest value (0.86 g/cm^3) of tapped density, which might be because of the fact that it was dried and grinded and as a consequence had more pores in the moment of measurement.

Almost all raw materials have very low level of humidity (Table 4.1). The reason for it is the production process, which stands behind these materials. For instance, blast furnace slag, foundry sand, and wood ash are the wastes of high temperature processes, which have no contact at all with water. Waste glass after wet polishing process does not retain moisture due to the lack of porosity of the particles and hydratable elements in its chemical composition. Only red mud had high (32.2%) humidity due to the fact that NaOH is added to the bauxite ore as a solution. When the red mud is separated and excluded from the following process it is already humid. Yalcin et al. (2001) identified 40-50% humidity of red mud in his research. Usually there is no point for companies to spend energy to dry it as they use open air storages, which means that when it rains red mud absorbs the water.

4.3 CHEMICAL COMPOSITION OF THE RAW MATERIALS

The chemical compositions of all raw materials under study are given in a single Table 4.3 to make it easier to compare the results and understand the impact on the structure formation processes, physical and chemical properties of the later developed ceramics. The results of chemical compositions show significant difference in elements contents (Table 4.3).

Table 4.3 - Chemical composition of the raw materials under study (by XRF method).

Oxides	Oxides content (wt.%) in the raw materials					
	Red mud	Blast furnace slag	Foundry sand	Waste glass	Wood ash	Clay (reference)
Fe_2O_3	29.9	62.1	1.2	0.8	0.5	6.1
SiO_2	15.5	13.8	91.2	75.2	1.8	53.3
SO_3	0.6	10.0	0.7	0.2	2.2	0.1
Al_2O_3	21.2	2.6	2.3	0.8	1.5	24.7
CaO	4.2	2.5	0.1	8.3	28.2	0.4
MgO	0.1	0.3	0.2	3.2	7.6	0.7
Na_2O	10.3	0.9	0.3	10.7	0.6	0.1
K_2O	0.4	0.4	0.1	0.3	22.8	1.0
MnO	0.2	0.6	0.0	0.3	1.4	0.1
TiO_2	2.4	0.4	0.1	0.0	0.1	1.4
P_2O_5	0.6	3.5	0.0	0.9	2.0	0.1
Cr_2O_3	< 0.1	0.3	0.0	0.0	0.0	< 0.1
V_2O_5	0.1	0.0	0.1	0.0	0.0	< 0.1
BaO	0.0	0.2	0.0	0.0	0.2	0.1
P_2O_5	0.0	0.1	0.0	0.0	0.0	0.0
SnO_2	0.0	0.1	0.0	0.0	0.0	0.0
ZnO	< 0.1	0.1	0.0	0.0	< 0.1	< 0.1
CuO	0.0	0.1	0.0	0.0	< 0.1	0.0
ZrO_2	0.2	< 0.1	0.0	0.0	0.0	0.1
MoO_3	0.0	< 0.1	0.0	0.0	0.0	0.0
Loss on ignition	14.4	1.7	3.7	0.3	29.9	11.5
Total	100.0	100.0	100.0	100.0	100.0	100.0

4.3.1 Chemical composition of the red mud

The main object of research is red mud. It consists of Fe_2O_3 (29.9%), Al_2O_3 (21.2%), SiO_2 (15.5%) and Na_2O (10.3%). It has high loss on ignition (14.36%), which is probably because of carbonates content, hydroxide OH-group and water content after thermo-chemical Bayer process. Na_2O can be useful as a flux material, taking into account low melting point of majority of its forms.

Table 4.4 - Leaching and solubility of heavy metals from red mud

Metals	Leaching (mg/L)		Solubility (mg/L)	
	Obtained results	Standards * limits	Obtained results	Standards * limits
As	7.63	1.00	9.56	0.01
Ba	94.28	70.00	95.47	0.70
Cd	7.34	0.50	15.41	0.005
Pb	4.43	1.00	7.66	0.01
Cr total	18.46	5.00	22.67	0.05
Hg	1.47	*	3.81	*
Se	2.75	1.00	3.35	0.01
Al	28.76	*	36.44	0.20
Cu	16.29	*	30.08	2.00
Fe	98.31	*	108.75	0.30
Mn	55.11	*	69.43	0.10
Zn	68.48	*	84.13	5.00

Note: * did not mention in the Brazilian standards NBR 10004.

The presence in red mud of Zn (68.48 mg/L), Ba (94.28 mg/L), and Cr (18.46 mg/L) was indicated (Table 4.4) by AAS method. The results exceed Brazilian norms and regulations (NBR 10004), which means that red mud has high content of heavy metals. The content of As, Pb, Cr, and Hg in red mud was also presented in the paper of Gonda1-Zsombor et al. (2014). Another specialty of red mud is pH equal to 13.5. These two characteristics are the reason to classify red mud as hazardous material. Similar characteristics were also described by Liu et al. (2014) and Gonda1-Zsombor et al. (2014). At the same time Brazilian red mud, which was used in the presented research, does not contain any radioactive isotopes (137Cs, as the red mud from Vietnam, which was studied by Hai et al. (2014).

4.3.2 Chemical composition of the blast furnace slag

Blast furnace slag (Table 4.3) has very high content of ferrous oxides - 62.1%. The rest is presented by SiO_2 - 13.8%, SO_3 - 10.0%, Al_2O_3 - 2.6%, CaO - 2.5% and other oxides are presented less than 1% of the content. For byproducts of metallurgical processes it is typical to have high content of SO_3 and low loss on ignition (1.7%). One of the reasons for blast furnace slag to have such characteristics is high temperature (1500 °C) of production of byproduct. Chemical elements that have lower content than 1% are not described in details as they have little influence on properties of the developed ceramics, especially when the content of blast furnace slag in the mixture is low.

4.3.3 Chemical composition of the foundry sand

Foundry sand has the simplest chemical composition (Table 4.3). It consists mainly of SiO_2 (91.2%) and small part of Al_2O_3 (2.3%), which may be presented because of the contact with clay, when formed into a mold in the factory. It is also important to outline small content of Fe_2O_3 (1.2%), which appears as a thin layer on the surface of sand particles. All the other oxides vary in content between 0.1% and 0.3%. The reason for 3.7% loss on ignition might be explained by organic material content, which appeared in the sand later, when it was already stocked on the backyard of the factory.

4.3.4 Chemical composition of the waste glass

The main elements (Table 4.3) of waste glass are SiO_2 (75.2%), Na_2O (10.7%), and CaO (8.3%). Loss on ignition (0.3%) of waste glass is lower than loss on ignition of all others materials. Due to the fact that it is less than 1%, there is no reason for it to have impact on properties of the developed ceramics. The chemical composition of waste glass is typical for glass in general. Exactly because of the presented chemical composition the waste glass was chosen to be used as a flux material to decrease the melting point of the developed compositions.

4.3.5 Chemical composition of the wood ash

Wood ash has more diverse content comparing with other materials under study (Table 4.3): CaO - 28.2%, K_2O - 22.8%, MgO - 7.6%, and very high ignition loss (29.9%). There are two reasons for high loss on ignition: large quantity of under-burned wood and high capacity of ash to absorb water from air. Wood ash in this study has been applied as an alternative material to waste glass because of the high content of K_2O, which could serve as a flux material. Due to the fact that normally red mud is stored in open air deposits, it is too humid to be used directly for ceramics production. Taking it into consideration, the use of wood ash, which when mixed with red mud decreases humidity of the composition in general, might be technologically attractive. At the same time, when there is an option of drying the material without energy consumption, it might be economically viable.

4.3.6 Chemical composition of the clay

Natural clay is used traditionally in the local brick plants as the main raw material, and in the presented study was used as reference to ceramics made of natural materials on industrial scale. It consists (Table 4.3) of SiO_2 (53.3%), Al_2O_3 (24.7%), and Fe_2O_3 (6.1%). It has high loss on ignition (11.5%), which might be the result of high organic content and different forms of water contents.

4.4 MINERAL COMPOSITION OF THE RAW MATERIALS

Mineral composition of the raw materials was determined by powder method with X-ray Diffraction (XRD) with the radiation λCu-Kα. A deciphering of the obtained diffractogram patterns was performed under the program High Score with the data bank PDF-2.

On the basis of results of analysis, majority of materials, except foundry sand, was determined as amorphous material. There are two main reasons to determine the material as an amorphous. The first one is high intensity of X-ray background. The second one is low intensity of mineral's peaks.

4.4.1 Mineral composition of the red mud by XRD method

Mineral composition of red mud is basically represented by minerals (Figure 4.2), which are typical for bauxite ore ($Al_2O_3 \bullet nH_2O$). It seems that some of them were not completely grinded and destructed during Bayer process. Hematite (Fe_2O_3) and magnetite (Fe_3O_4) are also presented in mineral composition. The intensity and quantity of peaks combined with light brown color of red mud means that there is more hematite than magnetite.

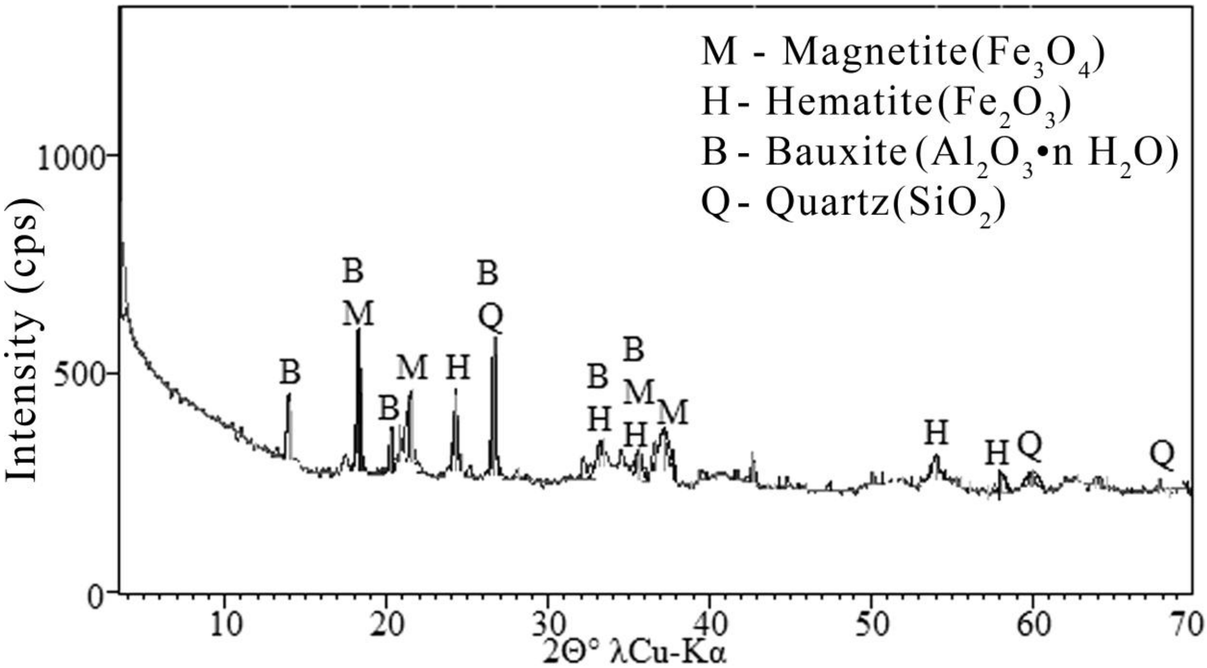

Figure 4.2 - Diffractogram pattern of the red mud by XRD method.

There is also the main barren mineral quartz (SiO_2). Presence of all these minerals is also confirmed by the chemical composition, which was determined by XRF method. The horizontal line of the graph, which is placed well above the zero line, shows the X-ray background. It is higher than peaks themselves, except two peaks where 2Θ° = 18.5° and 27°, which means that the major part of the material is amorphous. It was formed during grinding process in the situation of high alkalinity of Bayer process.

4.4.2 Mineral composition of the blast furnace slag by XRD method

Chemical composition of blast furnace slag (Table 4.3) presents high content of iron oxide Fe_2O_3 (63.6%). There is also SiO_2 (13.8%) and SO_3 (10.0%), which all together equals to 87.4% of total content.

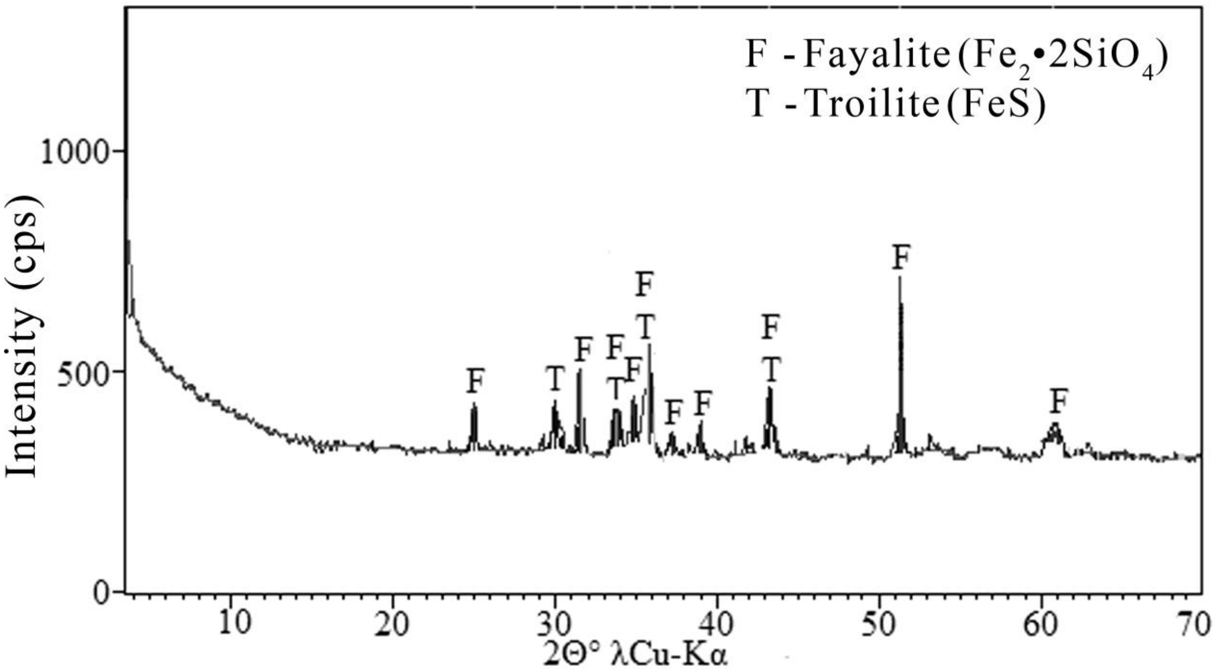

Figure 4.3 - Diffractogram pattern of the blast furnace slag by XRD method

For this reason, mineralogical composition of the blast furnace slag (Figure 4.3) is presented by only two main minerals of these three oxides: fayalite – Fe_2•$2SiO_4$ and troilite - FeS. Just as on the diffractogram of the red mud (Figure 4.2), on the diffractogram of the blast furnace slag (Figure 4.3) the line that shows X-ray background is higher that majority of peaks of mineralogical structures of fayalite and troilite. The reason for that is glassy amorphous structure of the material, which was formed because of the high temperature (about 1500°C) of melting process.

4.4.3 Mineral composition of the foundry sand by XRD method

Foundry sand contains 91.2% SiO_2 (Table 4.3). It is represented by the only crystalline mineral quartz (Figure 4.4). Small quantity of the chemical (8.8%) and mineralogical impurities are presented on the XRD pattern as rather low X-rays background.

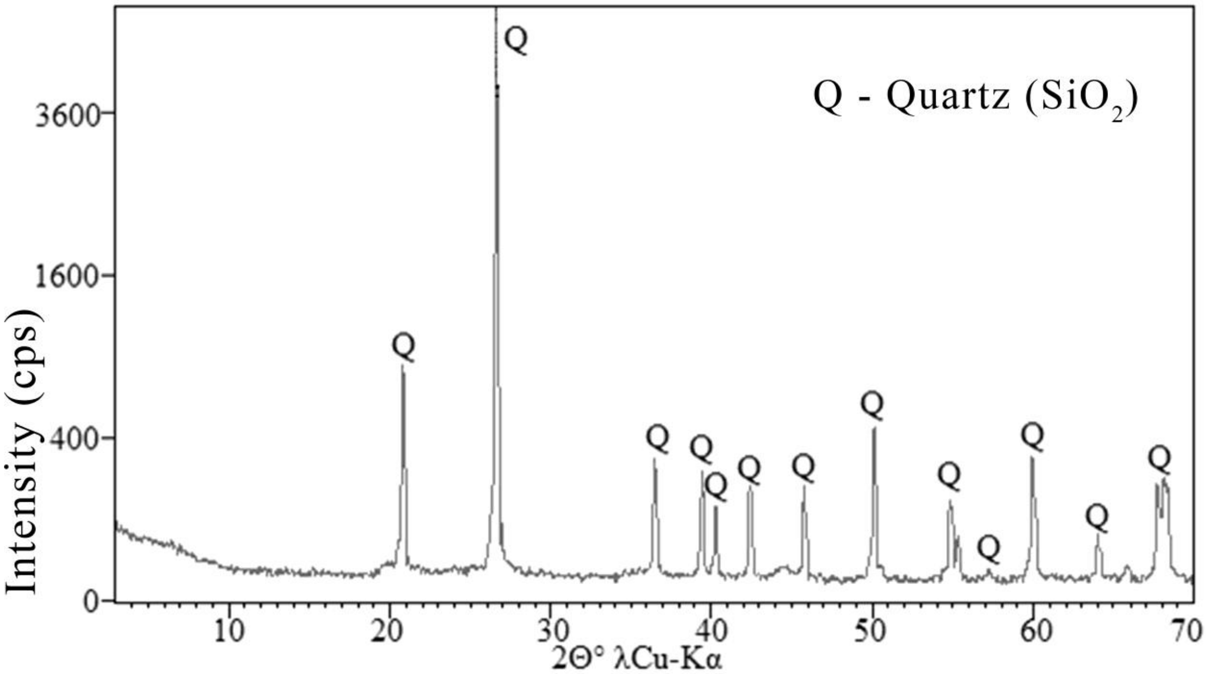

Figure 4.4 - Diffractogram pattern of the foundry sand by XRD method.

Almost half of the material, which is not SiO_2, is loss on ignition (3.7%). It should be carbonates and hydrates, that tend to degrade during firing process.

4.4.4 Mineral composition of the waste glass by XRD method

The mineral composition of waste glass is presented by quartz (Figure 4.5). The intensity is very low – a bit more than 100 counts per second. Almost the whole curve is presented by amorphous glass which has typical halo between 12° and 38° of 2Θ° λCu-Kα.

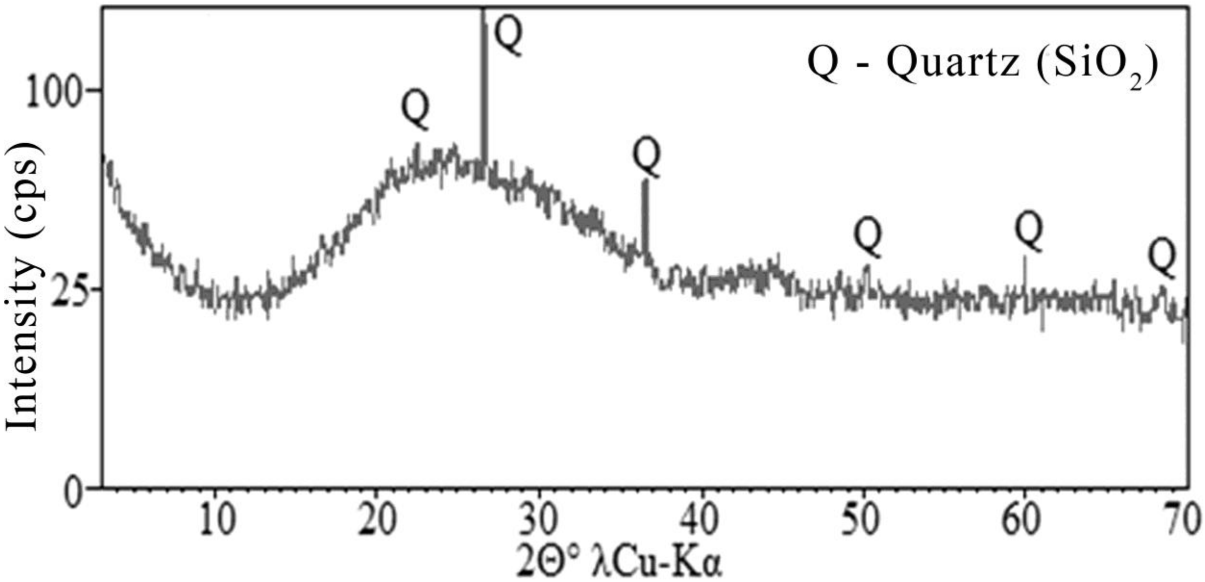

Figure 4.5 - Diffractogram pattern of the waste glass by XRD method.

The X-ray background is very high comparing with the height of quartz peaks. The highest peak, which has intensity over 100 counts per second (2Θ° = 26.63° λCu-Kα) is lower than the X-ray background.

4.4.5 Mineral composition of the wood ash by XRD method

The diffractogram (Figure 4.6) of wood ash shows, that this materials is presented by four main minerals: afwillite ($Ca_3Si_2O_6(OH)_2(H_2O)_2(Si_5O_{18})$), albite ($(Na,Ca)Al(Si, Al)_3O_8$), orthoclase ($K(Al, Fe)Si_2O_8$) and quartz ($SiO_2$). These minerals were expected to appear on the diffractogram pattern according to the chemical composition of the material.

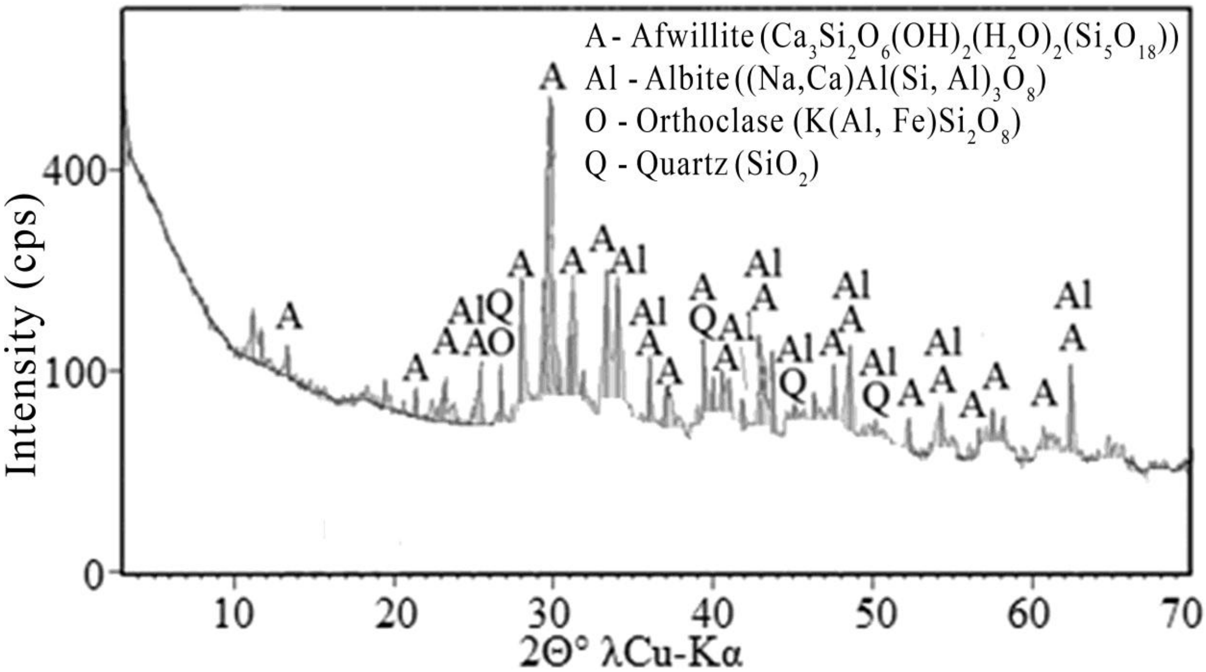

Figure 4.6 - Diffractogram pattern of the wood ash by XRD method.

The only high peak is afwillite, which reaches 400 counts per second when 2Θ° is about 30°. It means that wood ash is also presented by mainly amorphous material. Another argument to support this statement comes from chemical composition. A loss on ignition (29.9%) is high (Table 4.3). It means that there was big amount of wood that remained under-burned after firing.

4.4.6 Mineral composition of the clay by XRD method

The mineralogical composition of natural clay (Figure 4.7) correlates with previously determined chemical composition (Table 4.3). Two minerals were identified: illite ($KAl(Si, Al)_4(OH)_2 \cdot nH_2O$) and quartz ($SiO_2$).

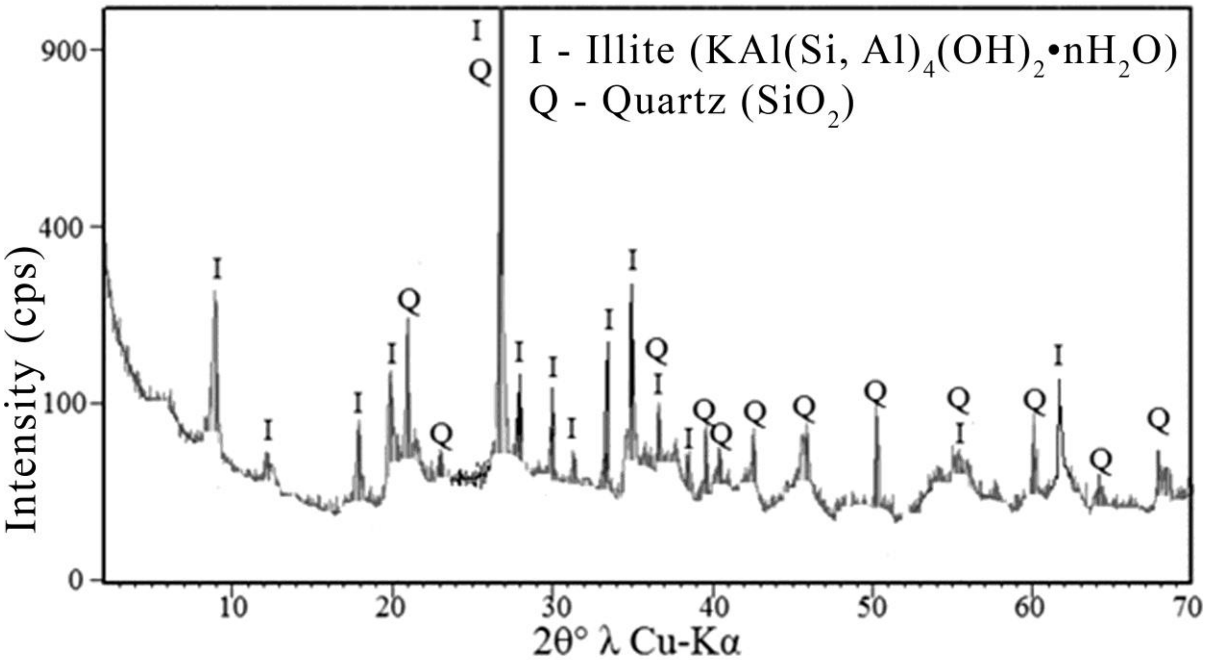

Figure 4.7 - Diffractogram pattern of the natural clay by XRD method.

Along with high peaks of minerals there is also high X-ray background being presented, which means typical for natural materials, especially clay, amorphous content.

4.5 MORPHOLOGICAL STRUCTURE AND MICRO-CHEMICAL COMPOSITIONS OF THE RAW MATERIALS

Morphological structure of the samples was analyzed using SEM images and micro-chemical composition was determined by EDS method.

4.5.1 Morphological structure and micro-chemical composition of the red mud

The red mud consists of (Figure 4.8) different particle sizes and shapes, mainly oval and rounded, which is typical for amorphous substances, with widely varying pore shapes and dimensions. It seems, they are not linked chemically, but has only mechanical contacts with each other.

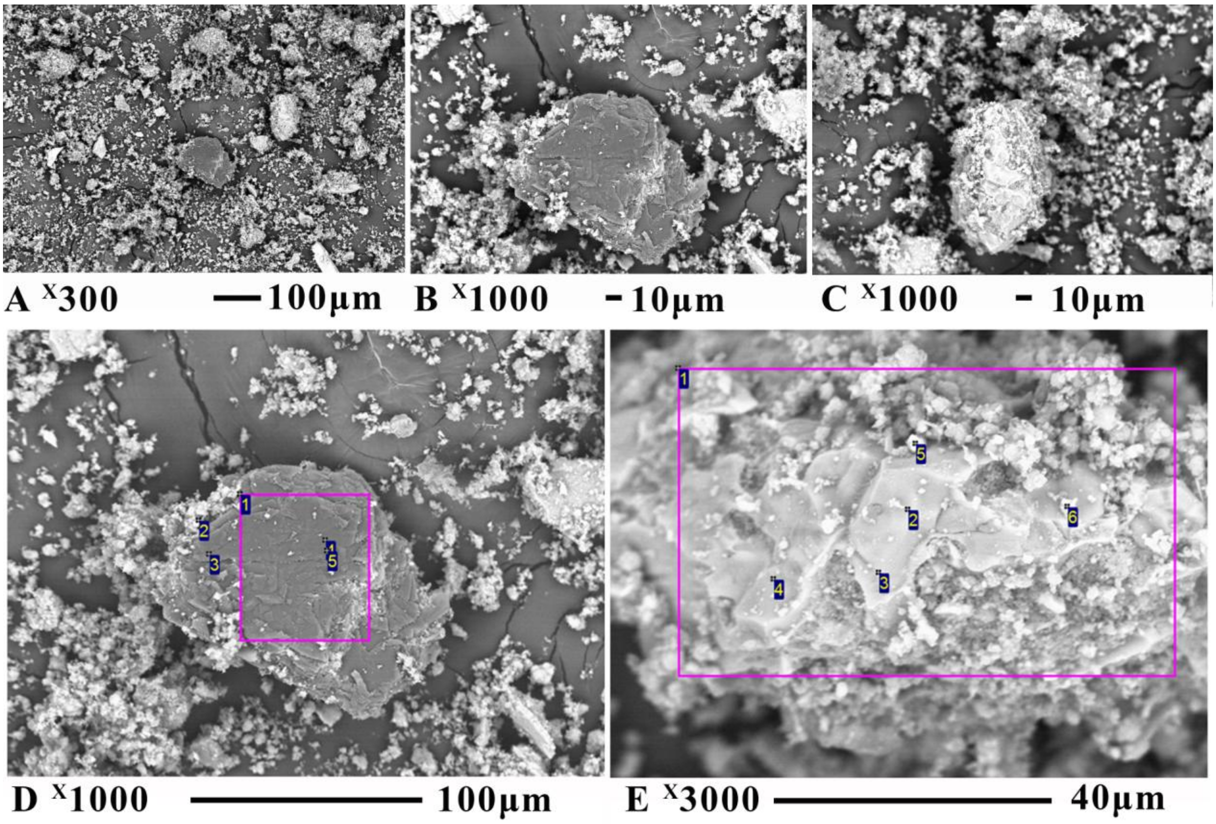

Figure 4.8 - SEM micro images and EDS of red mud with different magnification.

Micro chemical composition of red mud was tested by EDS microanalyses (Figure 4.8 - D and Table 4.5). The content of each chemical element at the area and four points located in different particles' forms is mainly coincides with results of XRF analyses of the raw materials.

Table 4.5 - Chemical composition of the red mud (Figure 4.8) - D by EDS method.

Points	Na	Al	Si	Ca	Ti	Fe	Total
1- area	14.88	23.07	11.23	0.00	0.00	50.82	100.00
2	12.85	48.40	14.63	2.57	1.36	20.20	100.00
3	0.00	49.53	0.00	0.00	0.00	50.47	100.00
4	0.00	44.76	0.00	0.00	0.00	55.24	100.00
5	0.00	47.26	0.00	0.00	0.00	52.74	100.00
Min.	12.85	23.07	11.23	2.57	1.36	20.20	
Max.	14.88	49.53	14.63	2.57	1.36	55.24	

Analysis of the points demonstrates a great level of typical heterogeneity of each point in comparison with each other. For example, the content of Na in four points of red mud varied from 0 to 14.88%, Al 23.07 - 49.53%, Ca from 0 to 2.57%, Si from 0 to 14.63%, Fe 20.20 - 55.24%. Such level of heterogeneity of the points is inevitable for the substances with extremely complex chemical compositions of amorphous materials. Similar results on superficial chemical characteristics were presented by Hind et al. (1999).

Table 4.6 - Chemical composition of the red mud (Figure 4.8 – E) by EDS method.

Points	Na	Al	Si	Ca	Ti	Fe	Total
1-area	12.61	20.11	6.72	2.14	1.69	56.74	100.00
2	3.39	19.17	1.74	2.16	1.93	71.60	100.00
3	2.86	6.99	0.80	1.87	2.87	84.61	100.00
4	4.32	24.86	2.13	1.98	0.51	66.19	100.00
5	11.36	24.85	5.48	2.01	1.28	55.03	100.00
6	5.35	26.42	2.18	1.80	1.07	63.19	100.00
Min.	2.86	6.99	0.80	1.80	0.51	55.03	
Max.	12.61	26.42	6.72	2.16	2.87	84.61	

The same heterogeneity was identified in other points of another particle of the material (Figure 4.8 - E, Table 4.6). The content of Na in five points of red mud varied from 2.86 to 11.36%, Al 6.99- 26.42%, Si from 0.80 to 5.48%, Fe 55.03- 84.61%.

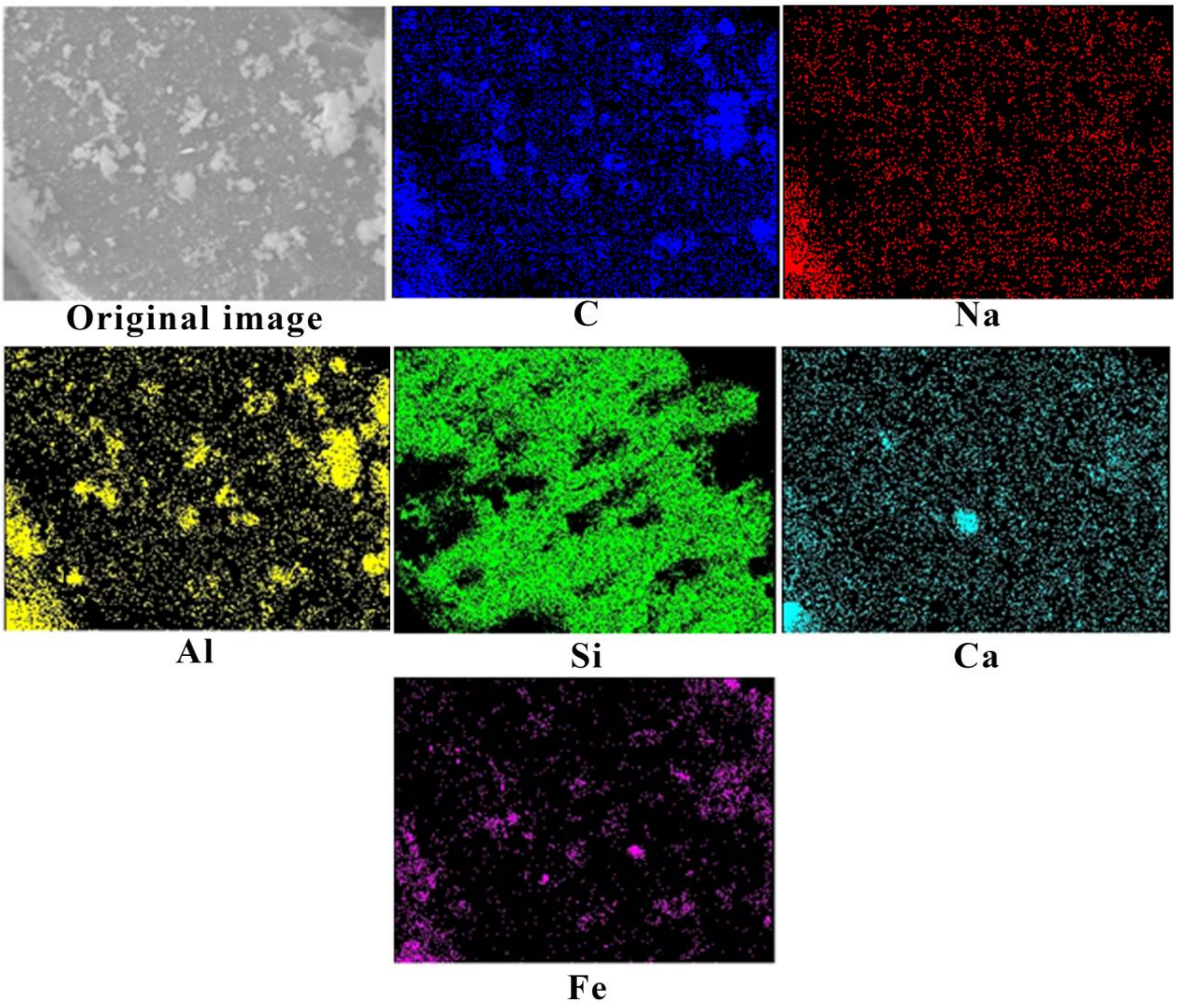

Figure 4.9 - Mapping the chemical states of an element inside a red mud sample (using tomographic X-ray absorption spectroscopy).

Heterogeneity of the red mud’s composition was also proved with mapping of the chemical states of an element inside a sample using tomographic X-ray absorption spectroscopy. According to the results, (Figure 4.9) atoms of each chemical element are located in a chaotic manner, showing significant difference in concentration.

4.5.2 Morphological structure and micro-chemical composition of the blast furnace slag

The particles of blast furnace slag present a great variety of sizes and forms. Majority of particles (Figure 4.10 - A and B) has a size of a few microns in diameter. The minority of them is bigger and reaches the size from 200 to 300 microns. The sharp-edged shape is typical for these particles. The reason for this is the process of material’s preparation. Blast furnace slag was milled and was only mechanically crushed. There was no influence of acid or high temperature. When compared with blast furnace slag, red mud does not have sharp edges as bauxite ore has gone through not only mechanical crushing, but also heating and dilution in acid, which allowed recovery of alumina followed by production of red mud.

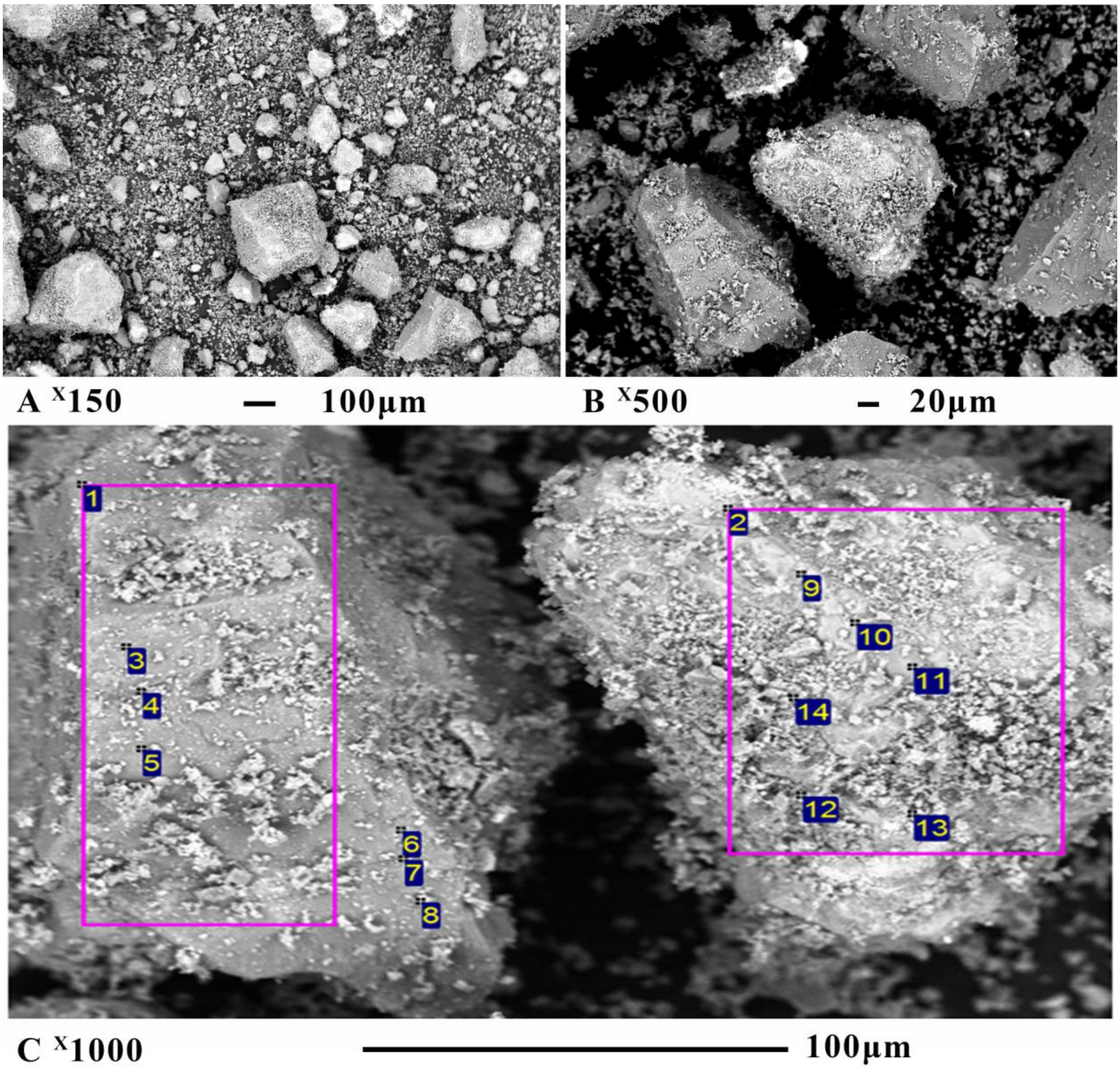

Figure 4.10 - SEM micro images and EDS of blast furnace slag with different magnification.

Chemical characterization of blast furnace slag’s particles (Figure 4.10 and Table 4.7) demonstrated lack of common chemical characteristics.

Table 4.7 - Chemical composition of the blast furnace slag (Figure 4.10 – C) by EDS method.

Points	Na	Al	Si	S	Cl	K	Ca	Mn	Fe	Mg	Pb	Ba	Total
1-area	2.48	2.15	13.51	8.49	0.94	0.75	2.99	0.94	67.76	0.00	0.00	0.00	100.0
2-area	1.77	1.52	5.24	19.82	0.82	0.55	1.27	69.00	0.00	0.00	0.00	0.00	100.0
3	0.00	0.00	15.03	3.15	0.00	0.00	1.97	1.38	77.75	0.71	0.00	0.00	100.0
4	0.00	0.96	1.46	1.37	0.00	0.30	4.01	1.38	90.52	0.00	0.00	0.00	100.0
5	0.84	0.93	7.18	4.01	0.00	0.00	2.33	0.97	68.46	0.00	15.28	0.00	100.0
6	0.00	0.84	16.48	1.31	0.00	0.00	2.45	1.29	76.79	0.85	0.00	0.00	100.0
7	5.24	11.75	27.04	2.29	1.45	9.09	6.09	0.00	34.39	0.00	0.00	2.66	100.0
8	0.87	0.86	4.48	20.81	0.00	0.00	1.19	0.00	71.80	0.00	0.00	0.00	100.0
9	1.51	0.54	1.90	24.10	0.69	0.00	0.47	0.00	69.87	0.00	0.00	0.00	100.0
10	3.16	1.04	10.13	10.37	1.35	0.00	1.91	0.81	71.23	0.00	0.00	0.00	100.0
11	1.44	0.70	1.10	2.59	0.00	0.00	0.00	0.00	94.17	0.00	0.00	0.00	100.0
12	0.00	2.10	4.65	3.51	0.00	0.00	0.80	0.00	88.94	0.00	0.00	0.00	100.0
13	1.12	1.13	4.95	26.69	0.96	0.70	1.49	0.00	62.97	0.00	0.00	0.00	100.0
14	0.00	0.95	3.24	3.98	0.00	0.00	0.81	0.00	90.52	0.00	0.50	0.00	100.0
Min.	0.84	0.54	1.10	1.37	0.69	0.55	0.47	0.81	62.97	0.71	0.50	0.00	
Max.	5.24	2.10	27.04	26.69	1.45	9.09	6.09	69.00	94.17	0.85	15.28	2.66	

The difference presented in both areas and points. Comparing two areas, the content of Mn in the first area is 0.94% and in the second is 69.00%. There is also significant difference, when Fe content is compared: the first area – 67.76%, the second – 0%. The same diversity is also presented by points: the minimum content of Si is 1.10% and the maximum 27.04%; the content of S changes from 1.37% to 26.69% from point to point; the content of Ca is between 0.47% and 6.09%; the content of Pb also differs significantly from 0.50% to 15.28%, etc. The reason for this might be the thermal shock that slag received while cooling after reaching the melting temperature of ore at about 1500°C. This quick change in thermal condition also influences the crystalline structure of the blast furnace slag (Figure 4.3) as there is no enough time to form crystals, which is the reason for significant amount of amorphous material.

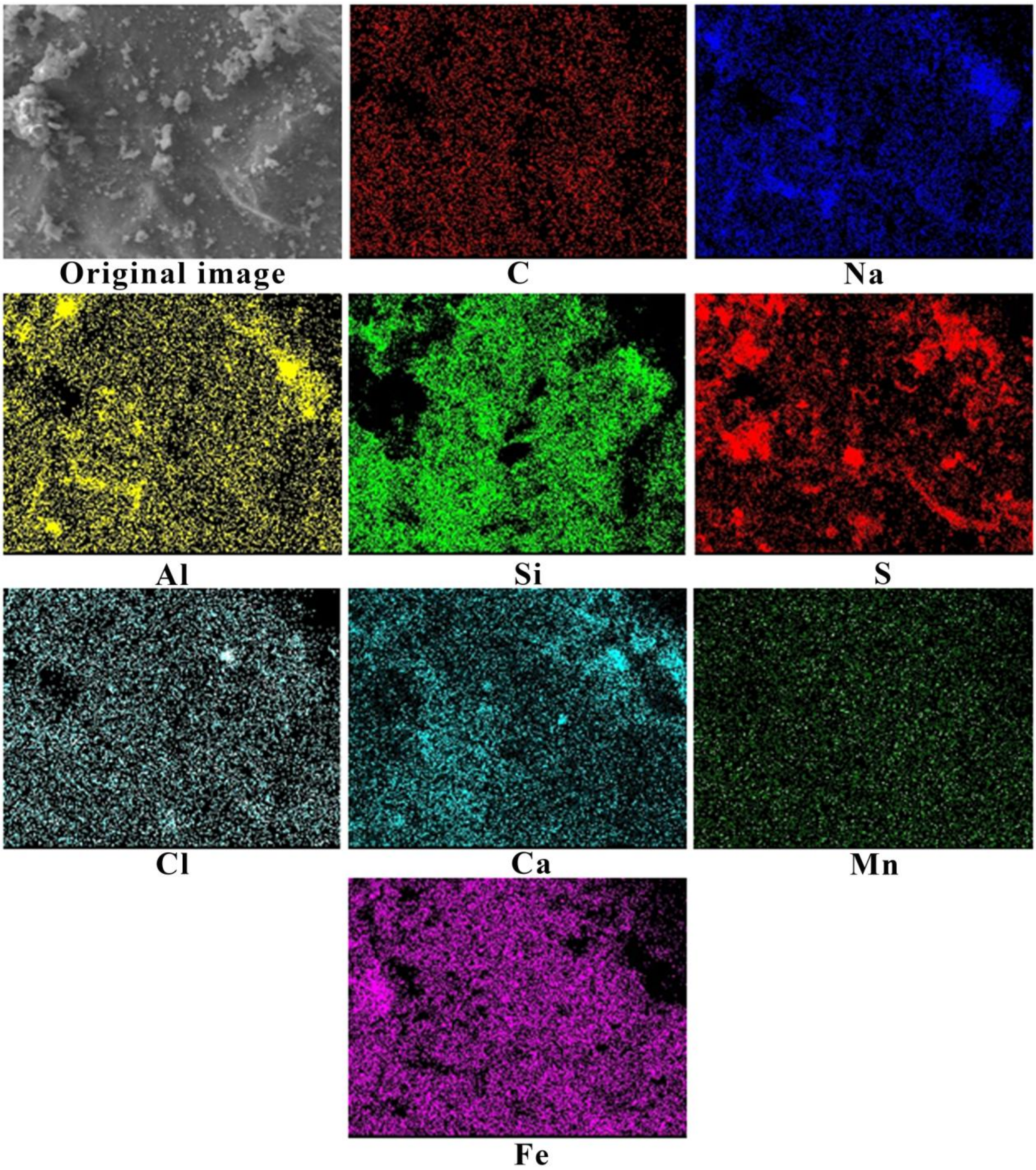

Figure 4.11 - Mapping the chemical states of an element inside a blast furnace slag sample (using method of tomographic X-ray absorption spectroscopy).

The principal chemical elements in the blast furnace slag were studied with mapping method by tomographic X-ray absorption spectroscopy (Figure 4.11). The result demonstrates relatively uniform placement of the elements, without separated clots formations, which is due to dominance of amorphous phase in the material. The major amount of points can be observed in the image representing Fe, which is due to 62.1% content. The minor density element is Mn, which is only 0.6% content. The least uniform placement is identified in case of S and Si.

4.5.3 Morphological structure and micro-chemical composition of the foundry sand

According to images received by SEM (Figure 4.12) method the size of the foundry sand’s particles can be estimated as 100-300μm, which supports results of grain size test of the material. When studied on magnification of 300 times, the monolith structure of the particles can be observed. There are few superficial damages being detected. Due to the fact that this sand received thermal shock (about 1300°C) when was used as a mold for production of detail, structural changes are inevitable. These structural changes might be hidden inside the particles. If the mold was used only once or twice, it may withstand thermal shocks without significant visible superficial changes.

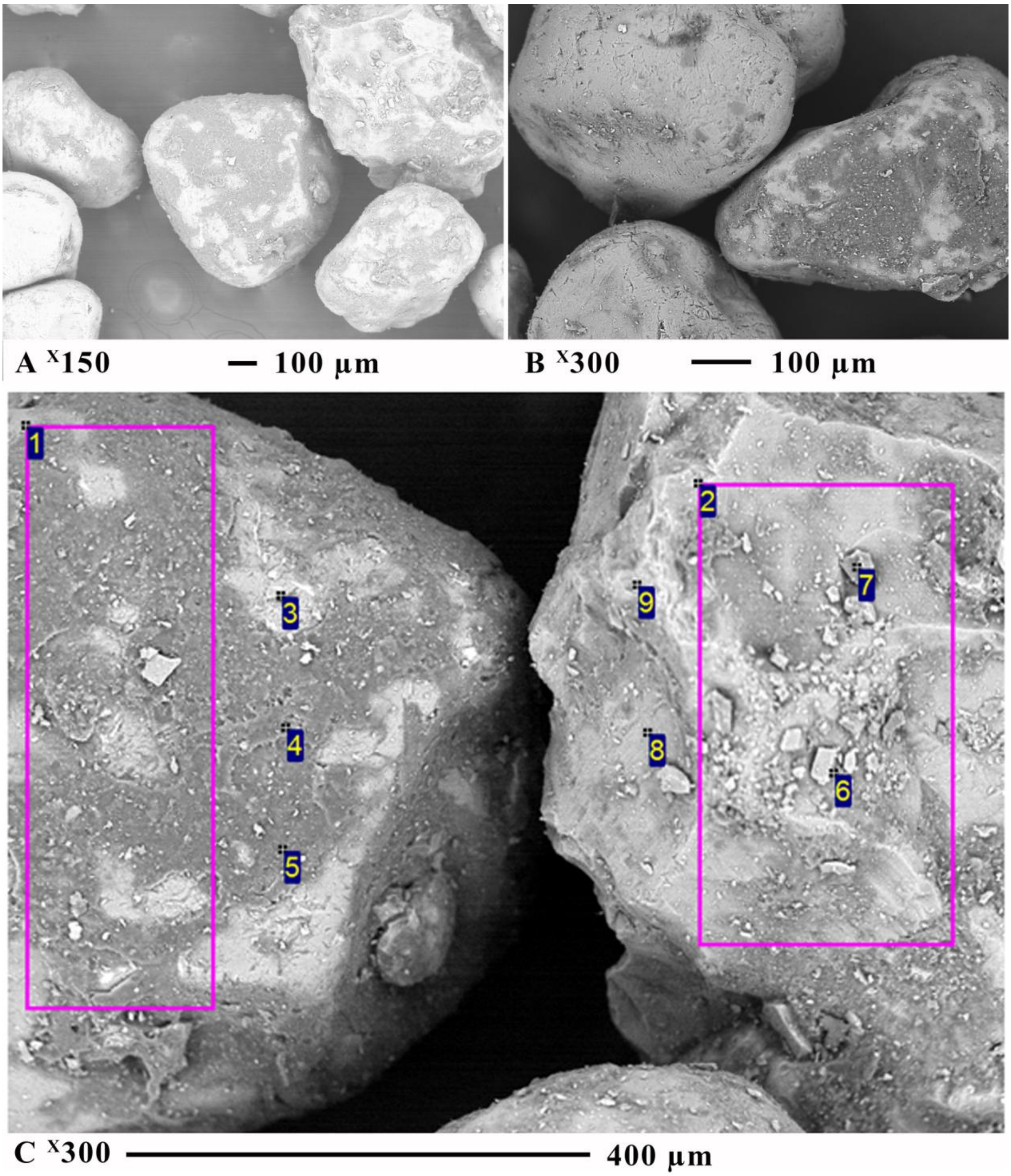

Figure 4.12 - SEM micro images and EDS of foundry sand with different magnification.

Micro-chemical composition was determined by EDS method (Figure 4.12 - C and Table 4.8) and is represented by only four chemical elements. The major component is Si, which varies from point to point between 80.58 and 99.51%. Lower content have Fe (1.25 - 11.28%) and Al (0.49 - 10.22%). The lowest content has Na (2.24 - 5.92%).

Table 4.8 - Chemical composition of the foundry sand (Figure 4.12 – C) by EDS method.

Points	Na	Al	Si	Fe	Total
1-area	0.00	2.71	91.86	5.43	100.0
2-area	2.68	0.89	95.18	1.25	100.0
3	0.00	0.49	99.51	0.00	100.0
4	0.00	2.44	92.48	5.08	100.0
5	0.00	10.22	80.58	9.20	100.0
6	2.24	0.00	97.76	0.00	100.0
7	5.92	3.99	90.09	0.00	100.0
8	0.00	6.52	82.19	11.28	100.0
9	0.00	3.95	96.05	0.00	100.0
Min.	2.24	0.49	80.58	1.25	
Max.	5.92	10.22	99.51	11.28	

Due to the fact that foundry sand is not a pure natural sand, but sand, which was mixed with clay to form the mold and then had contact with liquid metal, it may present micro pollutants when micro-chemical composition is analyzed. By micro pollutants is meant: clay particles, additives of forming mixtures; iron oxides foil on the surface of sand particles, etc. According to XRF (Table 4.3) and XRD results (Figure 4.4) the foundry sand sample has very high purity and crystallization, but analysis of micro elements identifies some other minor quantity elements.

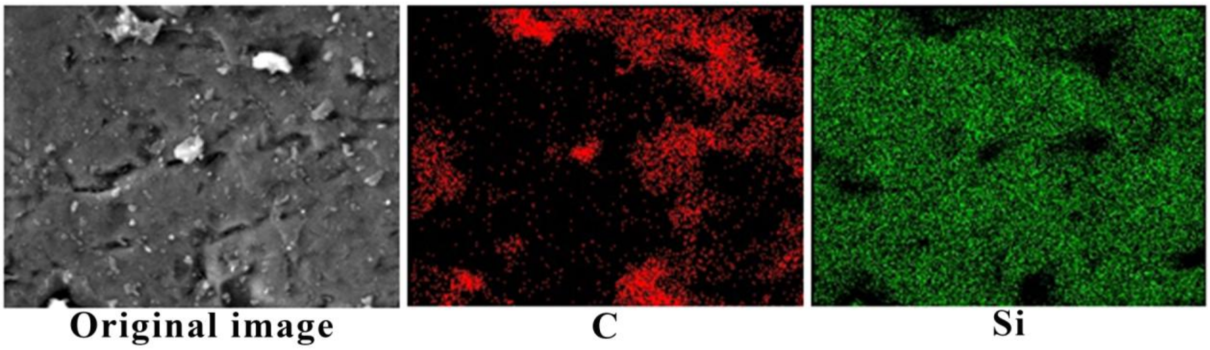

Figure 4.13 - Mapping the chemical states of an element inside a foundry sand sample (using tomographic X-ray absorption spectroscopy).

Mapping of the chemical states of elements in the foundry sand by tomographic X-ray absorption spectroscopy (Figure 4.13) shows the dominance of Si and C in the composition of the material. Despite the fact that Fe, Al and Na were identified by SEM method (Table 4.8), there were no signs of presence of these elements in mapping method. The reason for it might be the difference in approach of two methods. The presence of C might be due to firing process on the surface of the particle in the moment of thermal shock, when liquid metal contacts with the sand. Non-uniformity of elements placement means poor condition of homogenization on the micro scale.

4.5.4 Morphological structure and micro-chemical composition of the waste glass

The images (Figure 4.14) proved by SEM method showed that size of the waste glass particles vary significantly between 1 and 200 µm.

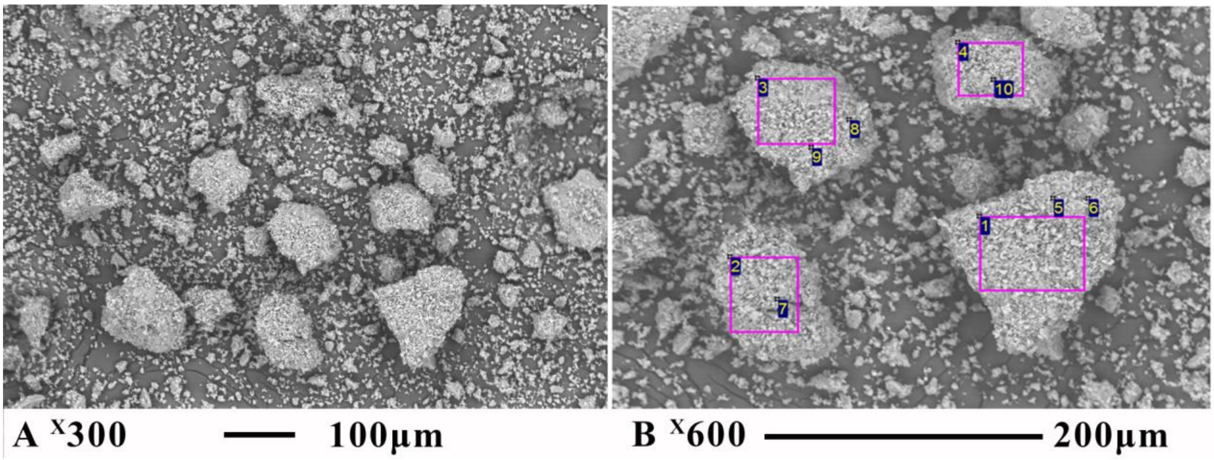

Figure 4.14 - SEM micro images and EDS of waste glass with different magnification.

Mostly all the particles have irregular shape with rounded edges. It does not look like a broken glass, and the reason for that is polishing process, which is aimed to remove all sharp edges.

Table 4.9 - Chemical composition of the waste glass (Figure 4.14 – B) by EDS method.

Areas	Points	Na	Mg	Al	Si	K	Ca	Fe	Total
Area 1	1	13.27	3.62	1.01	62.89	0.55	18.66	0.00	100.00
	5	10.63	3.53	0.89	62.62	0.70	20.09	1.54	100.00
	6	5.88	2.23	1.28	50.83	0.00	35.11	4.68	100.00
Area 2	2	11.49	3.47	1.13	64.35	0.00	19.57	0.00	100.00
	7	8.45	2.71	1.38	69.69	0.83	16.94	0.00	100.00
Area 3	3	13.24	3.68	0.86	61.66	0.00	20.57	0.00	100.00
	8	5.72	1.36	1.08	30.01	0.00	61.82	0.00	100.00
	9	9.41	3.12	0.91	57.55	0.63	28.38	0.00	100.00
Area 4	4	13.96	3.95	1.09	64.91	0.54	14.96	0.59	100.00
	10	11.18	3.91	0.86	59.05	0.00	25.01	0.00	100.00
Min.		5.72	1.36	0.86	30.01	0.54	14.96	0.59	
Max.		13.96	3.95	1.38	69.69	0.83	61.82	4.68	

Comparison of the chemical composition of points, which belong to the same particle, presents high heterogeneity of the content. For example, in the particle, which has area 1 the Na content in one point is 10.63%, while the content of another point close to it is 5.88%. The similar results were obtained by other elements, for example Si, which varied between 50.83% and 62.62%. When another particle is taken for a detailed analysis, which has area 3 and points 8 and 9, the content of Si is changing from 30.01% to 57.55% and Ca from 28.38% to 61.82%.

At the same time, there is no significant difference between chemical compositions of each particle. Comparing area 1, 2, 3 and 4, the content of Na was between 11.49% and 13.96%, Si was between 61.66% and 64.91%, and Ca was between 14.96% and 20.57%. This is due to the fact that area in general might demonstrate more stabilized result than the exact point, which is usually about only 0.2 μm in size.

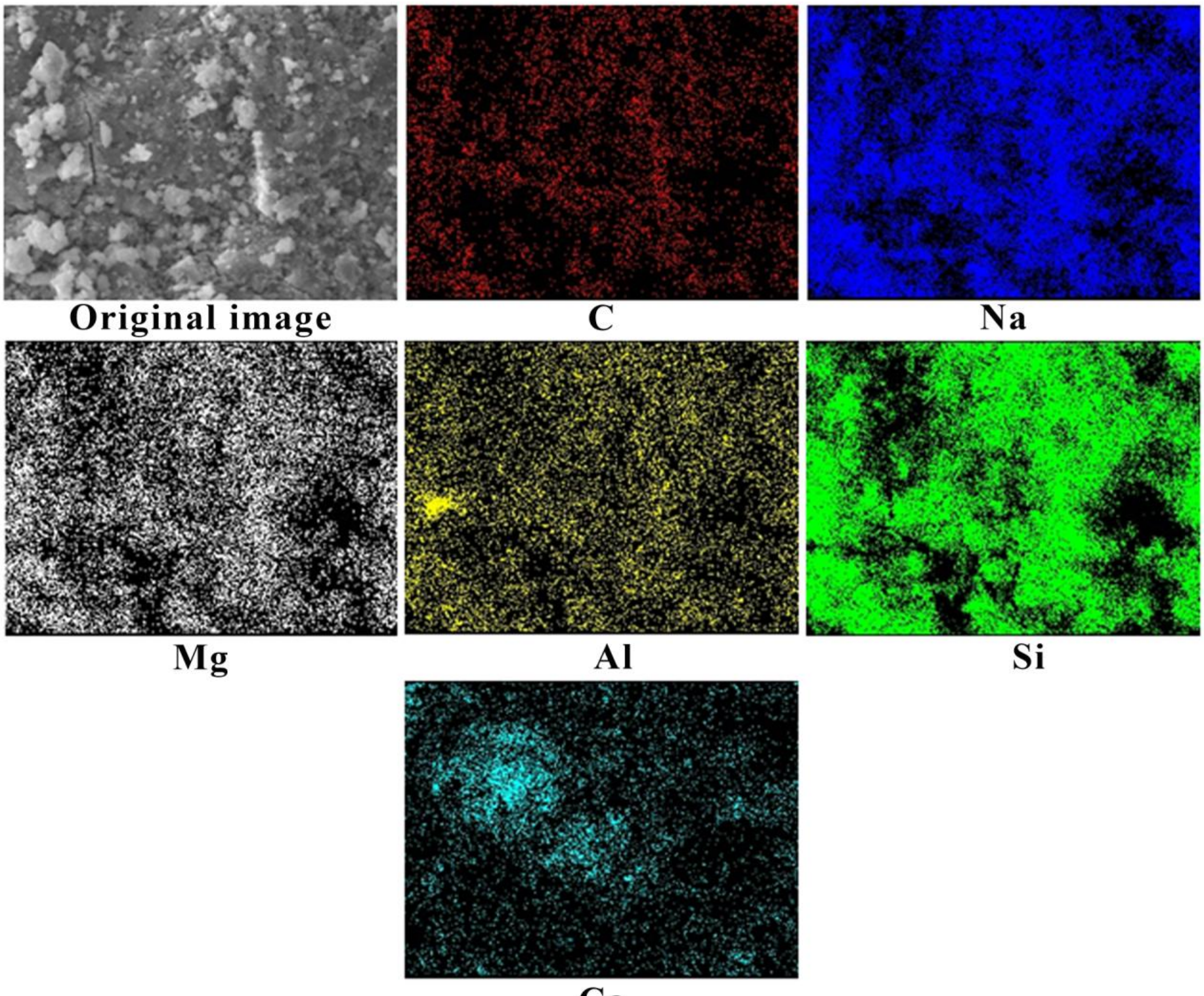
Original image
C
Na
Mg
Al
Si
Ca

Figure 4.15 - Mapping the chemical states of an element inside a waste glass (using tomographic X-ray absorption spectroscopy).

The mapping method also gives information on heterogeneity of the material. According to the images (Figure 4.15) the highest density has Si. Na seems to be less dense. Atoms of Al and Ca have high dispersion, but tend to form clot like formations in particular places.

4.5.5 Morphological structure and micro-chemical composition of the wood ash

The morphology of wood ash is presented by variety of shapes (Figure 4.16). Comparing with previous images of other materials the organic background of these fibers becomes impossible to not to notice. When magnification of 1000 times is applied (Figure 4.16 - E and F) the fibrous structure of the material becomes obvious. High porosity of the material is also one of the reasons for high water absorption capacity.

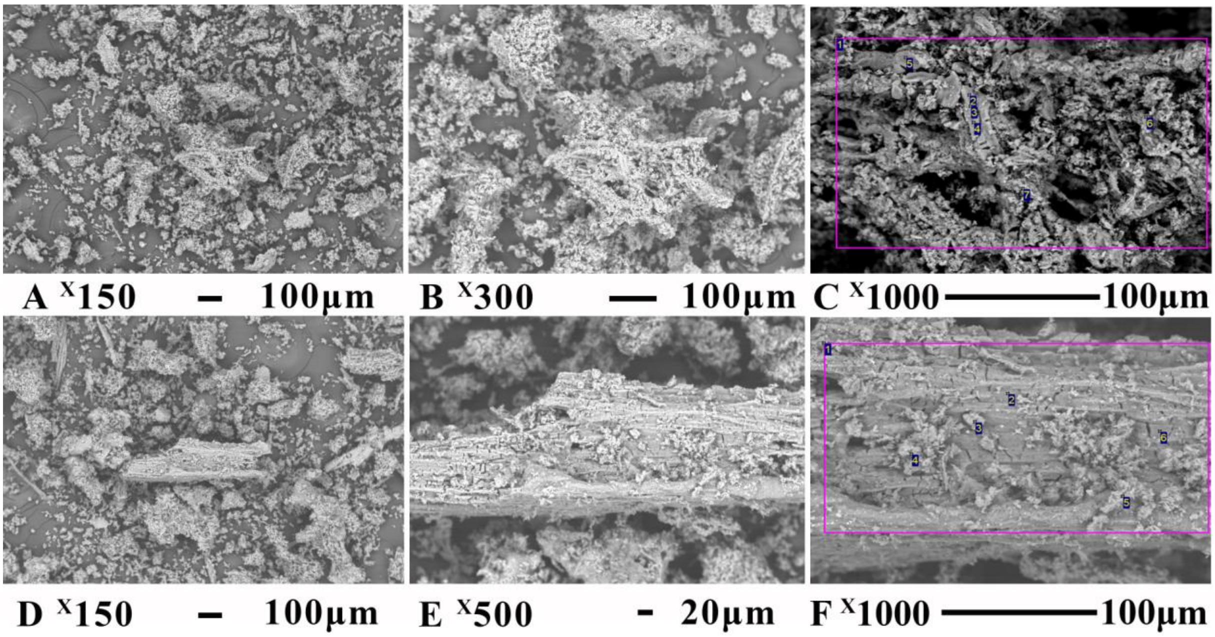

Figure 4.16 - SEM micro images and EDS of wood ash with different magnification.

The micro-chemical composition of the wood ash was studied in two distinct areas: description of the first one (Figure 4.16 - C) is the Table 4.10 and another one (Figure 4.16 - F) was described in the Table 4.11.

Table 4.10 - Chemical composition of the wood ash (Figure 4.16 – C) by EDS method.

Points	Na	Mg	Al	Si	S	Cl	K	Ca	Mn	Total
1- area	0.77	17.68	1.54	1.02	1.81	2.15	48.74	24.15	2.15	100.00
2	0.00	18.62	1.01	0.00	0.00	0.00	50.41	28.01	1.95	100.00
3	0.00	7.78	0.00	0.00	0.00	0.00	59.68	30.99	1.55	100.00
4	0.00	4.05	0.00	0.00	0.00	0.00	61.15	34.79	0.00	100.00
5	0.00	5.07	0.00	0.00	0.00	0.00	60.97	33.27	0.70	100.00
6	0.00	14.89	0.85	0.00	0.00	0.54	53.49	28.88	1.35	100.00
7	2.31	13.42	0.97	0.00	2.95	5.53	54.38	19.28	1.16	100.00
Min.	0.77	4.05	0.85	1.02	1.81	0.54	48.74	19.28	0.70	
Max.	2.31	18.62	1.54	1.02	2.95	5.53	61.15	34.79	2.15	

The chemical composition of the points 2, 3 and 4 (Table 4.10), which are located very close to each other, present high heterogeneity as the content of Mg rises from 4.05 to 18.62%. There is also significant difference in Ca content, which drops from 34.79 to 28.01%.

Table 4.11 - Chemical composition of the wood ash (Figure 4.16 – F) by EDS method.

Points	Na	Mg	Al	Si	P	S	Cl	K	Ca	Mn	Total
1- area	0.82	8.87	0.89	0.00	2.27	2.48	4.24	57.71	21.35	1.38	100.00
2	1.12	1.31	0.00	0.00	2.28	1.85	5.88	64.28	23.28	0.00	100.00
3	0.00	0.91	0.00	0.00	0.00	0.00	0.00	62.17	36.92	0.00	100.00
4	2.64	5.12	1.52	0.00	0.00	2.30	2.44	53.81	31.05	1.13	100.00
5	1.16	14.97	2.84	1.29	2.05	3.08	4.86	46.00	22.81	0.95	100.00
6	0.00	4.55	1.52	0.00	3.54	2.14	4.77	60.31	23.17	0.00	100.00
Min.	0.82	0.91	0.89	1.29	2.05	1.85	2.44	46.00	21.35	0.95	
Max.	2.64	14.97	2.84	1.29	3.54	3.08	5.88	64.28	36.92	1.38	

All the 5 points and 1 area are located on the same fiber of relatively big size, which was analyzed (Figure 4.16 - F) present inconsistency (Table 4.11) of chemical composition. For example, the radical change in content of Mg in the points might be observed, when points 3 (0.91%) and 5 (14.97%) are compared. Significant difference is presented in content of K and Ca. Even comparison of areas', which tend to have more stabilized chemical composition does not let identify similarities.

There are no solid evidences of crystalline structures, which were identified by XRD method (Figure 4.6). In order to point out afwillite $Ca_3Si_2O_6(OH)_2(H_2O)_2(Si_5O_{18})$, albite (Na, Ca)Al(Si, Al)$_3$O$_8$, orthoclase K(Al, Fe)Si_2O_8 and quartz SiO_2 by EDS method, more analyses should be made. Unfortunately, this research faces limitation in terms of the crystalline structure analysis as there is little amount of these minerals and they have small size.

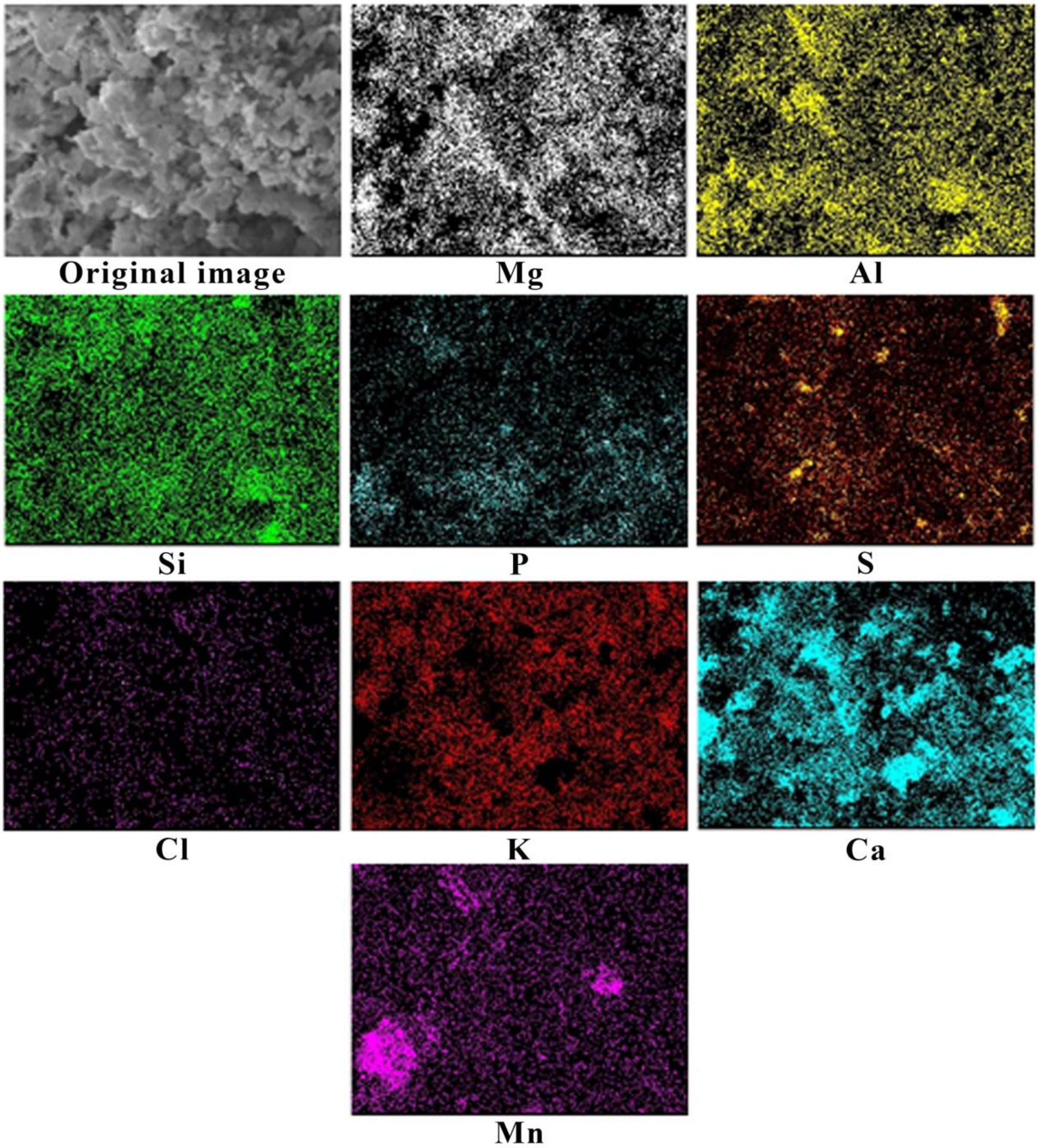

Figure 4.17 - Mapping the chemical states of an element inside a wood ash sample (using tomographic X-ray absorption spectroscopy).

Some clots formations of chemical elements (Ca, S, Mg and Mn) were identified by tomographic X-ray absorption specter (Figure 4.17) of wood ash. It might be presumed that these locations are the places of crystalline formations, which were identified by XRD method (Figure 4.6), but were not identified by EDS method (Figure 4.16). Comparison of chemical compositions of the minerals (afwillite, albite, orthoclase and quartz) and mapping results does not confirm this hypothesis.

The highest density is presented by Ca, which is 28.2% of chemical composition according to Table 4.3. An unexpected result was demonstrated by Mn, which has only 1.4% of content in the material, but presents some dense areas on the image. At the same time K that supposed to be 22.8% is not presenting any dense areas and seems to be distributed uniformly.

4.5.6 Morphological structure and micro-chemical composition of the clay

The clay, which was used to prepare reference samples, was provided by local brick factory and later was analyzed by SEM method. No special characteristics of the particles were identified, as particles vary significantly.

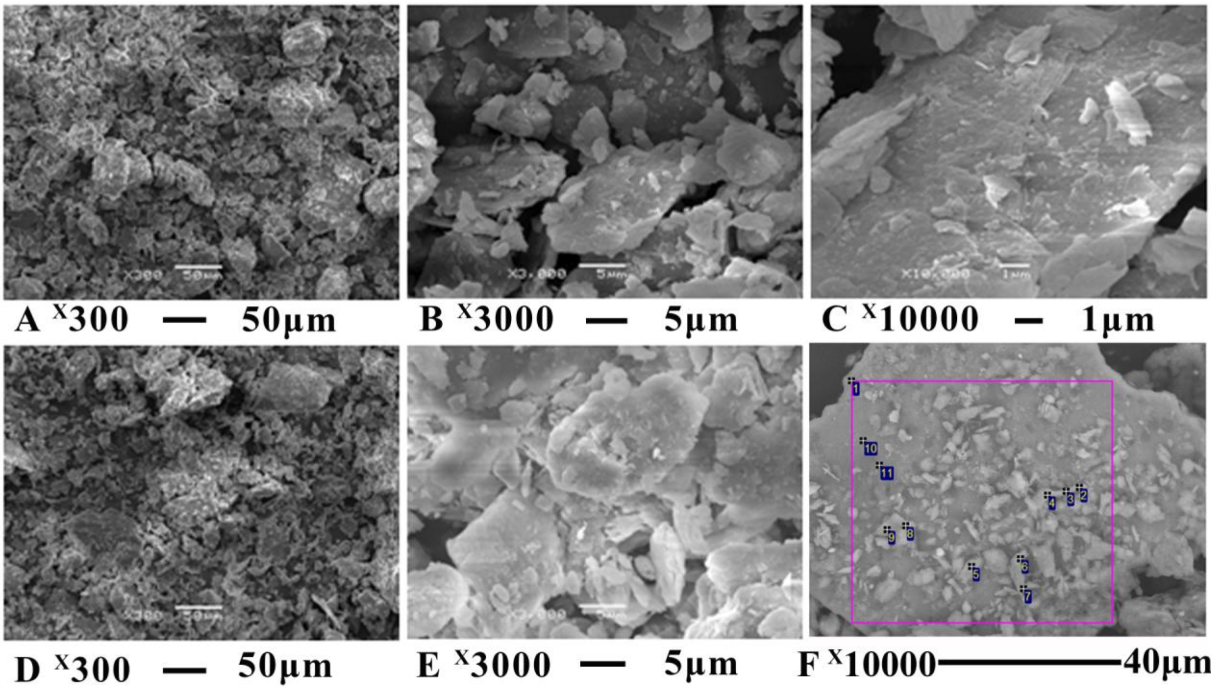
A ^{X}300 — 50µm **B** ^{X}3000 — 5µm **C** ^{X}10000 – 1µm

D ^{X}300 — 50µm **E** ^{X}3000 — 5µm **F** ^{X}10000——————40µm

Figure 4.18 - SEM micro images and EDS of clay with different magnification.

According to the XRD method, minerals of illite and quartz are presented in the clay (Figure 4.7). Particles, which look like fishscales are typical for illite. At the same time massive particles are typical for quartz.

Table 4.12 - Chemical composition of the clay (Figure 4.18 – F) by EDS method.

Points	Mg	Al	Si	K	Ca	Ti	Fe	Total
1-area	0.00	7.90	89.27	0.57	0.00	0.00	2.26	100.0
2	0.56	9.79	86.31	0.00	0.40	0.00	2.94	100.0
3	0.00	8.63	88.43	0.00	0.00	0.00	2.95	100.0
4	0.00	8.67	88.68	0.00	0.00	0.00	2.65	100.0
5	0.56	17.34	76.37	0.00	0.00	0.58	5.15	100.0
6	0.44	19.52	75.21	0.00	0.00	0.56	4.27	100.0
7	0.00	2.22	97.78	0.00	0.00	0.00	0.00	100.0
8	0.00	14.70	79.68	0.00	0.00	0.67	4.95	100.0
9	0.00	16.21	78.08	1.11	0.00	0.00	4.61	100.0
10	0.00	2.21	97.79	0.00	0.00	0.00	0.00	100.0
11	0.00	2.15	97.85	0.00	0.00	0.00	0.00	100.0
Max.	0.56	19.52	97.85	1.11	0.40	0.67	5.15	
Min.	0.44	2.15	75.21	0.57	0.40	0.56	2.26	

There are some differences between chemical compositions of each point (Table 4.12), but they are not significant and accord with the result of chemical composition of the clay in general (Table 4.3).

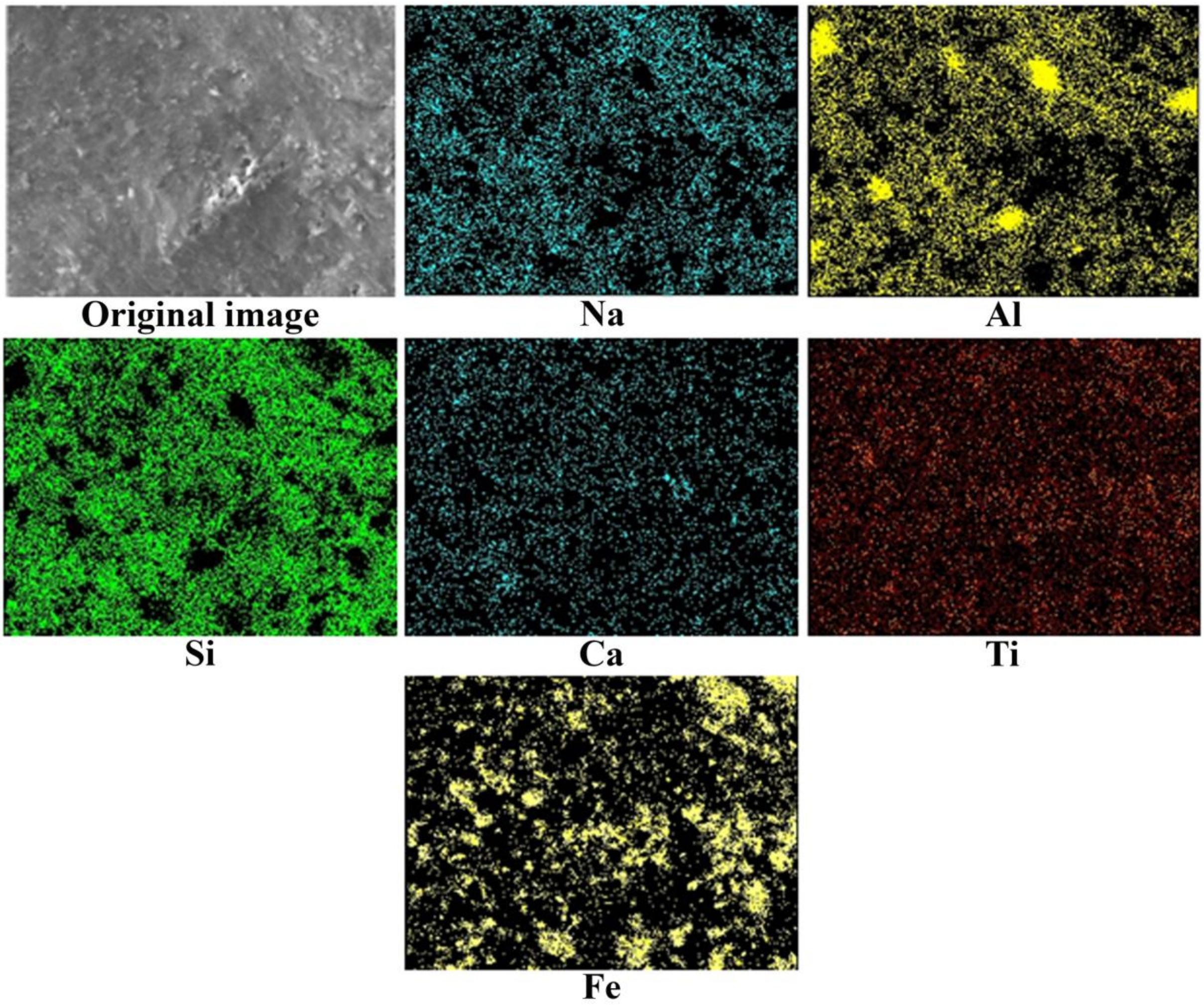

Figure 4.19 - Mapping the chemical states of an element inside a clay sample (using tomographic X-ray absorption spectroscopy).

Images of chemical elements position by method of tomographic X-ray absorption specter confirm the dominance of the Si (53.3%), Al (24.7%) and Fe (6.1%) in the clay, with relatively small content of other chemical elements. Fe presents some clots, which is typical for it, and Ti shows the most uniform dispersion in the sample.

4.6 THERMOCHEMICAL CHARACTERISTICS OF THE RAW MATERIALS

The analysis of thermochemical reactions during firing process of the materials was performed through study of curves obtained by differential thermal analysis (DTA) and thermogravimetric analysis (TGA).

4.6.1 Thermochemical characteristics of the red mud

Crucial chemical elements of the red mud (Table 4.3) are Fe_2O_3 (29.9%) and Al_2O_3 (21.2%). Due to hydro-thermal chemical processes, which take place during Bayer method application to bauxite ore, both these elements have condition of hydro minerals. That is why they have crystalline structures (Figure 4.2) and majority of amorphous phase of iron and aluminum hydroxides ($Fe_2O_3 \bullet nH_2O$ and $Al_2O_3 \bullet nH_2O$), which tend to change their state. Firing process of thermochemical analysis affects both elements and this is the reason why it is impossible to differentiate and quantitatively determine role of each element separately.

The processes, which go along with firing process (Figure 4.20 and Table 4.13), in terms of aluminum hydroxides $Al_2O_3 \bullet nH_2O$ might be described as following: at the temperature of 110-120°C weakly bounded or not bounded at all water disappears; at the temperature of 200-250°C gibbsite (γ-AlO(OH)) starts to lose crystallized molecules of water and transforms into boehmite; when the temperature rises up to 500°C boehmite transforms into γ-Al_2O_3 and when it reaches 850°C it transforms into α-Al_2O_3 (BROWN (2011)).

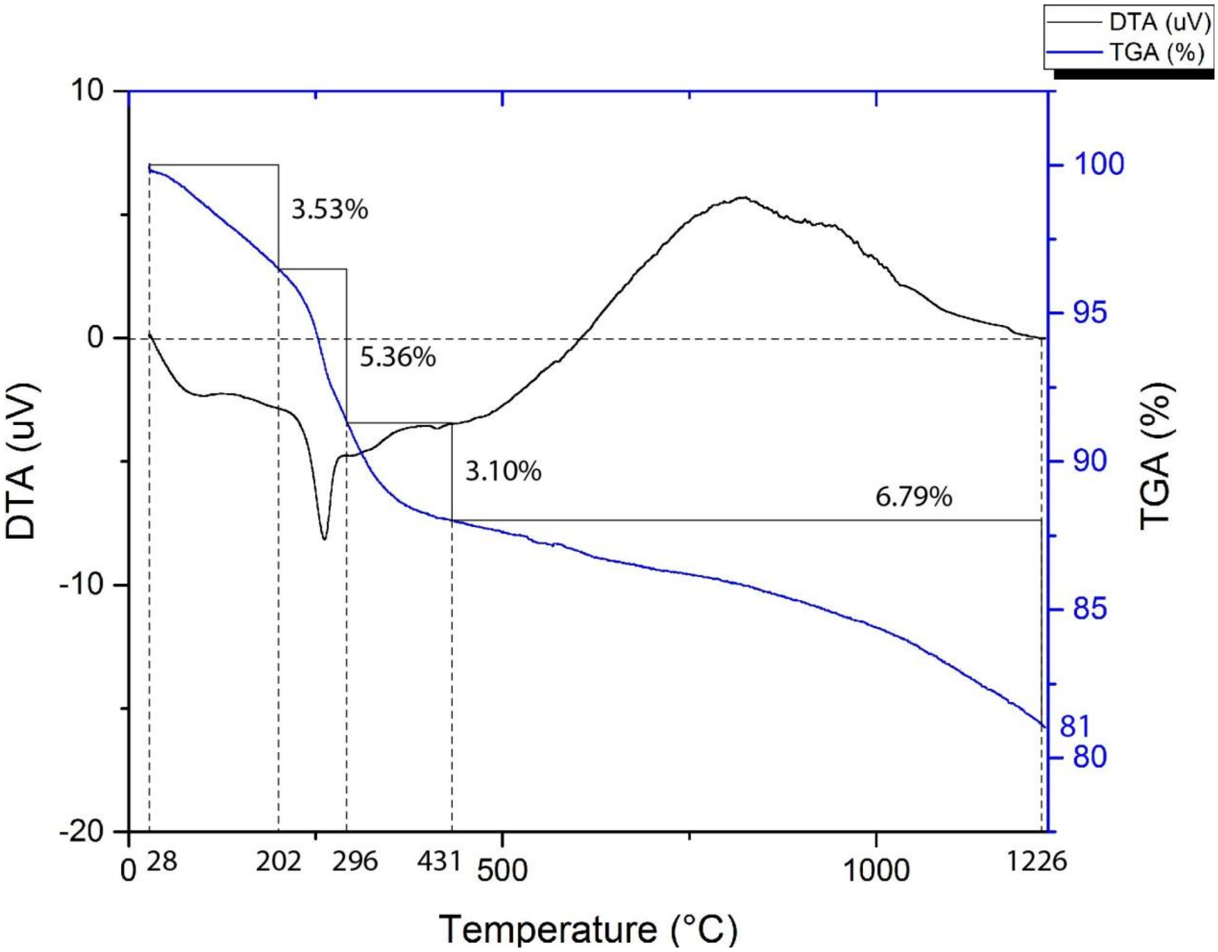

Figure 4.20 - DTA and TGA curves of the red mud.

Table 4.13 - The endothermic and exothermic effects of the red mud by DTA and TGA curves (Figure 4.20)

Hydrooxides	Thermo-chemical processes, temperature of reaction (°C) and weight loss (%)			
Effect	Endothermic effect 1. 28-202°C.	Endothermic effect 2. 202-296°C.	Exothermic effect 1. 296-431°C.	Exothermic effect 2. 431-1226°C.
Al	Removal of free or weakly bounded water. Weight loss 3.53%.	loses crystal water molecules by $Al(OH)_3$ and converted to boehmite γ-$AlO(OH)$ Weight loss 5.36%	boehmite is converted into anhydrous γ-Al_2O_3 Weight loss 3.10%	The transformation γ-Al_2O_3 γ-Al_2O_3→ α-Al_2O_3 Weight loss 6.79%.
Fe		Amorphous gel transformation to (α, β, ɣ and δ) of FeOOH	FeOOH→ɣ-Fe_2O_3→ Fe_3O_4 Weight increase	Fe_3O_4 →Fe (700-750°C). Weight loss. Formation of dross-Fe_3O_4 (900-1000°C). Weight increase

All these transformations are heat consuming. They are endothermic, except only one exothermic process of γ-Al_2O_3 to α-Al_2O_3 transformation. The main part of heat consumption was due to evaporation of water and decomposition of gibbsite (γ-AlO(OH)).

The first smooth endothermic effect of red mud hydroxides at 28°-202°C with 3.53% weight loss is due to the process of free or weakly bounded water FeOOH dehydration. The beginning of amorphous gel transformation to the various crystalline forms (α, β, ɣ and δ) of FeOOH explains the second endothermic effect between 202° and 296°C. At the same temperature began also the transformation of FeOOH → ɣ-Fe_2O_3 (maghemite) → Fe_3O_4 with total weight loss 5.36%. This process smoothly transforms into recovery of Fe_3O_4 to Fe till 700°-750°C (BROWN (2011)).

4.6.2 Thermochemical characteristics of the blast furnace slag

Due to the fact that there is 10.0% of SO_3 and 62.1% of Fe_2O_3 (Table 4.3) there is high chemical activity being provoked while heating process. It leads to synthesis of ferric sulfide and ferric sulfate. When the slag has been stored in the metallurgical plant for several years acting naturally with the environment, hydrated new growths formed itself and took the shape of $FeSO_4 \cdot 7H_2O$ formations.

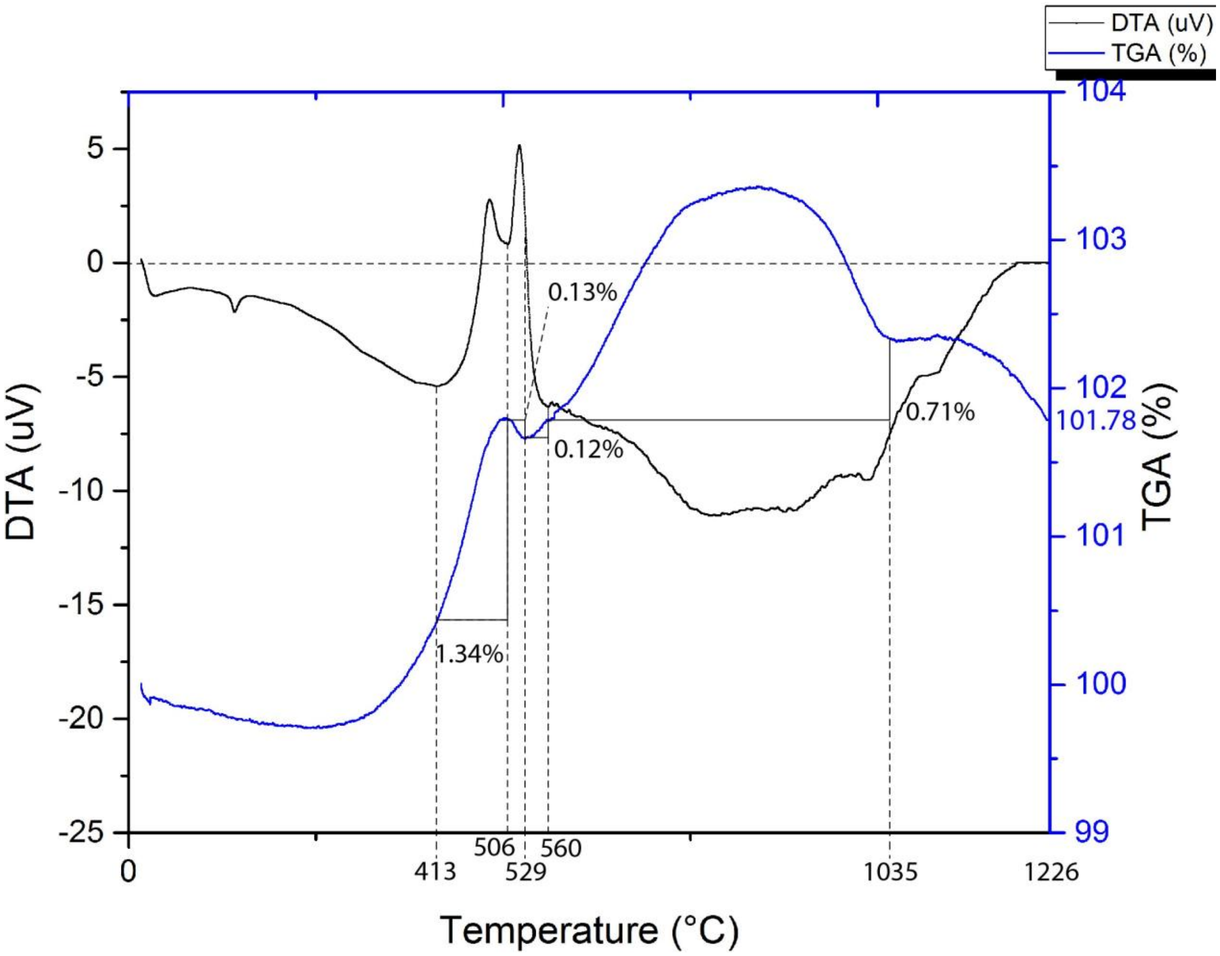

Figure 4.21 - DTA and TGA curves of the blast furnace slag

Table 4.14 - The endothermic and exothermic effects of the blast furnace slag by DTA and TGA curves (Figure 4.21)

Thermo-chemical processes, temperature of reaction (°C) and weight loss (%)			
Endothermic effect 1. 25-413°C.	Exothermic effect 1. 413-506°C.	Exothermic effect 2. 506-560°C.	Exothermic effect 3. 560-1035°C.
1. Removal of free and chemisorbed water 2. Amorphous Fe-contained gel transformation to (α, β, ɣ and δ) FeOOH	$Fe_2(SO_4)_3$ melting process. Weight gain 1.34%	FeOOH→ ɣ-Fe_2O_3→ hematite → Fe_3O_4 magnetite. Weight loss 0.01%	1. Pyrite FeS_2→hematite Fe_2O_3→magnetite Fe_3O_4 →Fe up to 700-750°. Weight loss. 2. $FeSO_4$→Fe_2O_3 700-750°. SO_2 and SO_3 burning. Weight loss. 3.Deflagration Fe_3O_4 formation 900-1000°. Common weight increase 0.71%

During heating process of the sample up to 1225°C, the following thermochemical reactions were identified (Table 4.14):

1. The weak endothermic effect at the temperature 25-413°C, which was due to evaporation of not bounded or weakly bounded water. Transformation of FeOOH. (KIMJASHOV (2010)).
2. The exothermic effect 1 at the temperature 413-506°C demonstrates the beginning of $Fe_2(SO_4)_3$ melting process and transformation of it into α-Fe_2O_3 hematite (KIMJASHOV (2010)).
3. The exothermic effect 2 at the temperature 506-560°C, which goes along the transformation $FeOOH \rightarrow \gamma$- $Fe_2O_3 \rightarrow$ hematite $\rightarrow Fe_3O_4$ magnetite with weight loss 0.01% .
4. The enduring and smooth exothermic effect 3 at the temperature 700-750°C presents the complete transformation into Fe_2O_3 and deflagration gas mixture of SO_2 and SO_3 (BROWN (2011)).

The beginning of the third exothermic effect on the DTA curve might involve the endothermic effect of iron sulfide decomposition in the shape of pyrite mineral FeS_2, which starts at 500°C and ends after 730°C (CHANTURIA (2009)). Taking into consideration small content of FeS_2 in the blast furnace slag, the process of decomposition might appear on the DTA curve between 680 and 770°C.

4.6.3 Thermochemical characteristics of the foundry sand

The total weight loss upon firing at 1226°C is 3.7% (Figure 4.22 and Table 4.15), of which 2.43% before reaching 511°C might be because of the removal of the physically adsorbed water molecules and the beginning of clayey structures decomposition.

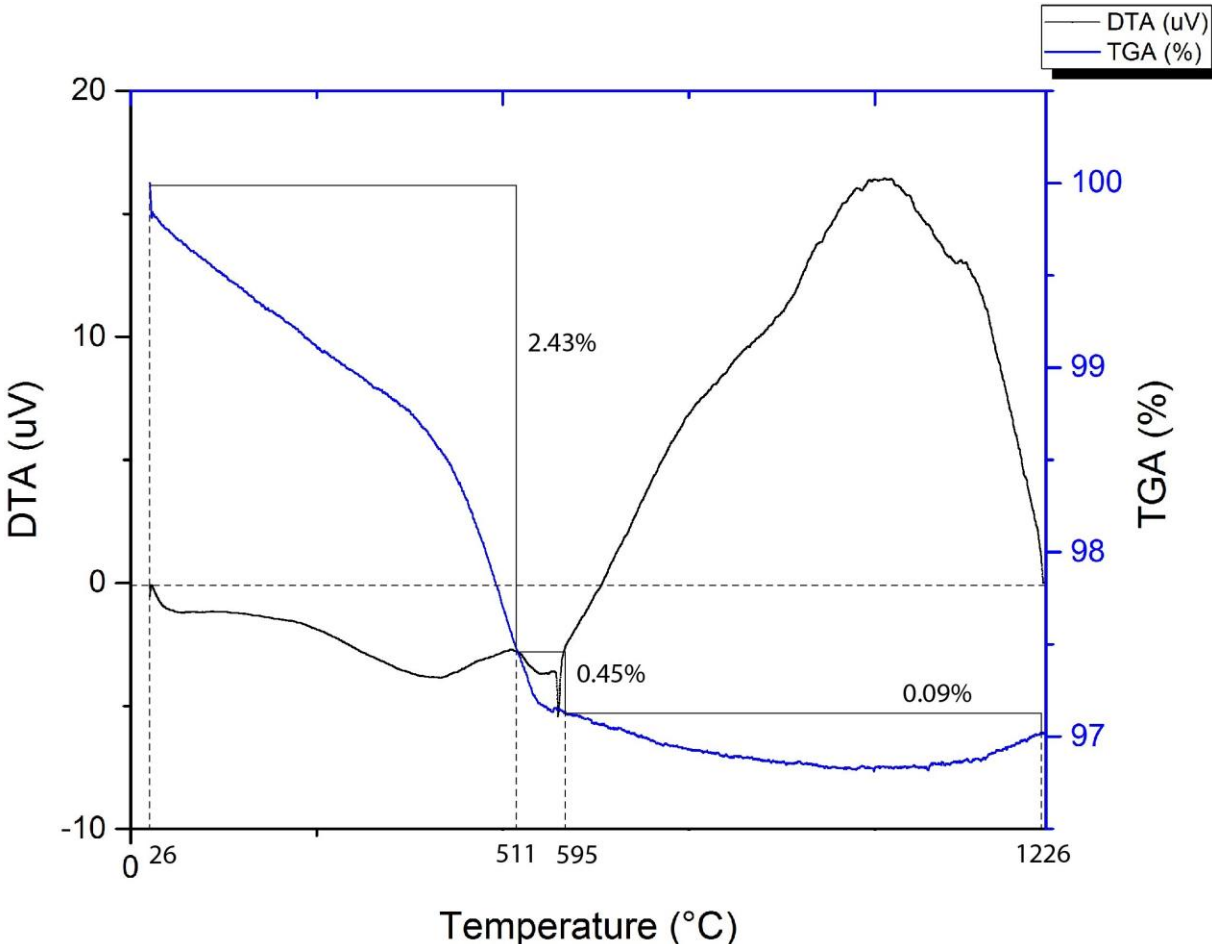

Figure 4.22 - DTA and TGA curves of the foundry sand

Table 4.15 - The endothermic and exothermic effects of the foundry sand by DTA and TGA curves (Figure 4.22)

Thermo-chemical processes, temperature of reaction (°C) and weight loss (%)		
Endothermic effect 1. 26-511°C.	Endothermic effect 2. 511-595°C.	Exothermic effect 1. 595-1226°C.
Evaporation of the physically adsorbed water. Weight loss 2.43%.	The beginning of clayey structures collapse. Weight loss 0.45%.	Burning of organic additives. Weight loss 0.09%.

Exothermic peak between 595°C and 1226°C with 0.09% weight loss might be result of organic additives that are usually used as binders and plasticizers additives during mold shaping. They were used on the casting factory before the foundry sand has been stored as a residue.

4.6.4 Thermochemical characteristics of the waste glass

The waste glass was obtained on the automobile glass polishing enterprise. It consists of the hydrated fine glass dust with two levels of water binding, which might be detected due to two endothermic effects on the DTA curve (Figure 4.23).

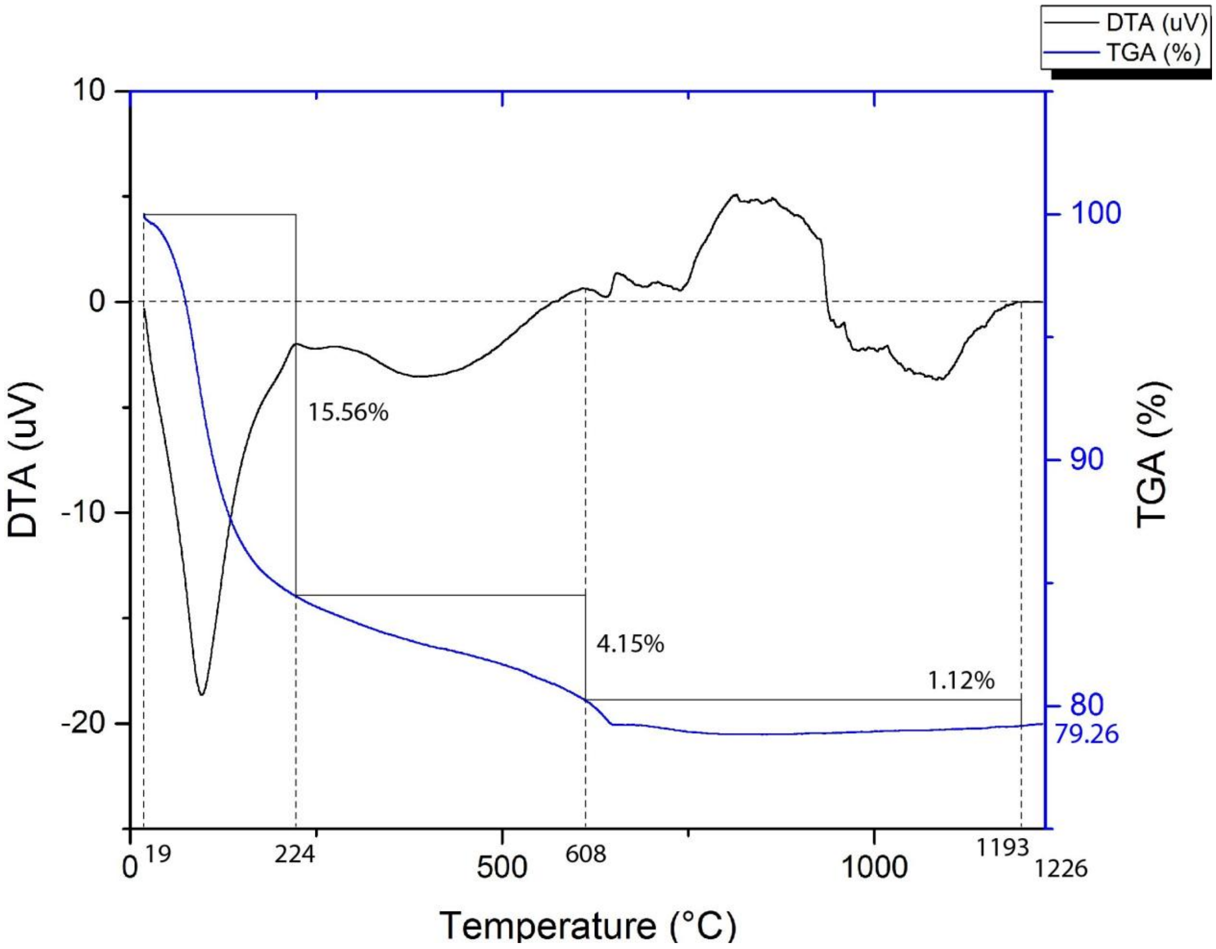

Figure 4.23 - DTA and TGA curves of the waste glass

Table 4.16 - The endothermic and exothermic effects of the waste glass by DTA and TGA curves (Figure 4.23)

Thermo-chemical processes, temperature of reaction (°C) and weight loss (%)		
Endothermic effect 1. 19-224°C.	Endothermic effect 2. 224-608°C.	Exothermic effect 1. 608-1226°C.
Evaporation of the physically adsorbed water. Weight loss 15.56%.	Removal of bounded water. Weight loss 4.15%.	Waste glass crystallization from amorphous phase. Weight loss 1.12%.

The first endothermic effect at 19-224°C accompanied by 15.56% weight loss on the TGA curve related to physically weakly bonded water molecules in the glass. Another endothermic effect at 224-608°C with 4.15% weight loss on the TGA curve can match to the removal of chemisorbed water. The only exothermic effect between 608° and 1193°C and weight loss 1.12% is due to waste glass crystallization after being in amorphous phase.

4.6.5 Thermochemical characteristics of the wood ash

Thermochemical reactions of the wood ash, which took place during firing process, are complex due to the firing of particles of two types: particles that remained under burned after the previous firing, and ash particles, for which it was the second firing process. The organic mass is actually a fuel and this fact complicated the analysis.

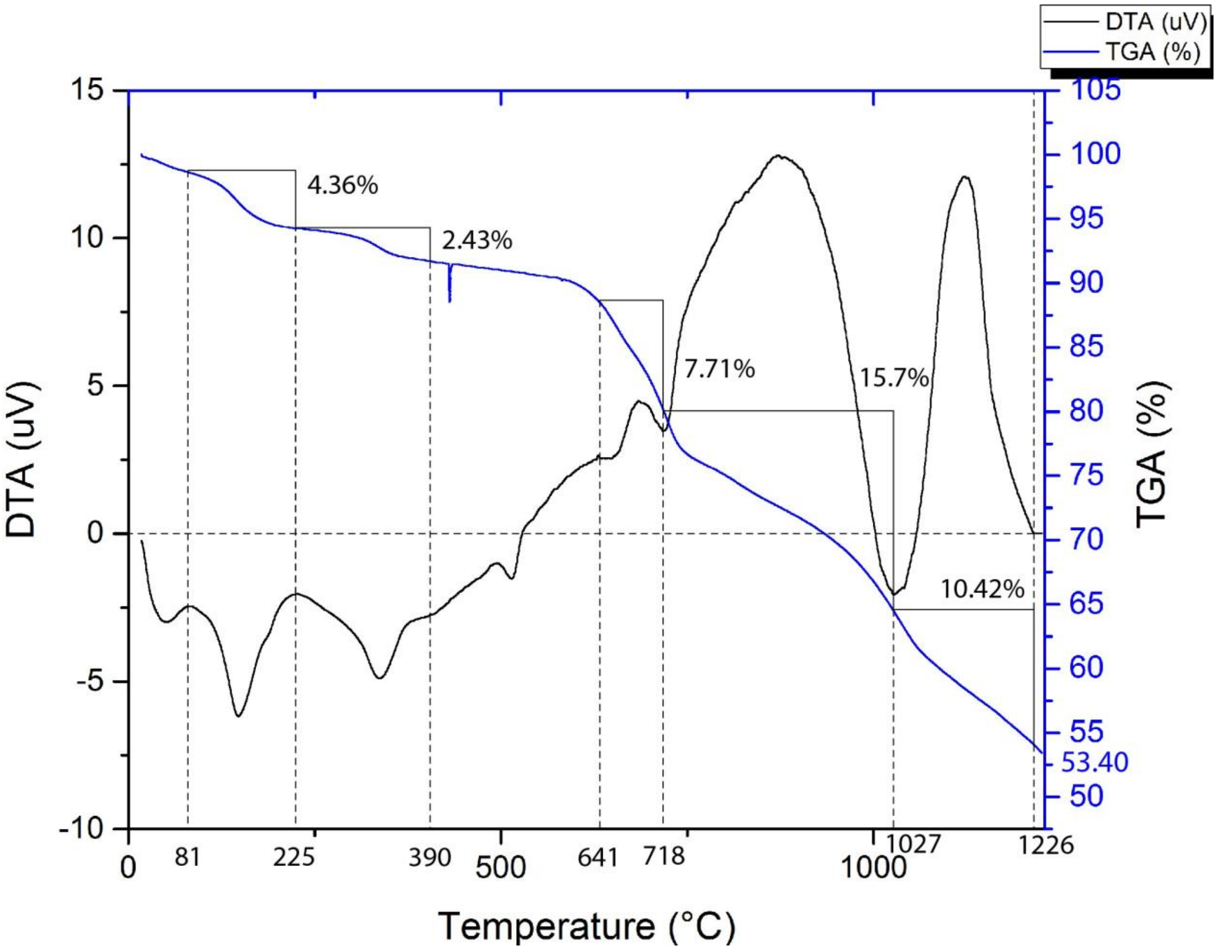

Figure 4.24 - DTA and TGA curves of the wood ash

Burning of this material as one of the ceramic components, repeats the process of pyrolysis, in which under burned particles of wood participate one more time. During this stage, mainly decomposition of the CO, CO_2, CH_4, H_2, H_2O, gases, resin and some inorganic elements takes place (MARYANDYSHEV (2016)). Due to these processes, there are two endothermic effects on the DTA curve (Figure 4.24 and Table 4.17), which occur at 81-225°C and 225-390°C with weight loss 4.36% and 2.43% consequently. In the end of this phase the wood turns into char, which starts to burn producing heat. This is the moment of transition from endothermic to exothermic effects.

Table 4.17 - The endothermic and exothermic effects of the wood ash by DTA and TGA curves (Figure 4.24)

Thermo-chemical processes, temperature of reaction (°C) and weight loss (%)				
Endothermic effect 1. 81-225°C.	Endothermic effect 2. 225-390°C.	Exothermic effect 1. 641-718°C.	Exothermic effect 2. 718-1027°C.	Exothermic effect 3. 1027-1215°C.
Evaporation of the water. Gases and resin burning. Weight loss 4.36%.	Decomposition of lignin, burning of pyrolysis gases. Weight loss 2.43%.	Burning of the char. Weight loss 7.71%.	Flame combustion of char. Weight loss 15.7%.	Smoulding phase of char combustion. Weight loss 10.42%.

The burning of the char is divided into two parts: the first one is flame combustion of char at 718-1027°C and 15.7% weight loss, and the second one is smoulding phase of char combustion without flames at 1027-1215°C and 10.42% weight loss.

The normal temperature of wood's self ignition is about 420-450°C. But as it is demonstrated in the Figure 4.24, this process starts prominently later, at 641-718°C with 7.71% weight loss, and the process of combustion itself keeps on going up to 1027°C with the most significant weight loss of 15.7%. Only after that, at 1027°C the phase of smoulding takes place.

4.6.6 Thermochemical characteristics of the clay

Thermochemical analysis of the clay (Figure 4.25) demonstrated three endothermic effects and one exothermic effect. The first endothermic effect is determined at the temperature of 19-119°C with weight loss 1.88%. At this stage, basically evaporation of water is in the process. The second endothermic effect is due to decomposition of illite ($KAl (Si, Al)_4(OH)_2 \cdot nH_2O$), and the water ($nH_2O$), which exists in his structure at the temperature 183-302°C, with 1.21% weight loss. The third one is due to final stage of illite decomposition and removal of $(OH)_2$ group at 364-618°C with significant weight loss 6.32%.

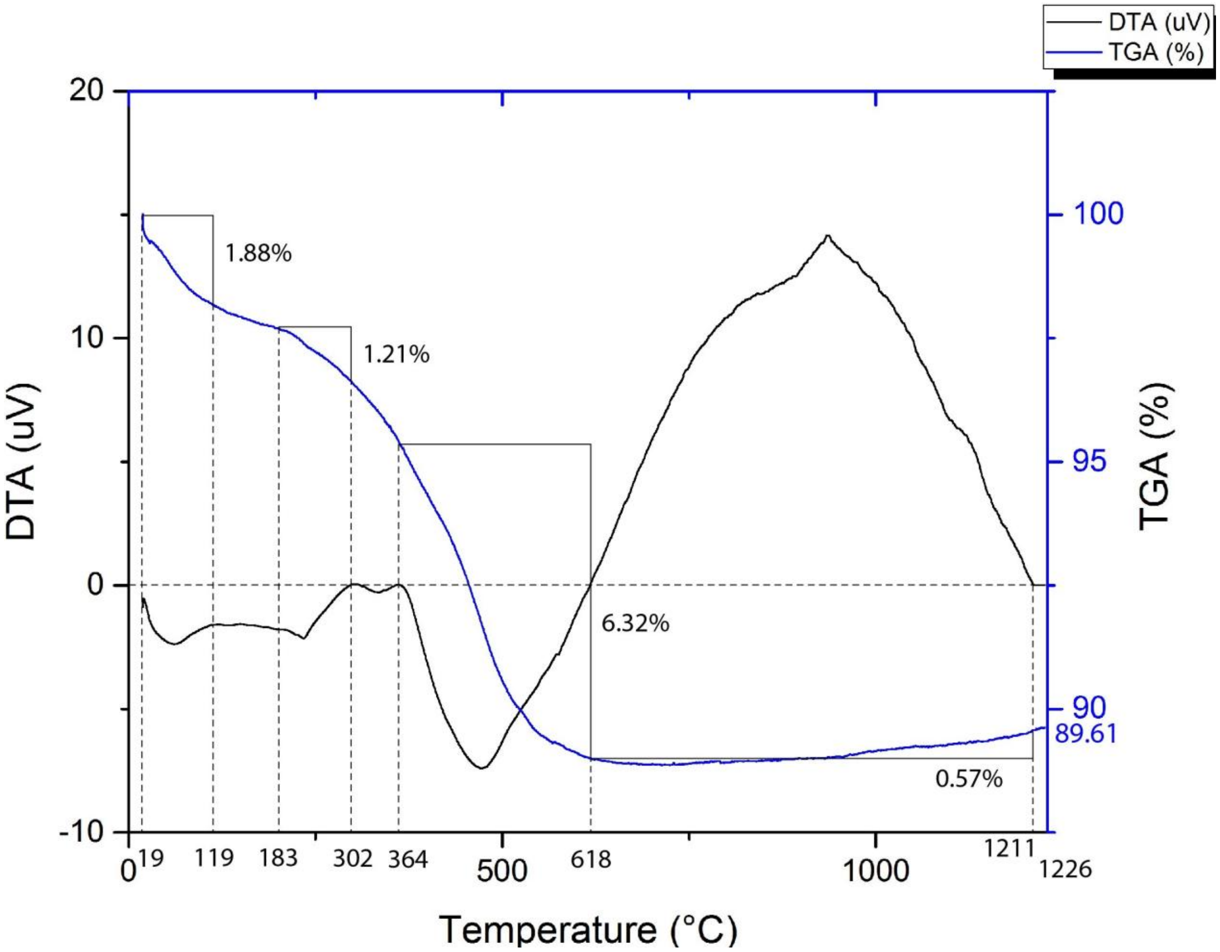

Figure 4.25 - DTA and TGA curves of the clay

Table 4.18 - The endothermic and exothermic effects of the clay by DTA and TGA curves (Figure 4.25)

Thermo-chemical processes, temperature of reaction (°C) and weight loss (%)			
Endothermic effect 1. 19-119°C.	Endothermic effect 2. 183-302°C.	Endothermic effect 3. 364-618°C.	Exothermic effect 1. 618-1211°C.
Evaporation of the water. Weight loss 1.88%.	Decomposition of illite and escape of nH_2O out of it. Weight loss 1.21%.	Decomposition of illite and escape of $(OH)_2$ group out of it. Weight loss 6.32%.	Pyrolysis of organic particles. Weight gain 0.57%.

The only exothermic effect appeared at the second part of thermal analysis at the temperature 618-1211°C, and the reason for it was pyrolysis of the natural organic particles of the clay.

5 CHARACTERIZATION OF THE DEVELOPED CERAMICS

To choose the optimal compositions of the ceramics, which consist of industrial wastes only (bauxite tailings, blast furnace slag, foundry sand, waste glass and wood ash), the following characteristics of the ceramic material were analyzed: flexural strength, using a three point flexural strength technique, water absorption, linear shrinkage and density. All tests to determine these characteristics were taken at the following sintering temperatures: 800°C, 900°C, 1000°C, 1050°C, 1100°C, 1150°C, 1200°C and 1225°C. The values of the physical properties and their standard deviations were obtained as an average of 10 samples' measurements. The amount of samples was chosen in accordance to standard deviation. When the average of 10 samples characteristics was calculated, the standard deviation was low. It means that the results of measurements could be treated with high confidence. In order to ease comparison of the tested characteristics, the compositions were grouped as follows: one-component, two-component, and three-component mixtures.

5.1 FLEXURAL STRENGTH OF THE DEVELOPED CERAMICS

To identify the optimal percentages of initial components of ceramics with the best physical and chemical properties were prepared and studied 24 compositions.

Table 5.1 - Flexural strength of ceramic compositions at different firing temperatures.

№	Compositions content, wt.%					Flexural strength (MPa) of ceramics at different temperatures (°C)							
						800	900	1000	1050	1100	1150	1200	1225
0	Reference clay composition					5.36	5.68	7.09	8.72	10.08	14.65	13.36	6.05
	RM	BFS	FS	WG	WA								
1	40	40	20	0	0	0.38	0.85	1.16	1.76	3.23	5.76	6.20	10.29
2	50	30	20	0	0	0.67	1.12	1.40	1.84	2.98	4.15	6.09	9.73
3	60	20	20	0	0	1.00	1.34	1.82	2.22	2.86	5.89	4.51	3.52
4	70	10	20	0	0	1.08	1.84	2.20	3.38	4.84	5.62	4.25	*
5	100	0	0	0	0	0.00	0.00	0.45	0.93	4.34	6.06	12.17	12.32
6	90	10	0	0	0	2.21	2.66	3.13	4.24	5.51	7.42	12.27	13.10
7	90	0	10	0	0	1.83	2.17	3.03	4.37	5.27	8.43	10.54	9.07
8	80	20	0	0	0	2.27	2.44	2.64	3.62	4.65	7.81	14.28	15.96
9	80	0	20	0	0	1.48	1.79	2.12	4.61	6.33	8.26	7.51	6.91
10	70	30	0	0	0	1.26	2.08	2.34	3.15	4.72	8.49	10.65	16.36
11	70	0	30	0	0	1.80	2.53	3.05	3.67	5.76	8.02	7.90	6.64
12	60	40	0	0	0	1.21	1.67	2.26	4.30	5.01	8.10	10.11	18.05
13	60	0	40	0	0	1.25	1.83	2.48	3.47	4.24	7.93	7.70	6.28
14	50	50	0	0	0	1.59	2.17	3.34	5.39	8.12	13.05	15.55	19.78
15	50	0	50	0	0	1.03	1.55	2.13	2.79	4.10	6.85	6.13	5.69
16	50	30	0	20	0	1.26	1.81	2.11	3.56	3.88	6.04	9.83	*
17	50	30	0	0	20	1.60	2.06	2.99	3.42	4.17	4.76	3.34	*
18	50	0	30	20	0	3.26	4.40	4.98	5.86	9.10	*	*	*
19	50	0	30	0	20	1.91	1.95	2.42	2.91	*	*	*	*
20	60	20	0	20	0	1.66	2.23	2.94	2.94	6.32	9.67	4.27	*
21	60	20	0	0	20	1.58	2.12	2.71	3.03	5.96	7.50	2.47	*
22	60	0	20	20	0	2.98	4.04	5.80	5.93	5.75	*	*	*
23	60	0	20	0	20	1.69	3.19	3.25	3.37	5.33	*	*	*
24	80	0	0	20	0	1.30	2.18	4.30	5.77	14.07	3.06	*	*
	RM	BFS	FS	WG	WA	800	900	1000	1050	1100	1150	1200	1225

Note: RM – red mud, BFS – blast furnace slag, FS – foundry sand, WG – waste glass, WA – wood ash. *- the samples melted after firing.

There is also a reference composition was prepared, which was made of natural clay in accordance to brick factory production method, to use it for comparison of ceramics made of industrial wastes only and ceramics made of natural clay in traditional way (Table 5.1).

5.1.1 One-component compositions of the developed ceramics

There are only two compositions, which consist of a one component. Composition, which has number 0 in the Table 5.1, is absolutely natural material based mixture. It was prepared in accordance with brick factory production technique at it is pure clay. The point is to compare new compositions with that, which has been used for hundreds of years and now fits into the national quality norms for construction materials. Another one-component composition number 5 consists of red mud only.

According to the Brazilian standard NBR 15270-3/05 the flexural strength of solid bricks is classified as follows: Class A < 2.5 MPa; Class B from 2.5 to 4.0 MPa; and Class C > 4.0 MPa.

The reference composition is number 0. It consists of clay, which represented by main clay mineral illite ($KAl(Si,Al)_4(OH)_2 \bullet nH_2O$) and quartz (SiO2) (Figure 4.7). The chemical composition is also presented by typical for clay chemical elements (Table 4.3).

Flexural strength of the clay samples grew steadily along with increase of firing temperature, due to more intense sintering process. At all temperatures samples attended the Brazilian norm NBR 15270-3/05 to Class C, which supposed to have higher strength than 4 MPa. Significant increase in strength was identified between 1100°C and 1150°C from 10.08 to 14.65 MPa. This peak of strength also determined the following decrease in strength after firing at higher temperatures, as there was no improvement at 1200°C and there was significant drop at 1225°C, which meant excessive sintering and only 6.05 MPa of flexural strength. It is important to notice, that even after firing at inappropriately high temperature, the samples (Figure 5.1) did not lose the sharp edges and did not melt.

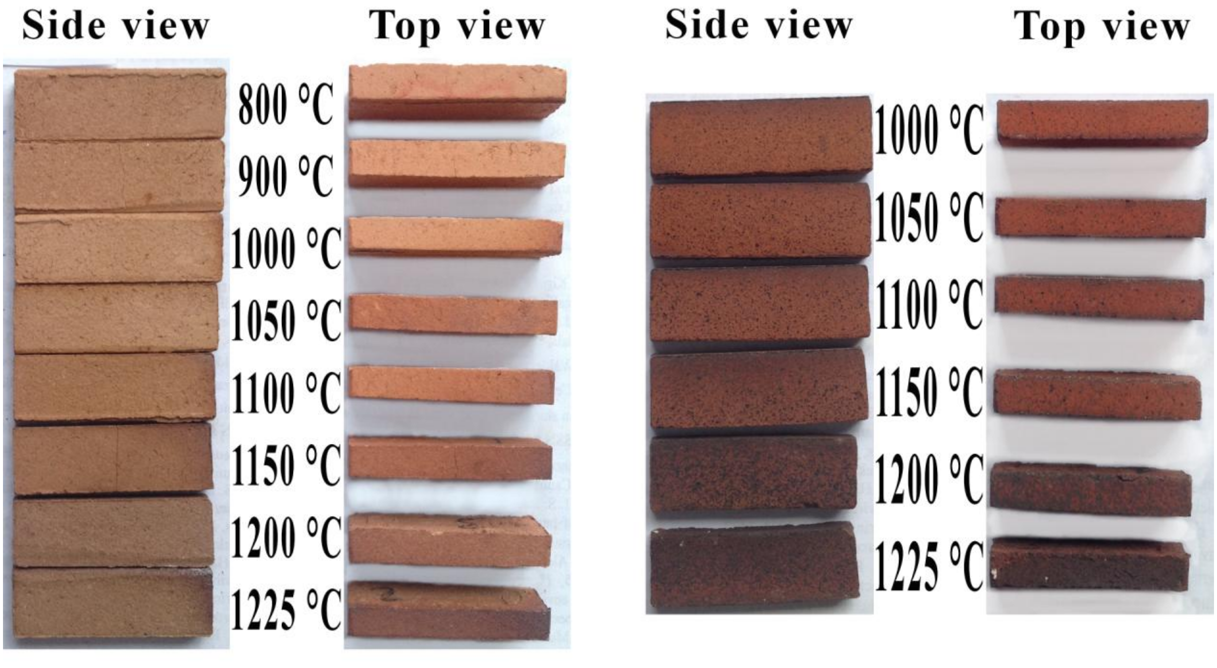

Composition 0

Composition 5

Figure 5.1 - Samples of composition 0 and composition 5 at different temperatures.

At the same time, flexural strength of composition 5, which contains red mud only, becomes noticeable only after firing at 1100°C as it reaches 4.34 MPa. There is also steady growth in flexural strength as the firing temperature increases. Significant growth takes place between 1150°C and 1200°C, as the flexural strength increases almost in two times from 6.06 to 12.17 MPa. Such a dramatic change usually takes place right before the excessive firing temperature. The result of 1225°C firing proves it by showing very slow growth from 12.17 to 12.32 MPa.

The color of the red mud ceramic samples (Figure 5.1) turns from almost orange to dark brown or even black at some exact places of the samples, which were fired at 1225°C. This characteristic of color change is common for all samples even those, which were made of natural material. The reason for that is content of iron oxides, which are presented in all materials. According to Pontikes et al. (2007), who cited Prasad and Sharma (1986), the minimal sintering temperature should be 1050°C, while the maximal is 1120°C, because at the higher temperature the samples become dark and heavy. In the presented research the color of the samples is already dark at 1000°C, and the reason for it is high ferrous content in used red mud.

The chemical composition of red mud (Table 4.3) is following: Fe_2O_3 - 29.9%, SiO_2 - 15.5%, Al_2O_3 - 21.2%, Na_2O - 10.3% and CaO - 4.2%. The mineralogical composition is based on two iron minerals hematite (Fe_2O_3) and magnetite (Fe_3O_4), tailings of bauxite ore bauxite ($Al_2O_3 \bullet nH_2O$), and quartz (SiO_2). Both iron minerals hematite and magnetite have high melting point between 1591° and 1597°C. The identified decrease of flexural strength and change of the samples' color indicates that these two minerals were close to melting point within 370°C.

At the same time, there are some components of the red mud, which have significantly lower melting points. For example, Al_2O_3 in shape of $Al(OH)_3$ reaches melting point at 300°C, Na_2O in shape of NaOH starts to melt at 323°C. These two components together are equal to 31.5%, so their role as flux components is quite doubtful.

According to the Figure 4.2 there is high content of amorphous material. Due to the fact that during Bayer process a bauxite ore is processed using thermochemical reactions to decompose particles, the crystalline structures as a result are destroyed. The lack of crystalline connections allows decreasing the melting point. As a result, together with flux components, the melting point of the red mud decreases.

5.1.2 Two-component compositions of the developed ceramics

There are three different groups of two-component compositions. The first one is compositions, which contain red mud and blast furnace slag. The second one has red mud and foundry sand as main components. And the third one is technically cannot be classified as two-component, but it is dedicated to compositions, which contain all three components as additional compositions to determine the role of each component and their interaction with one another when combined.

The first one to take into consideration is group with red mud and blast furnace slag. The compositions number 6, 8, 10, 12, and 14 present the increasing content of blast furnace slag and decreasing content of red mud as following: composition 6 – 10% blast furnace slag, 8 – 20%, 10 – 30%, 12 – 40% and 14 – 50%. The compositions, in which blast furnace slag would take major part, were not prepared as the samples become very fragile due to insufficient quantity of binding material, which is red mud.

According to the results of flexural strength test (Table 5.1) the strength grew not only as the firing temperature was increasing, but also as the content of blast furnace slag was increasing. When compared at the same temperature, for example 1225°C, composition 5, which is made of pure red mud, has 12.32 MPa flexural strength, and when 10% of blast furnace slag is added the strength increases up to 13.10 MPa. This sequence goes on resulting in 19.78 MPa strength of the composition containing 50% of blast furnace slag.

The reason for such a role of blast furnace slag is the melting point of the components' minerals. Main chemical elements of the blast furnace slag are: Fe_2O_3 - 62.1%, SiO_2 - 13.8%, SO_3 - 10.0%, Al_2O_3 - 2.6%, which all together equals to 88.5% content. Contrary to red mud, blast furnace slag has small amount of flux components such as Na_2O (0.9%) and K_2O (0.4%).

The mineral composition of blast furnace slag (Figure 4.3) is presented by two minerals: iron sulfate fayalite - $Fe_2{\cdot}2SiO_4$, which has melting point at 1205°C (FERRO (2008)) and iron sulfide troilite – FeS. Diffractogram pattern of blast furnace slag also presents high X-ray background, which is higher than majority of crystalline peaks. It means high content of glass like material, which was formed during ore melting process at the temperature of 1500°C.

With an increase of firing temperature, the effectiveness of chemical interaction between particles also increases. The composition 5, which contain red mud only, has bigger amount of flux material, than compositions, which contain blast furnace slag. That is why composition 5 almost reached the peak of melting at 1225°C, while compositions containing blast furnace slag continued to gain strength at this temperature with effective chemical interaction between the particles. The evidence of this idea is that compositions 6, 8, 10, 12, and 14 had increase in strength comparing 1200°C and 1225°C, meaning that they still had potential for further growth. When the samples were analyzed, no signs of melting were identified (Figure 5.2), the edges are sharp. The color has changed from dark brown to almost black as the temperature has risen from 1000°C to 1225°C.

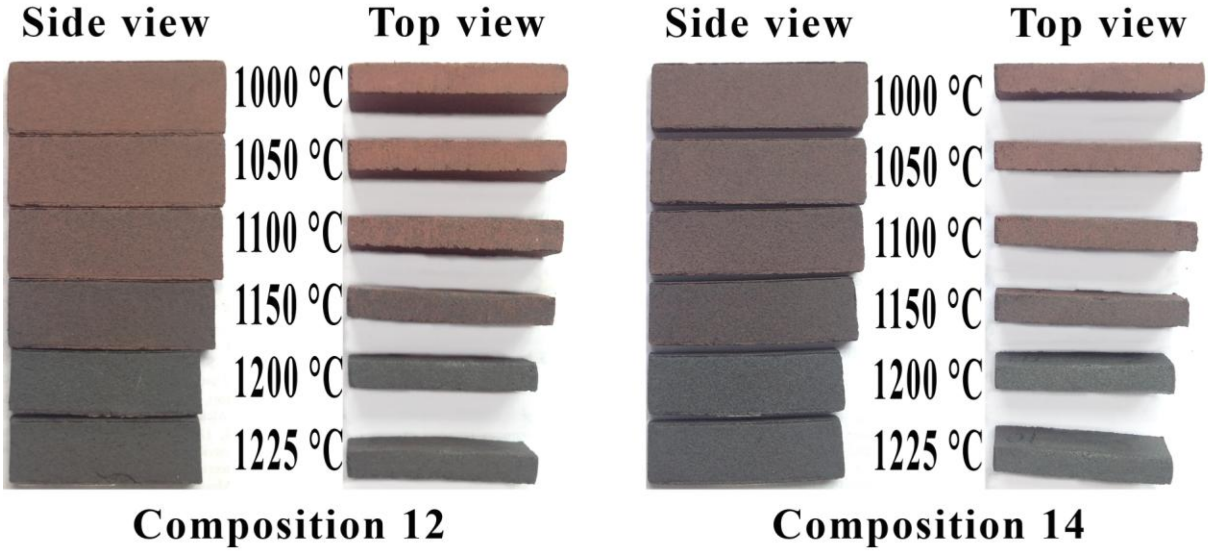

Figure 5.2 - Samples of composition 12 and composition 14 at different temperatures.

The maximum flexural strength of all two-component samples was reached by composition 14 at the temperature 1225°C – 19.78 MPa, which is 35% more than the strongest samples made of natural clay at 1150°C – 14.65 MPa. Composition 14 consists of red mud (50%) and blast furnace slag (50%). That is why it turns almost completely black after sintering at 1225°C.

When 10% of blast furnace slag is substituted by 10% of red mud, meaning transition from composition 14 to composition 12, the flexural strength decreases at all firing temperatures. Samples of composition 12 have lighter color than those of composition 14, which tend to be almost black especially after sintering at 1225°C.

Compositions 8 and 10, which were fired at 1225°C, present higher strength (15.96 and 16.36 MPa) than samples of composition made of natural clay (14.65 MPa). It means that developed compositions reached the dead-burnt condition.

When influence of blast furnace slag in two-component compositions was studied, it is a turn for foundry sand to be analyzed. For the better comparison the same percentage was chosen. The substitution of 10, 20, 30, 40, and 50% of red mud by foundry sand was used in compositions 7, 9, 11, 13, and 15. According to the Table 5.1 after firing at 1000°C these compositions reached flexural strength between 2.13 and 3.03 MPa, which means that they come to terms with the class A and class B of the Brazilian norm NBR 15270-3/05. After firing at 1050°C, compositions 7 and 9 attended the class C reaching more than 4 MPa of flexural strength. After firing at 1100°C all compositions presented higher strength than needed to be classified as a class C. Mymrin et al. (2014) presented even higher results of flexural strength reaching 14 MPa, while adding foundry sand to other industrial wastes and sintering at 950-1050°C.

At the temperature of 1150°C 4 out of 5 compositions containing red mud and foundry sand reached the maximum flexural strength, and at higher temperature they tend to lose the strength. Composition 7 has the maximum flexural strength equal to 10.54 MPa at 1200°C, which is lower than the result of composition 5 (12.17 MPa) containing red mud only at the same temperature. Keep on comparing composition 7 and 5 it is important to mention that at firing temperature of 1225°C the composition 5 did not start to lose the strength, while composition 7 demonstrated decrease equal to 1.47 MPa. This means that composition 7 received excessive firing, which led to melting.

The foundry sand mainly consists of SiO_2 (91.2%) and presented by quartz (**Figure 4.4**) in terms of mineral composition. Quartz has melting point between 1713°C and 1728°C. For this reason, it is usually described as a filler material, which is chemically inert. In case of the presented study it is red mud and blast furnace slag that should be chemically active components, as they are rich in flux components and amorphous phase. While comparing the flexural strength of composition 5 and compositions 7, 9, 11, 13, and 15 at 1150°C the idea that foundry sand is a filler material does not seem to be obvious. The substitution of red mud by 10% of foundry sand causes increase in flexural strength while firing up to 1150°C, which is the critical temperature for these compositions. Composition 15, which consists of 50% red mud and 50% blast furnace slag, also presented higher strength of 6.85 MPa than composition 5 presenting 6.06 MPa. Compositions 7, 9, 11, and 13 presented even higher flexural strength (8.43, 8.26, 8.02, 7.93 MPa), which means that it cannot be stated that foundry sand acts as a filler material.

The foundry sand might be activated by alkaline properties of the red mud, which has pH = 13.5 in combination with $Al(OH)_3$ melting point at 300°C. Normally silicates are hardly soluble in alkaline conditions. This might change as the components reach temperatures between 1000°C and 1200°C. As a result, the foundry sand becomes active and starts to participate in processes of new crystalline formations.

The mechanical damages of the foundry sand particles’ surface improve chemical activity and lead to more effective interaction between red mud and foundry sand. The critical temperature for compositions containing red mud and foundry sand is 1150°C. At this point compositions start to melt and content of the quartz does not bring any improvement.

The color of the composition 15 samples' (Figure 5.3) looks good especially at the lower temperatures. After passing critical temperature samples start to melt and lose their sharp edges. There is even visible tendency to swell of the samples as they reach 1200°C and 1225°C.

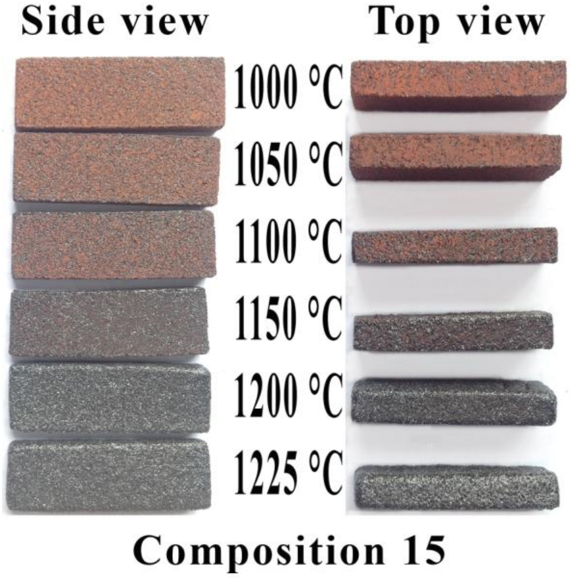

Figure 5.3 - Samples of the composition 15 at different temperatures.

As the role of both foundry sand and blast furnace slag was analyzed, the comparison of two components might be carried out. The percentage of substituted material is equal in compositions 6 and 7 (10%), 8 and 9 (20%), 10 and 11 (30%), 12 and 13 (40%), 14 and 15 (50%), which makes them more suitable for comparison in pairs.

When compared in pairs, there are 31 pairs, in which substitution of red mud by blast furnace slag or foundry sand presented a higher flexural strength than it was in composition 5, which contains red mud only. Among these 31 pairs, there are 18, in which an improvement was caused by the blast furnace slag and the rest 13 pairs received improvement because of foundry sand's impact. At the temperatures 800°C, 900°C and 1000°C the flexural strength of the samples containing blast furnace slag in 9 cases higher than the flexural strength of the samples containing foundry sand, and in 6 cases it is lower. At the same time, when temperatures 1100°C, 1150°C and 1200°C are chosen for comparison, the samples containing blast furnace slag are also gaining in 7 cases against 4 cases, when foundry sand reaches higher flexural strength results. In majority of cases the difference in strength is not significant, for example composition 6 and 7 at 1000°C present 3.13 and 3.03 MPa. The exception is the pair composition 14 and 15, which have 50% red mud content. In this case the difference in strength at some temperatures is significant, for example at 1050°C it is 5.39 and 2.79 MPa, or at 1100°C it is 8.12 and 4.10 MPa, or at 1200°C it is 15.55 and 6.13 MPa, or at 1225°C it is 19.78 and 5.69 MPa.

In general, it is blast furnace slag that has more positive impact on improvement of flexural strength, but the more detailed comparison would give more information on the roles of components.

The pair of compositions 6 and 7, in which the content of red mud is 90% and 10% were substituted by blast furnace slag (composition 6) and foundry sand (composition 7). At low temperatures 800°C and 900°C, 10% of each material improve significantly flexural strength of compositions when compared with composition 5. Reaching 1000°C, compositions 6 (3.13 MPa) and 7 (3.03 MPa) have 7 times stronger samples than composition 5 (0.45 MPa). But as the samples reach higher temperatures 1100°-1150°C, this difference almost disappears. By 1225°C the samples made of red mud are stronger than those of composition 7, but weaker than samples which contain 10% of blast furnace slag.

To sum up, the substitution of 10% by blast furnace slag or foundry sand leads to significant improvement at low temperatures (800-1050°C), and gives relatively good results at middle temperatures (1100°C and 1150°C). At the high temperatures blast furnace slag keeps on having positive impact on the composition, while foundry sand decreases the flexural strength.

The same comparison is carried out for compositions 8 and 9. Composition 8 consists of 80% red mud and 20% blast furnace slag. Composition 9 contains 80% of red mud and 20% of foundry sand. At the first look it seems that the influence is alike to those 10% in compositions 6 and 7, but in reality it is not. At 1050°C, 1100°C and 1150°C the flexural strength of composition 9 is higher than composition 8. As the temperature rises up to 1200°C flexural strength of composition 8 (14.28 MPa) gets twice higher than flexural strength of composition 9 (7.51 MPa). For the composition 9 the critical firing temperature was 1150°C at which it reached the maximum strength of 8.26 MPa and then started to lose it with increase of firing temperature and by 1225°C presented only 6.91 MPa. The composition 8 at the same time did not have breaking point at 1150°C and kept on gaining steadily the strength, reaching 15.96 MPa at 1225°C.

To summarize the comparison of influence blast furnace slag and foundry sand on the flexural strength in samples of composition 8 and 9 temperatures were divided in three groups. At low temperatures (800-1000°C) the difference in strength between two compositions is not big, so it is difficult to say which material had better influence on the composition in general. At middle temperatures (1050-1150°C) composition 9 achieved higher strength obtaining lower melting point by content of foundry sand. At high temperatures (1200-1225°C) the composition 9 started to melt, while composition 8 kept on increasing the strength because of high melting point of blast furnace slag.

As the content of blast furnace slag and foundry sand increases in compositions, the impact of each material becomes more obvious. The more blast furnace slag being used in composition the higher flexural strength. The more foundry sand being used in composition the lower flexural strength. When the maximum strength at all temperatures for pairs of compositions is highlighted it looks as following: 10% - 13.10 / 10.54 MPa, 20% - 15.96 / 8.26 MPa, 30% - 16.36 / 8.02 MPa, 40% - 18.05 / 7.93 MPa, and 50% - 19.78 / 6.85 MPa. As the content of red mud decreases in compositions, the positive impact of blast furnace slag on flexural strength increases.

At the same time, it is important to highlight the positive impact of foundry sand in composition 11 containing 30% at 800-1100°C and in composition 13 containing 40% at 800-1000°C. In all other cases the blast furnace slag took the lead in terms of strength.

In the case of such significant difference in influence on the composition’s flexural strength, the mixtures of all three components may help to identify the golden mean.

Compositions 2 and 14 have two things in common: 50% of red mud and 30% of blast furnace slag. The last 20% of content differ: composition 2 has foundry sand and composition 14 has blast furnace slag. As a result, there was no significant improvement at low temperatures and at the high temperatures composition 14 reached 19.78 MPa against maximum flexural strength 9.73 MPa of composition 2.

The same comparison could be made using compositions 3 and 12. They both have 60% of red mud and 20% of blast furnace slag. The negative impact of 20% of foundry sand might be identified, as there is significant difference 5.89 / 18.05 MPa in flexural strength showing no improvements with addition of foundry sand.

Compositions 4 and 10 also might be compared. 70% red mud and 10% blast furnace slag as a common content and 20% of foundry sand in composition 4 against 20% of blast furnace slag in composition 10%. The composition 4 did not reach 1225°C as it melted and presented the highest flexural strength at 1150°C equal to 5.62 MPa, which is relatively low in comparison to 16.36 MPa of composition 10.

At the same time, compositions 1, 2, 3, and 4 might be compared one with another. These compositions consist of three components, but additional flux components were not added. These compositions have 20% foundry sand content. The content of red mud changes from 40% to 70% and content of blast furnace slag changes from 40% to 10%.

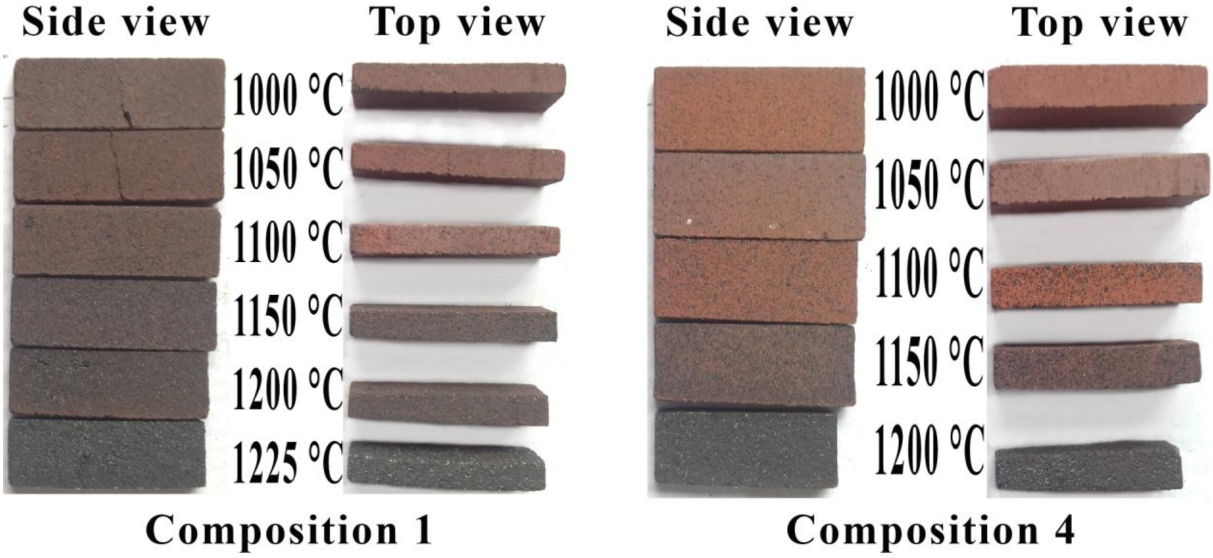

Figure 5.4 - Samples of composition 1 and composition 4 at different temperatures

The composition 1 is the most difficult to prepare as it has less than 50% of binding material, which makes it very fragile before firing process. It has the lowest flexural strength at low temperatures (800-1000°C) among this group of four compositions, but it is still stronger than the result presented by composition 5. There is steady growth of strength as the firing temperature increases, and at the middle temperature (1100-1150°C) the composition 1 reaches 3.23 and 5.76 MPa, which is slightly lower than the result of 4.34 and 6.06 MPa presented by composition 5 at the same temperatures. At high temperatures (1200-1225°C) the composition 1 reaches the highest result among four compositions presenting 10.29 MPa flexural strength. Still this result is lower than the result of composition 5, which reached 12.32 MPa containing red mud only.

Opposite to composition 1 behavior was presented by composition 4. It reached 1.08 MPa at 800°C, while composition 5 reached 0.93 MPa at 1050°C. It means that composition 4 is able to gain strength at low temperatures (800-1000°C). Maintaining this tendency composition 4 had better results at temperatures 1000-1100°C than composition 5, but at 1150°C composition 4 presented 5.62 MPa, which is lower than 6.06 MPa of composition 5. At 1150°C it reached the maximal flexural strength and at higher temperatures started to lose it ending up melting completely at 1225°C.

The color change during firing at different temperatures (Figure 5.4) represents the content of each composition. The samples of composition 1 at low temperature of 1000°C already have dark brown color and become dark grey as the temperature rises up to 1225°C, because of the high content of iron in the composition. Composition 4 at high temperature also becomes dark grey, but at the low temperature of 1000°C it has soft light brown color due to the low content of iron.

As four compositions compared simultaneously, there is a common tendency: to have higher strength than composition 5 at low temperatures; almost equal strength at middle temperatures, for example at 1100°C composition 1 has 3.23 MPa, composition 4 has 4.84 MPa, and composition 5 has 4.34 MPa, and at the temperature of 1150°C the composition 3 has 5.89 MPa and composition 5 has 6.06 MPa; and lower strength at high temperatures comparing with result of the composition 5.

There are also some obvious effects: as the content of red mud increases, the flexural strength at low temperatures increases; as the content of blast furnace slag increases, the flexural strength at high temperatures increases. The low melting point of foundry sand combined with red mud provided acceleration in strength gain at low temperatures, but at the same time it was the reason for early melting of the samples and as a consequence prevented compositions from reaching their full strength potential at high temperatures.

5.1.3 Three-component compositions of the developed ceramics

As it was presented in the group of compositions containing red mud, blast furnace slag and foundry sand, the highest results of flexural strength were achieved at high temperatures of 1200-1225°C. Due to the fact that on industrial scale higher temperatures mean bigger energy consumption for firing process, an attempt to decrease melting point of compositions and as a result to obtain high flexural strength at lower temperatures was made. The waste glass and wood ash were used as flux materials.

As the best results of composition 5 were reached at high temperatures the idea of testing the influence of waste glass on composition with red mud appeared in the research. The composition 24 has two components and consists of 80% red mud and 20% waste glass.

The composition 24 started to gain flexural strength at lower temperatures than composition 5. For example, at 900°C composition 24 already had 2.18 MPa, while composition 5 had 0 MPa. Similar strength of 4.34 MPa and 4.30 MPa was reached by compositions at different temperatures: the composition 5 achieved it at 1100°C, while the composition 24 reached it at 1000°C. As the temperature rises the composition 24 gains the highest strength 14.07 MPa at 1100°C, which is higher than maximal strength of composition 5 at 1225°C (12.32 MPa). Due to low melting point of waste glass, the composition 24 did not reach the high temperature (1200-1225°C). The impact of the waste glass in the composition resulted in lowering the melting point for almost 100°C and accelerating the strength gain at low temperatures. At the same time, the waste glass in general improved the strength of composition 24 presenting 14.07 MPa against 12.32 MPa of composition 5 without waste glass. Similar decrease of firing temperature almost for 100°C was achieved by Mymrin et al. (2012, 2014), Phonphuak et al. (2016), and Wei et al. (2016).

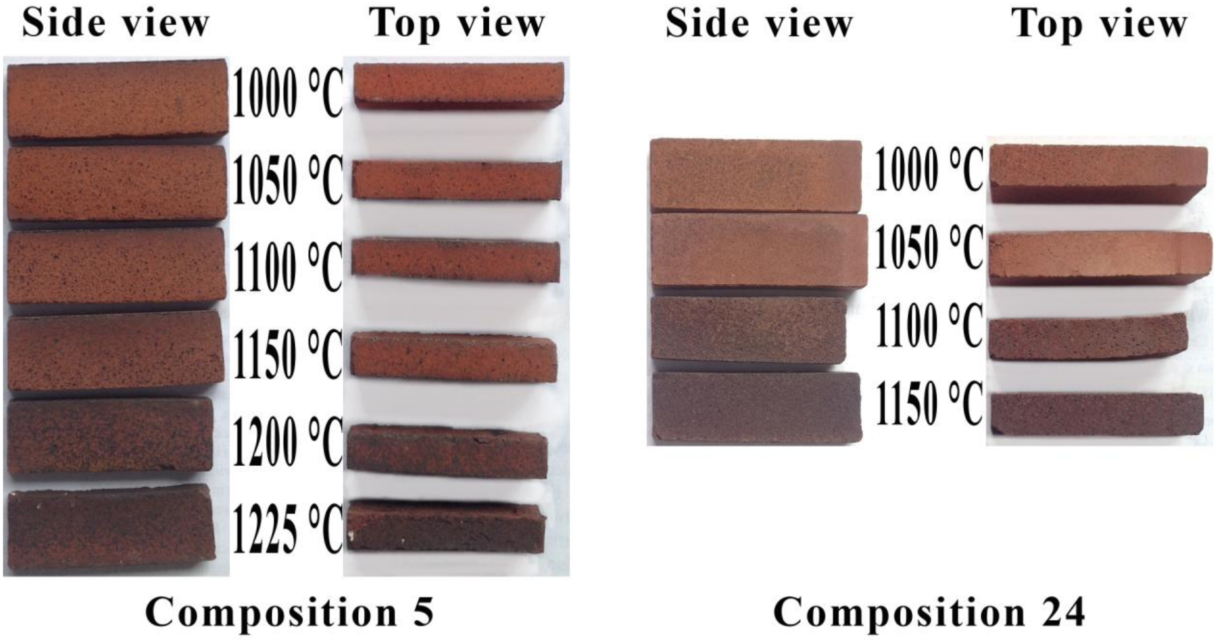

Figure 5.5 - Samples of composition 5 and composition 24 at different temperatures

The waste glass influenced not only melting point and flexural strength of the composition 24, but also the color. The samples' color became lighter as the content of iron in the final percentage got lower. The samples start to become darker as they reach 1100°C. At the same temperature the open superficial pores become more visible. At 1150°C the samples start to lose the flexural strength, but the edges are still sharp and there are no signs of tendency to melt.

Due to the fact that composition 14 and 12 demonstrated high flexural strength, the content of these compositions was taken as a reference for development of compositions 16-23. On the basis of composition 12 were prepared compositions 20 and 21, which also have 60% red mud and 20% blast furnace slag. Another 20% were filled with the waste glass in case of composition 20, and with the wood ash in case of composition 21. Ding et al. (2015) used blast furnace slag and waste glass at high temperatures to increase the pores closing process. As a result, samples had low bulk density 0.79 g/cm^3, low water absorption 2.71%, and high bending strength 14.34 MPa. Similar experiment has been done by Francis et al. (2013) using glass cullet and blast furnace slag for porous glass-ceramics production.

Compositions 22 and 23 were prepared on the basis of composition 13, containing 60% red mud and 20% foundry sand, and another 20% were substituted by the waste glass and the wood ash. In the same way, compositions 16, 17, 18, 19 were prepared on the basis of compositions 14 and 15.

The first pair to compare is compositions 16 and 17. Both compositions have 50% red mud and 30% blast furnace slag content. The difference is that composition 16 has 20% waste glass, while composition 17 has 20% wood ash. Compositions demonstrated similar flexural strength at low and middle temperatures, for example at 1050°C composition 16 reached 3.56 MPa, while composition 17 had 3.42 MPa. The change came as compositions reached high temperatures (1150-1200°C). Both of them melted at 1225°C, but at 1150°C composition containing waste glass had 6.04 MPa, when composition containing wood ash reached the maximal flexural strength of 4.76 MPa. With an increase of temperature, composition 16 improved the result reaching 9.83 MPa, while composition 17 started to lose strength presenting 3.34 MPa.

When both compositions are compared to reference composition 14, it becomes noticeable, that from the point of flexural strength both of them worse, than composition containing only red mud and blast furnace slag. In this case, idea of substitution of blast furnace slag by flux material did not end up with high strength at low temperature, as both compositions are weak. Blast furnace slag was used by Zhang et al. (2009, 2011) in the compositions containing red mud and coal gangue at 3:2 ratio with addition of clinker and gypsum for production of cementitious material, which presented 45.3-49.5 MPa compressive strength.

Another pair to compare is compositions 18 and 19. There is 50% red mud and 30% foundry sand content in both compositions. The composition 18 contains 20% waste glass, and composition 19 contains 20% wood ash. Composition 18 reached the highest flexural strength of all 24 compositions at the low temperature of 800°C, presenting 3.26 MPa. The combination of foundry sand with waste glass (Figure 5.6) started to give positive results at low temperatures and did not manage to maintain them at high temperatures melting completely at 1100°C. The peak of the strength of the composition 18 was identified at 1000°C, presenting 4.98 MPa. In case of composition 19 there was not active interaction between components at low temperatures, but significant change came at 1100°C and composition demonstrated flexural strength equal to 9.10 MPa.

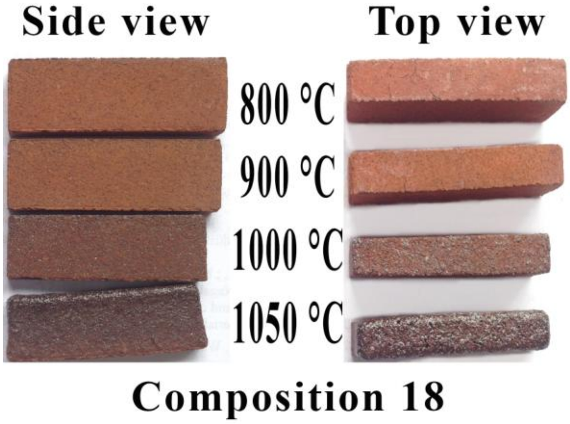

Figure 5.6 - Samples of the composition 18 at different temperatures

The comparison of both compositions with composition 15, shows that when waste glass is used as a flux material the composition achieves 4.98 MPa at 1000°C comparing with 4.10 MPa of the composition 15 at 1100°C, which means that by addition of 20% waste glass the temperature was lowered for almost 100°C. From the point of flexural strength, composition containing wood ash reaches 9.10 MPa at 1100°C, while composition containing red mud and foundry sand only did not reach this result at any firing temperature.

To sum up the results of four compositions it is important to highlight the effectiveness of wood ash in combination with foundry sand at middle temperature, and effectiveness of waste glass in combination with foundry sand at low temperatures. Both flux materials did not present any advantage when compared with blast furnace slag.

Moving to the compositions based on the compositions 12 and 13, compositions 20, 21, 22, and 23 are taken into consideration. All four compositions had 60% red mud and 20% foundry sand or blast furnace slag.

The first to compare is the pair of compositions 20 and 21. Composition 20 has 20% waste glass content, while composition 21 (Figure 5.7) has 20% wood ash content. Both compositions did not reach 1225°C, starting to melt and presenting decrease in flexural strength at 1200°C. It is difficult to identify difference of wood ash or waste glass impact as compositions have similar results at low and middle temperatures, reaching the peak at 1150°C. The composition 20 presented 9.67 MPa and composition 21 presented 9.50 MPa as a maximal strength.

Kumar et al. (2012) presented compositions containing 20% red mud and 80% fly ash, and 10% red mud and 90% fly ash, which had flexural strength 3.2-4.5 MPa and water absorption 6-7%. Bhaskar et al. (2014) presented composition, which consists of 50% red mud and 50% fly ash and reaches 5.5 MPa compressive strength and 10% water absorption.

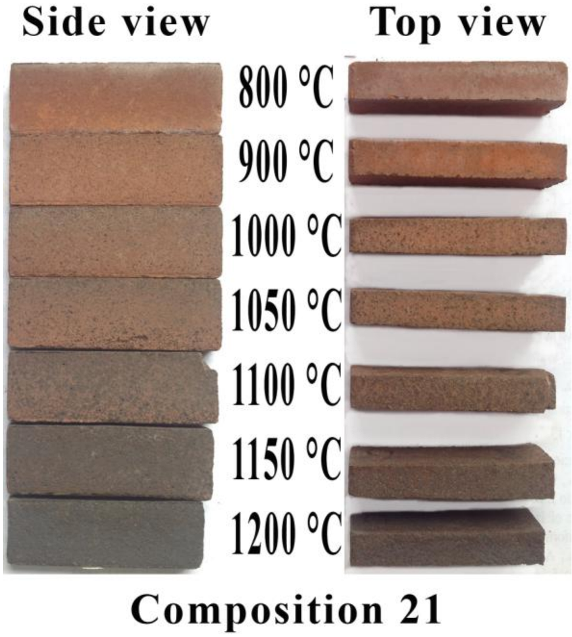

Figure 5.7 - Samples of the composition 21 at different temperatures.

When both compositions are compared to the reference composition 12 at 1150°C they present an advantage in strength gain as the composition 12 presented 8.10 MPa. At the same time, when temperature of 1100°C is taken for comparison, compositions 20 and 21 also present higher results 6.32 and 5.96 MPa than the composition 12 5.01 MPa. In this case, the use of both flux materials is reasonable and allows achieving better results.

The second pair to compare is compositions 22 and 23. These compositions also do not differ a lot in terms of flexural strength. Composition 22 (Figure 5.8) just like composition 18 demonstrated higher flexural strength at low temperature than composition 23, which gives another evidence of the active interaction between foundry sand and waste glass. At 800°C composition 22 achieved 2.98 MPa, while composition 23 reached 1.69 MPa. The composition 22 had a peak of flexural strength at 1050°C gaining 5.93 MPa, while composition 23 kept on increasing strength at 1100°C presenting the maximal strength of 5.33 MPa. Both compositions melted at 1150°C.

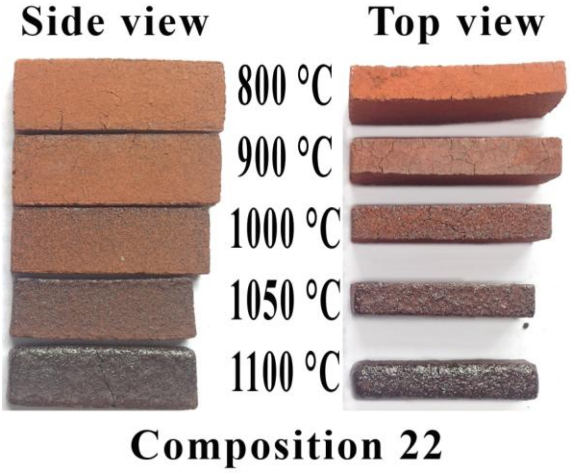

Figure 5.8 - Samples of the composition 22 at different temperatures.

When both compositions are compared with their reference composition 13, the temperature of 1100°C should be taken for highlighting results. Composition 13 at 1100°C presented 4.24 MPa, while composition 22 reached 5.75 MPa and composition 23 5.33 MPa. It means that use of flux materials allowed achieving higher flexural strength at the same temperature.

Summing up the comparison of these four compositions it is necessary to state, that in compositions containing 60% red mud the flux materials demonstrated ability to decrease the melting point achieving high flexural strength at lower temperatures.

As all the compositions being described it is time to compare two groups of four compositions. The first group is compositions 16, 17, 18, and 19. All of them had 50% red mud content. In the case, when red mud is combined with blast furnace slag the impact of flux materials is not significant. When the red mud is combined with foundry sand, both flux materials had strong influence on compositions improving their flexural strength at low or middle temperatures. The second group, in which all compositions (20, 21, 22, and 23) contained 60% red mud, presents the effectiveness of both flux materials in all four compositions. It means that depending on the aims and the demands of production, an optimal composition might be chosen, which would allow obtaining better results using different components at different temperatures.

The waste glass and wood ash have fulfilled the expectations as flux materials and might be effectively used for high strength ceramics production at low temperatures.

5.2 LINEAR SHRINKAGE OF THE DEVELOPED CERAMICS

The linear shrinkage is one of the most important characteristics of ceramic material. It correlates with content of the composition and the firing temperature. Because of linear shrinkage some compositions are suitable for production of tiles, while others are suitable only for brick production.

The linear shrinkage was calculated by measuring the length of the samples after firing taking into consideration that before the sintering process they were 60 mm long. The results presented in the Table 5.2.

Table 5.2 - Linear shrinkage of ceramic compositions at different firing temperatures

№	Compositions content, wt.%					Linear shrinkage (%) of ceramics at different temperatures (°C)							
						800	900	1000	1050	1100	1150	1200	1225
0	Reference clay composition					5.36	5.68	7.76	9.09	10.47	11.52	11.95	11.86
	RM	BFS	FS	WG	WA								
1	40	40	20	0	0	0.07	0.17	0.22	0.48	1.18	3.02	5.09	7.49
2	50	30	20	0	0	0.33	0.60	0.81	1.02	2.29	3.86	6.83	8.29
3	60	20	20	0	0	0.74	1.00	1.20	1.44	3.32	4.15	10.12	11.12
4	70	10	20	0	0	1.68	1.93	2.04	2.05	5.31	6.89	14.50	*
5	100	0	0	0	0	1.89	2.27	3.42	4.33	5.29	7.24	11.67	12.45
6	90	10	0	0	0	0.96	1.08	1.92	2.98	4.30	5.64	9.43	9.56
7	90	0	10	0	0	1.24	2.46	3.74	4.34	5.85	7.89	12.45	12.63
8	80	20	0	0	0	0.54	0.63	0.81	1.51	2.64	4.41	7.40	11.07
9	80	0	20	0	0	1.83	2.67	3.72	4.69	6.00	8.81	13.17	12.94
10	70	30	0	0	0	0.07	0.24	0.31	0.83	2.46	4.38	11.37	12.54
11	70	0	30	0	0	2.81	3.09	3.63	4.84	5.93	8.97	11.57	11.47
12	60	40	0	0	0	0.04	0.11	0.18	0.39	1.69	5.26	12.32	12.35
13	60	0	40	0	0	1.74	2.83	3.69	4.86	7.19	8.75	9.22	10.02
14	50	50	0	0	0	0.08	0.12	0.17	0.44	1.13	4.28	10.99	11.40
15	50	0	50	0	0	1.74	2.29	2.99	4.35	5.70	7.82	7.23	6.26
16	50	30	0	20	0	2.84	2.90	3.89	4.50	5.96	9.44	12.51	*
17	50	30	0	0	20	1.04	1.13	1.90	2.70	3.66	4.92	9.99	*
18	50	0	30	20	0	1.82	2.53	6.94	6.30	*	*	*	*
19	50	0	30	0	20	0.66	1.45	1.63	1.71	3.88	*	*	*
20	60	20	0	20	0	3.07	3.15	3.20	3.24	6.05	10.62	15.43	*
21	60	20	0	0	20	0.61	0.66	0.63	0.97	2.04	4.73	10.14	*
22	60	0	20	20	0	2.51	2.80	4.14	10.32	7.10	*	*	*
23	60	0	20	0	20	0.62	1.80	2.03	2.21	4.66	*	*	*
24	80	0	0	20	0	4.15	4.32	4.57	5.39	11.87	6.80	*	*
	RM	BFS	FS	WG	WA	800	900	1000	1050	1100	1150	1200	1225

Note: RM – red mud, BFS – blast furnace slag, FS – foundry sand, WG – waste glass, WA – wood ash. *- the samples melted after firing.

The composition 0, which is prepared using only natural clay at 800°C, presented high linear shrinkage 5.36%. The majority of samples, which were developed in the presented study, reached the same result at higher temperature of 1100-1150°C. The highest result of composition 0 is 11.95% at 1200°C. The reason for these results is decomposition of crystalline formations of illite and quartz, which were identified by XRD method.

When shrinkage of composition 0 and composition 5 are compared, the common thing is steady growth of this parameter for both compositions. Composition 5 reaches 11.67% at 1200°C presenting close to composition 0 at the same temperature result of 11.95%. At low temperatures composition 5 has significantly lower result of 1.89% at 800°C, while composition 0 has 5.36%.

The main difference between these two materials is that natural materials have high content of organic components, carbonates, hydrates and other thermally unstable elements. The composition 5 does not contain any clay mineral, such as illite for example, but it contains other minerals that have high temperature of melting (hematite and magnetite), which start to melt and present high shrinkage at 1150°C and 1200°C.

Taking into consideration compositions 1-15, important to mention that there are only industrial wastes and role of binding material is played by red mud, which has from 40% to 100% content depending on composition. The combinations of red mud and blast furnace slag present significant decrease in shrinkage of the samples, when compared to composition 5. At 1000°C there is twentyfold difference between compositions 12 or 14 and composition 5 (0.18% or 0.17% compared to 3.42%). This difference increase two times more as 0.17% of composition 14 are compared with 7.76% of composition 0. At 1200°C there is no significant difference in shrinkage between compositions. The reason for that might be content of Na. It decreases the melting point of the compositions containing blast furnace slag and fills the open pores during the sintering process. At the end of reaction it pushes particles towards each other.

When the impact of blast furnace slag compared with the impact of foundry sand, it should be stated that foundry sand causes higher shrinkage than blast furnace slag at all temperatures. For example, at 800°C composition 14 presents 0.08%, while composition 15 demonstrates 1.74%. The same tendency could be noticed even with smaller content of components. For example, at 800°C composition 6 presents 0.96%, while composition 7 presents 1.24%. To illustrate the same situation at high temperature, at 1200°C composition 9 has 13.17%, while composition 8 has 7.40%.

From the comparison of composition 1-4 the conclusion about stabilizing role of the blast furnace slag might be drawn as with the increase of temperature and increase of foundry sand content the shrinkage of the samples also increases.

Comparing the composition 5 and composition 24, the impact of the waste glass on shrinkage was identified. Addition of waste glass increases and accelerates the shrinkage at low temperatures. At 1050-1100°C there is increase from 5.39% to 11.87% in composition 24, which is almost two times more. Composition 5 did not experience such a change, as the shrinkage increases steadily through the temperature.

As the waste glass significantly increases the shrinkage of the samples, the influence of wood ash is different in terms of steadiness of increase. For example, composition 19 demonstrated steady increase of the shrinkage up to 1050°C and at 1100°C the shrinkage increased two times from 1.71% to 3.78%. It is important to mention, that at exactly 1100°C composition 19 reached the highest flexural strength before melting. Figure 5.9 presents that the sample almost began to boil turning into foam glass formation. The reason for it might be the escape of the gases, which were produced because of organic content of wood ash. To confirm this idea, the sample of the composition 23 was also presented. According to the image, at 1100°C the sample had many big opened pores, which means that organic material during firing was transforming into the gas and escaping the sample was creating these holes.

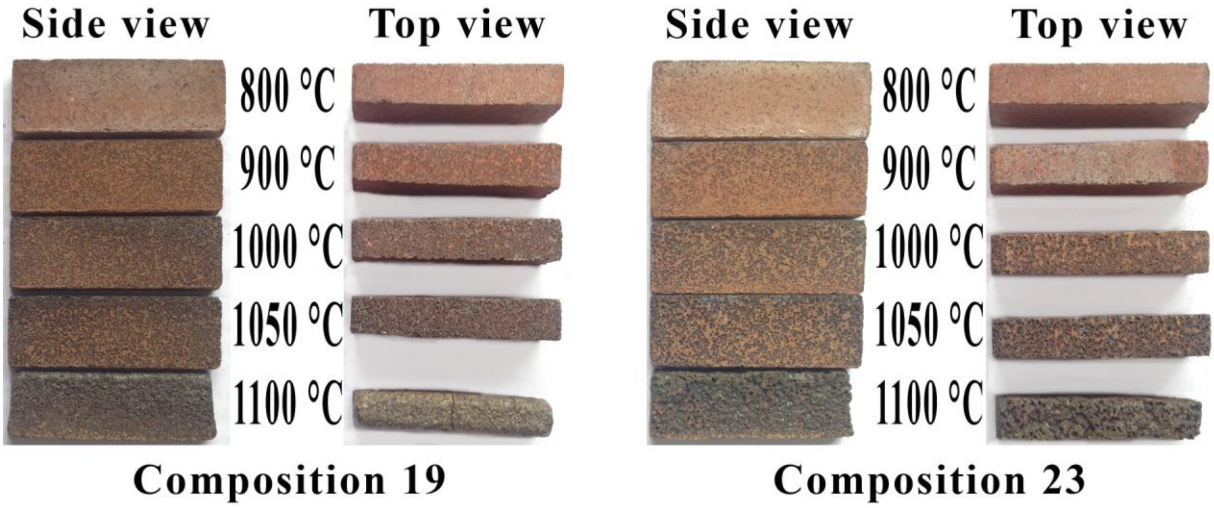

Figure 5.9 - Samples of the composition 19 and composition 23 at different temperatures.

There is general tendency in developed compositions: to have increase of the shrinkage with the increase of the temperature, which is caused by more effective sintering process; to present higher shrinkage with addition of foundry sand; the blast furnace slag presented stabilizing role in compositions; and both flux materials as they decrease melting point of the compositions, increase the linear shrinkage.

5.3 WATER ABSORPTION OF THE DEVELOPED CERAMICS

Water absorption is ability of the ceramic material to absorb the water. This is a crucial characteristic especially in terms of roof tiles production, as they should not absorb a lot of water. In general, the results of the water absorption test correlate with presence of open pores and formation of glass like surface of the samples. At higher temperatures the ability of the samples to absorb water decreases. Due to sintering process there is less space left between the particles of the sample. Results for the compositions developed in this research are presented in the Table 5.3.

Table 5.3 - Water absorption of ceramic compositions at different firing temperatures

№	Compositions content, wt.%					Water absorption (%) of ceramics at different temperatures (°C)							
						800	900	1000	1050	1100	1150	1200	1225
0	Reference clay composition					20.40	20.00	18.49	15.26	12.76	10.53	8.78	8.10
	RM	BFS	FS	WG	WA								
1	40	40	20	0	0	24.62	19.14	16.58	16.10	14.04	9.34	7.98	5.06
2	50	30	20	0	0	22.79	17.28	16.69	15.65	13.56	8.28	5.43	4.28
3	60	20	20	0	0	21.68	19.34	18.44	17.59	14.12	9.59	3.53	3.73
4	70	10	20	0	0	19.84	21.38	20.80	18.94	13.26	10.46	2.89	*
5	100	0	0	0	0	33.78	31.36	28.68	25.79	24.62	19.98	11.79	9.31
6	90	10	0	0	0	27.65	27.28	27.86	22.86	20.51	17.03	9.67	6.14
7	90	0	10	0	0	28.37	25.17	23.45	19.67	16.54	14.41	9.45	6.48
8	80	20	0	0	0	28.65	26.35	24.90	21.67	19.49	16.12	8.41	4.56
9	80	0	20	0	0	25.87	22.19	19.60	16.19	12.01	10.99	8.89	7.20
10	70	30	0	0	0	22.66	24.94	23.19	22.48	18.92	14.23	7.29	2.29
11	70	0	30	0	0	23.79	20.11	16.23	12.39	9.22	8.93	6.70	4.47
12	60	40	0	0	0	26.94	25.14	20.29	19.22	17.17	11.04	5.64	1.45
13	60	0	40	0	0	22.39	16.94	13.80	11.40	6.32	5.96	4.60	2.42
14	50	50	0	0	0	23.37	19.63	17.09	16.73	14.68	9.16	2.86	2.09
15	50	0	50	0	0	18.12	14.75	11.24	8.60	5.54	2.77	2.69	2.35
16	50	30	0	20	0	31.75	32.16	28.17	23.34	16.57	3.59	0.68	*
17	50	30	0	0	20	24.40	23.53	22.51	21.90	19.91	12.53	4.49	*
18	50	0	30	20	0	31.54	26.65	9.58	2.64	*	*	*	*
19	50	0	30	0	20	25.64	22.64	18.27	12.41	3.13	*	*	*
20	60	20	0	20	0	34.01	33.55	27.49	23.63	13.10	3.43	0.97	*
21	60	20	0	0	20	28.79	27.80	25.92	25.39	20.88	14.32	8.25	*
22	60	0	20	20	0	35.22	31.09	15.64	2.61	2.04	*	*	*
23	60	0	20	0	20	29.35	24.71	20.06	18.76	6.03	*	*	*
24	80	0	0	20	0	26.25	26.04	25.33	23.23	10.61	16.02	*	*
	RM	BFS	FS	WG	WA	800	900	1000	1050	1100	1150	1200	1225

Note: RM – red mud, BFS – blast furnace slag, FS – foundry sand, WG – waste glass, WA – wood ash. *- the samples melted after firing.

Water absorption of composition 0 decreases from 20.40% at 800°C to 8.10% at 1225°C due to effective interaction between particles. Similar tendency had composition 5, at 800°C 33.78%, while at 1225°C it is only 9.31%. In general, there is correlation between flexural strength, linear shrinkage and water absorption. Higher strength caused by better sintering, which is accompanied by high linear shrinkage and as a result has lower water absorption.

The influence of the blast furnace slag on water absorption is significant. It participates in formation of glass like surface due to high content of amorphous phase and as a result decreases the water absorption in compositions where it is combined with red mud.

Addition of 20% blast furnace slag, replacing 20% red mud, in composition 24 results it formation of composition 20. It has high 34.01% water absorption at 800°C, which decreases at 900°C to 33.55% and then significantly decreases ending up with 0.97% at 1200°C. When composition 20 and 24 are compared, it becomes clear that water absorption of composition 20 is higher at majority of the temperatures, reaching the close to composition 24 value only at 1050°C, when samples of composition 24 start to melt already. For this reason, the peak of maximal strength of composition 20 takes place 50°C later than peak of the composition 24.

When composition 16 and 20 are compared, it is demonstrated that increase of 10% blast furnace slag content leads to decrease of water absorption.

Comparing composition 22 and 24, which both have 20% waste glass content, the addition of the foundry sand leads to increase of water absorption at 800°C. The composition 22 has 35.22%, while composition 24 has 26.25%. At the same time, there is quick reduction of water absorption of composition 22 as it gets fired at 1000°C, presenting 15.64%.

The foundry sand increases the water absorption of the composition, especially at temperatures lower than 1050°C.

To determine the influence of waste glass, the comparison of composition 5 and 24 was carried out. As it is presented in the Table 5.3 with addition of waste glass the composition becomes more water resistant. For example, at 800°C composition 5 has 33.78%, while composition 24 has 26.25%. When samples are fired at higher temperatures, for example, at 1100°C composition 5 presents 24.62%, while composition 24 presents 10.61%.

The conclusion is that waste glass has significant positive effect on water absorption characteristics of the samples.

When in composition 22 the waste glass is substituted by wood ash resulting in formation of composition 23, at the temperatures 800-1000°C the water absorption is slightly lower, presenting 29.35%, 24.71%, and 20.06%, while composition 22 presents 35.22%, 31.09%, and 15.64% reaching lower value at higher temperature. The crucial change takes place at 1050°C, when composition 22 presents 2.61% and composition 23 presents 18.76%.

To confirm this behavior of wood ash, the compositions 18 and 19 were also compared. At 1050°C there is significant difference between water absorption of composition 18 (2.64%) and composition 19 (12.41%).

On the basis of two presented comparisons the conclusion might be the following: waste glass has more influence on water absorption of ceramic samples than wood ash. Wood ash is not as effective as waste glass when it comes to water resistance.

5.4 DENSITY OF THE DEVELOPED CERAMICS

The density of the samples was calculated as the weight of the samples was divided to the volume of the samples, which is measured in accordance to three dimensions of the sample. That is why there is crucial influence of the initial components on the weight of the sample and as a consequence on the density. The superficial bubbles and cracks of the samples also had influence. The results are presented in the Table 5.4.

Table 5.4 - Density of ceramic compositions at different firing temperatures

№	Compositions content, wt.%					Density (g/cm^3) of ceramics at different temperatures (°C)							
						800	900	1000	1050	1100	1150	1200	1225
0	Reference clay composition					1.56	1.58	1.61	1.70	1.77	1.84	1.87	1.80
	RM	BFS	FS	WG	WA								
1	40	40	20	0	0	1.82	1.87	1.93	1.88	1.96	2.03	2.11	2.16
2	50	30	20	0	0	1.85	1.88	1.89	1.85	1.92	2.02	2.16	2.18
3	60	20	20	0	0	1.69	1.72	1.76	1.74	1.85	1.94	2.21	2.18
4	70	10	20	0	0	1.58	1.60	1.63	1.62	1.78	1.90	2.24	*
5	100	0	0	0	0	1.28	1.31	1.35	1.42	1.44	1.55	1.89	1.96
6	90	10	0	0	0	1.38	1.42	1.47	1.50	1.56	1.62	1.82	1.87
7	90	0	10	0	0	1.40	1.43	1.47	1.50	1.55	1.65	1.81	1.75
8	80	20	0	0	0	1.47	1.52	1.55	1.58	1.65	1.72	1.99	2.16
9	80	0	20	0	0	1.42	1.48	1.52	1.57	1.65	1.78	2.11	2.09
10	70	30	0	0	0	1.53	1.59	1.64	1.62	1.72	1.81	2.26	2.47
11	70	0	30	0	0	1.52	1.57	1.64	1.68	1.74	1.95	2.09	2.04
12	60	40	0	0	0	1.71	1.75	1.77	1.77	1.82	1.97	2.24	2.54
13	60	0	40	0	0	1.60	1.64	1.68	1.74	1.87	2.09	1.97	1.95
14	50	50	0	0	0	1.85	1.88	1.90	1.90	1.96	2.14	2.40	2.51
15	50	0	50	0	0	1.71	1.74	1.80	1.86	1.97	2.07	1.92	1.81
16	50	30	0	20	0	1.36	1.38	1.44	1.56	1.70	2.12	2.35	*
17	50	30	0	0	20	1.50	1.51	1.50	1.51	1.59	1.73	2.17	*
18	50	0	30	20	0	1.30	1.37	1.66	1.58	*	*	*	*
19	50	0	30	0	20	1.39	1.41	1.42	1.42	1.66	*	*	*
20	60	20	0	20	0	1.30	1.31	1.39	1.54	1.75	2.02	2.26	*
21	60	20	0	0	20	1.39	1.40	1.41	1.42	1.54	1.65	1.93	*
22	60	0	20	20	0	1.23	1.29	1.54	1.81	1.61	*	*	*
23	60	0	20	0	20	1.34	1.35	1.35	1.33	1.53	*	*	*
24	80	0	0	20	0	1.33	1.35	1.37	1.40	1.66	1.50	*	*
	RM	BFS	FS	WG	WA	800	900	1000	1050	1100	1150	1200	1225

Note: RM – red mud, BFS – blast furnace slag, FS – foundry sand, WG – waste glass, WA – wood ash. *- the samples melted after firing.

The density of composition 0 steadily increases as the firing temperature rises. At 800°C the density is 1.56 g/cm^3 and by 1200°C it is already 1.87 g/cm^3. Changes in the density demonstrate complete sintering of the samples.

Composition 5 demonstrated lower density than composition 0, presenting 1.28 g/cm^3 at 800°C, with increase to 1.35 g/cm^3 at 1000°C, and 1.96 g/cm^3 at 1200°C. The samples at high temperature became dark due to oxidation of Fe.

The compositions, which contain blast furnace slag, even at low temperature 800°C, have higher density than composition 5. The increase of firing temperature led to increase of density. All compositions 6, 8, 10, 12, and 14 have increase in terms of 0.01-0.05 g/cm^3 comparing different temperatures, but at 1100°C all of them demonstrated significant growth of density. The maximum density was identified in composition 12, which contains 40% blast furnace slag and 60% red mud. The density of the samples reached 2.54 g/cm^3 after firing at 1225°C. The second after the highest value of density was presented by composition 14, which consists of 50% red mud and 50% blast furnace slag. At 1225°C it reached 2.51 g/cm^3.

Contrary to combination of red mud and blast furnace slag, combinations of foundry sand and red mud have lower melting point reaching the maximum density. For example, compositions 7, 9, and 11 reach the highest density at 1200°C, while compositions 13 and 15 have it at 1150°C. There are no radical changes in dynamic of the growth. The density steadily increases with an increase of the firing temperature.

Addition of 20% waste glass to red mud in composition 24 does not have strong impact on the density. But at 1100°C there is significant increase from 1.40 to 1.66 g/cm^3. This is exact temperature of maximal strength of composition. At 1150°C there is decrease of density and decrease in strength.

To determine the influence of wood ash compositions 22 and 23 were compared. The switch of 20% waste glass to 20% wood ash, with the same quantity of red mud and foundry sand resulted in increase of density at low temperatures.

6 PHYSICOCHEMICAL PROCESSES DURING CERAMICS' STRUCTURE FORMATION.

The study of physicochemical processes of ceramics structure formation was performed by complementary methods – XRD, DTA, TGA, SEM, EDS, Mapping, LAMMA and AAS using compositions 5, 14, 15, and 24. These compositions were chosen due to the following reasons:

1. The composition 5, which consists of red mud only, was chosen to study the impact of red mud on the changes of mechanical properties and structure formation processes of the developed ceramics at the temperatures 1000°C, 1150°C and 1225°C;
2. The influence of blast furnace slag on physicochemical processes was determined on the composition 14 containing 50% of the blast furnace slag and 50% of red mud. It was important to understand the processes of structure formation of ceramics with the best mechanical properties, particularly, with the maximum flexural strength at almost all sintering temperatures, presenting 19.78 MPa at the highest temperature 1225°C;
3. The role of foundry sand was studied on the composition 15 with also the maximum 50% addition to red mud;
4. The impact of the waste glass in the structure formation processes was investigated on the composition 24, which consists of 80% red mud and 20% waste glass. This is the composition that has the highest flexural strength (14.07 MPa) at the low sintering temperature (1100°C).

All of these compositions have high content of red mud (100%, 50%, 50% and 80% respectively). It is easy to prepare these compositions as they have only one or two components. Role of each component with increase of the sintering temperature becomes more definitive. They also have high flexural strength 12.32 MPa, 19.78 MPa, 6.85 MPa, and 14.07 MPa, which correspond to demands of class C NBR (> 4.0 MPa).

6.1 STRUCTURE FORMATION PROCESSES OF COMPOSITION 5

The composition 5 consists of 100% red mud. Physicochemical processes were studied at different temperatures. The results are presented on the Figure 6.1 - Figure 6.5 and Table 6.1 - Table 6.3.

6.1.1 Mineral transformation of the composition 5 at different temperatures

The deciphering of X-rays diffractograms (Figure 6.1) of ceramics structure formation after sintering at 1000°, 1150° and 1225°C shows very high background at all three graphs in comparison with relatively low crystal peaks. This is the evidence that amorphous material dominates crystalline. Very low intensity (1500 cps) on the Figure 6.1 - A of red mud sintering at 1000°C automatically decreased till 1000 cps with increase of sintering temperatures till 1150°(Figure 6.1 - B) and 1225°C (Figure 6.1 - C). At the same time, the increase in the crystalline structures peaks intensity, especially of albite $Na(Al\bullet Si_3O_8)$ at the angle $2\Theta° = 30.9°$ becomes obvious. The reason for such contradiction might be increase of the amorphous phase quantity and perfection of crystal structure with increasing of X-rays reflectivity. The evidences that support this idea are presented in the Table 5.4, which gives information about the changes of apparent density of the composition 5. This process of amorphous phase compacting does not prevent the perfection of the previously existing minerals crystal structures at high temperatures of sintering with the increasing of their diffraction ability.

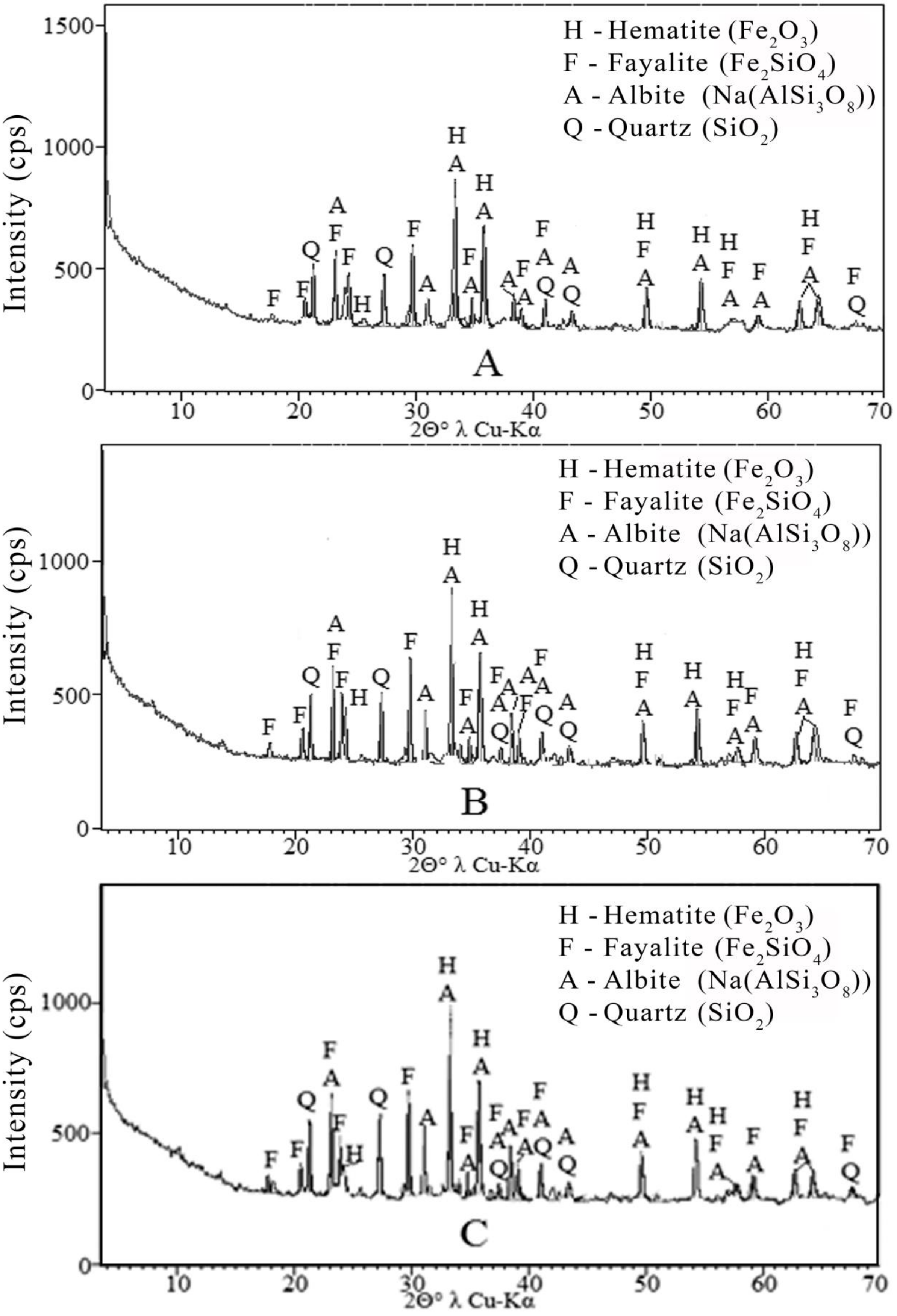

Figure 6.1 - Diffractogram pattern of composition 5 after sintering at: A – 1000°C, B – 1150°C and C – 1225°C

Mineralogical composition of the composition 5 did not change during the sintering (Figure 6.1 and Table 6.1). The main difference between the results is crystals' peaks intensities (I, %) after sintering at different temperatures. This might be result of the increase of the mineral content or the perfection of crystalline structure.

The overwhelming majority of minerals peaks have a coincidence of their positions on the scale 2Θ° with the peaks of other minerals. Anisotropy of the crystal lattices characteristics and properties does not allow determining the reason of the intensity change (increase or decrease) of coincident peaks of two or more minerals. Therefore, assessment of the peaks intensity changes can be carried out only by a few peaks, which are free from such a coincidence. The Table 6.1 contains some minerals peaks free of a coincidence with decreasing intensities as the following: three peaks of fayalite Fe_2SiO_4 at 2Θ° = 17.8°, 20.5° and 29.6°, one peak of hematite Fe_2O_3 at 2Θ° = 24.2° and one peak of quartz SiO_2 at 2Θ° = 27.2°. Only albite $Na(AlSi_3O_8)$ has two independent peaks with increasing intensity during temperature increase, particularly at 2Θ°= 30.9° and 38.3°.

Table 6.1 - Changes of minerals peaks disposition (d, Å) and intensities (I, %) on diffractogram patterns of composition 5 after sintering at different temperatures (Figure 6.1).

2Θ°	Composition 5 - 1000°C			Composition 5 - 1150°C			Composition 5 - 1225°C		
	d, Å	I, %	Minerals	d, Å	I, %	Minerals	d, Å	I, %	Minerals
17.80	4.90	11.47	F	4.90	8.20	F	4.90	5.97	F
20.50	4.30	18.02	F	4.30	17.28	F	4.30	16.46	F
21.20	4.10	42.42	Q	4.10	39.18	Q	4.10	36.54	Q
23.10	3.80	53.71	F; A	3.80	55.27	F; A	3.80	54.97	F; A
23.90	3.70	41.55	F	3.70	39.73	F	3.70	36.65	F
24.20	3.60	37.93	H	3.60	26.91	H	3.60	22.27	H
27.20	3.20	44.44	Q	3.20	40.52	Q	3.20	38.37	Q
29.60	3.00	61.03	F	3.00	60.58	F	3.00	58.64	F
30.90	2.88	24.83	A	2.88	30.55	A	2.88	34.91	A
33.30	2.68	100.0	A;H	2.68	100.0	H; A	2.69	100.0	H;A
34.10	2.63	9.36	A	2.63	11.10	A	2.63	12.61	A
34.80	2.57	22.23	F;A	2.57	14.92	F;A	2.57	15.24	F;A
35.80	2.50	73.01	A;H	2.50	65.11	H; A	2.51	65.74	H; A
37.50	2.39	7.63	Q; F; A	2.39	8.97	Q; F; A	2.39	9.13	Q; F; A
38.30	2.34	21.82	A	2.34	27.73	A	2.34	30.50	A
39.00	2.30	14.09	A;F	2.30	18.81	F;A	2.30	19.96	F;A
41.00	2.20	22.00	A;Q;F	2.19	18.78	Q; F	2.19	21.19	Q; F; A
43.30	2.08	12.88	A;Q	2.08	10.60	Q; A	2.08	10.05	Q;A
49.60	1.83	31.99	A;H;F	1.83	25.81	H;F;A	1.83	27.11	H; F;A
54.30	1.68	38.87	A;H	1.68	32.77	H; A	1.69	34.18	H; A
57.70	1.59	11.23	H; F; A	1.59	9.12	H; F; A	1.59	8.55	H;F;A
59.10	1.56	10.17	A; F	1.56	15.72	F; A	1.56	14.73	F;A
62.70	1.48	21.91	A;H;F	1.48	19.57	H;M;F; A	1.48	17.04	H;F;A
64.20	1.44	19.32	A;H;F	1.44	16.53	H; F;A	1.44	15.30	H; F; A
67.50	1.38	8.37	Q; F	1.38	6.73	Q; F	1.38	5.88	Q; F

It is well known from the chemistry of silicates and aluminosilicates about their property of low solubility in alkaline medium. Perhaps albite, which also belongs to the class of aluminosilicates, is the exception of this rule due to the high (11.8%) Na_2O content. It also has chemical affinity with red mud, which also contains 10.3% Na_2O (Table 4.3). Probably sodium atoms of the NaOH solution of Bayer process are entering into the crystal lattice of albite better at high temperatures of red mud sintering. Taking it into consideration this improvement of the structure, the diffraction ability of albite is increasing with slow increase of its peaks intensities. The reagent is chemically highly active (pH = 13.5). Alkali enters into chemical interaction with milled bauxite ore to form such type of salts as carbonates Na_2CO_3, and bicarbonates of sodium sulphate Na_2SO_4. All these components have a very low melting temperature (NaOH - 323°C, $NaHCO_3$ - 270°C, Na_2CO_3 - 852°C, Na_2SO_4 - 883°C) and can serve as a good flux during firing of the ceramic.

High alkalinity of red mud is one of the reasons for quartz (SiO_2) crystals melting. It causes loss of quartz peaks intensities at temperatures of these experiments, which are lower than its normal melting point (1703°C). The melting point of fayalite Fe_2SiO_4 is rather low (1200°C), but its melting also begins at 1000°C because of the same reasons.

The chemical composition of the red mud (Table 4.3) includes 21.2% Al_2O_3. As a result of the super-based Bayer hydrothermal process, Al_2O_3 may advantageously be in the form of aluminum hydroxide $Al(OH)_3$ with melting point at 300°C.

London Centre of the National Poisons Information Service informed that NaOH melting point is 318.4°C. When it is dissolved with 45% concentration the boiling point of NaOH is 136-137°C.

With a total amount Al_2O_3 + Na_2O equal to 31.5%, they can be attributed to the fluxes of the investigated compositions. Another component, which can reduce the melting point of red mud, is its amorphous phase, which according to XRD pattern quantitatively prevailing in red mud (Figure 4.2).

In the XRD patterns of composition 5 (Figure 6.1) was not detected magnetite Fe_3O_4, which initially presented in small quantity in the XRD pattern of red mud (Figure 4.2). It is possible that it continues to be presented in the composition 5 after chemical destruction during its firing at 1000°C and higher temperature, but in an amount that is lower than the sensitivity of the XRD method (5%). The cumulative effect of these two factors (the presence of above mentioned fluxes and the predominance of the amorphous material) can radically reduce the melting point (1594°C) of ferrous minerals hematite and magnetite with slow decrease of their peaks intensities.

6.1.2 Thermochemical reactions in the composition 5

The study of the thermochemical reactions was performed using the deciphered curves of differential thermal analysis (DTA) and thermogravimetric analysis (TGA). The main chemical components of red mud (Table 4.3) are Fe_2O_3 - 29.9%, Al_2O_3 - 21.2% and SiO_2 - 15.5%. As a result of thermochemical reactions during Bayer method application, these elements are in the form of some minerals in the crystalline form (Figure 4.2) and are mostly in the form of amorphous aluminum and iron hydroxide of varying compositions $Al_2O_3 \bullet nH_2O$ and $Fe_2O_3 \bullet nH_2O$. The process of red mud sintering has the thermal impact on the both hydroxides. Each of them has its own behavior in terms of endothermic and exothermic effects. Therefore, it is impossible to separate these effects and determine each of them in red mud and mixtures containing red mud. Phase equilibria in the systems Fe - Al - O and Fe - Si - O during the heating till 1300°C was studied by Kimjashov (2010).

During firing of hydroxide Al_2O_3•nH_2O the following processes take place: at 110-120°C - removal of free or weakly bound water; at 200-250°C - gibbsite γ-AlO(OH) loses crystal water molecules and converts to boehmite; at a temperature about 500°C boehmite converts into anhydrous γ-Al_2O_3; at a temperature about 900°C the γ-Al_2O_3 transforms into α-Al_2O_3 (BROWN (2011)).

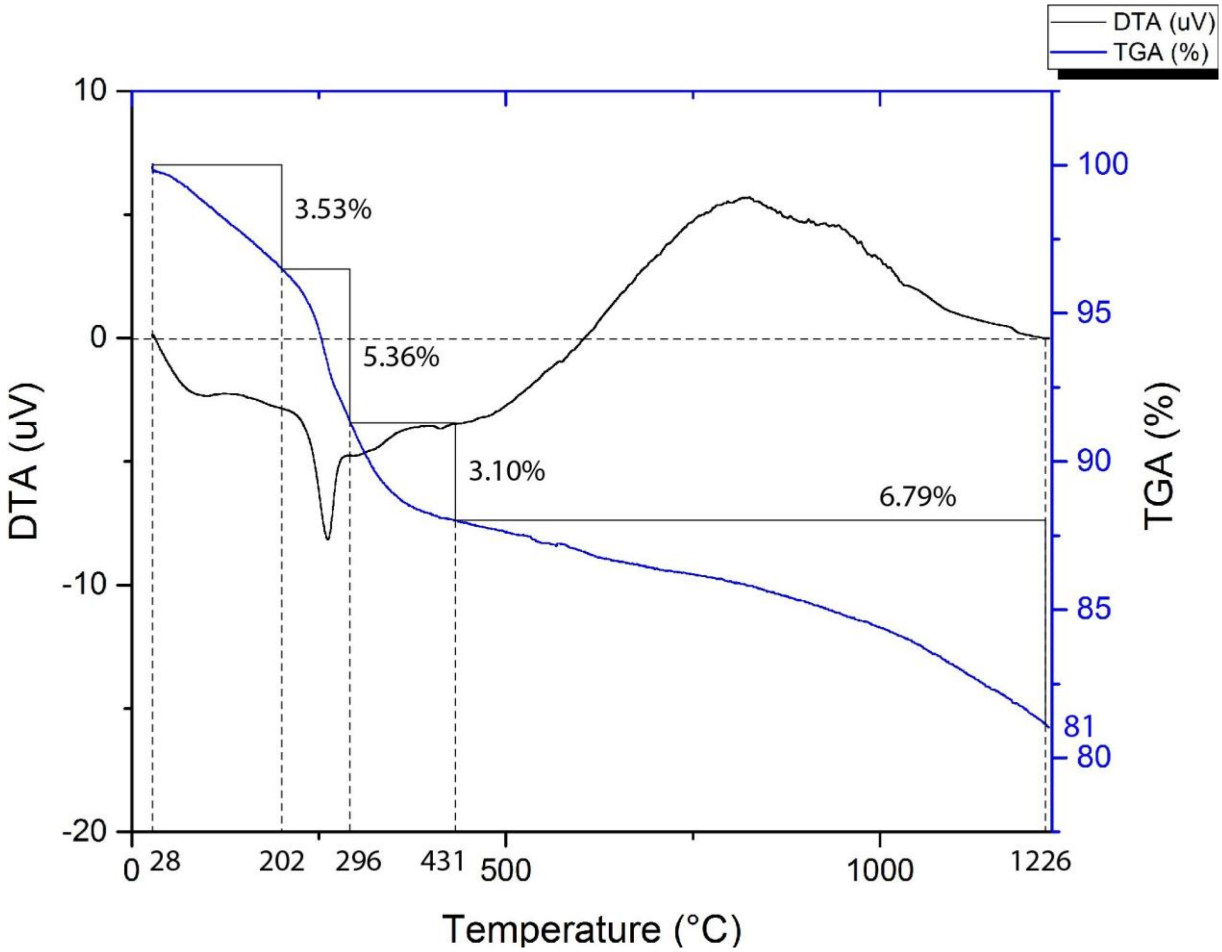

Figure 6.2 - DTA and TGA curves of composition 5

Table 6.2 - The endothermic and exothermic effects of the composition 5 by DTA and TGA curves (Figure 6.2)

Hydroxides	Thermo-chemical processes, temperature of reaction (°C) and weight loss (%)			
Effect	Endothermic effect 1. 28-202°C.	Endothermic effect 2. 202-296°C.	Exothermic effect 1. 296-431°C.	Exothermic effect 2. 431-1226°C.
Al	Removal of free or weakly bounded water. Weight loss 3.53%.	loses crystal water molecules by $Al(OH)_3$ and converted to boehmite γ-$AlO(OH)$. Weight loss 5.36%	boehmite is converted into anhydrous γ-Al_2O_3. Weight loss 3.10%.	The transformation γ-Al_2O_3 γ-$Al_2O_3 \rightarrow \alpha$-$Al_2O_3$. Weight loss 6.79%.
Fe		Amorphous gel transformation into (α, β, γ and δ) of $FeOOH$.	$FeOOH \rightarrow \gamma$-$Fe_2O_3 \rightarrow Fe_3O_4$. Weight increase.	$Fe_3O_4 \rightarrow Fe$ (700-750°C). Weight loss. Formation of dross-Fe_3O_4 (900-1000°C). Weight increase.

All these transformations occurred with a considerable amount of heat absorption (endothermic process) except transformation of the γ-Al_2O_3 into the α-Al_2O_3 (exothermic reaction). The majority of heat is generated at 500-600°C due to decomposition of gibbsite γ-AlO(OH).

Different type of processes took place in terms of $Fe_2O_3 \bullet nH_2O$ transformations. During the red mud firing FeOOH appeared in the form of the first smooth endothermic effect at 28°-100°C and 3.53% weight loss. It also belongs to the process of free or weakly bonded water FeOOH dehydration. The beginning of amorphous gel transformation to the various crystalline forms (α, β, ɣ and δ) of FeOOH is the reason for the second endothermic effect between 202°C and 296°C. At the same temperature the transformation of FeOOH → ɣ-Fe_2O_3 (maghemite) → Fe_3O_4 began with total weight loss 5.36%. This process smoothly transforms into recovery of Fe_3O_4 to Fe up to 700°-750°C (BROWN (2011)).

6.1.3 Morphological structure development of the composition 5

Comparison of the raw red mud SEM micro images before its sintering (Figure 4.8) with the micro images of composition 5 after sintering at 1000°C (Figure 6.3 - A, B and C) shows lack of significant changes in the morphological structures. Red mud particles at all magnifications remained disintegrated. They do not change their sizes and morphology. This is the reason why ceramics did not have strength, had high water absorption and low density.

As firing temperature increases up to 1150°C (Figure 6.3 - D, E and F) the micro morphology becomes denser. The amount of pores decreases, which is especially easy to identify comparing photos B and E at 5000 magnification. Some particles began melting (Figure 6.3 - F), gluing neighboring particles in hardened aggregated units and thus increasing the strength of the samples till 6.06 MPa. Increase of the firing temperature for another 75°C to 1225°C (Figure 6.3 - G, H and I) leads to melting of the all particles. The best image to observe it is Figure 6.3 - G.

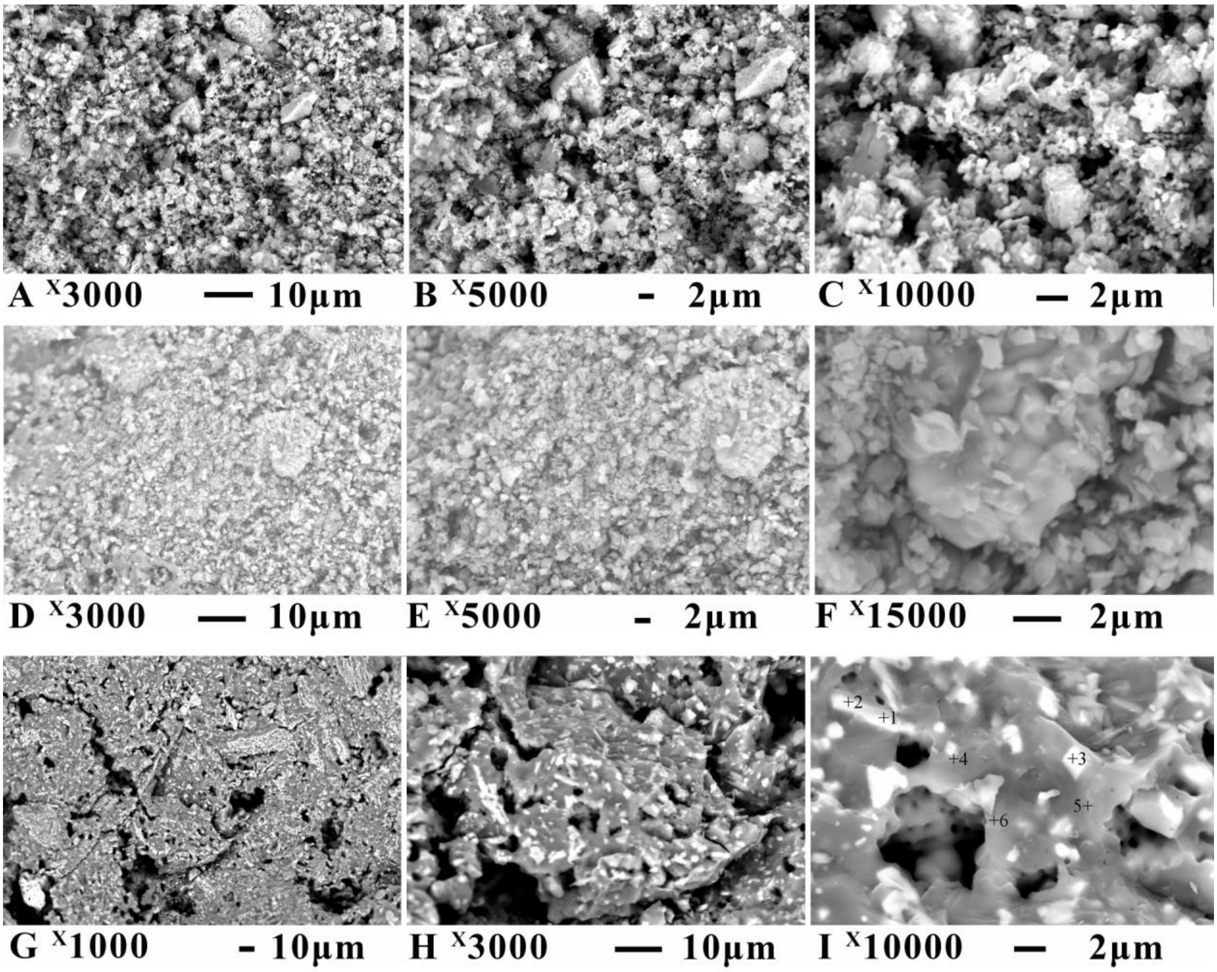

Figure 6.3 - SEM micro images of composition 5 after sintering at: 1000°C - A, B and C; 1150°C - D, E and F; 1225°C - G, H and I.

The area of the pores in the images has remained relatively extensive, but the melting of all particles leads to their complete integration in the whole volume by smooth shiny glass-like new formations with a total flexural strength of the ceramics 12.32 MPa (Table 5.1).

6.1.4 Micro-chemical analysis of new formations in the composition 5

Chemical analyses of these new formations of the total area and 6 points of SEM image of Figure 6.3 - I, was performed by EDS method and demonstrated (Table 6.3) very high level of heterogeneity. The combinations of chemical elements and their percentage contents in each point of the EDS analysis are very different comparing to each other. For example, Na content varied between 0 and 14.10 wt%, Al – between 0 and 16.26%, etc. Presented high level of the heterogeneity of the chemical compositions is typical for amorphous structures. The EDS analysis shows also presence of large amount of heavy metals in these points, such as Cr 6.40%, Ni 5.05% and Cu 2.09%. All of them (except Zn) were located also by AAS method in the quantities highly exceeding the Brazilian norms NBR 15270.

Table 6.3 - Chemical composition of the composition 5 (Figure 6.3 – I) by EDS method.

Point	Chemical elements content, wt.%												
	Na	Al	Si	S	K	Ca	Cr	Fe	Ni	Cu	Zn	Ba	Total
Total area	12.09	4.13	26.18	2.25	5.09	3.54	3.25	33.18	2.81	2.09	2.24	3.15	100.0
1	3.26	0.00	49.60	25.21	0.89	0.00	0.59	10.79	9.12	0.00	0.54	0.00	100.0
2	7.16	9.04	13.23	0.20	1.15	5.48	6.51	45.09	0.00	12.14	0.00	0.00	100.0
3	1.96	16.26	4.91	1.66	29.56	0.00	14.37	4.67	4.37	14.93	3.75	3.56	100.0
4	0.00	6.75	11.48	6.69	5.18	6.07	2.24	52.78	0.26	0.00	1.13	7.42	100.0
5	14.10	0.00	0.00	12.22	13.05	0.00	0.00	49.35	6.20	2.40	2.68	0.00	100.0
6	10.78	2.76	33.56	0.00	1.40	0.00	6.11	34.61	2.38	0.26	4.17	5.81	100.0

In order to obtain some results except EDS analysis results, was made laser micro-mass analysis (LAMMA) in 6 points of the composition 5 sample’s surface.

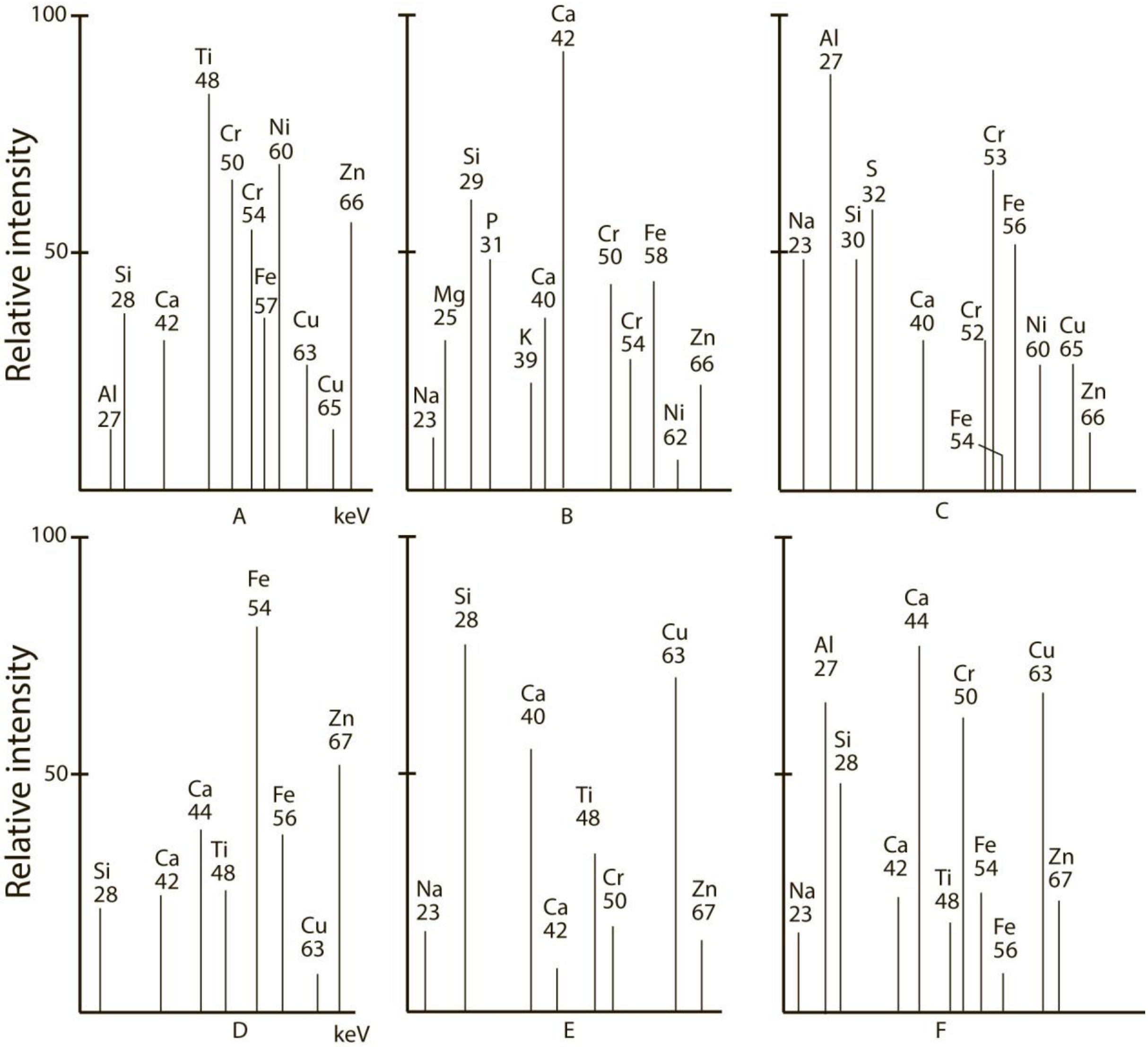

Figure 6.4 - Isotopes laser micro-mass analysis of new formations of composition 5 after sintering at 1225°C.

As it might be presumed according to the Figure 6.4, all points demonstrate rather big difference in quantities of isotopes and intensities of their peaks. This data confirms great level of heterogeneity on microscale.

6.1.5 Mapping the chemical states of an element inside the composition 5

Mapping by the method of tomographic X-ray absorption spectroscopy sample (Figure 6.5) demonstrates the states of the principle chemical elements in the ceramics of the composition 5 after sintering at 1225°C. The glowing colored dots indicate the location of the micro-particles of the corresponding chemical elements. The black spaces on the images indicate deep pores, in which the equipment could not reach the bottom to determine states of the elements.

White oval on SEM photo shows one of the largest holes in the presented surface. It coincides with similar ovals of similar size in the same points of the C, Na, Al and Si mapping. The size of the oval is smaller in the Ca, Ni and significantly smaller at K map and almost disappears at the Fe map, which means a significant content of these elements near the area of the ovals. However, the center of a small oval on the Fe map correlates with the bottom of the hole, which might be observed at SEM image. High content of Fe (29.9%) in red mud (Table 4.3) is presented in the form of agglomerates of particles of various shapes and sizes.

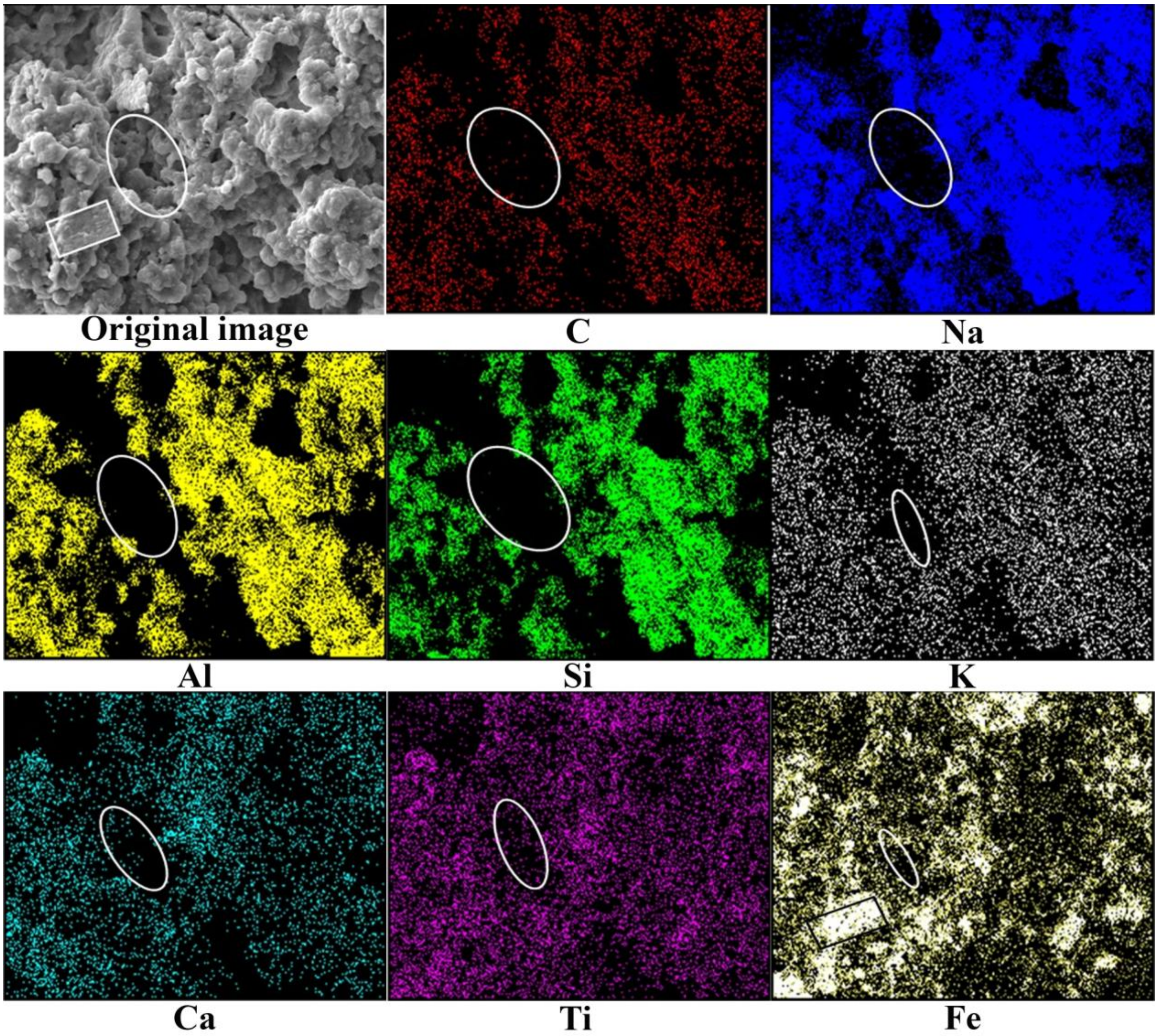

Figure 6.5 - Mapping the chemical states of an element inside a composition 5 sample (using tomographic X-ray absorption spectroscopy).

The largest agglomerated piece of Fe particles is highlighted with white rectangle size of about 20 x 10µm. There are also high particles concentrations observed in the maps of Na, Al and Si. Particles of Ca and Ti have lower concentrations on the sample’s surface.

6.2 STRUCTURE FORMATION PROCESSES OF COMPOSITION 14

The composition 14 was chosen for the study of physicochemical processes of ceramics structure formation as the most attractive from different points of view. Firstly, it has high content of red mud (50%). Secondly, it is easy to prepare the composition as it has only two components in the same quantity. Thirdly, it has very high flexural strength of 8.12 MPa, corresponding to demands of class C NBR (> 4.0 MPa) at relatively low temperature of 1100°C and much higher (19.78 MPa) at 1225°C.

In order to present full study of physic-chemical characteristics of composition 14 and role of each component in the processes of structure formation in this section are also presented characteristics of compositions 12, 20 and 21. They all have red mud and blast furnace slag as main components.

6.2.1 Mineral transformation of the composition 14 at different temperatures

The composition 14 consists of two components, which have very different chemical and mineral compositions. As a result they chemically interact with each other and this interaction accelerates with increase of firing temperature. Comparison of the XRD patterns of the composition 14 sintered at 1000°C, 1100°C, 1200°C and 1225°C (Figure 6.6) demonstrates the presence of hematite Fe_2O_3, fayalite Fe_2SiO_4, albite $NaAlSi_3O_8$ and quartz SiO_2 with very high content of amorphous materials. After sintering at 1200° and 1225°C, the intensity has reduced on the XRD patterns from 1500 (of Figure 6.6 - A and B after sintering at 1000° and 1100°C) to 1000 counts per second (Figure 6.6 - C and D). It means a decrease in amount of crystalline phases in the ceramics with its transition to the amorphous state.

Basically it is very difficult to assess the change of the peaks intensity using only the XRD graphs. Table 6.4 presents more detailed information on peaks intensity. The vast majority of these peaks of different minerals are coinciding and the only peaks, which are free from these coincidences, can serve as indicators of growth or reduction of the minerals crystal contents or their perfection of the crystal structures during the sintering.

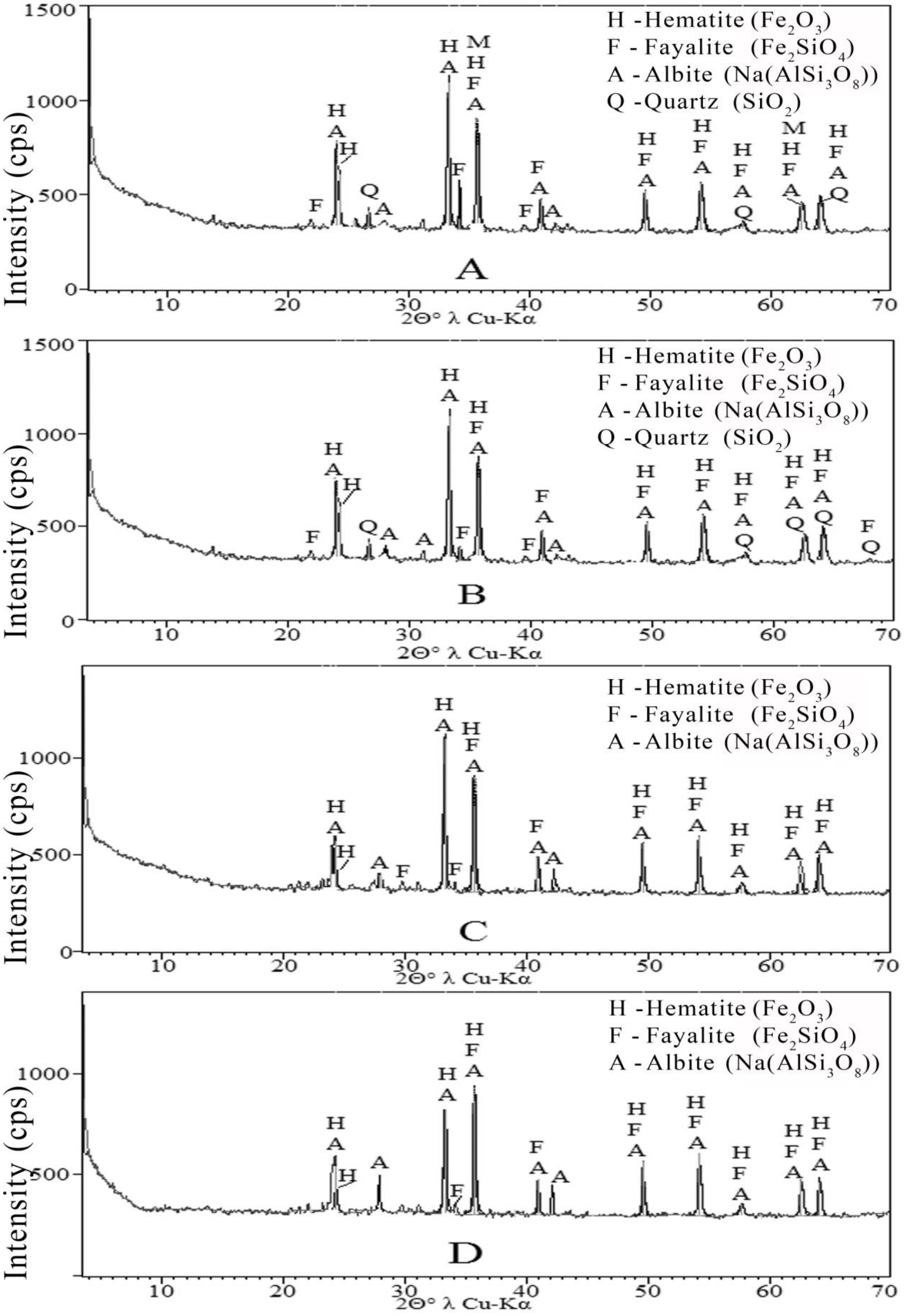

Figure 6.6 - Diffractogram pattern of the composition 14 at: A – 1000°C, B – 1100°C, C – 1200°C and D – 1225°C.

As it is presented in the Table 6.4 a significant decrease of fayalite free peak intensity at 2Θ° = 34.2° from 9.53 to 5.17% and complete disappearance of another free peak at 2Θ° = 22.0° at the temperature 1100°C. Ozturk et al. (2015) stated that addition of 33% blast furnace slag causes synthesis of anorthite, but in terms of his experiment there were also clay, sand, limestone, and kaolin involved in the process of firing.

Almost the same happened with the only free of coincidence peak of other iron mineral hematite Fe_2O_3 at 2Θ° = 24.2°. At 1000°C very high intensity value I = 32.76% slowly decreased till 22.32% at 1150°C and collapsed till 5.73% at 1225°C. At the same time in terms of flexural strength was detected increase from 13.5 to 19.78 MPa. This means complete melting of fayalite, almost complete melting of hematite and the inclusion of their iron atoms in the amorphous phase of the ceramics. This transition may be the cause of such increase of samples' strength at this range of temperatures.

Table 6.4 - Changes of minerals peaks disposition (d, Å) and intensities (I, %) on diffractogram patterns of composition 14 after sintering at different temperatures (Figure 6.6).

2Θ°	Composition 14 - 1000°C			Composition 14 - 1100°C			Composition 14 - 1150°C			Composition 14 - 1225°C		
	d, Å	I, %	Symbol	d, Å	I, %	Symbol	d, Å	I, %	Symbol	d, Å	I, %	Symbol
22.00	4.00	6.20	F	4.00	4.20	F						F
24.20	3.70	36.73	H; A	3.70	34.34	H; A	3.70	27.74	H; A	3.60	18.37	H; A
24.20	3.60	32.76	H	3.60	29.22	H	3.60	22.32	H	3.60	5.73	H
26.60	3.30	11.57	Q	3.30	7.24	Q						Q
27.80	3.10	5.80	A	3.10	8.84	A	3.10	10.24	A	3.10	13.47	A
33.20	2.69	100.0	H; A	2.69	100.00	H; A	2.69	100.0	H; A	2.69	100.0	H; A
34.20	2.62	9.53	F	2.62	8.25	F	2.61	6.74	F	2.62	5.17	F
35.70	2.51	68.89	H;F;A	2.51	71.29	H;F;A	2.51	75.62	H;F;A	2.51	76.76	H;F;A
40.90	2.20	21.34	F; A	2.20	21.13	F;A	2.20	23.13	F; A	2.20	21.64	F; A
42.20	2.14	3.84	A	2.15	5.20	A	2.14	6.43	A	2.15	11.86	A
49.60	1.83	28.13	H;F;A	1.84	30.12	H;F;A	1.83	33.14	H; F; A	1.83	33.33	H;F;A
54.20	1.69	33.51	H;F;A	1.69	33.64	H;A	1.69	37.74	H; A	1.69	38.12	H;F;A
57.60	1.59	6.61	H;F;A;Q	1.59	6.37	H;F;A	1.59	6.87	H; A	1.59	7.26	H;F;A
62.50	1.48	19.98	H;F;A	1.48	17.42	H;F;A	1.48	16.82	H;F;A	1.48	21.97	H;F;A
64.10	1.45	18.89	H;F;A;Q	1.45	17.17	H;F;A	1.45	20.67	H;F;A			H;F;A

The only free from coincidence quartz peak at 2Θ° = 26.6° disappeared at 1150°C similar to the 2Θ° = 26.6° peak of fayalite. This indicates almost complete melting, and the possible inclusion of silicon atoms in the crystal lattice of albite $NaAlSi_3O_8$. Albite, just like in the composition 5 (Table 6.1 and Figure 6.1) has increase of intensity peaks at 2Θ° = 27.8° and 42.2°. It seems to be due to adsorption of SiO_2 of quartz. The partly inclusion of melted

SiO_2 in amorphous phase of the ceramics is also possible. Phase transitions of these three minerals also might be the reason for an increase of samples’ strength at this range of temperatures.

6.2.2 Thermochemical reactions in the composition 14

To clarify the process of phase transformation of the composition 14 during the sintering at 25°-1225°C were conducted the studies of thermochemical reactions by DTA and TGA methods (Figure 6.7). Comparison of these curves of the composition 14 with the curves of its raw materials, which are red mud and blast furnace slag, allows identifying the similarity of thermal effects.

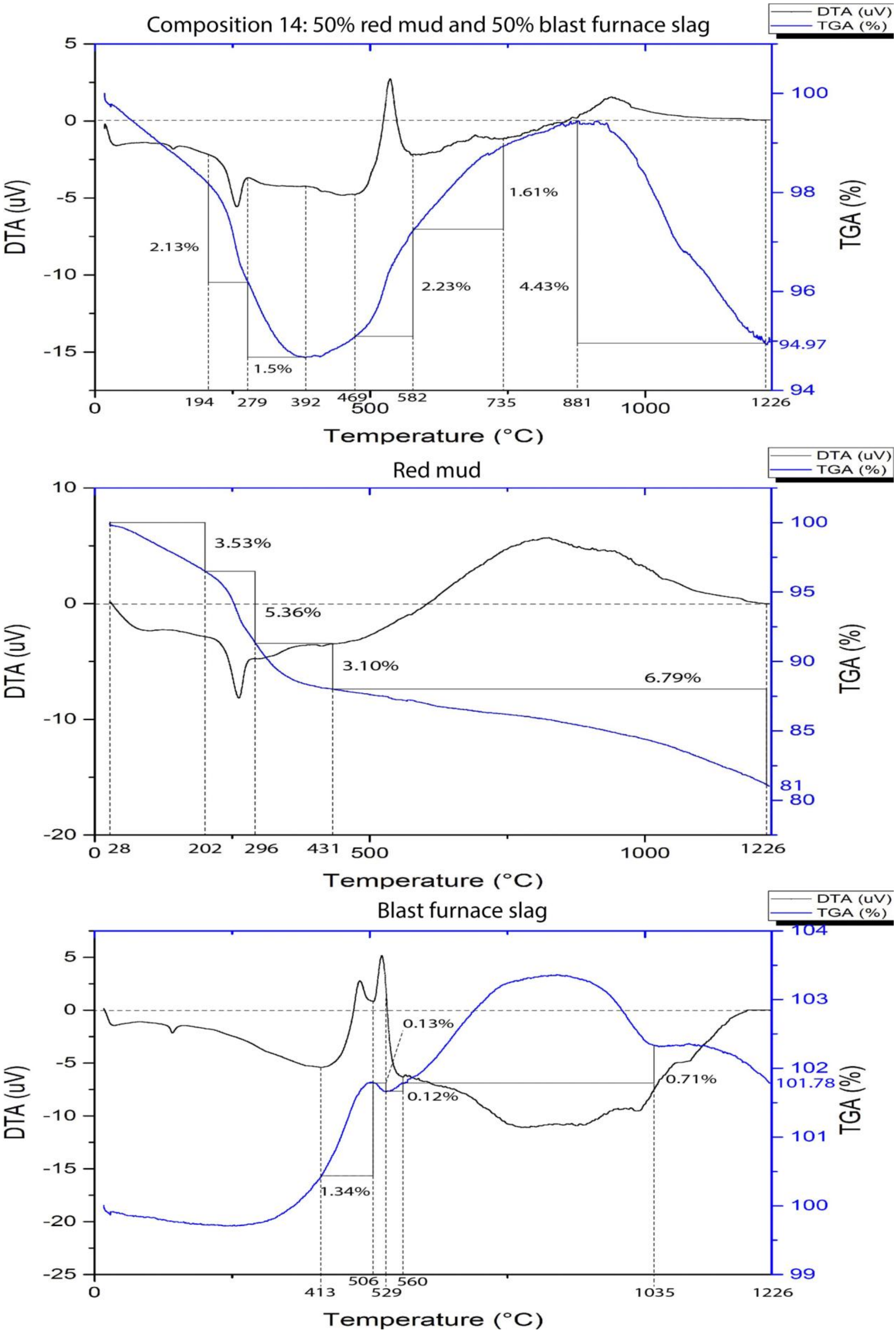

Figure 6.7 - DTA and TGA curves of composition 14.

Table 6.5 - The endothermic and exothermic effects of the composition 14 by DTA and TGA curves (Figure 6.7)

Thermo-chemical processes, temperature of reaction (°C) and weight loss (%)					
Endothermic effect 1. 28-202°C.	Endothermic effect 2. 202-279°C.	Endothermic effect 3. 279-469°C.	Exothermic effect 1. 469-582°C.	Exothermic effect 2. 582-735°C.	Exothermic effect 3. 881-1227°C.
Removal of free or weakly bound water Weight loss 3.53%.	1. Loses crystal water molecules by $Al(OH)_3$ and converted to boehmite γ-AlO(OH) 2. Amorphous gel transformation to (α, β, ɣ and δ) of FeOOH.	Boehmite is converted into anhydrous γ-Al_2O_3 Weight loss 1.5%.	1.γ-AlO(OH)→ γ-Al_2O_3; 2.FeOOH → ɣ-Fe_2O_3 → Fe_3O_4 Weight increase 2.33%.	Fe_3O_4→ Fe Weight increase 1.61%.	1. ɣ-Al_2O_3 →α-Al_2O_3 2. Fe_3O_4→Fe 3. SO_2 firing 4.Dross formation Fe_3O_4 Weight loss 4.43%

The endothermic effect between 194°C and 279°C correlates with endothermic effect of red mud between 202°C and 296°C, which indicates a decrease in the loss of crystal structure water of gibbsite $Al(OH)_3$ with its transition to boehmite ɣ-$AlO(OH)_4$. Weight loss during this reaction of the composition 14 is significantly smaller (2.13%) than that of the red mud (5.36%). The reason for this might be the content of 50% red mud in the original mixture and imprecision of the selected points of the beginning and the end temperatures on the DTA and TGA curves (JOHNSON (1971)).

The second endothermic effect of the composition 14 between 279°C and 392°C with little tolerance repeats another endothermic effect of red mud between 296°C and 431°C. The coincidence of their weight loss values 1.50% and 3.10% is also quite logical and corresponds to the conversion reaction of boehmite ɣ-$AlO(OH)_4$ in anhydrous γ-Al_2O_3 (KATO et al. (1981)) .

The sharp peak of the exothermic reaction between 469°C and 582°C with a weight loss is corresponding to 2.23% two-headed blast furnace slag exothermic effect at 413° - 560°C with a total weight loss of 1.47%.

The presence in the chemical composition of the blast furnace slag of 10.0% SO_3 and high (62.1%) iron content (Table 4.3) inevitably leads to their combination during heating of the composition 14 in the forms of iron hydrates, iron sulfates and iron sulfides.

Smooth exothermic effect in red mud between 582°C and 735°C with weight increase on the TGA curve for 1.61% occurred due to the transition of anhydrous boehmite ɣ-Al_2O_3 to α-Al_2O_3 (JOHNSON (1971)). Therese is also a chain of the transitions in the blast furnace slag FeOOH → ɣ-Fe_2O_3 → Fe_3O_4 at the same temperature (KATO et al. (1981)). It means melting of $Fe_2(SO_4)_3$ and the start of combustion SO_2 gas formed due to transition of $Fe_2(SO_4)_3$ to Fe_2O_3. The appearance of this exothermic effect in the blast furnace slag corresponded to thermo-chemical decomposition of FeS_2 in an oxidizing environment of air with following transfer to the $FeSO_4$ + SO_2 and burning of the released gas. Typically, this reaction takes place at 630-650°C, which coincides with the peak turning point at 582° - 735°C. Total weight increase equals to 2.33%

The third exothermic effect of the composition 14 at 735° - 1227°C includes four different thermo-chemical reactions. The transition $\gamma\text{-}Al_2O_3 \rightarrow \alpha\text{-}Al_2O_3$; transition $Fe_3O_4 \rightarrow Fe$ up to 700-750 °C; reduction in weight of the sample as a result of the following final release of SO_2 and burning of the released gas; the formation of Fe_3O_4. The total weight loss of these processes is 4.43%.

Probably, the formation of iron dross and SO_2 combustion process leads to blackening of samples (Figure 5.2), which appeared at the temperatures from 1200°C to 1225°C. The maximum intensity of these processes at 1225°C resulted in the maximum flexural strength. Flexural strength of the composition 14 has reached 19.78 MPa at 1225°C, the linear shrinkage value reached 11.40%, the density at 800°C was 1.85 g/cm^3, and at 1225°C increased to 2.51 g/cm^3, and the water absorption of the samples decreases from 23.37% at 800°C to 2.09% at 1225°C.

6.2.3 Thermochemical reactions in the composition 12

The thermochemical reactions of the composition 12, which consists of 60% red mud and 40% blast furnace slag, were carried out (Table 6.6) for a more detailed analysis of the blast furnace slag's role in the formation of ceramic structure. Comparison of the DTA and TGA curves of the compositions 12 and 14 during sintering shows that, in general, thermochemical reactions of raw materials repeated in the composition 12 with the following qualitative and quantitative changes:

1. The small increase of weight loss of the endothermic effects 1 and 2 and a reduction weight loss effect of the first exothermic effect of the composition of 12;
2. Due to 10% increase of red mud content and the same decrease of the blast furnace slag content in the composition 12, the peak of exothermic effect 2 between 582°C

and 735°C, which is easy to detect at the DTA curve of the composition 14, became invisible on the DTA curve of the composition 12. The exothermic effect 2 supposed to reflect the full transformation $Fe_3O_4 \rightarrow Fe$.

The reason for the peak to disappear might be the slowdown of iron restoration process in an alkaline medium of red mud, as the content of red mud has increased comparing with composition 14. The slowdown of iron restoration process might be one of the reasons for lower strength the composition 12 comparing with the composition 14 (Table 5.1), especially at 1050° and more.

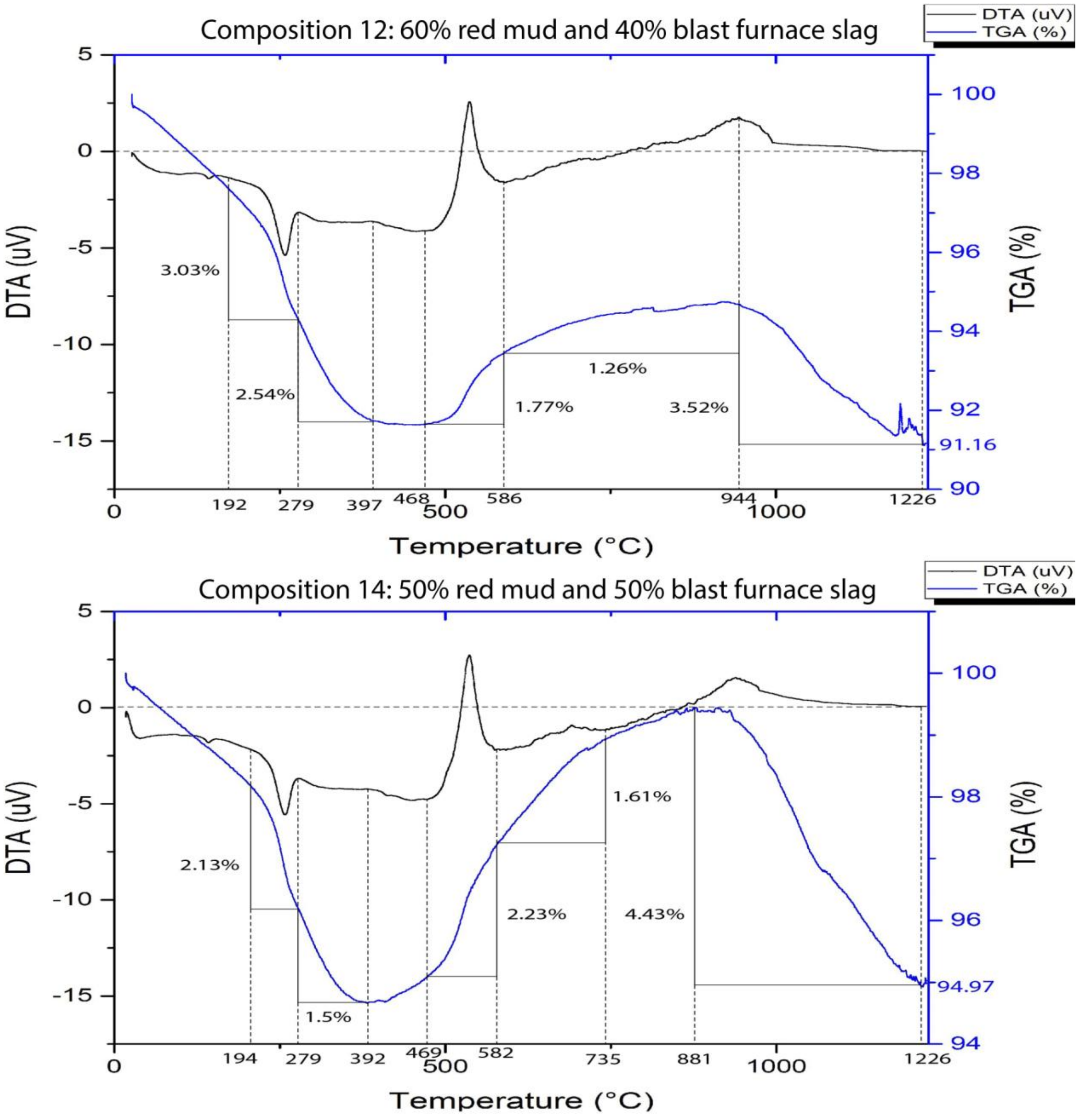

Figure 6.8 - DTA and TGA curves of compositions 12 and 14.

Table 6.6 - The endothermic and exothermic effects of the composition 12 by DTA and TGA curves (Figure 6.8).

Thermo-chemical processes, temperature of reaction (°C) and weight loss (%)			
Endothermic effect 1. 192-279°C.	Endothermic effect 2. 279-397°C.	Exothermic effect 1. 468-586°C.	Exothermic effect 2. 881-1227°C.
1. Removal of free or weakly bound water Weight loss 3.03%. 2. Amorphous gel transformation to (α, β, ɣ and δ) of FeOOH.	The loss of crystal water molecules by $Al(OH)_3$ and converted to boehmite γ-AlO(OH) Weight loss 2.54%.	1. γ-AlO(OH)→ γ-Al_2O_3; 2. FeOOH → ɣ-Fe_2O_3 → Fe_3O_4 Weight increase 1.77%.	Dross formation Fe_3O_4 900-1000° Weight increase 4.43%.

Due to the exothermic reaction phase after sintering at 1225°C the samples of the composition 12 have flexural strength 18.05 MPa, the linear shrinkage of up to 12.35%, a density of 1.71 g/cm^3 at 800° increases to 2.54 g/cm^3 at 1225°C, and the water absorption of the samples decreases from 26.94% at 800°C to 1.45% at 1225°C.

The similarity of chemical and mineral composition of compositions 14 and 12 determined the similarity of their thermochemical reactions, which in terms determined the highest flexural strength comparing to other compositions of the research.

The lack of new crystalline formations and barely noticeable increase in the content of the amorphous phase in the compositions 12 and 14 allow suggesting that the values of the mechanical properties of ceramics are also achieved by the synthesis of solid crystalline solutions.

Thermochemical interaction of the components of the amorphous and crystalline phases at high temperatures may result in the creation of one-dimensional, linear and volumetric dislocations and formations. It may also cause appearance of vacancies at the lattice points or internodes. There might be a large number of substituted single atoms and complexes of atoms in lattices, lattice twinning, and many other types of violation of the translational symmetry of the crystal. All these violations in large quantities can lead to the displacement of atomic planes of lattices and changes in the position of peaks (d / n, Å) or their intensity as indicated in Table 6.1, Table 6.4, Table 6.10, and Table 6.14. Analysis of the creation and growth of the solid solutions is impossible by XRD method, as these new formations might be out of the sensitivity of the method (about 5%). It is important to highlight that the synthesis of large quantities of solid solutions of these structures may serve as one of the main factors for growth of the flexural strength of the materials under study.

6.2.4 Morphological structure development of the composition 14

Comparison of the SEM micro images of composition 14 after sintering at 1000°C and 1150°C at the same magnification of 3000 times shows transition from melting of exact points (Figure 6.9 - A, B and C) to the melting of relatively large areas (Figure 6.9 - D, E and F). This is the main reason why flexural strength increased from 3.34 to 13.05 MPa. After sintering at 1225°C (Figure 6.9 - G, H and I) practically all particles of the mixture have melted and become chemically interacted.

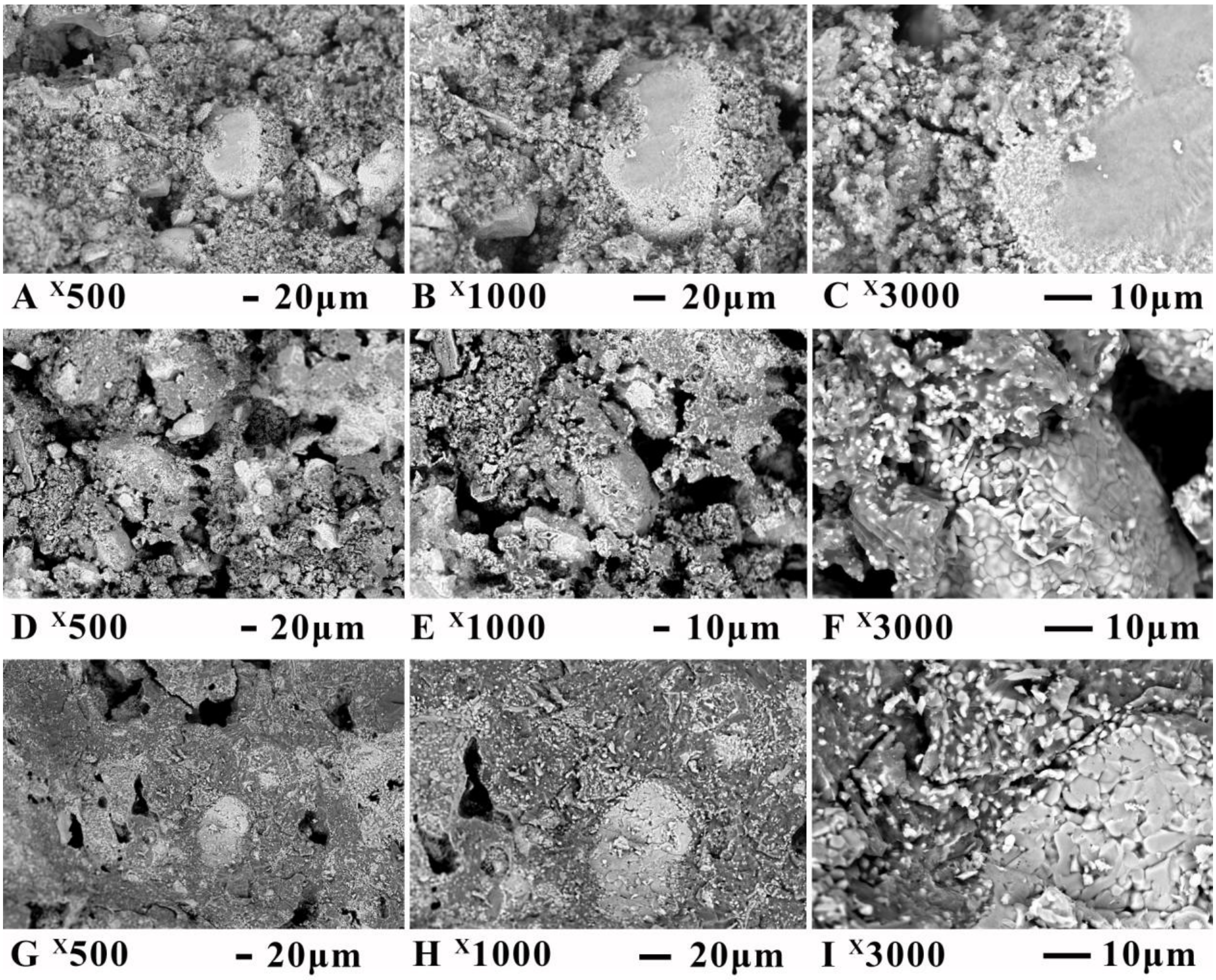

Figure 6.9 - SEM micro images of composition 14 after sintering at: 1000°C - A, B and C; 1150°C - D, E and F; 1225°C - G, H and I.

Pores in ceramic almost disappeared, and the sample presented almost monolithic structure. Flexural strength increased in 1.5 times, comparing with 1150°C, to 19.78 MPa with significant improvement of others mechanical characteristics.

6.2.5 Micro-chemical analysis of new formations in the composition 14

New formations of the composition 14, which were created at 1225°C, is the main reason for flexural strength increase. Their micro-chemical compositions were studied using the following methods: EDS method (Figure 6.10) and LAMMA (Figure 6.11) isotopes composition of three nearest points.

The studies by EDS method were conducted with magnification of 3000 times in three different areas (1, 2 and 3) and 11 points (Figure 6.10 and Table 6.7). Three areas show rather high heterogeneity. Fe content varied between 70.87%, 40.65% and 38.52%, Ca - between 0%, 5.33%, and 1.04%.

Chemical composition of relatively big (more than 40 µm) monolithic grain where the area 1 is located is very similar to the composition of fayalite Fe_2SiO_4 (FeO - 76% and SiO - 24%) contaminated by Zr (1.61%). Chemical composition of completely melted area 2, which has high content of all principal elements (Na, Al, Si, S, Ca and Fe) of red mud and blast furnace slag, seems to be the result of their combined melting and chemical interaction.

The area 3 is the contact zone between the fayalite grain (area 1) and the usual mixture of molten blast furnace slag and red mud (area 2). Points 7, 8, and 9 (Table 6.7) contain the same elements, but in very different percentage. This is the evidence of very high heterogeneity and strong chemical interaction.

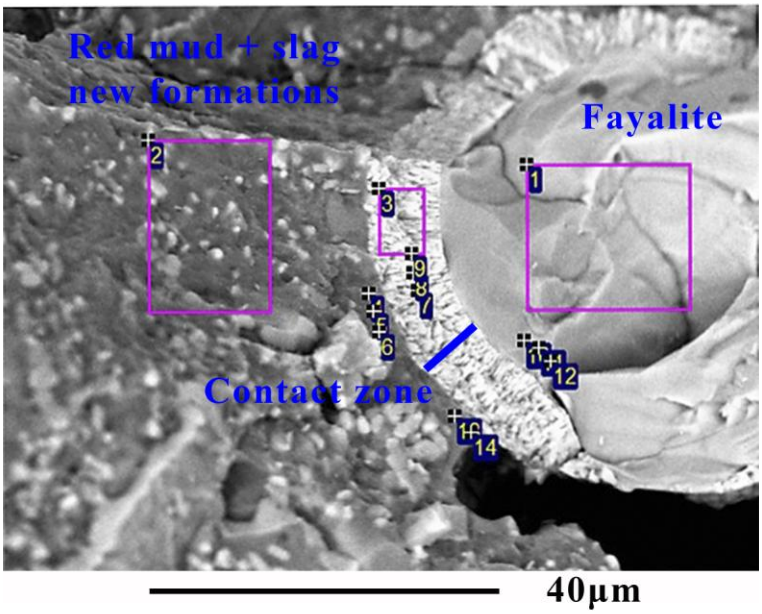

Figure 6.10 - EDS analysis of composition 14 after sintering at 1225°C.

Chemical compositions of the points 4, 5, 6, 13, and 14 at the locations between the areas 2 and 3 also indicate heterogeneity of chemical composition. Careful study of the boundary lines with zoom in on both sides of the contact zone between grain of fayalite and mixture of red mud with blast furnace slag shows absence of visible defects on these lines. There are no cracks or pores being detected in the zone of contact. It seems that both materials are strongly fused at a temperature of 1225°C and formed a new amorphous glass-like material.

Table 6.7 - Chemical composition of the composition 14 (Figure 6.10) by EDS method.

Areas	Chemical elements, wt.%												Total
Points	N	Na	Al	Si	S	Ca	Fe	Ni	Cu	Zn	Ba	Zr	
1	0.00	0.00	0.00	23.60	0.00	0.00	70.87	0.23	2.28	0.18	1.22	1.61	100.0
2	3.89	7.16	16.04	13.23	8.15	5.33	40.65	1.34	1.67	2.47	0.47	0.00	100.0
3	7.16	0.22	22.26	14.75	3.15	1.04	38.52	3.27	5.20	3.12	0.15	1.16	100.0
4	0.00	12.70	15.11	18.28	4.62	8.85	31.07	7.48	3.21	1.13	0.00	2.17	100.0
5	5.04	8.21	9.66	12.66	0.00	10.88	49.44	0.45	1.08	2.19	0.39	0.00	100.0
6	0.00	2.28	6.75	11.48	0.00	7.00	65.56	2.29	1.47	0.00	3.18	0.00	100.0
7	3.14	7.15	19.14	15.12	5.18	13.04	27.21	1.29	0.00	1.56	0.79	3.08	100.0
8	8.88	10.06	8.68	22.40	3.12	10.70	14.92	0.99	2.14	0.83	6.15	2.13	100.0
9	6.11	11.54	20.98	24.61	7.14	2.38	30.61	1.49	0.97	2.57	0.00	1.60	100.0
10	0.00	5.30	7.01	16.18	0.00	0.00	26.61	3.65	1.87	0.00	0.36	39.01	100.0
11	0.00	0.00	7.04	20.81	0.00	0.00	69.70	0.00	1.43	1.25	0.00	0.77	100.0
12	0.00	0.00	6.06	24.56	0.00	0.00	56.61	0.74	0.00	1.12	0.84	0.07	100.0
13	0.00	1.09	2.66	19.02	0.00	0.00	72.76	1.35	1.20	0.93	0.57	0.32	100.0
14	10.12	8.24	16.96	15.20	0.00	0.00	45.12	0.00	3.17	0.39	0.00	0.80	100.0
Max	10.12	12.70	22.26	24.61	8.15	13.04	72.76	3.65	5.20	3.12	6.15	39.01	
Min.	3.14	0.22	2.66	11.48	3.12	1.04	14.92	0.23	0.97	0.18	0.15	0.07	

Points 10, 11 and 12, which are located between the contact zone and the center of the fayalite grain, have demonstrated great similarity in chemical composition with fayalite.

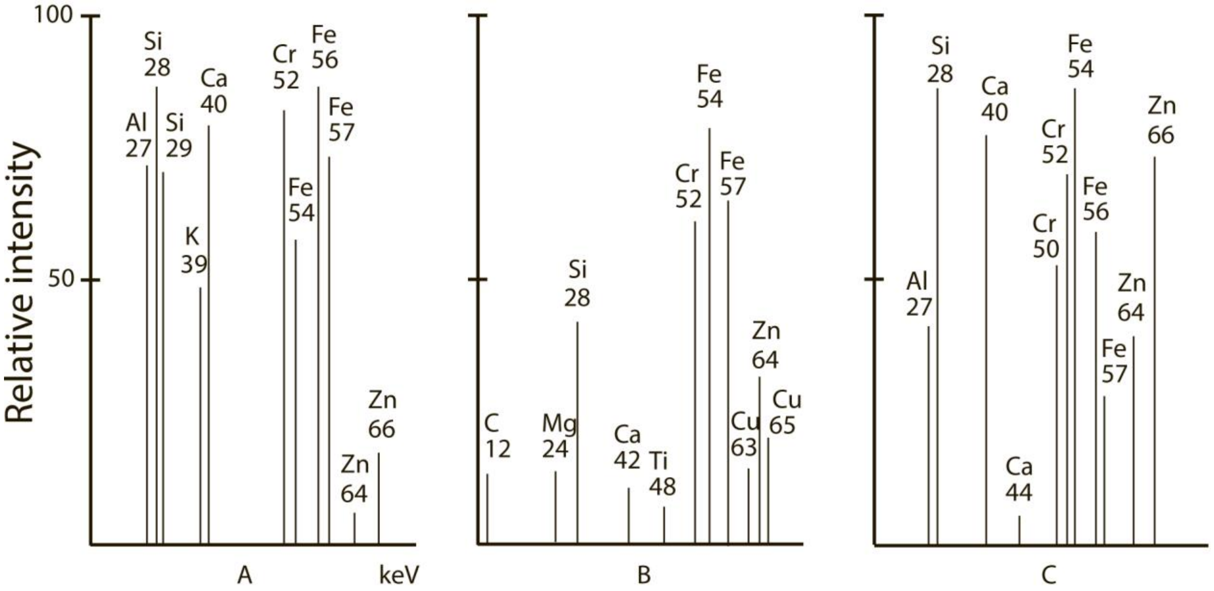

Figure 6.11 - Isotopes laser micro-mass analysis of new formations of composition 14 after sintering at 1225°C.

Similar results were obtained in isotopic compositions by laser micro-mass analyses (LAMMA) method. The sets of isotopes (Figure 6.11) and their percentage (peaks' height) also show a significant heterogeneity of compositions in the points for comparison.

6.2.6 Mapping the chemical states of an element inside the composition 14

The mapping the chemical states of an element inside the composition 14 obtained by tomographic X-ray absorption spectroscopy (Figure 6.12) demonstrates a high homogenization of the components. Only Na, Si and Fe tend to form agglomerates. This tendency was also identified in the composition 5 (Figure 6.5) for the elements Na, Al, Si and Fe.

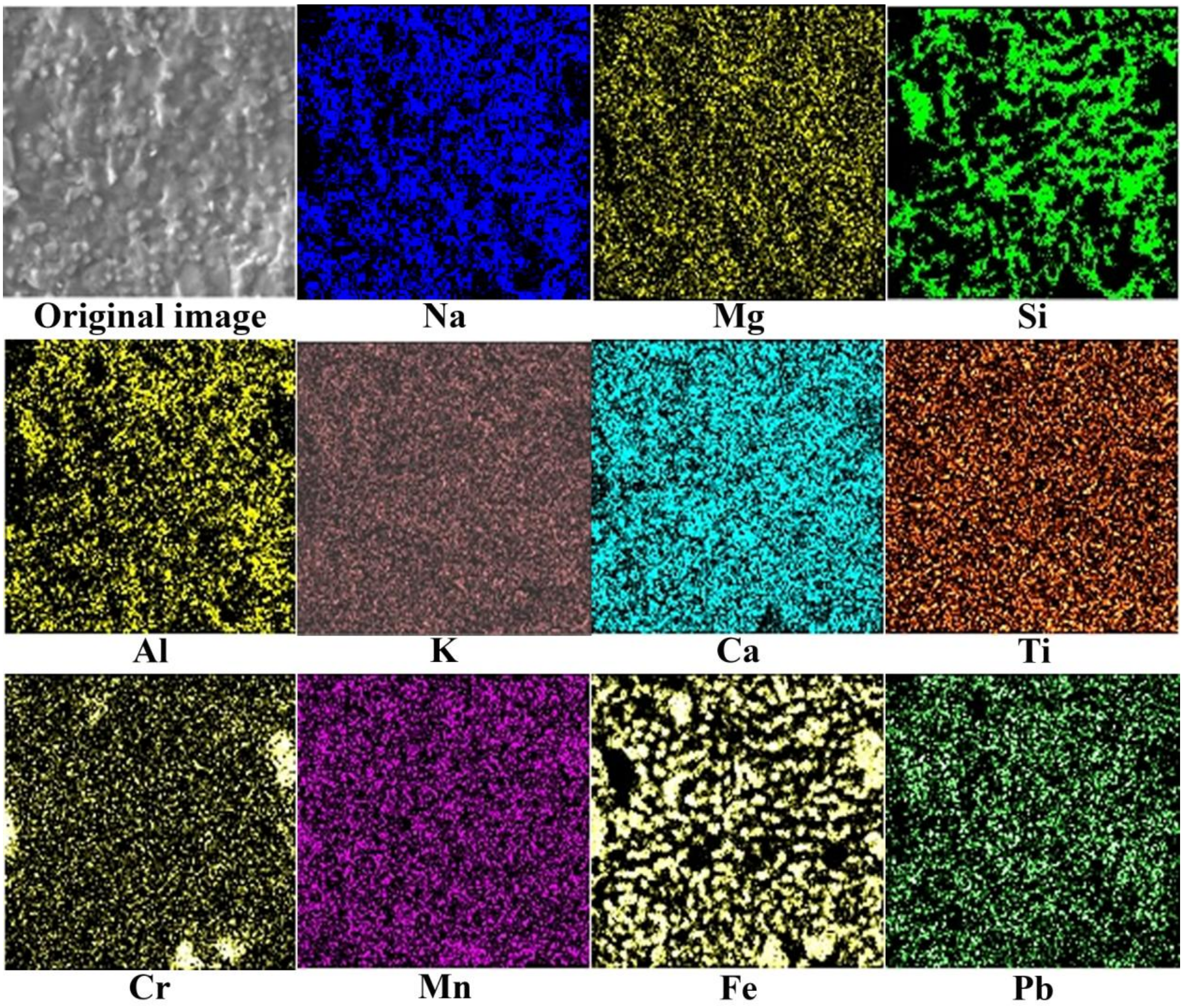

Figure 6.12 - Mapping the chemical states of an element inside a composition 14 sample (using tomographic X-ray absorption spectroscopy).

Mapping of the blast furnace slag as another component of the composition 14 (Figure 4.11) demonstrates a relatively uniform placement of elements in the samples without separate elements clots formation. Even very high (62.1%) iron content of the blast furnace slag is not the key factor of the clots formation, which is presented in Figure 6.12.

6.2.7 Thermochemical reactions in the composition 21

Replacement in the composition 12 of the 20% blast furnace slag by equal quantity of the wood ash creates the composition 21, which consists of: 60% red mud, 20% blast furnace slag, and 20% wood ash. Composition 21 presents further information on the role of blast furnace slag. It is important to analyze the result of interaction between wood ash (K_2O (22.8%) and CaO (28.2%)) and blast furnace slag. The chemical diversity, which has the composition 21, is the reason for active chemical reactions between the components.

Analysis of the thermochemical reactions of the composition 21 during heating is compared to similar reactions of its components (Figure 4.20, Figure 4.21 and Figure 4.24) allows identifying the following items of significant differences between them:

1. Endothermic effect of the composition 21 between 92°C and 211°C with a weight loss of 3.44% of the water is similar to endothermic effect of wood ash at 81-225°C with a weight loss of 4.36% of water (Figure 4.24). The reason is the evaporation of the pore and weakly bound water and gas output from wood ash resin.
2. The second endothermic effect between 211°C and 290°C is the result of removal of firmly bound water from all three components. At the same temperature takes place a decomposition of the wood ash lignin with combustion of the pyrolysis gases and the total weight loss 3.18%;
3. The first exothermic peak at 290°-622°C with the turning point at about 590°C is located on the place of the first exothermic effect of the blast furnace slag. The increase in weigh, which is demonstrated on thermogravimetric curve at this temperature, is 3.18% due to the coincidence of two exothermic effects. The first one is FeS_2 decomposition in the blast furnace slag with transition into $FeSO_4$ and combustion of the liberated SO_2. The second one is the beginning of coal combustion in wood ash. The total weight decrease on the thermogravimetric curve is 7.71%;
4. The second exothermic effect at 622°-1226°C and turning point at about 950°C is not similar to any of components. It is a product of the raw materials thermochemical interaction. Due to the serrated top of the exothermic peak, it would be rather more similar to the characteristic peak of endothermic effect of the waste glass (Figure 4.23), which indicates the process of crystallization from amorphous phase (**Figure 4.5**). In the composition 21 containing 60% red mud it may indicate the exothermic reactions with weight loss during the transitions $\gamma\text{-}Al_2O_3 \rightarrow \alpha\text{-}Al_2O_3$ and $Fe_3O_4 \rightarrow Fe$. This was previously investigated by Kimjashov (2010), who using the EDS method presented the conditions of phase equilibrium in the system Fe - Fe_2O_3 - SiO_2, Fe - Fe_3O_4 - $FeAl_2O_4$ at temperatures 827-1027°C and of the system Fe - Al - O at the temperatures 700°-1000°C.

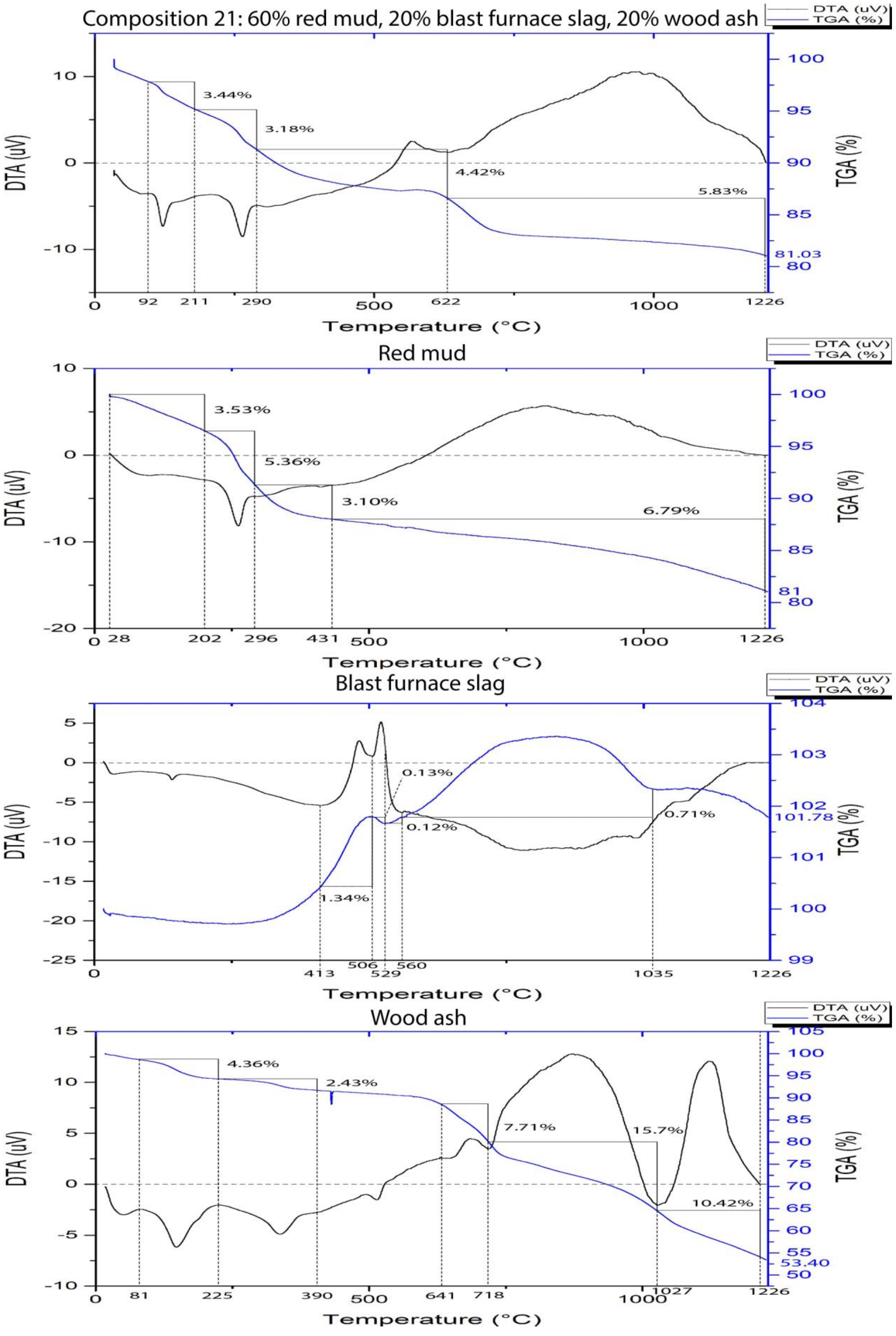

Figure 6.13 - DTA and TGA curves of composition 21.

Table 6.8 - The endothermic and exothermic effects of the composition 21 by DTA and TGA curves (Figure 6.13)

Thermo-chemical processes, temperature of reaction (°C) and weight loss (%)			
Endothermic effect 1. 92-211°C.	Endothermic effect 2. 211-290°C.	Exothermic effect 1. 290-622°C.	Exothermic effect 2. 622-1226°C.
1. Physically weakly bonded water 2. Output of gases and tar from wood ash. Total weight loss 3.44%	1. The collapse of the lignin 2. burning of pyrolysis of gases Total weight loss 3.18%	1.$FeS_2 \rightarrow FeSO_4 + SO_2$ burning 2. Start of coal combustion Total weight loss 4.42%	1. Dross formation Fe_3O_4 900-1000°C 2. Amorphous phase crystallization 3. Burning coal and decomposition, 718-1215°C. Total weight loss 5.83%

These processes are also complicated by the formation of dross Fe_3O_4 at 900-1000°C on the surface of iron and its interaction with atmospheric oxygen. At 718-1215°C in wood ash takes place flameless phase of smoldering cellulose coal, inevitable due to 29.9% loss on ignition of wood ash (Table 4.3). The total weight loss of the exothermic peak 2 is 5.83%.

With the increase of sintering temperature and the change of thermochemical reactions, the color of the samples also was changing (Figure 5.7). A pale red-brown at 800°C and 900°C, a bit more gray at 1000°C and 1050°C, at 1100°C brown with black dots, dark brown at 1150°C, and almost black at 1200°C.

The consistent behavior of all these thermochemical reactions creates ceramic structures with mechanical properties that exceed the requirements of the Brazilian standards. Maximal flexural strength of composition 21 (9.50 MPa) is achieved at 1150°C. At 1200°C the composition 21 reaches a maximum linear shrinkage of 10.14%, density - 1.93 g/cm^3 and water absorption - 8.25%.

6.2.8 Thermochemical reactions in the composition 20

The composition 20 consists of 60% red mud, 20% blast furnace slag, and 20% waste glass. Deciphering of DTA and TGA curves that characterize the thermochemical process of the composition 20 supposed to be easier than composition 21, as the behavior of waste glass should be more predictable than wood ash. The reason for this is the difference in chemical compositions of wood ash and waste glass (Table 4.3).

All three components have at low temperatures the endothermic peaks of different intensities, and therefore they are presented in the composition at 19°-188°C as the loss of weakly bonded water of all three raw materials. At the same time it is also loss of crystalline structures water of gibbsite $Al(OH)_3$ with its transition to boehmite in ɣ-$AlO(OH)_4$, that is typical to all compositions containing red mud. As a result the total weight loss is 6.21%.

Next endothermic effect at 188-291°C and 3.69% water loss is caused by the red mud, in which the removal of chemisorbed water takes place.

The exothermic effect is very smooth. It looks like the main course is presented by red mud, which is the main material of the composition, and there is a compromise between the DTA curves of blast furnace slag and waste glass.

The consequences of these thermochemical reactions during composition 20 sintering at 1150°C are the flexural strength of the samples - 9.67 MPa, the linear shrinkage - 10.62%, the density - 2.02 g/cm^3 and the water absorption - 3.43%.

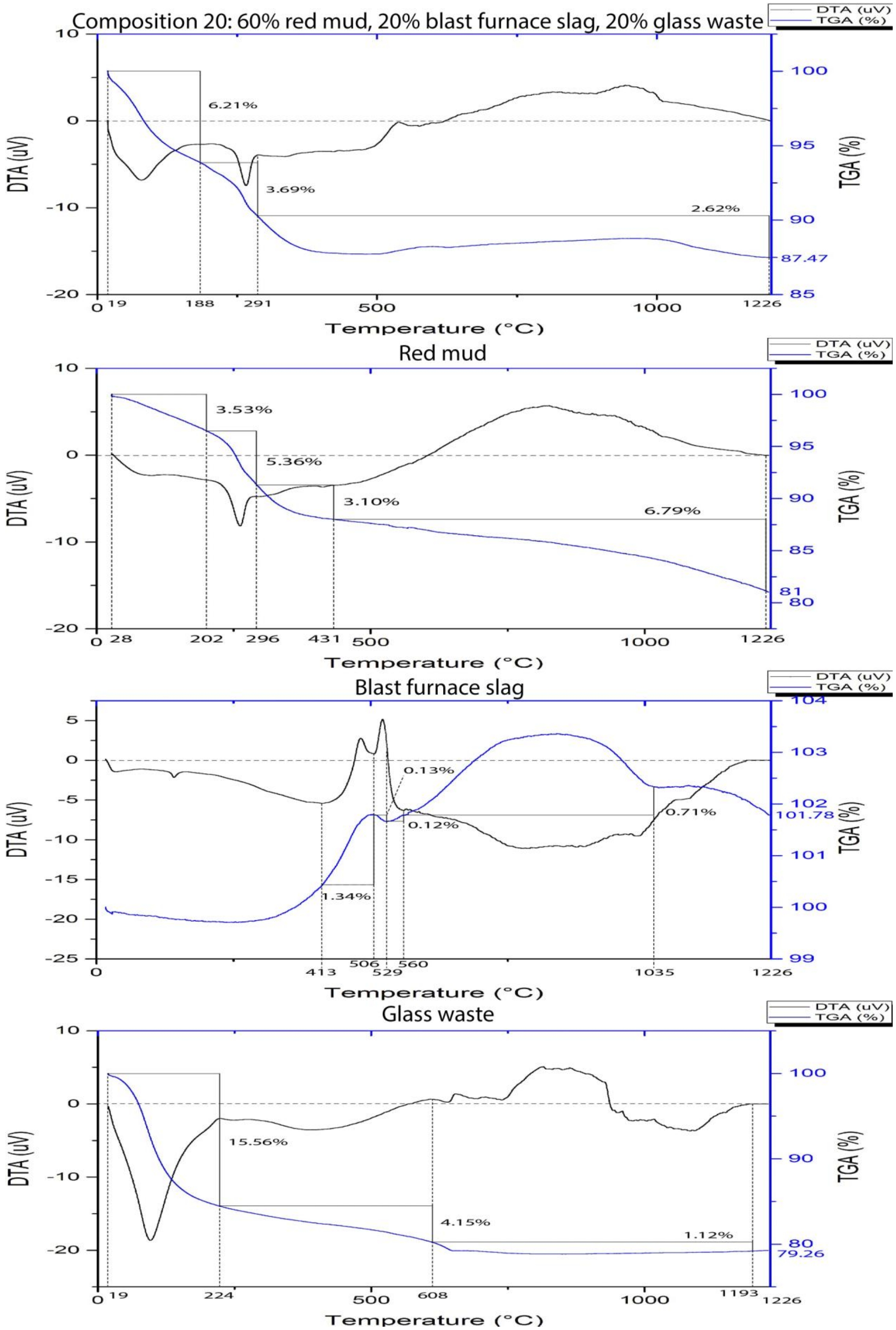

Figure 6.14 - DTA and TGA curves of composition 20.

Table 6.9 - The endothermic and exothermic effects of the composition 20 by DTA and TGA curves (Figure 6.14)

Thermo-chemical processes, temperature of reaction (°C) and weight loss (%)		
Endothermic effect 1. 19-188°C.	Endothermic effect 2. 188-291°C.	Exothermic effect 1. 291-1226°C.
Physically weakly bonded water. Weight loss 6.21%	Removal of chemisorbed water. Weight loss 3.69%	1. The formation of dross Fe_3O_4 at 900-1000°C 2. Waste glass crystallization of amorphous phase Weight loss 2.62%

There are three additional compositions that were characterized in terms of thermochemical reactions for improvement of analysis of composition 14. Composition 12 was studied to determine the impact of blast furnace slag. Composition 20 was studied to describe the interaction between red mud and blast furnace slag when waste glass is applied. And composition 21 was studied to determine the impact of chemically complex wood ash on blast furnace slag and their interaction.

Transformation of composition 14 into composition 12 decreases the thermochemical reactions to two endothermic and two exothermic effects of the DTA and TGA curves. Subsequent replacement in composition 12 of 20% blast furnace slag by 20% of waste glass makes the curves of DTA and TGA even smoother and more predictable. As a result there are two endothermic effects of weakly bonded and chemisorbed water. The only exothermic effect of the DTA and TGA curves shows the formation of dross Fe_3O_4 and amorphous phase crystallization of waste glass at 900-1000°C.

The replacement in composition 20 of 20% waste glass by 20% wood ash forms composition 21 and results in appearance of organic components with the demonstration of completely new thermochemical reactions. As a result there are intense thermochemical reactions: endothermic effect of the output of gases and tar from wood ash at 92-211°C, the endothermic effect of the lignin collapse, and pyrolysis of gases at 211-290°C. Two exothermic effects: the first one is burning of SO_2 and start of coal combustion at 290-622°C and the second one is formation of dross Fe_3O_4 and amorphous phase crystallization accompanied by coal burning and decomposition at 718°-1215°C.

6.3 STRUCTURE FORMATION PROCESSES OF COMPOSITION 15

Composition 15 like composition 14 is a key mixture of main materials. It consists of 50% red mud and 50% foundry sand. Analysis of structure formation process is one of the ways of further determination of red mud's and foundry sand's roles in the composition. Both components have equal contents and that is why composition 15 is fundamental for all compositions of the research, which contain these two materials.

Sintering temperatures for analysis were limited by 1150°C because at 1200°C the flexural strength began to decrease from 6.85 to 6.13 MPa. The reason for it is excessive melting of the samples.

6.3.1 Mineral transformation of the composition 15 at different temperatures

Due to the 50% content of foundry sand the highest crystalline peak at angle 2Θ = 26.6° and more than 4000 counts per second intensity after sintering at 1000°C (Figure 6.15 – A) and 3000 counts per second after 1150°C (Figure 6.15 – B) is quartz. The other peaks of quartz at 2Θ° = 45.8°, 50.1° and 54.9° have lower intensities. The peak at 2Θ° = 34.9° (Table 6.10), which is presented at 1000°C, disappeared with an increase of the temperature on the pattern at 1150°C. Strong reduction of all peaks intensity, including the principal peaks, means the decrease of crystalline quartz content. The reason for it is melting and transition to amorphous phase.

Both diffractogram patterns present high-temperature modification of quartz - cristobalite SiO_2. Probably, cristobalite was formed at the moment of contact of the foundry sand with liquid metal on the factory where foundry sand was obtained. Cristobalite is represented in Figure 6.15 by a lot of peaks, but only two of them, which are very weak, are free of coincidence at 2Θ = 22.0° and 27.2°. The first one was detected only after firing at 1150°C, and the second increased its intensity from 3.70% at 1000° to 5.38% at 1150°C. Probably the high firing temperature of the samples helps cristobalite not only to prevent melting, but to continue slow crystallization process despite alkaline environment of red mud.

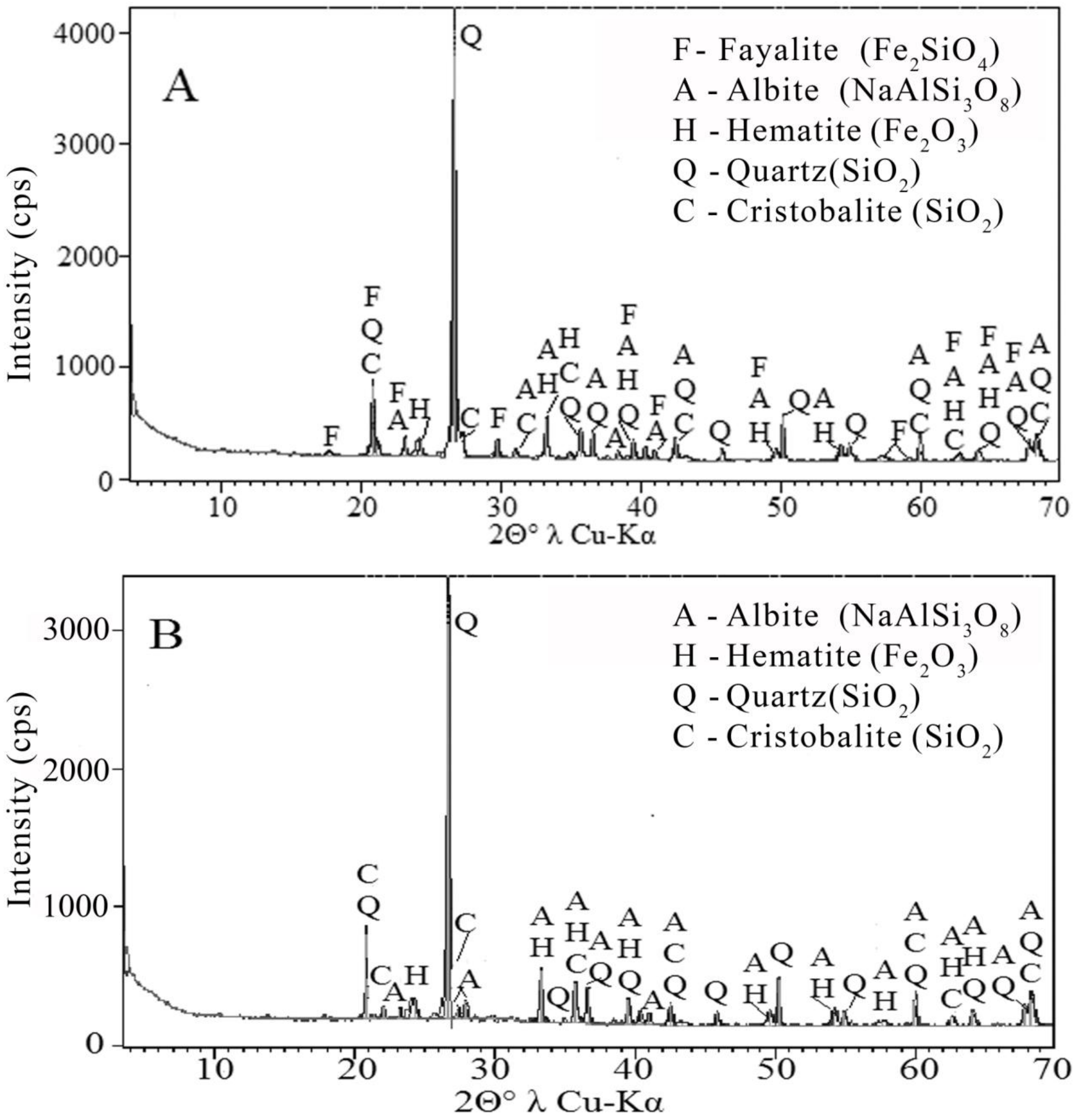

Figure 6.15 - Diffractogram pattern of the composition 15 at: A -1000°C and B – 1150°C.

Another important difference between the two difractogramas patterns Figure 6.15 A and B is the presence of rather weak, but free of the coincidence peaks of fayalite Fe_2SiO_4 at 2Θ° = 17.6° and 29.7° on the diffractogram A with disappearance on the diffractogram B. This process of fayalite peaks decrease during red mud sintering was already studied (Figure 6.1 and Table 6.1, Figure 6.6 and Table 6.4) and it continued to be mainly the same with small influence of other components. Only some small peak of albite at 2Θ° =23.1° (Table 6.10) show increase of intensity.

Table 6.10 - Changes of minerals peaks disposition (d, Å) and intensities (I, %) on diffractogram patterns of composition 15 after sintering at different temperatures (Figure 6.15).

2Θ°	Composition 15-1000°			Composition 15-1150°		
	d, Å	I, %	Mineral	d, Å	I, %	Mineral
17.60	5.00	0.94	F			F
20.80	4.20	16.45	Q; C	4.20	20.51	Q; C
21.10	4.20	2.39	Q; C			Q; C
22.00				4.00	3.23	C
23.10	3.80	4.48	A	3.80	5.92	A
24.20	3.60	3.88	H	3.60	5.02	H
26.60	3.30	100.0	Q	3.30	100.00	Q
27.20	3.20	3.70	C	3.20	5.38	C
29.70	3.00	4.27	F			F
31.00	2.88	2.04	A; C	3.25		A; C
33.20	2.69	9.64	A; H	2.69	12.48	A; H
34.90	2.56	1.40	Q			Q
35.60	2.51	6.96	A; H; C	2.51	9.87	A; H; C
36.50	2.45	6.16	Q; A	2.45	8.54	Q; A
38.30	2.34	1.97	A; C			A; C
39.40	2.28	4.89	Q; A; H	2.27	6.19	Q; A; H
40.30	2.23	3.27	Q; C	2.23	3.08	Q; C
40.90	2.20	2.25	A	2.20	2.86	A
42.50	2.12	5.30	Q; A; C	2.12	5.46	Q; A; C
43.20	2.09	1.24	A	2.08	0.85	A; H; C
45.80	1.98	4.89	Q	1.97	3.37	Q
49.60	1.83	2.84	A; H	1.83	3.64	A; H
50.10	1.81	10.56	Q	1.81	9.17	Q
54.20	1.68	3.60	A; H	1.69	3.92	A; H; C
54.90	1.67	4.06	Q	1.67	3.37	Q
57.10	1.61	1.04	Q; A	1.59	1.09	A; H; C
59.80	1.54	5.25	Q; A; C	1.54	6.14	Q; A; C
62.70	1.48	1.70	A; H; C	1.48	2.41	A; H; C
64.00	1.45	2.15	Q; A; H	1.45	3.32	Q; A; H
67.60	1.38	5.25	Q; A	1.38	5.06	Q; A
68.20	1.37	5.05	Q; A; C	1.37	6.39	Q; A; C

6.3.2 Thermochemical reactions in the composition 15

The coincidence of two large exothermic reactions of red mud (431°-1217°C) and foundry sand (595°-1225°C) seems to cause the exothermic effect, which is the reason for 7.61% weight loss.

Replacement of the blast furnace slag 50% (the composition 14) by 50% foundry sand (the composition 15) has negative impact on the mechanical properties of the samples. It might be caused by less active thermochemical reactions of structure formation of the composition 15. DTA and TGA curves (Figure 6.16) present only one endothermic and one exothermic peak. Endothermic peak of the composition 15 at 201-291°C and weight loss 4.69% indicates the removal of the free and weakly bound water.

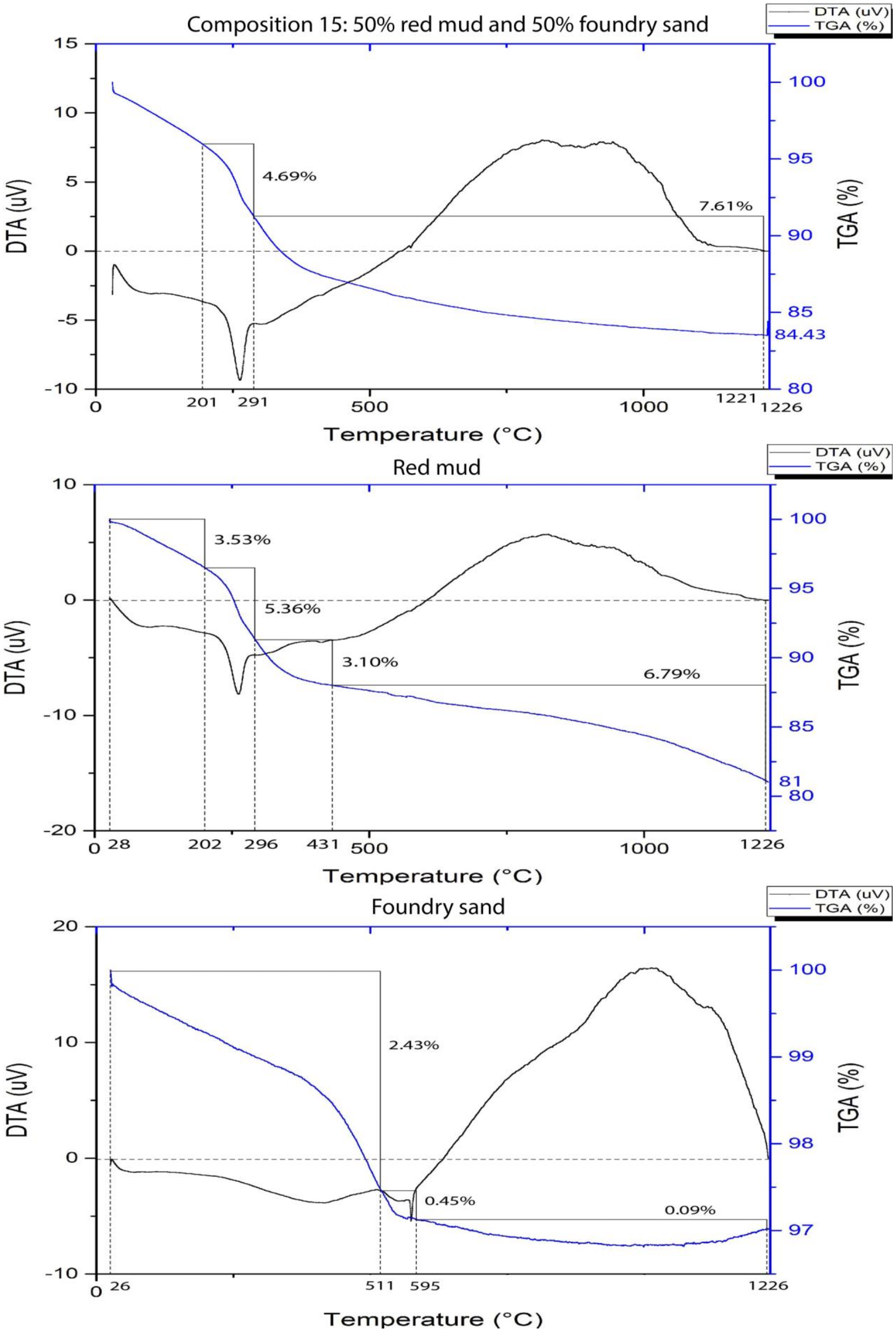

Figure 6.16 - DTA and TGA curves of composition 15.

Table 6.11 - The endothermic and exothermic effects of the composition 15 by DTA and TGA curves (Figure 6.16)

Thermo-chemical processes, temperature of reaction (°C) and weight loss (%)	
Endothermic effect 1. 201-291°C.	Exothermic effect 1. 291-1226°C.
Weight loss 4.69%.	Transformations $Al(OH)_3 \rightarrow \gamma$-$AlO(OH) \rightarrow \gamma$-$Al_2O_3 \rightarrow \alpha$-$Al_2O_3$. Weight loss 7.61%

This exothermic peak at 291-1226°C presents the formation of solid solutions of boehmite α-Al_2O_3, fayalite Fe_2SiO_4, hematite Fe_2O_3, albite $Na(AlSi_3O_8)$, quartz and cristobalite SiO_2 during sintering at 1225°C. The vast majority of these minerals is in the amorphous state (Figure 6.15 and Table 6.10). Some of them can transform in the crystalline state of solid solutions increasing exothermic effect. According to the experience that was gained working with materials of the research, deciphering the X-rays diffractograms usually presents the decrease in the intensity of the peaks as the firing temperature rises. The exception is albite $Na(AlSi_3O_8)$.

A decrease of intensity is not inconsistent with the idea of the formation of solid solutions of complex chemical and crystal-chemical systems. In the research the evidence (Figure 6.1 and Table 6.1) of coexistence of two transitions at the same time has already been presented when the composition 5 was analyzed. The same characteristics were found in terms of composition 15. That is why these two transitions form an idea of formation. The first transition is partial melting of almost all minerals of to a glassy amorphous state. The second one is synthesis of new crystalline bodies during cooling or improvement of crystalline structure of albite. The adoption of this idea of solid crystalline solutions synthesis facilitates the understanding of the processes, which take place. It also gives the reason for an increase of the mechanical properties.

The thermochemical reactions illustrate not only the changes of mechanical properties of the ceramics, but the color change of composition 15 (Figure 5.3) from aesthetically very attractive at low temperatures to red-brown at 1150°-1200°C and black at 1225°C. The rounding of the edges after firing at 1150°C, the bloating of the faces at 1200°C, blistered surfaces appearance at 1225°C mean the excessive melting of the samples. All these negative effects correlate with a sharp drop in the curve of DTA exothermic peak starting at 950° -1000°C with a weight loss of the samples.

Weight loss of the foundry sand samples is a result of the decomposition of organic binding components, which are added when molding form is prepared on the factory. The foundry sand composition always presents some combustible additives (peat, sawdust, coal dust or synthetic resins), plasticizers (usually refractory clay, such as kaolinite), refractory asbestos, cementing additives (gypsum, amon phosphate, silica sol, phosphate, ethyl silicate, etc.). All of them increase exothermic effect of the ceramics at high temperatures. This also inevitably increases the porosity of the ceramic structure.

As a result of thermochemical reactions the composition 15 has the highest flexural strength 6.85 MPa after firing at 1150°C, reducing the strength till 5.65 MPa at 1225°C. The linear shrinkage at 1150° reaches 7.82%, density - 2.07 g/cm^3 at 1150°C, and the water absorption is 2.77%.

6.3.3 Thermochemical reactions in the composition 22

The composition 22 consists of 60% red mud, 20% foundry sand, and 20% waste glass. It presented chemical interaction on the DTA and TGA curves (Figure 6.17) in the form of two small endothermic effects and one large exothermic effect. The first endothermic effect is located at 22°-201°C and shows the evaporation of pore and weakly bonded water as weight loss reaches 6.84%. The second endothermic effect takes place between 201°C and 285°C presenting 4.28% weight loss, which coincides at temperature and shape with red mud’s curve. It indicates the content in the composition 22 of crystal-bonded water from gibbsite $Al(OH)_3$ with its transition when heated to boehmite ɣ-$AlO(OH)_4$.

The rest of the thermal curve, at 285°-1266°C and the turning point at about 820°C, is exothermal effect with 5.18% weight loss. The form of this exothermic effect is a combination of the exothermic peaks of red mud, foundry sand and waste glass. In red mud takes place the transition of anhydrous boehmite ɣ-Al_2O_3 to α-Al_2O_3 at this temperature. In foundry sand there is the process of organic residues burning. Waste glass has the process of the amorphous phase crystallization. The result of these processes in composition 22 is that after firing at 1050°C composition begins to melt and loses its flexural strength at 1100°C from 5.93 to 5.75 MPa. It also forms at 1150°C rounded edges of the samples (Figure 5.8).

As a result of these processes the ceramics of composition 22 begins to change its color (Figure 5.8). It starts with a light brown at 800°C and dark brown at 1000°C and changes to muddy brown at 1050°C. At this temperature it also starts to have rounding of the edges of the samples. At 1100°C the color becomes almost black, all the surfaces of the samples are melted, rounded and shiny.

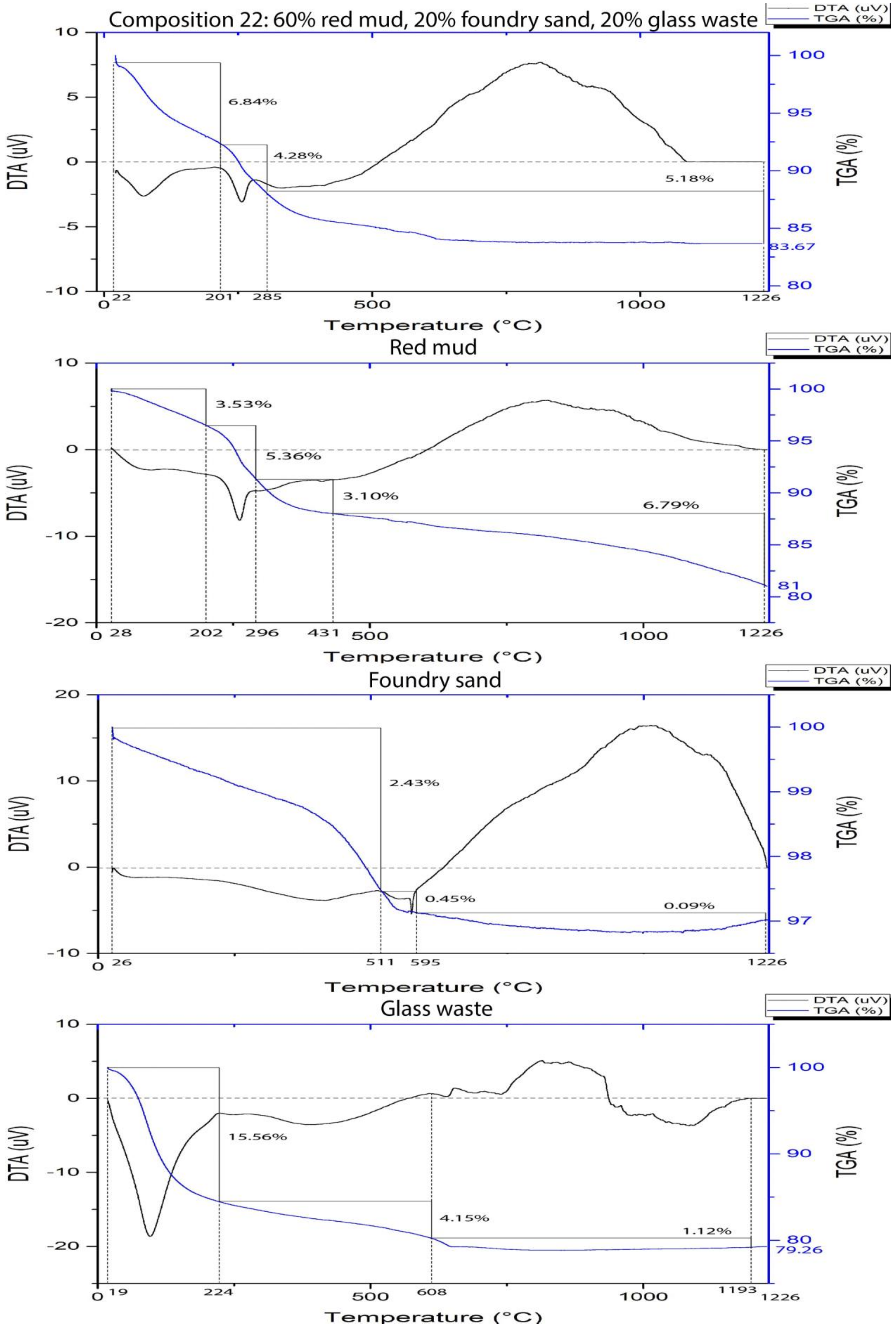

Figure 6.17 - DTA and TGA curves of composition 22.

Table 6.12 - The endothermic and exothermic effects of the composition 22 by DTA and TGA curves (Figure 6.17)

Thermo-chemical processes, temperature of reaction (°C) and weight loss (%)		
Endothermic effect 1. 22-201°C.	Endothermic effect 2. 201-285°C.	Exothermic effect 1. 285-1226°C.
Physically weakly bonded water Weight loss 6.84%	Removal of chemisorbed water. Weight loss 4.28%	γ-$Al_2O_3 \rightarrow$ α- Al_2O_3 Burning of organic material in foundry sand. Crystallization of amorphous phase of waste glass. Weight loss 5.18%

All these changes happened due to the thermochemical interactions of the raw materials at different temperatures. The result of these thermal effects is mechanical properties of the samples. The flexural strength reached 5.93 MPa at 1050°C, linear shrinkage - 10.32%, density - 1.81 g/cm^3, and water absorption was 2.61%. Such low result of water absorption means nearly complete pore closing by molten amorphous structure with a small inclusion of crystalline phase.

6.3.4 Morphological structure development of the composition 15

Analysis of the composition 15 ceramics by scanning electron microscopy (Figure 6.18) presents a significant difference of micro structure after firing at 1000°C, 1150°C and 1225°C. There are large grains of foundry sand in the samples of composition 15 after firing at 1000°C (Figure 6.18 - A, B and C), which are surrounded by sintered shapeless agglomerates of fine particles of red mud. Between them are often presented large pores and many grains of foundry sand, which have little or no contact with the red mud and this is the reason for low flexural strength (2.13 MPa) of the samples at 1000°C.

The area of the pores decreases slightly on the Figure 6.18 - D, E and F after firing at 1150°C, and significantly increases the number of monolithic melted components (Figure 6.18 - E.). Many particles of red mud also melted (Figure 6.18 - F). In general, these effects increased the flexural strength of the samples to 6.85 MPa.

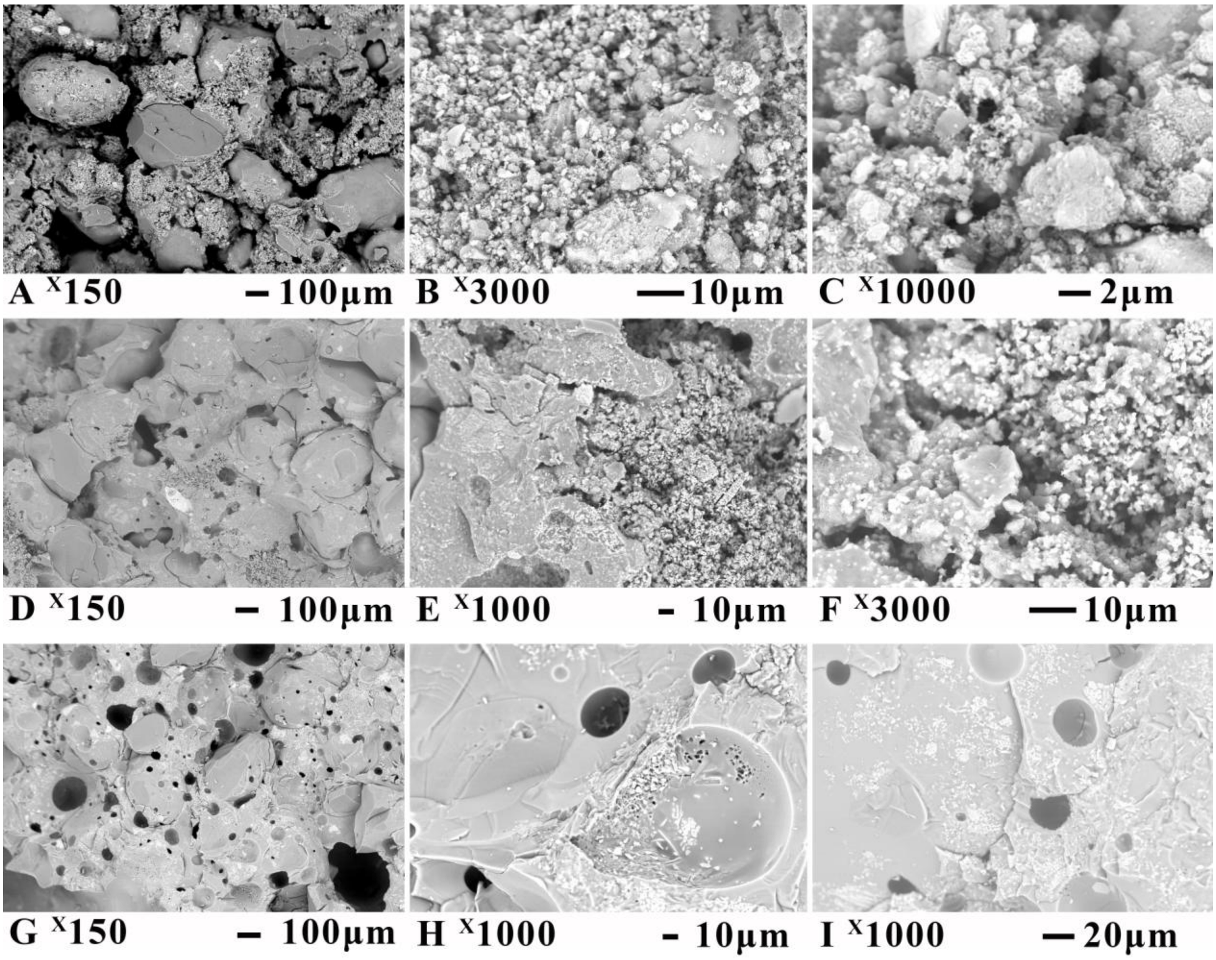

Figure 6.18 - SEM micro images of composition 15 after sintering at: 1000°C - A, B and C; 1150°C - D, E and F; 1225°C - G, H and I.

More intense melting of the samples at 1225°C made almost all pores disappear (Figure 6.18 - G, H and I). Foundry sand particles become covered with molten red mud.

On the surface of the molten materials there are hemispherical pores of gas micro-bubbles. They were formed during the chemical interaction of the initial components, or during the combustion of organic substances of components, and release of CO_2 carbonates.

6.3.5 Micro-chemical analysis of new formations in the composition 15

The results of chemical analysis of particles surfaces (Figure 6.19) confirmed the idea that these big particles in shape of grains are the particles of the foundry sand. Chemical composition demonstrated content of Si in terms of 81.37% and 64.78% in two areas (Table 6.13).

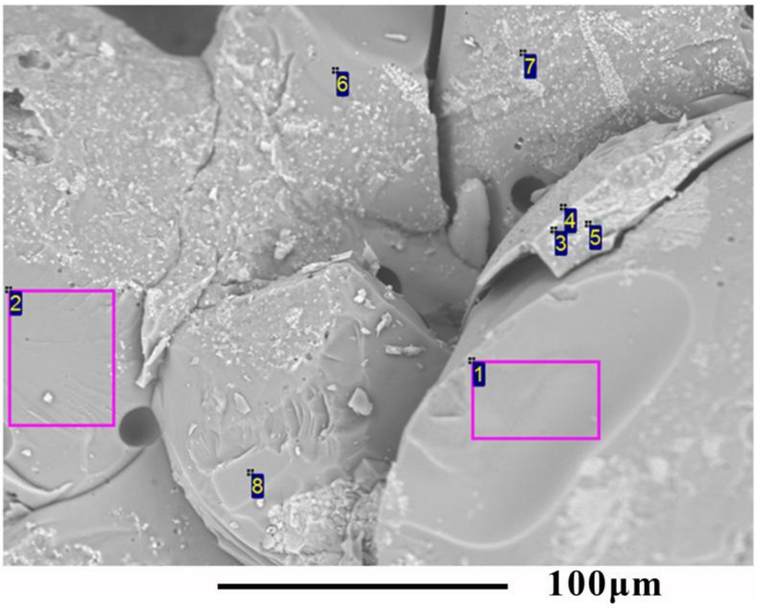

Figure 6.19 - EDS analysis of composition 15 after sintering at 1225°C.

There is high heterogeneity of the elements according to the results of the Table 6.13. The content of each element varies significantly. For example, Al varied between 2.63% and 22.91%, Si varied between 17.60% and 81.37%. The content of Fe also was not uniform between 8.41% and 62.49%.

Table 6.13 - Chemical composition of the composition 15 (Figure 6.19) by EDS method.

Area or point	Chemical elements contents, wt.%								Total
	Na	Al	Si	S	K	Ca	Ti	Fe	
1	6.21	2.63	81.37	0.00	0.44	0.95	0.00	8.41	100.00
2	9.98	9.29	64.78	0.00	1.02	1.46	1.65	11.82	100.00
3	8.40	11.55	25.36	0.00	0.00	3.13	2.39	49.17	100.00
4	16.04	19.42	38.68	0.00	0.32	3.22	0.84	21.49	100.00
5	7.19	10.46	17.60	0.00	0.00	0.87	1.40	62.49	100.00
6	9.51	10.53	67.93	0.00	0.97	0.80	0.96	9.31	100.00
7	11.23	22.91	41.14	2.95	0.00	9.38	0.70	11.70	100.00
8	9.14	8.38	65.15	0.00	0.75	2.48	3.68	10.43	100.00
Max.	16.04	22.91	81.37	2.95	1.02	9.38	3.68	62.49	
Min.	6.21	2.63	17.60	2.95	0.32	0.80	0.70	8.41	

Another analysis to prove heterogeneity is micro-mass analysis of the surface layer of vapor tumors under the influence of a laser beam (Figure 6.20).

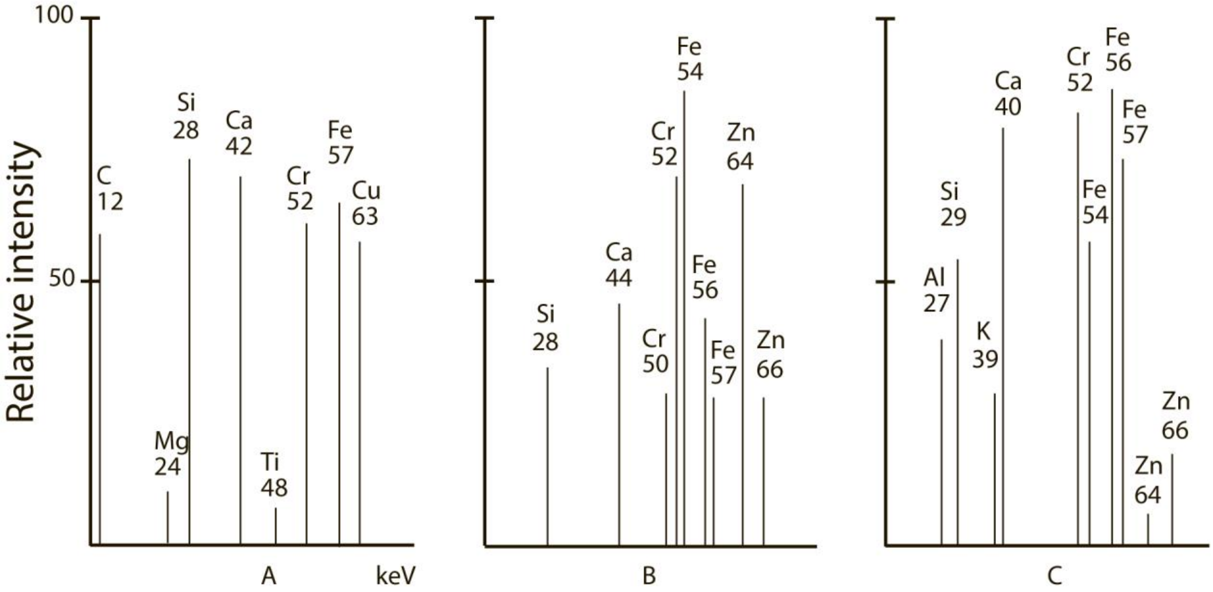

Figure 6.20 - Isotopes laser micro-mass analysis of new formations of the composition 15 after sintering at 1225°C.

Automatic exchange rate span of these micro-particles on their mass spectrum of isotopes gives vaporized point. Matching isotope composition shows a very large difference in the isotope in each set of adjacent sample points and their percentages expressing the intensity of each peak isotope.

6.3.6 Mapping the chemical states of an element inside the composition 15

Analysis by tomographic X-ray absorption spectroscopy method (Figure 6.21) of almost perfectly flat surface demonstrated rather large degree of homogenization of the chemical elements in composition 15. This information was obtained by testing the degree of uniformity of the distribution of chemical elements after firing the sample at 1150°C.

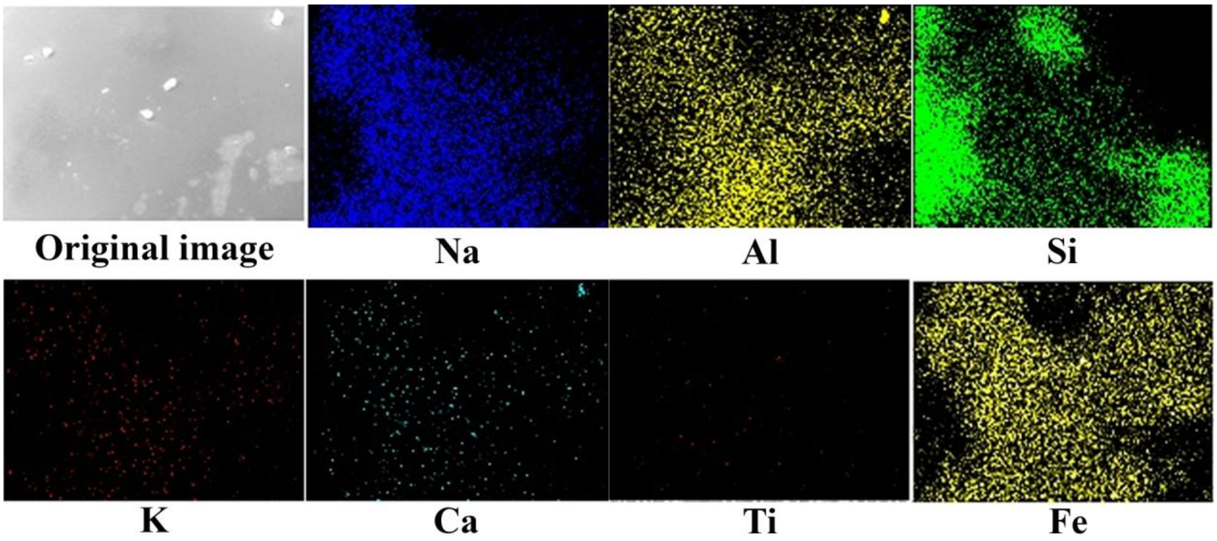
Original image
Na
Al
Si
K
Ca
Ti
Fe

Figure 6.21 - Mapping the chemical states of an element inside a composition 15 sample (using tomographic X-ray absorption spectroscopy).

The densest distribution of chemical elements is Fe content in both components of the mixture, as well as Al and Na, apparently due to their high content. The most uneven distribution of elements observed in Si. The most uniform - Ca and K. The rarest - Ti, that corresponds its minimum content among the elements presented in the graphs Figure 6.21.

6.4 STRUCTURE FORMATION PROCESSES OF COMPOSITION 24

The reason for studying physicochemical processes in composition 24 was that containing only two components it presented high flexural strength at low temperature. To specify composition 24 consists of 80% red mud and 20% waste glass. At 1100°C it presented 14.07MPa flexural strength. The aim of this part of study was to understand the influence of waste glass on the structure formation processes of red mud as the main material of this research.

6.4.1 Mineral transformation of the composition 24 at different temperatures

Due to high content of red mud the mineral composition of red mud must play a decisive role in raw mix and in tendencies during firing. Red mud mainly consists (Figure 4.2) of amorphous substances with inclusions of hematite Fe_2O_3, bauxite $Al_2O_3 \cdot nH_2O$, quartz SiO_2, and magnetite Fe_3O_4. Waste glass also mainly consists of (Figure 4.5) amorphous glass with small inclusion of quartz SiO_2.

As a result of firing of composition 24 at 1000°C in the XRD pattern Figure 6.22 - A appear minerals fayalite Fe_2SiO_4, nepheline $Na_2O \cdot Al_2O_3 \cdot 2SiO_2$, and albite $NaAlSi_3O_8$. It means that bauxite Al_2O_3•nH_2O, hematite Fe_2O_3, magnetite Fe_3O_4 and quartz SiO_2, which were presented in the red mud before firing, completely disappeared. Obviously, very high iron content (29.9% of red mud (Table 4.3)) made part of fayalite Fe_2SiO_4, and aluminum (21.2%) created nepheline Na_2O•Al_2O_3•2SiO_2 and albite $NaAlSi_3O_8$. Quartz SiO_2 is presented in the composition of all three minerals.

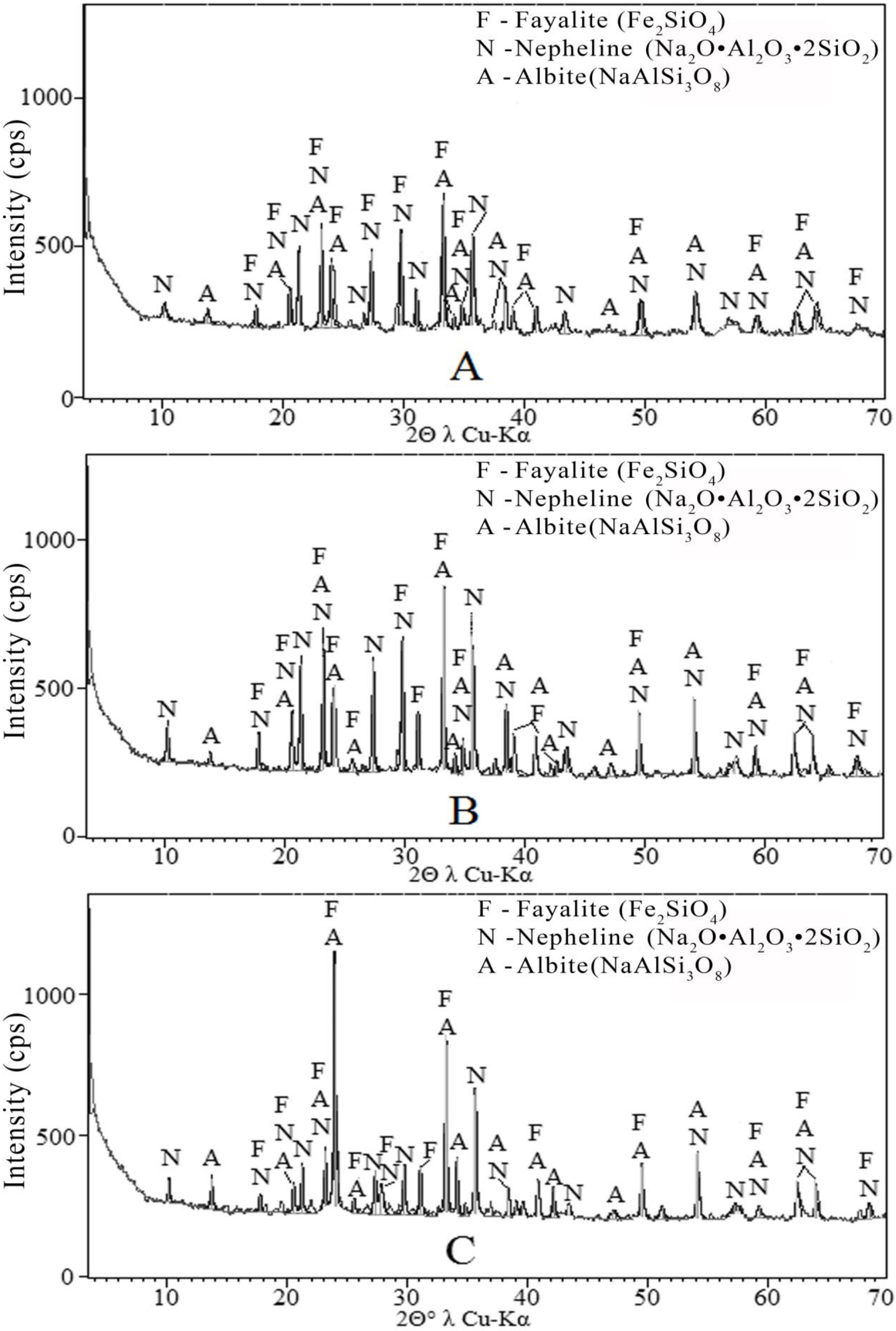

Figure 6.22 - Diffractogram pattern of the composition 24 at: A - 1000°C, B – 1100°C and C – 1150°C.

The content of amorphous phase is high, and intensity of minerals' peaks is low after firing at 1000°C (Figure 6.22 - A). As the firing temperature is rising up to 1100°C and 1150°C (Figure 6.22 - B and C) the intensity of peaks increases.

The heating of composition 24 at temperatures between 1000°C and 1150°C did not present any difference in terms of mineralogical composition. There might be some differences, but as they have not appeared it means that these minerals were within the sensitivity of the XRD method (about 5wt.%). The only that have changed is the amount of each mineral and amorphous material (Table 6.14).

Table 6.14 - Changes of minerals peaks disposition (d, Å) and intensities (I, %) on diffractogram patterns of composition 24 after sintering at different temperatures (Figure 6.22).

	Composition 24-1000°			Composition 24-1100°			Composition 24-1150°		
	d, Å	I, %	Symbol	d, Å	I, %	Symbol	d, Å	I, %	Symbol
10.10	8.60	10.89	N	8.60	19.75	N	8.60	8.93	N
13.70	6.40	7.51	A	6.40	8.59	A	6.40	12.63	A
17.70	4.90	15.15	F; N	4.90	19.16	F; N	4.90	6.70	F; N
20.50	4.30	28.72	F; A; N	4.30	30.70	F; A; N	4.30	11.16	F; A; N
21.20	4.10	57.50	N	4.10	57.93	N	4.10	18.99	N
23.10	3.80	74.52	F; A; N	3.80	73.07	F; A; N	3.80	25.02	F; A; N
23.90	3.70	49.29	F; A	3.70	40.78	A; F	3.70	100.0	A; F
25.50				3.40	5.66	F; A	3.40	5.96	F; A
27.20	3.20	57.90	N	3.20	59.76	N	3.20	18.25	N
						F; N	3.20	11.06	F; N
27.70	2.99	73.39	F; N	2.90	71.88	F; N	3.00	20.05	F; N
29.70	2.88	31.42	F; N	2.87	32.50	N	2.87	19.45	N
33.20	2.69	100.0	F; A	2.69	100.0	F; A	2.69	68.64	F; A
34.10	2.62	12.80	A	2.61	13.02	A	2.62	23.14	A
34.80	2.57	22.42	F; A; N	2.57	19.08	F; A; N	2.57	5.18	F; A; N
35.60	2.51	72.92	N	2.51	78.42	N	2.51	51.23	N
38.40	2.34	33.96	A; N	2.33	37.81	A; N	2.34	12.19	A; N
39.00	2.30	22.03	F; A; N	2.30	9.99	F; A; N	2.30	6.44	F; A; N
39.60							2.27	5.82	A
40.80	2.19	20.07	F; A	2.20	22.67	F; A	2.20	15.06	F; A
42.10							2.14	12.12	A
43.40	2.08	16.37	N	2.07	17.87	N	2.08	5.28	N
47.10				1.92	3.56	A	1.92	6.49	A
49.50	1.83	25.07	F; A; N	1.83	33.22	F; A; N	1.83	22.46	F; A; N
54.10	1.69	31.49	A; N	1.69	40.93	A; N	1.69	26.76	A; N
57.20				1.60	7.21	N	1.60	5.64	N
59.20	1.55	15.46	F; A; N	1.55	13.87	F; A; N	1.55	4.63	F; A; N
62.40	1.48	21.72	F; A; N	1.48	19.75	F; A; N	1.48	14.48	F; A; N
63.90	1.44	20.18	F; A; N	1.45	16.21	F; A; N	1.45	13.33	F; A; N
68.40				1.38	7.92	F; N	1.37	5.31	F; N

Five peaks of nepheline at 2Θ° = 10.1°, 21.2°, 27.2°, 35.6° and 43.4°, which are free of coincidence with the peaks of others minerals, are growing up with increase of sintering temperature to 1100°C. It means additional synthesis of this mineral or significant perfection of its crystalline structure. The sixth free peak of nepheline at 2Θ° = 57.2° appeared on the XRD pattern at 1100°C with I = 7.21°. At 1150°C all of them have decreased significantly because the melting point of nepheline is 1200°C, and the high content of fluxes in red mud decreased the total melting point of the components. At the same time flexural strength of the samples decreased nearly 5-fold (from 14.07 to 3.06 MPa, Table 5.1), which means almost complete melting of the samples at the temperature 1150°C. The only mineral, which is slowly increasing the intensity of two peaks between 1000°C and 1150°C is albite at 2Θ° = 13.7° and 34.1°. After sintering at 1150°C their intensity increased 1.5 – 2 times.

On the basis of the results from the Table 6.4 (composition 14 consisting of 50% red mud and 50% blast furnace slag) and the Table 6.10 (composition 15 consisting of 50% red mud and 50% foundry sand), it can be confidently assumed that with increase of the firing temperature intensity of fayalite peaks is reducing.

Comparison of two sets of XRD patterns – of red mud only (composition 5, Figure 6.1) and the same red mud, but with 20% waste glasss (composition 24, Figure 6.22) presented the information about the role of waste glass. In composition 24 it is participating in synthesis of nepheline $Na_2O \bullet Al_2O_3 \bullet 2SiO_2$.

6.4.2 Thermochemical reactions in the composition 24

Composition 24 consists of 80% red mud and 20% waste glass. Due to this fact, thermal characteristics of the red mud have significant impact in the thermochemical reactions in the composition 24 during thermal analysis. The first endothermic effect at 28°-202°C in red mud, and at 19°-224°C in waste glass results in endothermic effect in composition 24 at 32°-162°C and weight loss 7.02%.

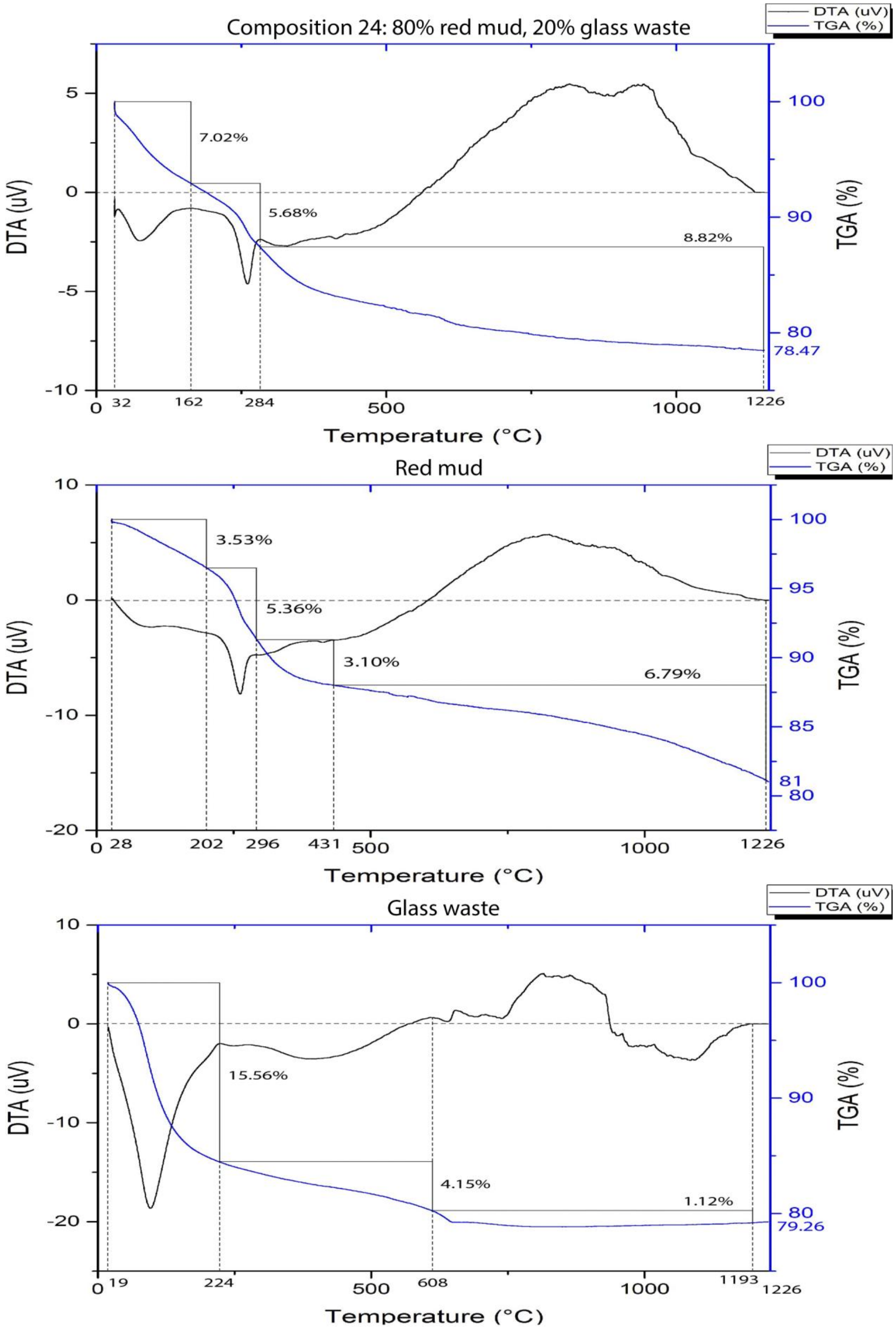

Figure 6.23 - DTA and TGA curves of composition 24.

Table 6.15 - The endothermic and exothermic effects of the composition 24 by DTA and TGA curves (Figure 6.23)

Thermo-chemical processes, temperature of reaction (°C) and weight loss (%)		
Endothermic effect 1. 32-162°C.	Endothermic effect 2. 162-284°C.	Exothermic effect 1. 284-1225°C.
Physically weakly bonded water evaporation Weight loss 7.02%	Removal of chemisorbed water Weight loss 5.68%	γ-$Al_2O_3 \rightarrow \alpha$-$Al_2O_3$ Burning of organic material in foundry sand. Crystallization of amorphous phase of waste glass. Weight loss 8.82%

The second endothermic effect of composition 24 presents weight loss of 5.86% at 162°-284°C and is the result of removal of strongly bonded and chemisorbed water. It comes from the red mud, as the waste glass has very weak endothermic effect at this temperature with the turning point near 450°C.

Exothermic effect of composition 24 at the temperature 284°-1225°C has a two-headed structure and weight loss 8.82%. It is actually a sum of two exothermic effects at this temperature of the red mud and waste glass. As has been mentioned above, in the red mud exothermic effect is caused by the transition of anhydrous boehmite γ-Al_2O_3 to α-Al_2O_3. In waste glass crystallization process of an amorphous phase takes place.

Samples color changes (Figure 5.5) during sintering of composition 24 from red-brown after firing at 1000°C to brown at 1150°C. There is no evidence of surface melting. As a result of these processes increases the flexural strength of samples to 14.07 MPa at 1100°C and decreases till 3.06 MPa at 1150°C. At 1100°C linear shrinkage reaches 11.87%, density - 1.66 g/cm^3, water absorption - 10.61%.

6.4.3 Morphological structure development of the composition 24

The comparison of the microstructures of the composition 24 (Figure 6.24) shows a great influence of firing temperatures on the mechanical properties of the material. After sintering at 1000°C, images of the ceramics at higher magnification (Figure 6.24 - B and C) present great quantity of pores between grains. There is little amount of melted material that supposed to bind grains together. That is why flexural strength at 1000°C of composition 24 is only 4.30 MPa.

The amount of melted material increased after sintering at 1100°C (Figure 6.24 - D, E and F). There is still relatively big quantity of closed and opened pores, but flexural strength of the ceramics reached the maximal result 14.07 MPa.

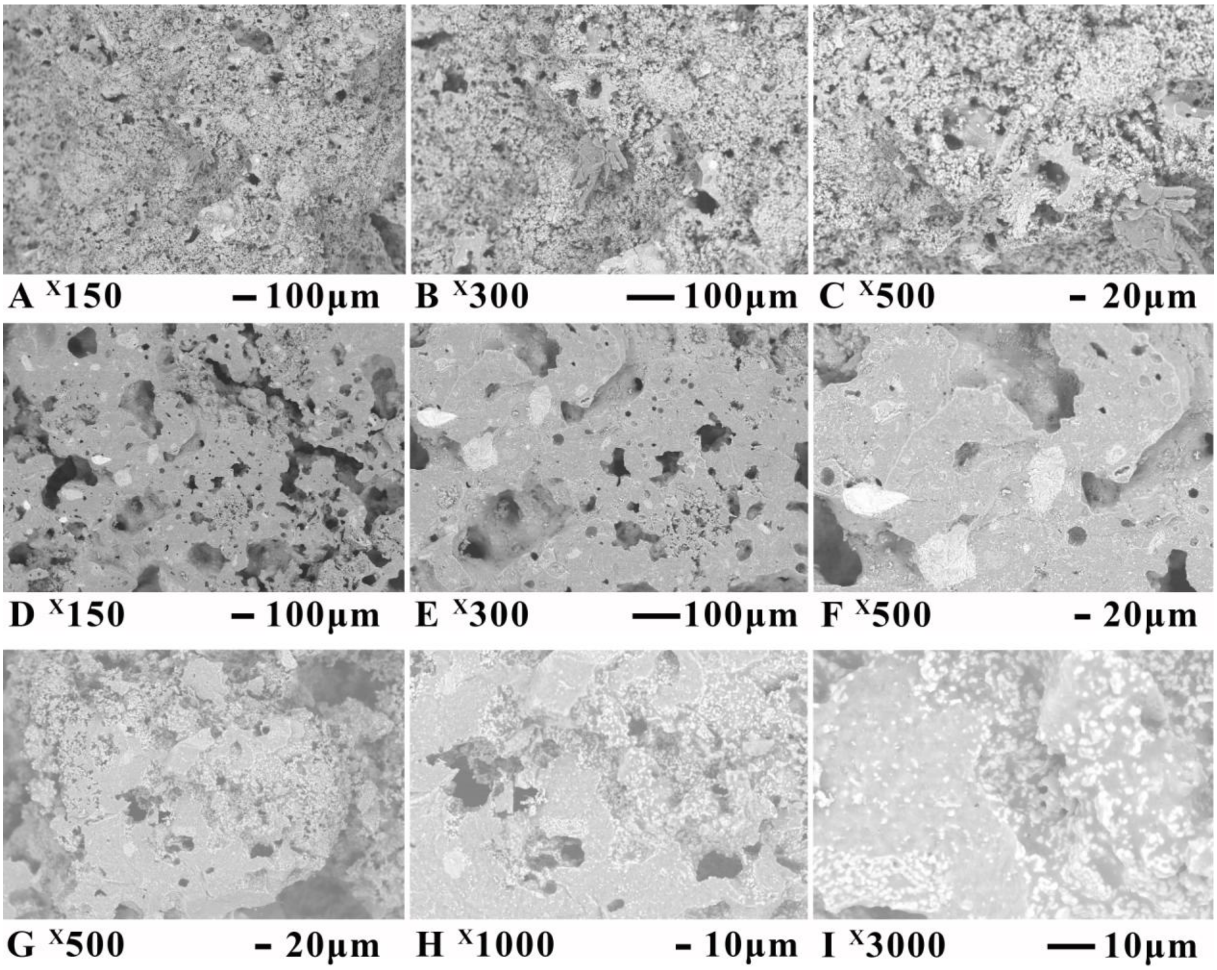

Figure 6.24 - SEM micro images of composition 24 after sintering at: 1000°C - A, B and C; 1100°C - D, E and F; 1150°C - G, H and I.

The images (Figure 6.24 - G, H and I), which show the structure of the sample as it received excessive heating, present sharp reduction of molten area and the appearance of a great number of small pores. The difference in the structure is the reason for the decrease of the flexural strength from 14.07 MPa at 1100°C to 3.06 MPa at 1150°C.

6.4.4 Micro-chemical analysis of new formations in the composition 24

Micro-chemical analysis of new formations in the composition 24 after sintering at 1100°C were realized by EDS and LAMMA method. Figure 6.25 presents the location of the areas and points on the SEM image. The common chemical composition of total area 1 contains practically all chemical elements of the mixed raw materials (red mud and waste glass). Chemical composition of the area 2 is rather similar to albite $NaAlSi_3O_8$ with the inclusion of a large number of pollutants. At the same time the presence of very deep holes of the exhaust gases on the surface of the material might be the evidence that this is not a grain of albite, but that this is a new melted formation.

Analysis of the 9 points in different places of the surface presents a significant difference of the chemical compositions of the closest and remote points. The reason for it is chemical and physical interaction between components and synthesis of new amorphous glass-like formation. All these processes take place as the sample starts to melt and gain flexural strength.

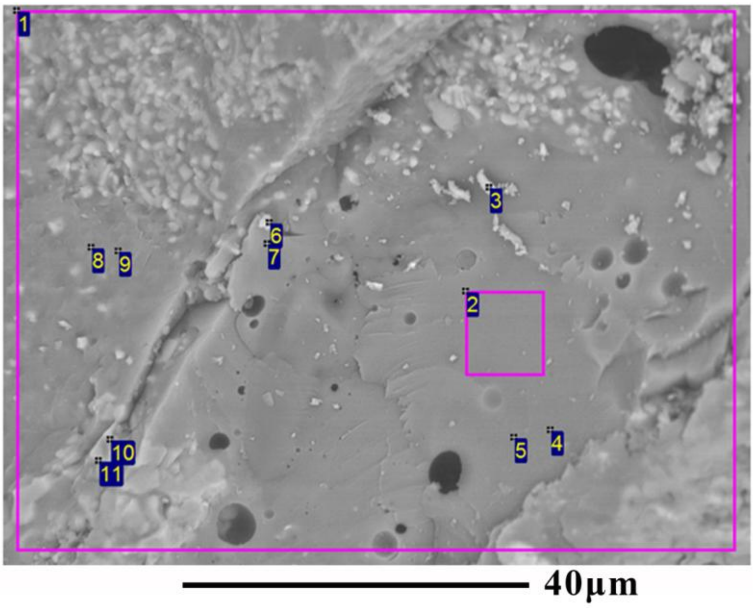

Figure 6.25 - EDS analysis of composition 24 after sintering at 1150°C.

Total area 1 of the Figure 6.25 differs from the small area 2 in content of Na (12.59% and 4.04%), Si (41.01% and 66.60%), Ti (4.52% and 0.92%), and Fe (25.75% and 9.72%). All of the 9 analyzed points of the Table 6.16 did not demonstrate any similarity in practically all chemical elements contents. The exception is point 4 and 5, which are located close to each other on a very smooth surface. The only difference between them is the content of Ni (0 and 6.37%). The reason for it might be micro particle on surface of the sample with high Ni content, which plays a role of a pollutant.

Table 6.16 - Chemical composition of the composition 24 (Figure 6.25) by EDS method.

Areas	Chemical elements contents (wt.%) of the composition 24												Total
points	Na	Al	Si	K	Ca	Ti	Fe	Ni	Cu	Zn	Ba	Pb	
1	12.59	9.15	41.01	1.07	2.28	4.52	25.75	0.12	0.66	2.24	0.17	0.44	100.0
2	4.04	8.01	66.60	2.17	1.26	0.92	9.72	1.34	0.87	2.33	2.48	0.26	100.0
3	15.94	15.35	48.51	1.04	3.62	0.00	8.51	3.28	3.29	0.00	0.45	0.00	100.0
4	9.45	8.98	61.05	2.16	1.32	1.00	10.54	0.00	1.89	0.93	1.31	1.37	100.0
5	9.51	8.86	58.02	2.38	0.99	0.86	10.72	6.37	0.57	1.12	0.34	0.26	100.0
6	3.36	11.08	55.34	2.71	3.60	1.00	19.12	0.57	2.14	0.00	0.11	0.97	100.0
7	7.60	8.82	47.42	2.46	3.54	0.82	19.10	0.33	4.18	0.00	3.48	2.25	100.0
8	17.52	18.23	47.41	1.13	5.02	0.58	7.85	0.00	0.57	1.69	0.00	0.00	100.0
9	5.10	17.46	54.18	1.69	3.94	0.83	8.20	2.90	0.66	1.37	0.00	3.67	100.0
10	7.92	7.48	26.41	0.75	0.98	14.72	31.28	4.50	2.41	0.64	1.18	1.73	100.0
11	9.92	6.44	19.06	0.97	0.84	34.61	19.15	3.96	0.00	3.67	1.38	0.00	100.0
Max.	15.94	18.23	66.60	2.71	5.02	34.61	31.28	6.37	4.18	3.67	3.48	3.67	
Min.	4.04	6.44	19.06	0.75	0.84	0.58	7.85	0.33	0.57	0.64	0.17	0.26	

At the same time the chemical composition of the sample (Figure 6.25) differs significantly from the chemical compositions of minerals that were identified by XRD (Figure 6.22) - fayalite Fe_2SiO_4, nepheline $Na_2O•Al_2O_3•2SiO_2$ and albite $NaAlSi_3O_8$. None of these minerals has combination of Na, Al, Si and Fe atoms together, especially in so big quantities. So the attempt of the crystalline body discovery at these points had no success. The 6.37% Ni contents can be considered as not accidental pollutant on the ceramic surface, but as the main difference between the chemical compositions of these two points of the amorphous structure.

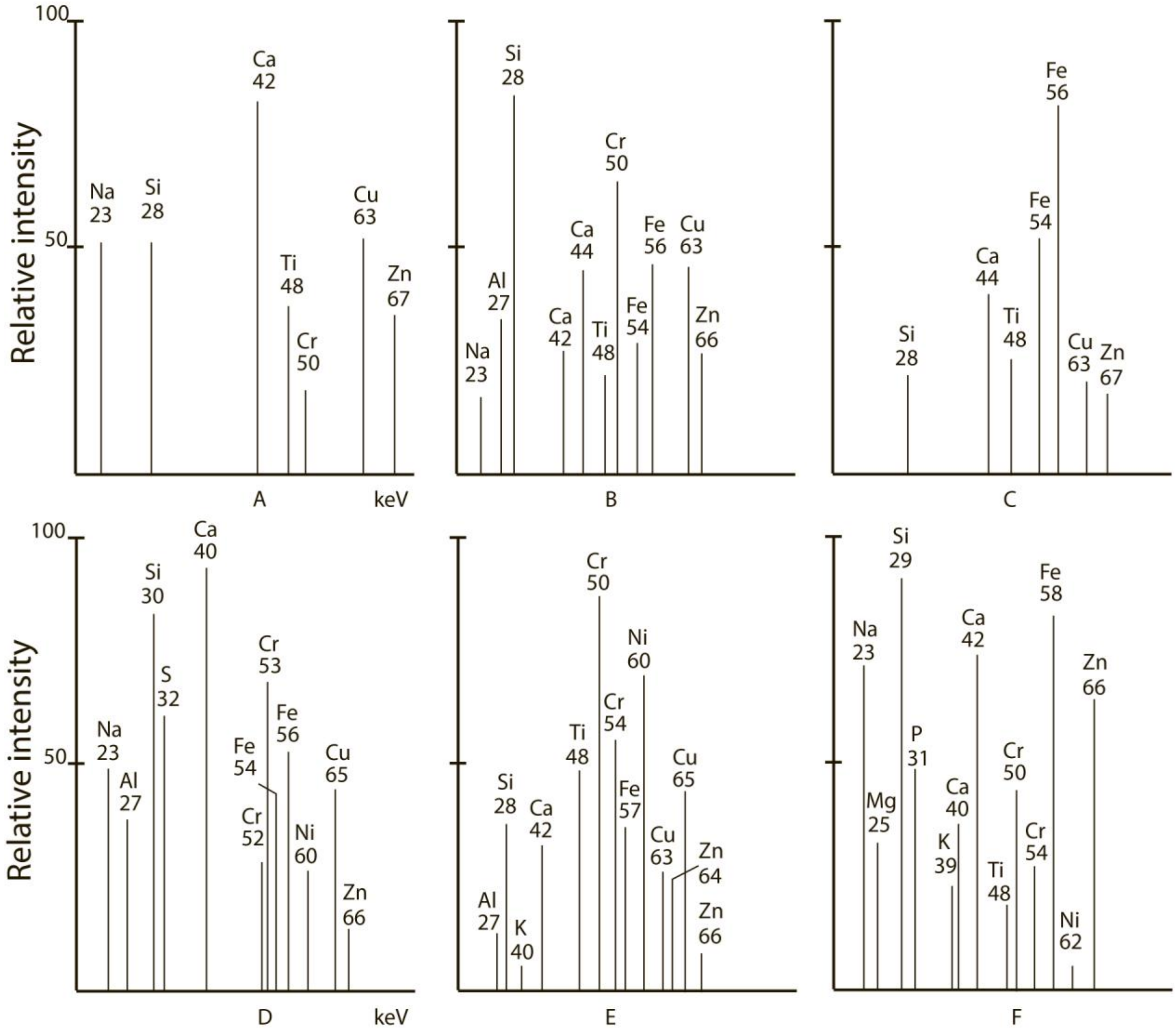

Figure 6.26 - Isotopes laser micro-mass analysis of new formations of composition 24 after sintering at 1225°C.

The results of application of the LAMMA method, fundamentally different from the EDS, give similar information: all 6 points of analysis (Figure 6.26) have different isotopic compositions with different percentage content (peaks intensity) of each isotope. This is another evidence of high heterogeneity of the sample.

6.4.5 Mapping the chemical states of an element inside the composition 24

Mapping the chemical states of an element presented on the Figure 6.27, demonstrates some dark areas where no elements were identified.

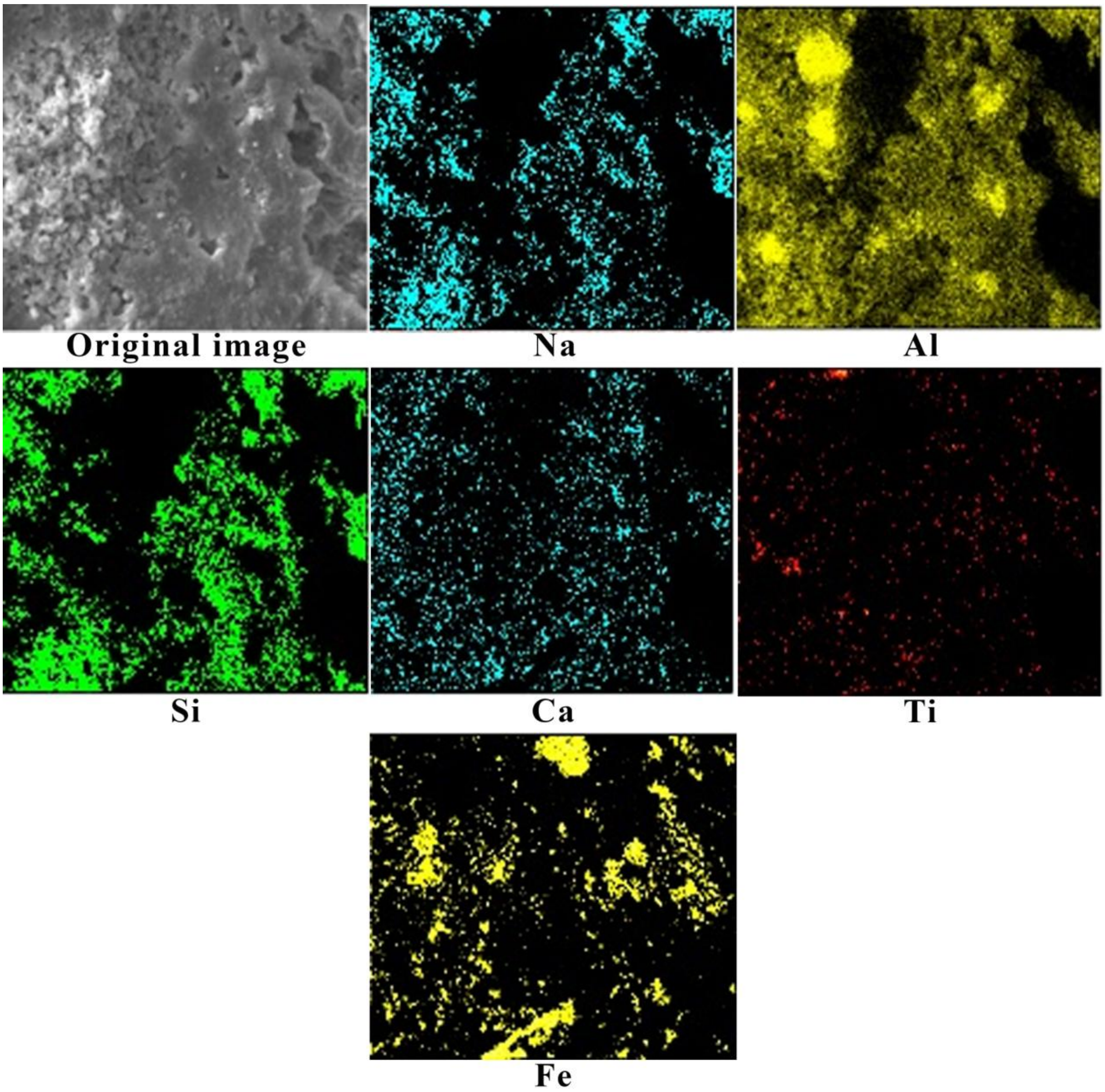

Figure 6.27 - Mapping the chemical states of an element inside a composition 24 sample sintered at 1150°C (using tomographic X-ray absorption spectroscopy).

The reason for this is not flat surface of the sample. In general analysis presents extremely high level of all elements distribution on the surface of composition 24.

7 ENVIRONMENTAL CHARACTERISTICS OF THE DEVELOPED CERAMICS

High content of metals and especially of heavy metals in red mud and consequently in all developed compositions, including particularly studied compositions 5, 14, 15 and 24 by EDS and LAMMA methods (Figure 6.3 – I, Figure 6.10, Figure 6.19, Figure 6.25 and Figure 6.4, Figure 6.11, Figure 6.20, Figure 6.26), makes the study of environmental properties of the ceramics by leaching and solubility methods extremely necessary.

The study of leaching (Table 7.1) and solubility (Table 7.2) of hazardous red mud extraction by AAS method showed that the content of metals, including heavy metals (Zn, Ni, Ba, Cd, Pb, Sn, Hg, Se, Cr, etc.) exceeded Brazilian toxicity norms (NBR 10004).

Ceramics of the composition 5 was selected for this study because it consists of 100% red mud. The composition 24 was selected for this study to understand the role of 20% waste glass addition on the leaching and solubility of metals from red mud.

The composition 14, which has 50% red mud and 50% blast furnace slag content, has the biggest amount of all compositions of blast furnace slag. It also presented the best flexural strength practically at all sintering temperatures, including 1225°C - 19.78 MPa. Therefore, it is important to check the influence of blast furnace slag on the chemical (environmental) properties of the composition.

The composition 15 consists of 50% red mud and 50% foundry sand. It is also the biggest foundry sand content in composition. This is the best composition to check influence of foundry sand on the environmental properties of ceramics.

First of all, red mud as a raw material without sintering (25°C) and composition 5 after sintering at 1225°C (Table 7.1) should be compared. After firing, red mud presents strong chemical binding of heavy metals in insoluble condition. Composition 5 attends demands of NBR 10004 after sintering at 1225°C. For example, the values of Ba leaching from ceramics is 46 times less than from red mud as raw material and 35 times less then NBR demands. Cd leaching has similar decrease of values in 147 and 10 times, etc.

Different results were obtained by composition 14. Ba leaching from composition 14 is 83 times lower than from raw red mud and with 61 times lower than it should be to pass the NBR regulations. Cd leaching from composition 14 is 245 times lower than from raw red mud and 17 times lower than it should be to pass the NBR regulations. Other metals have similar decrease of leaching values.

Table 7.1 - Leaching tests results of red mud and of compositions 5, 14, 15 and 24 sintered at their maximal temperatures.

Elements	Leaching values, mg/L					
	Red mud (25°C)	Comp.5 (1225°C)	Comp. 14 (1225°C)	Comp. 15 (1150°C)	Comp. 24 (1100°C)	NBR 10004
As	7.63	0.47	0.21	0.32	0.40	1.00
Ba	94.28	2.03	1.14	1.58	2.21	70.00
Cd	7.34	0.05	0.03	0.04	0.08	0.50
Pb	4.43	0.32	0.18	0.22	0.44	1.00
Cr total	18.46	1.78	1.21	1.49	2.67	5.00
Hg	1.47	0.04	0.018	0.29	0.07	*
Se	2.75	0.23	0.13	0.17	0.49	1.00
Al	28.76	2.56	0.10	0.14	3.17	*
Cu	16.29	0.19	0.05	0.08	0.24	*
Fe	98.31	1.69	0.72	1.07	2.18	*
Mn	55.11	0.85	0.24	0.41	0.39	*
Zn	68.48	0.03	0.01	0.01	0.16	*

Note: *- not determined by Brazilian sanitary Norms 10004.

Even better results were obtained in terms of solubility test Table 7.2. Red mud before the sintering has extremely high values of all metals exceeding NBR regulations. For example, there is 956 times more As in raw red mud than it should be in terms of NBR regulations. The same tendency is applied to all metals that were tested: 3082 times more Cd, 453 times - Cr, 766 times more Pb, 3810 times more Hg, 363 times more Fe.

After sintering at 1225°C the compositions 5 has the solubility of As more than 10 times less than NBR regulations. Cd was not detected, Cr solubility decreased 453 times, Pb decreased more than 766, Hg decreased more than 3810 times, and solubility of Fe decreased 362 times.

Table 7.2 - Solubility tests results of red mud and of compositions 5, 14, 15 and 24 sintered at their maximal temperatures.

Elements	Solubility values, mg/L					
	Red mud (25°C)	Comp.5 (1225°C)	Comp. 14 (1225°C)	Comp. 15 (1150°C)	Comp. 24 (1100°C)	NBR 10004
As	9.56	<0.001	<0.001	<0.001	<0.001	0.01
Ba	95.47	0.044	0.027	0.032	0.052	0.7
Cd	15.41	0	<0.005	0	<0.005	0.005
Pb	7.66	<0.01	<0.01	<0.01	<0.01	0.01
Cr total	22.67	0.01	0.02	0.02	0.04	0.05
Hg	3.81	<0.001	<0.0002	<0.001	<0.001	0.001
Se	3.35	<0.001	<0.001	<0.001	<0.001	0.01
Al	36.44	0.04	0.01	0.05	0.05	0.2
Cu	30.08	1.28	0.65	0.87	1.47	2.0
Fe	108.75	0.07	0.05	0.06	0.09	0.3
Mn	69.43	0.08	0.00	0.05	0.06	0.1
Zn	84.13	1.46	0.36	0.69	1.72	5.0

The lowest results were presented by composition 14 for almost all metals. This composition has the best mechanical properties after sintering at almost all temperatures, especially at 1225°C (19.78 MPa). The effective mechanical binding of the raw materials particles also means the effective chemical bonding or encapsulation of the atoms and ions in new glass-like formations. These processes create ecologically clean ceramics, which correspond to strict health standards.

8 CONCLUSIONS

8.1 THE MAIN CONCLUSION

In the presented research were developed 24 compositions, which do not contain any natural material. All the components are industrial wastes and majority of developed ceramics attend general norms and regulations for construction materials.

Due to the fact that there are different types of materials for civil construction, it is difficult to develop a material that would fit into all the norms and regulations and would also fit into different production methods. That is why were chosen only 4 types of final products that could be made on the basis of the presented compositions: ceramic wall tiles, ceramic roof tile, traditional brick, and porous brick for thermal and acoustic isolation. Important to notice, that for production process few adaptations should be made. For example, in case of ceramic wall tiles production, higher compaction pressure and lower humidity of the raw composition should be applied. In case of traditional bricks production, in terms of industrial extruder use, humidity of raw composition should be increased for higher plasticity of the material. There are four compositions, which were chosen as suitable for implementation on industrial scale. Each composition presents specific type of final product.

Composition 14 (Figure 5.2), containing 50% red mud and 50% blast furnace slag, is suitable for ceramic wall tiles production at the following temperature:

1. At 1100°C: flexural strength - 8.12 MPa, linear shrinkage - 1.13%, water absorption - 14.68%, density - 1.96 g/cm^3.
2. At 1150°C: flexural strength - 13.05 MPa, linear shrinkage - 4.28%, water absorption - 9.16%, density - 2.14 g/cm^3.
3. At 1200°C: flexural strength - 15.55 MPa, linear shrinkage - 10.99%, water absorption - 2.86%, density - 2.40 g/cm^3.

Composition 14 has high strength at high temperature, low shrinkage, and low water absorption. On the basis of these mechanical properties some adaptations should be made for wall tiles production of composition 14 when sintered at 1150°C as it the optimal firing temperature.

Composition 18 (Figure 5.6), containing 50% red mud, 30% foundry sand, and 20% waste glass, is suitable for traditional brick production. When fired at 1000°C the composition presents flexural strength – 4.98 MPa, linear shrinkage – 6.94%, water absorption - 9.58%, density – 1.66 g/cm^3. All these characteristics are similar to properties, which bricks have made of natural clay. The key characteristics are low firing temperature, not high water absorption, and normal flexural strength.

Composition 21 (Figure 5.7), containing 60% red mud, 20% blast furnace slag, and 20% wood ash, is suitable for production of porous brick for thermal and acoustic isolation. When fired at 1150°C it has the following characteristics: flexural strength – 7.50 MPa, linear shrinkage – 4.73%, water absorption - 14.32%, density – 1.65 g/cm^3. The key factors are low density and high flexural strength. High water absorption in terms of these products is not a problem, as these bricks are usually covered with some other material.

Composition 22 (Figure 5.8), containing 60% red mud, 20% foundry sand, and 20% waste glass, is suitable for roof tiles production. When fired at 1050°C it has the following characteristics: flexural strength – 5.93 MPa, linear shrinkage – 10.32%, water absorption - 2.61%, density – 1.81 g/cm^3. The key factors are high flexural strength and very low water absorption, which is the crucial property for roof tiles.

This is the main conclusion made in terms of application of the developed materials. Scientific conclusions made in terms of physicochemical processes and study of ceramics properties are listed in the specific conclusion.

8.2 THE SPECIFIC CONCLUSIONS

8.2.1 General conclusion on mechanical properties of the developed ceramics

The flexural strength of samples, which are made only of red mud, presented a high strength. It exceeds three times strength presented in norms NBR 15270-3/05 for the strongest Class C (more than 4.0 MPa). At 1100°C the composition already has 4.34 MPa and as the firing temperature increases the highest flexural strength increases too.

Addition to red mud of 10-50% blast furnace slag results in up to 35% higher flexural strength than the strength of traditional ceramic materials made of natural clay. At the same time, compositions containing red mud and blast furnace slag present 60% higher strength than the ceramic samples made of only red mud. The highest strength of 19.78 MPa is obtained at 1225°C by the composition 14, which consists of 50% red mud and 50% blast furnace slag.

Addition to red mud of 10-50% foundry sand also increases flexural strength of the samples comparing with composition made of red mud only. Some compositions begin to meet the requirements of NBR 15270-3/05 Class B (between 2 and 4 MPa) after firing at 800°C and Class C (more than 4.0 MPa) at 900°C.

Addition to red mud of 20% waste glass dramatically accelerates the growth of the strength of ceramic samples as the temperature increases. Waste glass reduces the temperature for 125°C for obtaining the maximum strength of 14.07 MPa.

The strongest samples of compositions containing blast furnace slag almost twice stronger than the strongest samples made of foundry sand.

The substitution of foundry sand with waste glass increases the flexural strength at all temperatures and decreases the temperature of the maximal strength. Replacement of the waste glass by the wood ash mainly causes decrease of the samples flexural strength.

The shrinkage increases as the samples sintered at higher temperatures. The only exception is excessive melting. At the temperature lower than 1200°C the shrinkage of red mud is 2-3 times lower than shrinkage of the natural clay. At 1200°C there is no significant difference between these two materials. At 1225°C red mud has higher shrinkage than natural clay.

The linear shrinkage of the compositions containing foundry sand is higher than linear shrinkage of compositions containing blast furnace slag. Blast furnace slag played stabilizing role. At the same time, in the highly alkaline composition the foundry sand works as an accelerator of melting process.

Addition of waste glass causes the decrease of linear shrinkage and peak strength temperature. Substitution of waste glass by wood ash presents decrease of linear shrinkage and flexural strength at all temperatures.

Water absorption serves as an indirect sign of open pores. Normally, with an increase of temperature pores tend to close. Addition of blast furnace slag to red mud accelerates decrease of open pores, which has positive impact on flexural strength. Addition of foundry sand allows decreasing water absorption of red mud. It might even work better than the blast furnace slag at some temperatures, for example at 1150°C.

The waste glass and wood ash work as flux materials decreasing the water absorption. Wood ash reacts better at low temperatures, while waste glass improves flexural strength at high temperatures. This causes acceleration of strength gain, which sometimes does not allow reaching full potential of the composition.

The density increases with an increase of firing temperature. The red mud presents 1.28 g/cm^3 at 800°C, 1.55 g/cm^3 at 1150°C, and 1.89 g/cm^3 at 1200°C. All compositions demonstrated significant growth of density at 1200°C and 1225°C.

The blast furnace slag increases the density of compositions containing red mud. The maximum density 2.54 g/cm^3 was reached by composition containing 60% red mud and 40% blast furnace slag.

The foundry sand in combination with red mud presents compositions with low density, comparing to compositions containing blast furnace slag, especially at low temperatures.

Addition of waste glass and wood ash causes the decrease of density of the samples.

8.2.2 General conclusion on physicochemical processes inside the samples

Mineral composition of red mud basically presented by bauxite ore $Al_2O_3 \cdot nH_2O$, which was not milled during Bayer process, iron minerals hematite Fe_2O_3 and magnetite Fe_3O_4, and quartz SiO_2. Blast furnace slag contains fayalite – $Fe_2 \cdot 2SiO_4$ and troilite - FeS. Foundry sand is represented by the only crystalline mineral quartz SiO_2. Waste glass consists of amorphous phase of glass with small content of crystalline quartz SiO_2. Wood ash is presented by afwillite $Ca_3Si_2O_6(OH)2(H_2O)_2$ (Si_5O_{18}), albite$(Na,Ca)Al(Si, Al)_3O_8$, orthoclase $K(Al, Fe)Si_2O_8$ and quartz SiO_2. All these materials, except foundry sand, have high content of glass-like amorphous phase.

The results of XRD diffractograms deciphering of ceramics from red mud show that initial mineralogical composition was presented by hematite Fe_2O_3, fayalite Fe_2SiO_4, albite $Na(Al \bullet Si_3O_8)$ and quartz SiO_2. After sintering at 1000°C, 1150°C, and 1225°C none of them have changed and only some crystal peaks of albite slightly increased intensity. The increase of X-ray background is a precise indicator of the synthesis of an additional amount of amorphous material.

The deciphering of curves of differential thermal analysis (DTA) and thermogravimetric analysis (TGA) obtained during the sintering of red mud up to 1225°C contains three endothermic and one exothermic effect of thermochemical reactions. The first endothermic effect confirms the removal of free or weakly bound water at 28-202°C. The second endothermic effect demonstrate the loses of crystal water molecules by $Al(OH)_3$ and conversion into boehmite γ-AlO(OH) at 202-296°C; at the same temperature occurred an amorphous gel transformation into (α, β, ɣ and δ) of FeOOH. The third endothermic effect at 296-606°C includes the processes of boehmite conversion into anhydrous γ-Al_2O_3 by and transformation of $FeOOH \rightarrow ɣ\text{-}Fe_2O_3 \rightarrow Fe_3O_4$. The only but the most significant exothermic effect at 606-1217°C is caused by the transformation $\gamma\text{-}Al_2O_3 \rightarrow \alpha\text{-}Al_2O_3$ and of $Fe_3O_4 \rightarrow Fe$ up to 700-750°C, and dross Fe_3O_4 formation at 900-1000°C.

Comparison of the initial red mud SEM micro images before its sintering with the micro images of ceramics after sintering at 1000° and 1150°C shows that earlier disintegrated red mud particles began melting, gluing and forming agglomerated units, and consequently increasing the strength of the samples till 6.06 MPa. Increase of the firing temperature up to 1225°C causes melting of the all particles. It means complete integration in the whole volume by smooth shiny glass-like new formations with a total flexural strength of the ceramics 12.32 MPa.

Comparison of the mineral compositions of the composition 14 studied by XRD method, demonstrate the increase of amorphous phase content with growth of sintering temperature at 1000°, 1100°, 1200°, and 1225°C. Chemical interaction of red mud and blast furnace slag accelerates with increase of firing temperature. Some part of crystalline phases of the raw materials decreases in amount, especially at 1200° and 1225°C, in the ceramics. There is a transition to the amorphous state of fayalite Fe_2SiO_4, hematite Fe_2O_3, accompanied by complete disappearance of Quartz SiO_2.

The results obtained with XRD studies were confirmed by DTA and TGA methods at 25°-1225°C. Three endothermic effects and three exothermic effects were identified on the DTA and TGA curves of composition 14. The reason for this is complicated chain of thermochemical reactions with transformation of aluminum and iron hydroxides in anhydrous melted substances.

Study of changes of morphological structure shows transition of micro points melting process of components to the melting of relatively large areas during temperature increase at 1000°C, 1150°C, and 1225°C of composition 14 sintering. There is also partial formation of a more monolithic structure. This process might be the reason for 19.78 MPa flexural strength.

The composition 15, which contains 50% red mud and 50% foundry sand, presented changes in mineral composition content after sintering at 1000°C and 1150°C.There is a decrease of quartz SiO_2 and fayalite Fe_2SiO_4 quantity with strong increase of X-ray background, which confirms the increase of quantity of amorphous materials.

The curves of DTA and TGA contain only one endothermic and one exothermic peak. Endothermic peak of the composition 15 at 201-291°C and weight loss 4.69% indicates the removal of the free and weakly bound water. The exothermic effect at 291°-1221°C is the result of the formation of solid solutions of boehmite α-Al_2O_3, fayalite Fe_2SiO_4, hematite Fe_2O_3, albite $Na(AlSi_3O_8)$, quartz and cristobalite SiO_2 during sintering at 1225°C. The vast majority of these minerals is in the amorphous state. Some of them can transform in the crystalline state of solid solutions. At the same time, deciphering the X-rays diffractograms usually shows the decrease in the intensity of the peaks, except albite.

During the sintering at 1000°C of composition 24, which contains 80% red mud and 20% waste glass, completely disappeared almost all initial minerals, such as bauxite $Al_2O_3 \cdot nH_2O$, hematite Fe_2O_3, magnetite Fe_3O_4 and quartz SiO_2. Some principal chemical elements of these minerals (75.2% SiO_2 from waste glass, 29.9% Fe_2O_3, 21.2% Al_2O_3 and 10.3% Na_2O from red mud, etc.) entered in newly formed crystal structures of minerals fayalite Fe_2SiO_4, nepheline $Na_2O \cdot Al_2O_3 \cdot 2SiO_2$ and albite $NaAlSi_3O_8$. The quantity or the perfection level of crystalline structure of nepheline increased at 1100°C, but almost disappeared at 1150°. The melting point of nepheline is 1200°C, but high contents of fluxes in red mud significantly decreased melting point of the composition 24. The fayalite peaks also reduced, similarly to the results of composition 14 and composition 15.

The study of new formations of the ceramics made by EDS, LAMMA and mapping methods demonstrated very high level of the heterogeneity of the chemical compositions on micro level, which is typical for amorphous structures.

Red mud has high content of heavy metals, far exceeding Brazilian norms and regulations. In the developed ceramics all of them are strongly bounded in insoluble vitreous structures. Leaching and solubility tests of the new ceramics show their complete environmental compatibility. Therefore, their application on industrial scale will have a positive impact on the environment. The key positive factors are: a prevention of the hazardous waste disposal, a prolongation service life of industrial landfills, and lack of need for further destruction on nature by mining of traditional raw materials.

9 RECOMMENDATIONS

In the end of the experimental part of the presented research, some compositions containing natural materials were prepared. Addition of natural clay, natural sand (presenting 3 different types in terms of granulometric composition: less than 0.15, 0.15-0.30, and 0.3-0.5mm), feldspar, and kaolin resulted in high flexural strength, low linear shrinkage, low water absorption, and relatively low firing temperature of the samples.

For example, composition containing 80% red mud, 10% natural sand, and 10% waste glass reached 8.02 MPa flexural strength after firing at 1100°C. At the same time, composition containing 50% red mud, 10% natural clay, and 40% quartz sand presented 9.02 MPa strength at 1100°C. Composition containing 60% red mud, 20% blast furnace slag, and 20% feldspar at firing temperature of 1150°C presented 2.66% water absorption, which is very low and suitable for wall tiles production. Some of the compositions presented very low value of linear shrinkage at high temperatures, which is valuable characteristic especially for wall tiles.

The obtained result is the solid evidence of significant potential of compositions containing natural materials and industrial wastes. For this reason, it is highly recommended to add natural materials into further research. Not only listed above materials could be used, but the different types of clay and sand should be considered. When compositions will be developed it is necessary to study physic-chemical interaction between particles of each material, as the influence of one material on another should not be underestimated.

It is also recommended to set some exact characteristics of the final product. This will increase applicability of the results and will make the research more exact. It is important to highlight as every final product has its own application and production method, this is why chosen materials should match these restrictions. For example, if the final product is not ceramic material in general, but exactly wall tile, this would mean low water absorption, high flexural strength, low linear shrinkage, high firing temperature and application of high pressure when the samples are fabricated. Or if the final product is ceramic brick, it means that raw composition before firing should have special plasticity. The reason for this is application of extruding machine in the production process, and when material is extruded it should not crumble.

To summarize, more attention should be paid to addition of natural materials and to the production method of the exact final product.

REFERENCES

ABNT. **NBR 7181**. GRANULOMÉTRICA, Solo–Análise. 1984.

ABNT, **NBR. 10004**. Resíduos sólidos–Classificação, 2004.

ABNT. **NBR 10005**: Lixiviação de resíduos: procedimento. Rio de Janeiro, 1987.

ABNT. **NBR 15270: 3/05**: Componentes Cerâmicos-Parte 3: Blocos Cerâmicos para Alvenaria Estrutural e de Vedação-Métodos de Ensaio. Rio de Janeiro (Brasil), 2005.

AGATZINI-LEONARDOU, S. et al. Titanium leaching from red mud by diluted sulfuric acid at atmospheric pressure. **Journal of hazardous materials**, v. 157, n. 2, p. 579-586, 2008.

ALONSO-SANTURDE, R. et al. Technological behaviour and recycling potential of spent foundry sands in clay bricks. **Journal of Environmental Management**, v. 92, n. 3, p. 994-1002, 2011.

AVILA-LÓPEZ, U.; ALMANZA-ROBLES, J. M.; ESCALANTE-GARCÍA, J. I. Investigation of novel waste glass and limestone binders using statistical methods. **Construction and Building Materials**, v. 82, p. 296-303, 2015.

BADANOIU, Alina Ioana et al. Preparation and characterization of foamed geopolymers from waste glass and red mud. **Construction and Building Materials**, v. 84, p. 284-293, 2015.

BAI, Jianguang et al. Preparation of foam glass from waste glass and fly ash. **Materials Letters**, v. 136, p. 52-54, 2014.

BARNETT, Robert J.; MEZNER, Michael B. **Process for treating red mud to recover metal values there from**. U.S. Patent n. 6,248,302, 19 jun. 2001.

BASAR, H. Merve; AKSOY, Nuran Deveci. The effect of waste foundry sand (WFS) as partial replacement of sand on the mechanical, leaching and micro-structural characteristics of ready-mixed concrete. **Construction and Building Materials**, v. 35, p. 508-515, 2012.

BHASKAR, Manoj; AKHTAR, Salim; BATHAM, Geeta. Development of the Bricks from Red Mud by Industrial Waste (Red Mud).

BIGNOZZI, M. C. et al. Glass waste as supplementary cementing materials: The effects of glass chemical composition. **Cement and Concrete Composites**, v. 55, p. 45-52, 2015.

BOBIRICĂ, Constantin et al. Influence of waste glass on the microstructure and strength of inorganic polymers. **Ceramics International**, v. 41, n. 10, p. 13638-13649, 2015.

BORGES, Américo José Preto; HAUSER-DAVIS, Rachel Ann; DE OLIVEIRA, Terezinha Ferreira. Cleaner red mud residue production at an alumina plant by applying experimental design techniques in the filtration stage. **Journal of Cleaner Production**, v. 19, n. 15, p. 1763-1769, 2011.

BORRA, Chenna Rao et al. Leaching of rare earths from bauxite residue (red mud). **Minerals Engineering**, v. 76, p. 20-27, 2015.

BOUDREAULT, Richard et al. **Processes for treating red mud**. U.S. Patent Application n. 14/687,909, 15 abr. 2015.

BROWN, Michael E.; GALLAGHER, Patrick K. **Handbook of thermal analysis and calorimetry: recent advances, techniques and applications**. Elsevier, 2011.

BROWNER, R. E. The use of bauxite waste mud in the treatment of gold ores. **Hydrometallurgy**, v. 37, n. 3, p. 339-348, 1995.

CHANTURIA, E. L.; GZOGYAN, S. P. Features of sulfide ferruginous quartzite mineralization. **Journal of mining science**, v. 45, n. 5, p. 495-498, 2009.

CHAURAND, Perrine et al. Environmental impacts of steel slag reused in road construction: A crystallographic and molecular (XANES) approach. **Journal of Hazardous Materials**, v. 139, n. 3, p. 537-542, 2007.

CHEAH, Chee Ban; PART, Wei Ken; RAMLI, Mahyuddin. The hybridizations of coal fly ash and wood ash for the fabrication of low alkalinity geopolymer load bearing block cured at ambient temperature. **Construction and Building Materials**, v. 88, p. 41-55, 2015.

CHEAH, Chee Ban; RAMLI, Mahyuddin. The implementation of wood waste ash as a partial cement replacement material in the production of structural grade concrete and mortar: An overview. **Resources, Conservation and Recycling**, v. 55, n. 7, p. 669-685, 2011.

CHEN, Xingjun; LU, Anxian; QU, Gao. Preparation and characterization of foam ceramics from red mud and fly ash using sodium silicate as foaming agent. **Ceramics International**, v. 39, n. 2, p. 1923-1929, 2013.

CHOWDHURY, S.; MANIAR, A.; SUGANYA, O. M. Strength development in concrete with wood ash blended cement and use of soft computing models to predict strength parameters. **Journal of advanced research**, v. 6, n. 6, p. 907-913, 2015.

CHOWDHURY, Swaptik; MISHRA, Mihir; SUGANYA, Om. The incorporation of wood waste ash as a partial cement replacement material for making structural grade concrete: An overview. **Ain Shams Engineering Journal**, v. 6, n. 2, p. 429-437, 2015.

COLLINS, Richard N.; CLARK, Malcolm W.; PAYNE, Timothy E. Solid phases responsible for Mn II, Cr III, Co II, Ni, Cu II and Zn immobilization by a modified bauxite refinery residue (red mud) at pH 7.5. **Chemical Engineering Journal**, v. 236, p. 419-429, 2014.

COURTNEY, Ronan; KIRWAN, Luke. Gypsum amendment of alkaline bauxite residue–Plant available aluminium and implications for grassland restoration. **Ecological Engineering**, v. 42, p. 279-282, 2012.

DEELWAL, Kusum; DHARAVATH, Kishan; KULSHRESHTHA, Mukul. Evaluation of characteristic properties of red mud for possible use as a geotechnical material in civil construction. **International Journal of Advances in Engineering & Technology**, v. 7, n. 3, p. 1053, 2014.

DING, Linfeng et al. Preparation and characterization of glass–ceramic foams from blast furnace slag and waste glass. **Materials Letters**, v. 141, p. 327-329, 2015.

DODOO-ARHIN, D. et al. Fabrication and Characterisation of Ghanaian Bauxite Red Mud-Clay Composite Bricks for Construction Applications. **American Journal of Materials Science**, v. 3, n. 5, p. 110-119, 2013.

ETXEBERRIA, M. et al. Properties of concrete using metallurgical industrial by-products as aggregates. **Construction and Building Materials**, v. 24, n. 9, p. 1594-1600, 2010.

FERRO, Riccardo; SACCONE, Adriana. **Intermetallic chemistry**. Elsevier, 2008.

FRANCIS, A. A.; RAHMAN, MK Abdel; DAOUD, A. Processing, structures and compressive properties of porous glass-ceramic composites prepared from secondary by-product materials. **Ceramics International**, v. 39, n. 6, p. 7089-7095, 2013.

FULFORD, George D.; LEVER, Gordon; SATO, Taichi. **Digestion with dilute acid, separation**. U.S. Patent n. 5,030,424, 9 jul. 1991.

FURLANI, E. et al. Preparation and characterization of sintered ceramics made with spent foundry olivine sand and clay. **Ceramics International**, v. 38, n. 4, p. 2619-2625, 2012.

GERHARD, Bayer et al. **Method for producing bricks from red mud**. U.S. Patent n. 3,886,244, 27 maio 1975.

GONDA1–ZSOMBOR, Andrea Kolencsik-Tóth1–Nóra; SZÉKELY1–BALÁZS, Fekete1–Márton Tóth1–István; KOVÁCS, Zákányi1–Ferenc Móricz2–Balázs. Physical and chemical characterization of red mud in terms of its environmental effects.

GONG, Y. et al. Recycling of waste amber glass and porcine bone into fast sintered and high strength glass foams. **Journal of Cleaner Production**, v. 112, p. 4534-4539, 2016.

GORDON, Junior N.; PINNOCK, Willard R.; MOORE, Marcia M. A preliminary investigation of strength development in Jamaican red mud composites. **Cement and Concrete Composites**, v. 18, n. 6, p. 371-379, 1996.

GRÄFE, M.; KLAUBER, Craig. Bauxite residue issues: IV. Old obstacles and new pathways for in situ residue bioremediation. **Hydrometallurgy**, v. 108, n. 1, p. 46-59, 2011.

GRÄFE, M.; POWER, Greg; KLAUBER, Craig. Bauxite residue issues: III. Alkalinity and associated chemistry. **Hydrometallurgy**, v. 108, n. 1, p. 60-79, 2011.

GUNEY, Yucel et al. Re-usage of waste foundry sand in high-strength concrete. **Waste Management**, v. 30, n. 8, p. 1705-1713, 2010.

GUO, Yuxi et al. Novel glass ceramic foams materials based on red mud. **Ceramics International**, v. 40, n. 5, p. 6677-6683, 2014.

HAI, Luu Duc et al. Material Composition and Properties of Red Mud Coming From Alumina Processing Plant Tanrai, Lamdong, Vietna. **International journal of Research In Earth and Environmental Science**, v. 1, n. 6, p. 1-7, 2014.

HE, Hongtao et al. The effect of incorporation of red mud on the properties of clay ceramic bodies. **Applied Clay Science**, v. 70, p. 67-73, 2012.

HIND, Andrew R.; BHARGAVA, Suresh K.; GROCOTT, Stephen C. The surface chemistry of Bayer process solids: a review. **Colloids and surfaces A: Physicochemical and engineering aspects**, v. 146, n. 1, p. 359-374, 1999.

IWU, Gregory Onyemauwa. **Method of treating bauxite waste red mud with acid and making construction bricks from the treated material**. U.S. Patent n. 3,985,567, 12 out. 1976.

JAMSHIDI, Ali et al. Analysis of structural performance and sustainability of airport concrete pavements incorporating blast furnace slag. **Journal of Cleaner Production**, v. 90, p. 195-210, 2015.

JANI, Yahya; HOGLAND, William. Waste glass in the production of cement and concrete–A review. **Journal of Environmental Chemical Engineering**, v. 2, n. 3, p. 1767-1775, 2014.

JAQUAYS, Charles. **Building and other materials containing treated bauxite tailings and process for making same**. U.S. Patent Application n. 10/690,729, 23 out. 2003.

JOHNSON, D. W.; GALLAGHER, P. K. Kinetics of the Decomposition of Freeze-Dried Aluminum Sulfate and Ammonium Aluminum Sulfate. **Journal of the American Ceramic Society**, v. 54, n. 9, p. 461-465, 1971.

JU, Shao-hua et al. Removal of cadmium from aqueous solutions using red mud granulated with cement. **Transactions of Nonferrous Metals Society of China**, v. 22, n. 12, p. 3140-3146, 2012.

KATO, ETSURO; DAEMON, KEIJI; NANBU, MASAO. Decomposition of two aluminum sulfates and characterization of the resultant aluminas. **Journal of the American Ceramic Society**, v. 64, n. 8, p. 436-443, 1981.

KAVAS, Taner. Use of boron waste as a fluxing agent in production of red mud brick. **Building and Environment**, v. 41, n. 12, p. 1779-1783, 2006.

KIM, Kidong; KIM, Kicheol; HWANG, Jonghee. Characterization of ceramic tiles containing LCD waste glass. **Ceramics International**, v. 42, n. 6, p. 7626-7631, 2016.

KIM, Kidong; KIM, Kicheol; HWANG, Jonghee. LCD waste glass as a substitute for feldspar in the porcelain sanitary ware production. **Ceramics International**, v. 41, n. 5, p. 7097-7102, 2015.

KIM, Min Sik et al. Use of CaO as an activator for producing a price-competitive non-cement structural binder using ground granulated blast furnace slag. **Cement and concrete research**, v. 54, p. 208-214, 2013.

KIMJASHOV A.A., 2010 Phase equilibria in systems Fe - Al - O and Fe - Si - O in the temperature range 1100 - 1300 K, Ph.D. these, South Ural State University, Chelyabinsk. https://www.susu.ru/abstract/file/abstract/kimjashov_alexander_anatoljevich.docx.

KLAUBER, Craig; GRÄFE, M.; POWER, Greg. Bauxite residue issues: II. options for residue utilization. **Hydrometallurgy**, v. 108, n. 1, p. 11-32, 2011.

KUMAR, Anuj; KUMAR, Sanjay. Development of paving blocks from synergistic use of red mud and fly ash using geopolymerization. **Construction and Building Materials**, v. 38, p. 865-871, 2013.

KUMAR, Sanjay et al. Mechanical activation of granulated blast furnace slag and its effect on the properties and structure of portland slag cement. **Cement and Concrete Composites**, v. 30, n. 8, p. 679-685, 2008.

LI, Xiao-bin et al. Recovery of alumina and ferric oxide from Bayer red mud rich in iron by reduction sintering. **Transactions of Nonferrous Metals Society of China**, v. 19, n. 5, p. 1342-1347, 2009.

LI, Yanzhong et al. Phosphate removal from aqueous solutions using raw and activated red mud and fly ash. **Journal of Hazardous Materials**, v. 137, n. 1, p. 374-383, 2006.

LI, Yiran et al. Feasibility study of iron mineral separation from red mud by high gradient superconducting magnetic separation. **Physica C: Superconductivity**, v. 471, n. 3, p. 91-96, 2011.

LI, Zaihui et al. Discovery of the REE minerals in the Wulong–Nanchuan bauxite deposits, Chongqing, China: Insights on conditions of formation and processes. **Journal of Geochemical Exploration**, v. 133, p. 88-102, 2013.

LIAO, Chang-Zhong; ZENG, Lingmin; SHIH, Kaimin. Quantitative X-ray diffraction (QXRD) analysis for revealing thermal transformations of red mud. **Chemosphere**, v. 131, p. 171-177, 2015.

LING, Tung-Chai; POON, Chi-Sun; WONG, Hau-Wing. Management and recycling of waste glass in concrete products: Current situations in Hong Kong. **Resources, Conservation and Recycling**, v. 70, p. 25-31, 2013.

LIU, Dong-Yan; WU, Chuan-Sheng. Stockpiling and comprehensive utilization of red mud research progress. **Materials**, v. 5, n. 7, p. 1232-1246, 2012.

LIU, Wanchao et al. Environmental assessment, management and utilization of red mud in China. **Journal of Cleaner Production**, v. 84, p. 606-610, 2014.

LIU, Wanchao et al. Experimental and simulative study on phase transformation in Bayer red mud soda-lime roasting system and recovery of Al, Na and Fe. **Minerals Engineering**, v. 39, p. 213-218, 2012.

LIU, Wanchao; YANG, Jiakuan; XIAO, Bo. Application of Bayer red mud for iron recovery and building material production from alumosilicate residues. **Journal of hazardous materials**, v. 161, n. 1, p. 474-478, 2009.

LIU, Wanchao; YANG, Jiakuan; XIAO, Bo. Review on treatment and utilization of bauxite residues in China. **International Journal of Mineral Processing**, v. 93, n. 3, p. 220-231, 2009.

LIU, Xiaoming et al. Structural investigation relating to the cementitious activity of bauxite residue—red mud. **Cement and Concrete Research**, v. 41, n. 8, p. 847-853, 2011.

LIU, Yanju; NAIDU, Ravi. Hidden values in bauxite residue (red mud): recovery of metals. **Waste management**, v. 34, n. 12, p. 2662-2673, 2014.

LIU, Yanyan et al. Recycling of iron from red mud by magnetic separation after co-roasting with pyrite. **Thermochimica Acta**, v. 588, p. 11-15, 2014.

LIU, Zhaobo; LI, Hongxu. Metallurgical process for valuable elements recovery from red mud—A review. **Hydrometallurgy**, v. 155, p. 29-43, 2015.

LÜBECK, A. et al. Compressive strength and electrical properties of concrete with white Portland cement and blast-furnace slag. **Cement and Concrete Composites**, v. 34, n. 3, p. 392-399, 2012.

ŁUKOWSKI, Paweł; SALIH, Ali. Durability of mortars containing ground granulated blast-furnace slag in acid and sulphate environment. **Procedia Engineering**, v. 108, p. 47-54, 2015.

MAHIEUX, P.-Y.; AUBERT, J.-E.; ESCADEILLAS, G. Utilization of weathered basic oxygen furnace slag in the production of hydraulic road binders. **Construction and Building Materials**, v. 23, n. 2, p. 742-747, 2009.

MARYANDYSHEV, P. A. et al. Thermal decomposition and combustion of coals, fuel wood, and hydrolytic lignin, as studied by thermal analysis. **Solid Fuel Chemistry**, v. 50, n. 3, p. 167-176, 2016.

MASTELLA, Miguel Angelo et al. Mechanical and toxicological evaluation of concrete artifacts containing waste foundry sand. **Waste management**, v. 34, n. 8, p. 1495-1500, 2014.

MAUTHOOR, Sumayya; MOHEE, Romeela; KOWLESSER, Prakash. Characterisation of electric arc furnace slags as concrete aggregate in a small island developing state: A preliminary study. **Construction and Building Materials**, v. 105, p. 459-464, 2016.

MILAČIČ, Radmila; ZULIANI, Tea; ŠČANČAR, Janez. Environmental impact of toxic elements in red mud studied by fractionation and speciation procedures. **Science of the Total Environment**, v. 426, p. 359-365, 2012.

MONOSI, Saveria; RUELLO, Maria Letizia; SANI, Daniela. Electric arc furnace slag as natural aggregate replacement in concrete production. **Cement and Concrete Composites**, v. 66, p. 66-72, 2016.

MYMRIN, V. A. et al. Structure formation of slag-soil construction materials. **Materials and structures**, v. 38, n. 1, p. 107-113, 2005.

MYMRIN, Vsévolod A.; PONTE, Haroldo A.; YAMAMOTO, Carlos I. Synthesis of new colloidal formations during the strengthening of different activated hydrated metallurgical slags. **Colloids and Surfaces A: Physicochemical and Engineering Aspects**, v. 220, n. 1, p. 211-221, 2003.

MYMRIN, Vsévolod et al. Environment friendly ceramics from hazardous industrial wastes. **Ceramics International**, v. 40, n. 7, p. 9427-9437, 2014.

MYMRIN, Vsévolod et al. Environment-friendly method of high alkaline bauxite's Red Mud and Ferrous Slag utilization as an example of green chemistry. **Green Chemistry**, v. 5, n. 3, p. 357-360, 2003.

MYMRIN, Vsévolod et al. Red clay application in the utilization of paper production sludge and scrap glass to fabricate ceramic materials. **Applied Clay Science**, v. 107, p. 28-35, 2015.

NITHYA, S.; ASHOK, P. EXPERIMENTAL STUDIES ON CONCRETE UTILISING RED MUD AS A PARTIAL REPLACEMENT OF CEMENT WITH HYDRATED LIME. **Growth**, v. 5, p. 0. (2016)

OBURGER, Eva et al. Environmental impact assessment of wood ash utilization in forest road construction and maintenance—A field study. **Science of the Total Environment**, v. 544, p. 711-721, 2016.

ÖZBAY, Erdoğan; ERDEMIR, Mustafa; DURMUŞ, Halil İbrahim. Utilization and efficiency of ground granulated blast furnace slag on concrete properties–A review. **Construction and Building Materials**, v. 105, p. 423-434, 2016.

OZDEMIR, Ilker; YILMAZ, Senol. Processing of unglazed ceramic tiles from blast furnace slag. **Journal of materials processing technology**, v. 183, n. 1, p. 13-17, 2007.

OZTURK, Zahide Bayer; GULTEKIN, Elif Eren. Preparation of ceramic wall tiling derived from blast furnace slag. **Ceramics International**, v. 41, n. 9, p. 12020-12026, 2015.

PASETTO, Marco; BALDO, Nicola. Experimental evaluation of high performance base course and road base asphalt concrete with electric arc furnace steel slags. **Journal of Hazardous Materials**, v. 181, n. 1, p. 938-948, 2010.

PATHAK, Neelam; SIDDIQUE, Rafat. Effects of elevated temperatures on properties of self-compacting-concrete containing fly ash and spent foundry sand. **Construction and Building Materials**, v. 34, p. 512-521, 2012.

PÉREZ-VILLAREJO, L. et al. Manufacturing new ceramic materials from clay and red mud derived from the aluminium industry. **Construction and Building Materials**, v. 35, p. 656-665, 2012.

PERRY, Dale L. **Handbook of inorganic compounds**. CRC press, 2016.

PHONPHUAK, Nonthaphong; KANYAKAM, Siwadol; CHINDAPRASIRT, Prinya. Utilization of waste glass to enhance physical–mechanical properties of fired clay brick. **Journal of Cleaner Production**, v. 112, p. 3057-3062, 2016.

PONTIKES, Yiannis et al. Effect of firing temperature and atmosphere on sintering of ceramics made from Bayer process bauxite residue. **Ceramics international**, v. 35, n. 1, p. 401-407, 2009.

PONTIKES, Yiannis; ANGELOPOULOS, G. N. Bauxite residue in cement and cementitious applications: current status and a possible way forward. **Resources, Conservation and Recycling**, v. 73, p. 53-63, 2013.

PONTIKES, Yiannis; NIKOLOPOULOS, P.; ANGELOPOULOS, G. N. Thermal behavior of clay mixtures with bauxite residue for the production of heavy-clay ceramics. **Journal of the European Ceramic Society**, v. 27, n. 2, p. 1645-1649, 2007.

POWER, Greg; GRÄFE, M.; KLAUBER, Craig. Bauxite residue issues: I. Current management, disposal and storage practices. **Hydrometallurgy**, v. 108, n. 1, p. 33-45, 2011.

PRABHU, G. Ganesh; HYUN, Jung Hwan; KIM, Yun Yong. Effects of foundry sand as a fine aggregate in concrete production. **Construction and Building Materials**, v. 70, p. 514-521, 2014.

PUSKAS, Ferenc. **Process for the utilization in the ceramics industry of red mud from alumina plants**. U.S. Patent n. 4,368,273, 11 jan. 1983.

PYTEL, Zdzisław. Evaluation of potential applications of recycled moulding and core sands to production of ceramic building materials. **Ceramics International**, v. 40, n. 3, p. 4351-4358, 2014.

QIN, Shuo; WU, Bolin. Effect of self-glazing on reducing the radioactivity levels of red mud based ceramic materials. **Journal of hazardous materials**, v. 198, p. 269-274, 2011.

QU, Yang; LIAN, Bin. Bioleaching of rare earth and radioactive elements from red mud using Penicillium tricolor RM-10. **Bioresource technology**, v. 136, p. 16-23, 2013.

RAMOS, Telma; MATOS, Ana Mafalda; SOUSA-COUTINHO, Joana. Mortar with wood waste ash: Mechanical strength carbonation resistance and ASR expansion. **Construction and Building Materials**, v. 49, p. 343-351, 2013.

RASHAD, Alaa M. Recycled waste glass as fine aggregate replacement in cementitious materials based on Portland cement. **Construction and Building Materials**, v. 72, p. 340-357, 2014.

REUTER, M.; XIAO, Y.; BOIN, U. Recycling and environmental issues of metallurgical slags and salt fluxes. In: **VII International conference on molten slags fluxes and salts, The South African Institute of Mining and Metallurgy**. 2004. p. 349-356.

REY-SALGUEIRO, Ledicia et al. Organic pollutants profiling of wood ashes from biomass power plants linked to the ash characteristics. **Science of the Total Environment**, v. 544, p. 535-543, 2016.

SAMAL, Sneha; RAY, Ajoy K.; BANDOPADHYAY, Amitava. Proposal for resources, utilization and processes of red mud in India—a review. **International Journal of Mineral Processing**, v. 118, p. 43-55, 2013.

SAMOUHOS, Michail et al. Greek “red mud” residue: A study of microwave reductive roasting followed by magnetic separation for a metallic iron recovery process. **Journal of hazardous materials**, v. 254, p. 193-205, 2013.

SCHWARZ, Marián; LALÍK, Vladimír. **Possibilities of Exploitation of Bauxite Residue from Alumina Production**. INTECH Open Access Publisher, 2012.

SCHWARZ-TATARIN, Anja; FREYBURG, Sabine. Influence of scrap glass powders and the maturing process in the unfired state on the body properties of a kaolinitic clay after firing. **Journal of the European Ceramic Society**, v. 30, n. 7, p. 1619-1627, 2010.

SEKAR, S. K. et al. Mechanical and fracture characteristics of Eco-friendly concrete produced using coconut shell, ground granulated blast furnace slag and manufactured sand. **Construction and Building Materials**, v. 103, p. 1-7, 2016.

SENFF, L.; HOTZA, D.; LABRINCHA, J. A. Effect of red mud addition on the rheological behaviour and on hardened state characteristics of cement mortars. **Construction and Building Materials**, v. 25, n. 1, p. 163-170, 2011.

SGLAVO, Vincenzo M. et al. Bauxite ‘red mud’ in the ceramic industry. Part 1: thermal behaviour. **Journal of the European Ceramic Society**, v. 20, n. 3, p. 235-244, 2000.

SGLAVO, Vincenzo M. et al. Bauxite ‘red mud’in the ceramic industry. Part 2: production of clay-based ceramics. **Journal of the European Ceramic Society**, v. 20, n. 3, p. 245-252, 2000.

SIDDIQUE, Rafat et al. Comparative investigation on the influence of spent foundry sand as partial replacement of fine aggregates on the properties of two grades of concrete. **Construction and Building Materials**, v. 83, p. 216-222, 2015.

SIDDIQUE, Rafat. Utilization of wood ash in concrete manufacturing. **Resources, Conservation and Recycling**, v. 67, p. 27-33, 2012.

SIDDIQUE, Rafat; NOUMOWE, Albert. Utilization of spent foundry sand in controlled low-strength materials and concrete. **Resources, Conservation and Recycling**, v. 53, n. 1, p. 27-35, 2008.

SILVA FILHO, E. B.; ALVES, M. C. M.; DA MOTTA, M. Lama vermelha da indústria de beneficiamento de alumina: produção, características, disposição e aplicações alternativas. **Revista Matéria**, v. 12, n. 2, p. 322-338, 2007.

SINGH, Gurpreet; SIDDIQUE, Rafat. Abrasion resistance and strength properties of concrete containing waste foundry sand (WFS). **Construction and Building Materials**, v. 28, n. 1, p. 421-426, 2012.

SKODA, Charles; BIRDWELL, Steven. **Stabilized red mud and methods of making the same**. U.S. Patent Application n. 13/859,699, 9 abr. 2013.

SMIČIKLAS, I. et al. The influence of citrate anion on Ni (II) removal by raw red mud from aluminum industry. **Chemical engineering journal**, v. 214, p. 327-335, 2013.

SNARS, K.; GILKES, R. J. Evaluation of bauxite residues (red muds) of different origins for environmental applications. **Applied Clay Science**, v. 46, n. 1, p. 13-20, 2009.

SUSHIL, Snigdha; BATRA, Vidya S. Catalytic applications of red mud, an aluminium industry waste: A review. **Applied Catalysis B: Environmental**, v. 81, n. 1, p. 64-77, 2008.

SWAMY, M. S. R.; PRASAD, T. P.; SANT, B. R. Thermal analysis of ferrous sulphate heptahydrate in air: Part I. Some general remarks and methods. **Journal of Thermal Analysis and Calorimetry**, v. 15, n. 2, p. 307-314, 1979.

TORKAMAN, Javad; ASHORI, Alireza; MOMTAZI, Ali Sadr. Using wood fiber waste, rice husk ash, and limestone powder waste as cement replacement materials for lightweight concrete blocks. **Construction and building materials**, v. 50, p. 432-436, 2014.

TORRES-CARRASCO, M.; PUERTAS, F. Waste glass in the geopolymer preparation. Mechanical and microstructural characterisation. **Journal of cleaner production**, v. 90, p. 397-408, 2015.

TORRES-CARRASCO, Manuel et al. Alkali activated slag cements using waste glass as alternative activators. Rheological behaviour. **Boletín de la Sociedad Española de Cerámica y Vidrio**, v. 54, n. 2, p. 45-57, 2015.

TSAKIRIDIS, P. E.; AGATZINI-LEONARDOU, S.; OUSTADAKIS, P. Red mud addition in the raw meal for the production of Portland cement clinker. **Journal of Hazardous Materials**, v. 116, n. 1, p. 103-110, 2004.

UPRETY, Bijaya K. et al. Biodiesel production using heterogeneous catalysts including wood ash and the importance of enhancing byproduct glycerol purity. **Energy Conversion and Management**, v. 115, p. 191-199, 2016.

VACLAVIKOVA, M. et al. Removal of cadmium, zinc, copper and lead by red mud, an iron oxides containing hydrometallurgical waste. **Studies in Surface Science and Catalysis**, v. 155, p. 517-525, 2005.

WEI, Yu-Ling et al. Recycling steel-manufacturing slag and harbor sediment into construction materials. **Journal of hazardous materials**, v. 265, p. 253-260, 2014.

WEI, Yu-Ling; CHENG, Shao-Hsian; KO, Guan-Wei. Effect of waste glass addition on lightweight aggregates prepared from F-class coal fly ash. **Construction and Building Materials**, v. 112, p. 773-782, 2016.

WU, Chuan-sheng; LIU, Dong-yan. Mineral phase and physical properties of red mud calcined at different temperatures. **Journal of Nanomaterials**, v. 2012, p. 2, 2012.

YALÇIN, Nevin; SEVINÇ, Vahdettin. The Characterization of a Bauxite Waste From The Bayer Process. **world**, v. 5, p. 12.

YALÇIN, Nevin; SEVINÇ, Vahdettin. Utilization of bauxite waste in ceramic glazes. **Ceramics International**, v. 26, n. 5, p. 485-493, 2000.

YANG, Jiakuan et al. Preparation of glass-ceramics from red mud in the aluminium industries. **Ceramics International**, v. 34, n. 1, p. 125-130, 2008.

YANG, Jiakuan; XIAO, Bo. Development of unsintered construction materials from red mud wastes produced in the sintering alumina process. **Construction and Building Materials**, v. 22, n. 12, p. 2299-2307, 2008.

YAO, Yuan et al. Characterization on a cementitious material composed of red mud and coal industry byproducts. **Construction and Building Materials**, v. 47, p. 496-501, 2013.

YE, Chuqiao et al. Preparation and properties of sintered glass–ceramics containing Au–Cu tailing waste. **Materials & Design**, v. 86, p. 782-787, 2015.

YEIH, Weichung et al. Properties of pervious concrete made with air-cooling electric arc furnace slag as aggregates. **Construction and Building Materials**, v. 93, p. 737-745, 2015.

YLINIEMI, Juho et al. Lightweight aggregates produced by granulation of peat-wood fly ash with alkali activator. **International Journal of Mineral Processing**, v. 149, p. 42-49, 2016.

ZHANG, Hao et al. Mechanism of red mud combined with Fenton's reagent in sewage sludge conditioning. **Water research**, v. 59, p. 239-247, 2014.

ZHANG, Mo et al. Synthesis factors affecting mechanical properties, microstructure, and chemical composition of red mud–fly ash based geopolymers. **Fuel**, v. 134, p. 315-325, 2014.

ZHANG, Na et al. Early-age characteristics of red mud–coal gangue cementitious material. **Journal of Hazardous Materials**, v. 167, n. 1, p. 927-932, 2009.

ZHANG, Na et al. Evaluation of blends bauxite-calcination-method red mud with other industrial wastes as a cementitious material: Properties and hydration characteristics. **Journal of hazardous materials**, v. 185, n. 1, p. 329-335, 2011.

ZHU, De-qing et al. Recovery of iron from high-iron red mud by reduction roasting with adding sodium salt. **Journal of Iron and Steel Research, International**, v. 19, n. 8, p. 1-5, 2012.

ZHU, Mengguang et al. Preparation of glass ceramic foams for thermal insulation applications from coal fly ash and waste glass. **Construction and Building Materials**, v. 112, p. 398-405, 2016.

ZIMMER, Erich; NAFISSI, Ahmad; WINKHAUS, Gunther. **Reclamation treatment of red mud**. U.S. Patent n. 4,119,698, 10 out. 1978.